GROWTH, ELECTRONIC STRUCTURE AND MAGNETISM OF SUPPORTED METAL NANOWIRES

THÈSE N^{O} 2184 (2000)

PRÉSENTÉE AU DÉPARTEMENT DE PHYSIQUE

ÉCOLE POLYTECHNIQUE FÉDÉRALE DE LAUSANNE

POUR L'OBTENTION DU GRADE DE DOCTEUR ÈS SCIENCES

PAR

Pietro GAMBARDELLA
laureato in fisica, Università degli Studi di Genova, Italie
de nationalité italienne

acceptée sur proposition du jury:

Prof. K. Kern, directeur de thèse
Dr C. Carbone, rapporteur
Prof. B. Deveaud-Plédran, rapporteur
Prof. U. Valbusa, rapporteur

Lausanne, EPFL
2000

Abstract

This thesis describes experiments with one-dimensional atomic chains grown by step decoration of vicinal Pt surfaces. The objective of the research was twofold: first, to characterize metal epitaxial growth on stepped substrates; second, to make use of this knowledge to fabricate arrays of monatomic metal wires in order to investigate their electronic and magnetic properties.

The first part focuses on molecular beam epitaxy (MBE) of Ag, Cu, Co, and Ni on densely stepped Pt surfaces (one monatomic step every 20 Å). Growth was investigated on the atomic scale as a function of the substrate temperature and coverage by means of thermal energy atom scattering (TEAS) and scanning tunneling microscopy (STM). A wide variety of growth scenarios has been characterized depending on the choice of the overlayer material and on the interplay between surface diffusion, strain and alloying. Uniform arrays of one-dimensional atomic chains of Ag, Cu, and Co can be fabricated in a well defined temperature range. The growth of alternate wires of different metals was also investigated.

In the second part we have studied the chemisorption of O_2, CO, and H_2 at Pt and at Ag-decorated Pt steps. We have identified the Pt edge atoms at the top of the step as the most active sites for O_2 dissociation. Controlled decoration of the Pt steps by monatomic Ag wires was used to locally vary the reactivity of the Pt edge atoms and to further elucidate the dissociation process. Ag decoration results in a selective modification of the adsorption rate of O_2, CO, and H_2 on Pt stepped surfaces.

The third part deals with the electronic and magnetic properties of Co monatomic wires grown on Pt(997). We have investigated the wire-induced valence band states by means of angle resolved photoemission (ARPES). Co $3d$ states attributed to monatomic chains display a double-peaked structure that suggests the presence of a one-dimensional exchange-split band. The magnetic behavior of the Co chains was studied by x-ray magnetic circular dichroism (XMCD). Co monatomic chains are superparamagnetic with blocking temperature between 5 and 10 K. The one-dimensional character of the wires shows up in a pronounced uniaxial magnetic anisotropy and in large values of the orbital magnetic moment compared to bulk Co and thin films.

Version Abrégée

Cette thèse est basée sur des expériences faites avec des fils atomiques unidimensionnels obtenus par la décoration des marches de surfaces vicinales de Pt. On a d'abord entamé l'étude de la croissance épitaxiale sur des tels substrats. En suite, on a utilisé cette connaissance pour fabriquer des ensembles ordonnés de fils monoatomiques métalliques avec le but d'en étudier les propriétés électroniques et magnétiques.

La première partie de ce travail traite de la croissance épitaxiale par jet moleculaire de Ag, Cu, Co, et Ni sur des surfaces vicinales de Pt avec une densité elevée de marches (une marche monoatomique chaque 20 Å). La croissance a été étudiée à une échelle atomique en fonction de la température et du recouvrement du substrat par diffusion d'hélium et par microscopie à effet tunnel. On a identifié plusieurs modes de croissance qui dépendent du choix du matériel déposé et de l'enjeu entre diffusion, contraintes mécaniques et formation d'alliage sur le substrat. Des ensembles uniformes des fils atomiques de Ag, Cu, et Co peuvent être fabriqués dans des conditions de température bien definies. La croissance alternée de rangées de différents métaux a aussi été étudiée.

En deuxième partie, on a etudié la chimisorption de O_2, CO, et H_2 sur des marches de Pt propres et décorées avec Ag. On a déterminé que la dissociation des molécules de O_2 se passe de préférence sur les atomes de Pt en haut de la marche. La décoration contrôlée des marches de Pt avec des fils atomiques d'Ag a permis de varier la réactivité chimique de la marche d'une façon locale et de gagner d'avantage d'information sur le processus de dissociation. De plus, la décoration des marches de Pt avec Ag produit une variation sélective du taux d'adsorption pour O_2, CO, et H_2.

Finalement, nous avons étudié les propriétés électroniques et magnétiques de fils de Co croît sur Pt(997). L'étude des états électroniques dûs aux fils de Co a été éffectuée par la photoémission aux rayons UV. Le spectre des états $3d$ dûs au Co montre deux pics qui suggèrent la présence de bandes électroniques séparées par l'échange magnétique. Le comportement magnétique des fils de Co a été analysé par le dichroisme magnétique circulaire de rayons X. Les fils monoatomiques de Co sont superparamagnétiques et ont une température de blocage entre 5 et 10 K. Le caractère unidimensionnel des chaînes atomiques de Co produit une anisotropie magnétique uniaxiale marquée. La valeur du moment magnétique orbital est élevée par rapport aux valeurs que l'on mesure dans des systèmes volumiques de Co et dans des couches minces, à cause de la faible coordination des atomes de Co dans les fils monoatomiques.

Contents

Chapter 1

TEAS and STM: two complementary methods

This chapter presents thermal energy atom scattering (TEAS) and scanning tunneling microscopy (STM). These two techniques have been employed to conduct the *in situ* characterization of the substrate and of the nanowire growth process (Secs. 2 and 3) as well as chemisorption studies (Sec. 4). The combination of TEAS and STM is particularly advantageous since it combines atomic insight with macroscopic-scale information and extreme surface sensitivity.

1.1 TEAS

Principles

In a typical He scattering experiment, a monochromatic beam of neutral He atoms is directed on the sample surface and its scattered intensity is measured by an ionization detector. For thermal energy beams (10-100 meV) the interaction between the incident He atoms and the surface is limited to the topmost substrate layer and it is totally non-destructive. The angular and the energy distribution of the intensity of the reflected He beam carries information on the morphology of the substrate, on the presence and structure of adsorbates and on inelastic scattering events between He and surface atoms [1,2]. The He-surface interaction potential V is the sum of an attractive contribution due to long-range van der Waals forces, and of a steep repulsive contribution originating from the overlap of the incoming atoms wavefunctions with those of the substrate atoms (Fig.1.1). Van der Waals attraction is responsible for the giant cross sections of adsorbates and defects which make TEAS an extremely sensitive probe for growth and

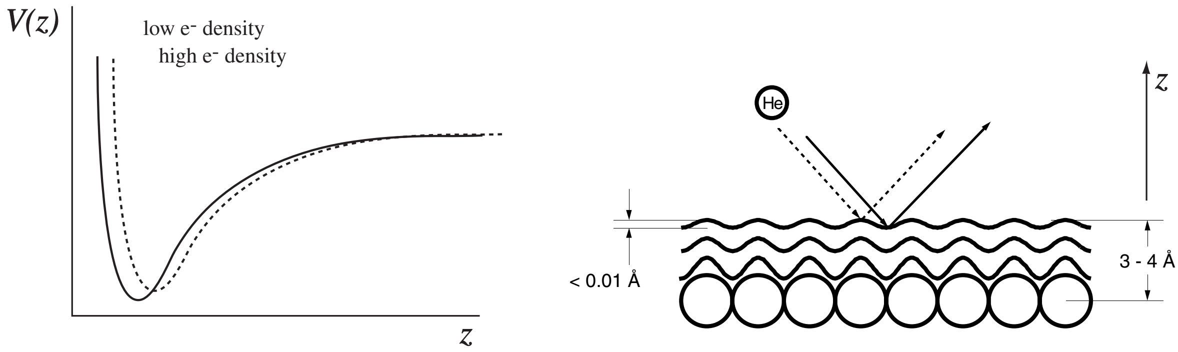

Figure 1.1: (a) Schematic He-surface potential as a function of z (normal to the surface). (b) Constant electron density contours determining the turning points of the He atoms.

chemisorption processes [3], while Pauli repulsion is proportional to the surface electron density at the classical turning points of the He atoms, and it determines the sensitivity of TEAS measurements to the surface atomic corrugation and structure [1, 2]. Here we concentrate on the ability of TEAS to monitor and characterize the formation of adsorbate structures, as well as the surface morphology, during metal deposition and exposure to gas molecules.

Surface structure determination by TEAS

The particle-wave dualism of He atoms is beautifully evidenced by diffraction experiments from periodic crystalline surfaces [4]. If the He-beam energy is known , one can determine the periodic corrugation of the substrate by measuring the angular positions of the diffraction peaks. Figure 1.2 shows an example of diffraction from a flat (110) Ni surface taken from Ref. [5]. Besides measuring the periodicity of the atomic lattice, He diffraction can be employed to characterize the structure of periodically stepped substrates. This aspect of TEAS turns out to be particularly useful in preparing and characterizing the Pt vicinal surfaces that have been employed in the present study. Consider the diffraction of a He beam from a perfectly periodic and atomically flat (zero corrugation) stepped surface, as the one depicted in Fig. 1.3. The zero corrugation approximation is reasonable because on flat close-packed metal surfaces, such as Pt(111), the atomic corrugation is of the order of 0.01 Å [6]. The plane of incidence of the He beam is taken to be perpendicular to the steps. The angles θ_i and θ_f are defined with respect to the (997) direction (normal to the macroscopic surface) and ϕ_i and ϕ_f are defined with respect to the (111) direction (normal to the terraces). They are related to each other by the following relationship: $(\theta_i, \theta_f) = (\phi_i + \alpha, \phi_f - \alpha)$ where α is the miscut angle with respect to the low-index (111) surface. $\chi = \phi_i + \phi_f = \theta_i + \theta_f$

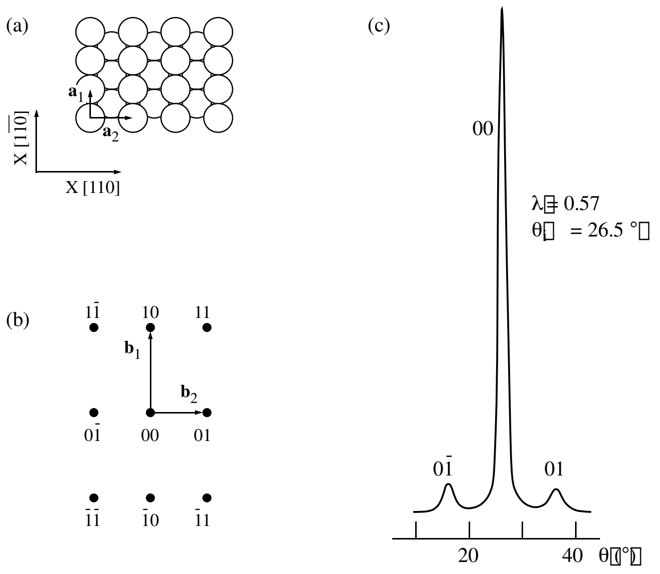

Figure 1.2: (a) Hard-sphere model of the Ni(110) surface. (b) Reciprocal lattice (c) He diffraction spectrum showing the first order diffraction peaks due to the atomic corrugation of the surface in the (110) direction (from Ref. [5]).

is the total scattering angle. In complete analogy with blazed reflection gratings known from optics, we may consider that He diffraction takes place on a periodic lattice with the terrace (considered as a mirror) as the unit cell [3]. The intensity of the He beam scattered from the surface can then be described as the product of a structure function G and of a form factor function A:

$$I = \mathrm{c}A^2G^2 \tag{1.1}$$

where c is a normalization factor. The structure function determines the position of the diffraction peaks and is given by the one-dimensional Bragg equation [7] for the step

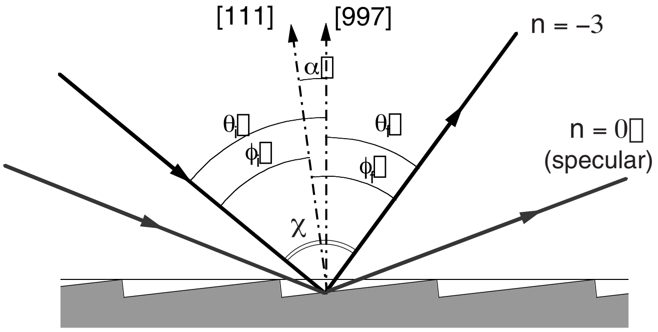

Figure 1.3: Sketch of step-down scattering from a periodically stepped surface, in this case a Pt(997) surface.

periodicity

$$G^2 = \sum_n \delta(\sin\theta_f - \sin\theta_i - \frac{n\lambda}{d}) \tag{1.2}$$

where λ is the He wavelength, n is the diffraction order and d is the step periodicity, equal to the step height h (=2.27 Å for Pt) divided by $\sin\alpha$. The intensity of the diffraction peaks defined by eq. 1.2 is modulated by the form factor A^2, i.e. by the diffraction pattern of a single terrace. Following the analogy with optics in the plane wave approximation, A^2 can be calculated by considering the diffraction from a single rectangular slit having the same width as the illuminated part of the substrate terraces [7]:

$$A^2 = \frac{\sin(\beta/2)^2}{(\beta/2)^2} \tag{1.3}$$

$$\text{with} \qquad \beta = \frac{2\pi}{\lambda}\,\tilde{d}\,(\sin\phi_i - \sin\phi_f) \tag{1.4}$$

where $\tilde{d} = h \cdot \left(\frac{1}{\tan\alpha} - \tan\phi_i\right)$ is the part of the terrace iluminated by the He beam.

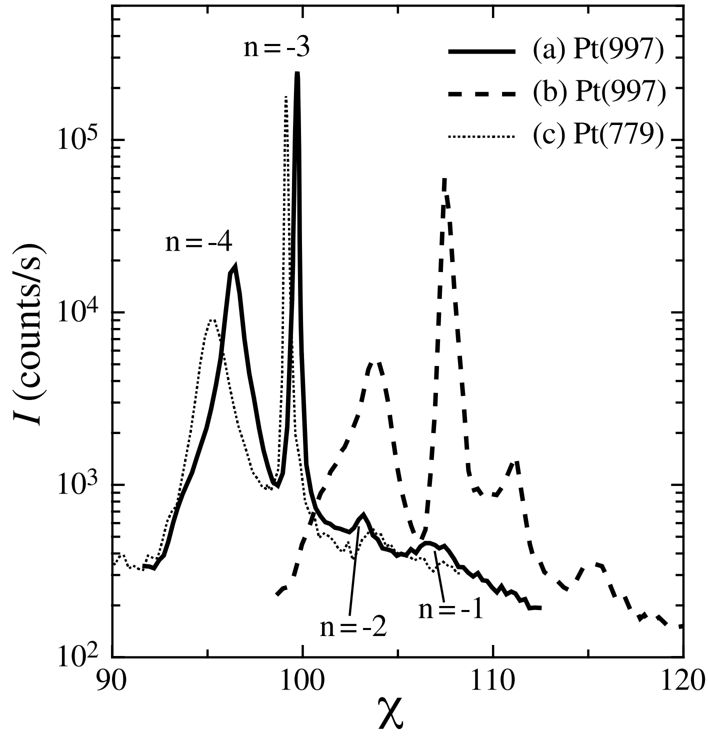

Figure 1.4: Diffraction of a 22 meV He beam from Pt(997) in ideal ($\theta_i = 56.4°$) and non-ideal ($\theta_i = 60°$) conditions for the $n = -3$ peak, solid line and dashed line, respectively. Note that the $n = -3$ non-ideal peak is larger with respect to the ideal case. The dotted line is the diffraction spectra of Pt(779) in the $n = -3$ ideal conditions ($\theta_i = 56.6°$).

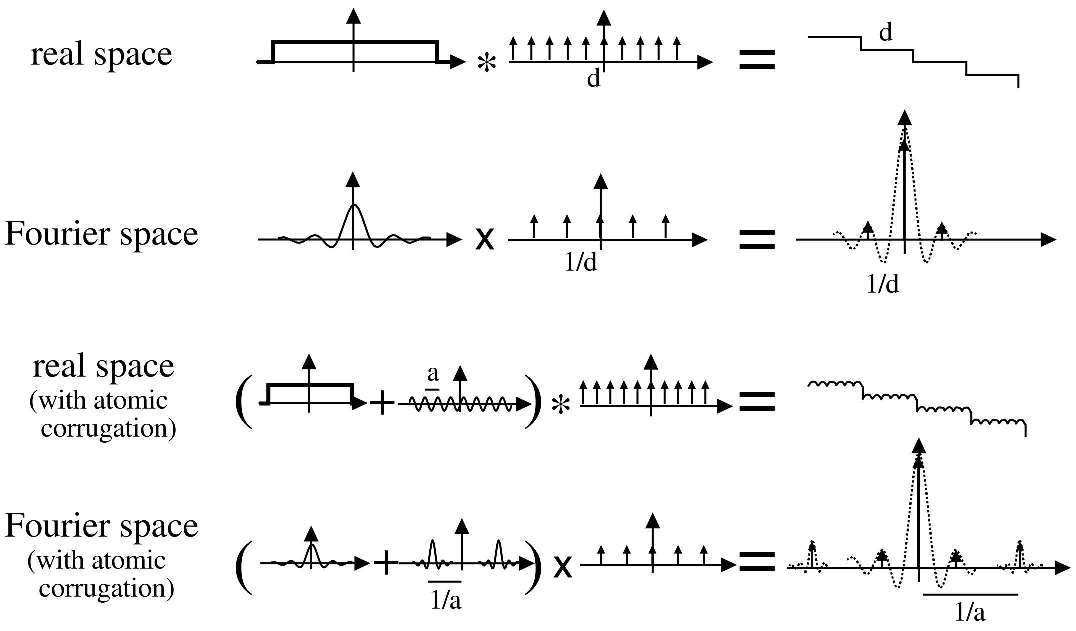

Figure 1.5: The convolution $(*)$ of a Heaviside function with a periodic δ array gives the periodic structure of a stepped surface. Its diffraction pattern can be calculated in reciprocal space by multiplying $(\times)$ the corresponding Fourier transforms. Adding the atomic corrugation to each terrace modulates further the envelope function A^2.

A variation of the angle of incidence θ_i leads to a continuous shift of the position of the diffracted beams given by Eq. 1.2 with respect to the form factor 1.3, which has its maximum in the specular direction to the terraces $(\phi_i = \phi_f)$. By a suitable choice of θ_i the diffracted beam of a certain order n can be made to coincide with the maximum of the form factor [3]; Eq. 1.2 then reduces to

$$cos\phi \;=\; \frac{n\lambda}{2h} \quad , \quad \text{where} \quad \phi = \phi_i = \phi_f \,. \tag{1.5}$$

In this so-called *ideal* condition [8–10] all the atoms on adjacent terraces scatter in-phase; the width of the n^{th} peak reaches a minimum which coincides with the instrumental resolution of the He beam. In *non-ideal* conditions the width of the diffraction peaks is mainly determined by the terrace width distribution of the surface. Figure 1.4 shows the diffraction pattern of a Pt(997) and Pt(779) surface: the $n = -4, -3, -2, -1$ diffraction orders are visible starting from the left; the position of their maxima, according to Eq. 1.2, yields the step periodicity of the surface d, once the value for λ is known. To determine λ one has to find the ideal condition for a given peak experimentally and then use Eq. 1.5. This procedure applied to the Pt(997) and Pt(779) crystals employed in this work yields a mean terrace width of 20.0 Å and 18.5 Å for the two surfaces, respectively, which is very close to the theoretical values reported in Fig. 2.3. The TEAS measurements of adsorbate (metals and gas molecules) coverage reported in the

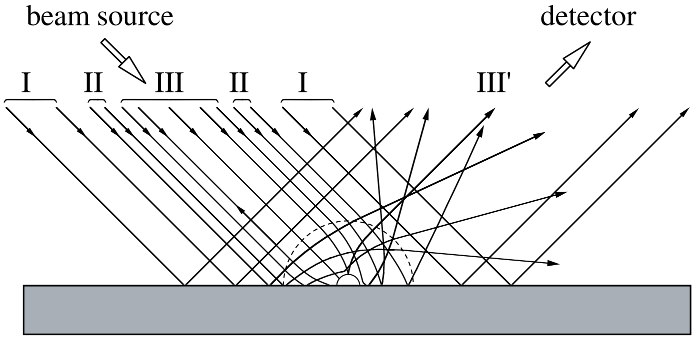

Figure 1.6: He scattering on an isolated adatom or defect on a flat surface (from Ref. [3]). Type I trajectories reflect undisturbed, type II and III scatter on the repulsive and attractive part of the potential, dashed line and solid line semi-circles, respectively. The long-range attractive part of the potential is responsible for values of the TEAS cross sections of isolated defects that are much larger than their geometric dimensions.

following chapters are taken by analysing the intensity of the $n = -3$ ideal peak and the $n = 0$ peak. The above expressions assume that the terrace corrugation is negligible. This is reasonable since metallic (111) surfaces exhibit a very smooth electronic density variation due to electron delocalization. A weak corrugation on the terraces however exists and gives rise to additional modulation of the diffraction spectrum at the positions given by the 1D-Bragg equation

$$\sin\phi_f - \sin\phi_i = \frac{m\lambda}{a} \tag{1.6}$$

where m is an integer and a is the periodicity of the corrugation on the terrace parallel to the scattering plane. Figure 1.5 shows how the position of the diffraction peaks in the reciprocal space is related to the real space geometry of a stepped surface.

TEAS sensitivity to adsorbates

The scattering of thermal He atoms from solid surfaces is extremely sensitive to the presence of adsorbates and defects. Adsorbed atoms, kinks, vacancies, and random steps affect the interaction of the He beam with the surface by strong local perturbations of the scattering potential (Fig. 1.6).

The superposition of random scattering centers on an otherwise periodic potential enhances the diffuse scattering, resulting in a strong decay of the in-plane reflected intensity. This is what happens during, e.g., the initial stages of metal deposition or gas exposure of the surface. Ordered layer of adsorbates impose a periodic structure on the interaction potential. Depending on whether He scattering from the adsorbate layer is predominantly elastic or inelastic (Debye-Waller effect), the surface in-plane reflectivity [3] will be closer to 1 or to 0, respectively. We will see in the following paragraphs that light admolecules in most cases act as diffuse scatterers reducing the in-plane intensity of the scattered He beam, whereas metal adatoms forming ordered structures have a non-zero reflectivity.

TEAS as a probe of CO, O, H chemisorption

The low Debye temperature of, e.g., CO, NO, O_2, O, Xe layers adsorbed on close-packed metal surfaces (i.e. the fact that the He atoms can easily exchange energy with the vibrational modes of the adsorbates) is responsible for the strong diffuse scattering of He atoms. [3]. Figure 1.7(a) evidences how the overall in-plane He intensity reflected by the surface is reduced upon oxygen adsorption. By positioning the detector in correspondence of one of the peaks shown in Fig. 1.7, one can monitor the reflectivity of the surface during adsorption. The decay of the He intensity due to CO (a) and O (b) adsorption on Pt(111) and Pt(997) is shown in Fig. 1.8. I/I_0 refers to the normalized height of the specular peak for Pt(111) and of the $n = -3$ peak for Pt(997). The intensity decreases monotonically until the complete saturation of CO and O adlayers. Since diffuse and coherent scattering are complementary phenomena, the attenuation of the relative peak intensities is a measure of the probability of diffuse scattering, hence it can be related to the adsorbate coverage. Provided that the peak maxima can be taken as a

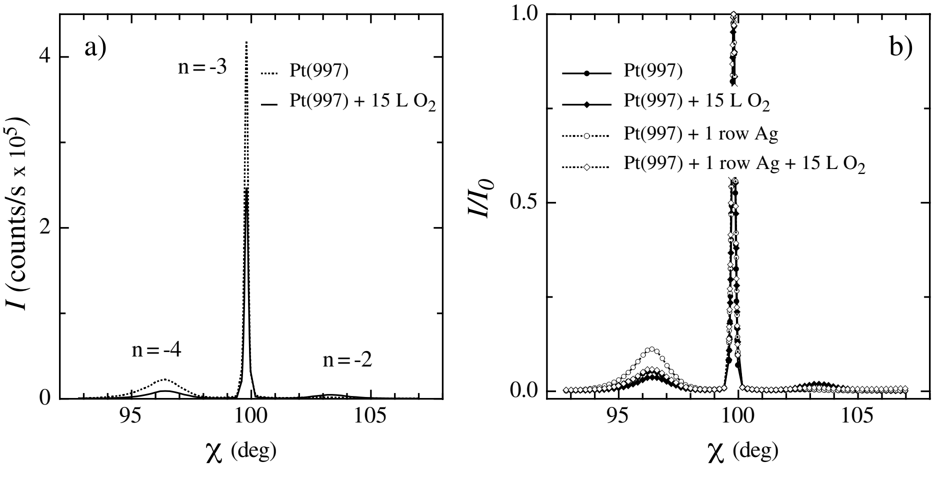

Figure 1.7: (a) TEAS diffraction pattern for a clean and partially-O covered Pt(997) surface at 400 K. (b) Normalized diffraction patterns for different O exposures for a clean and a Ag step-decorated Pt(997) surface.

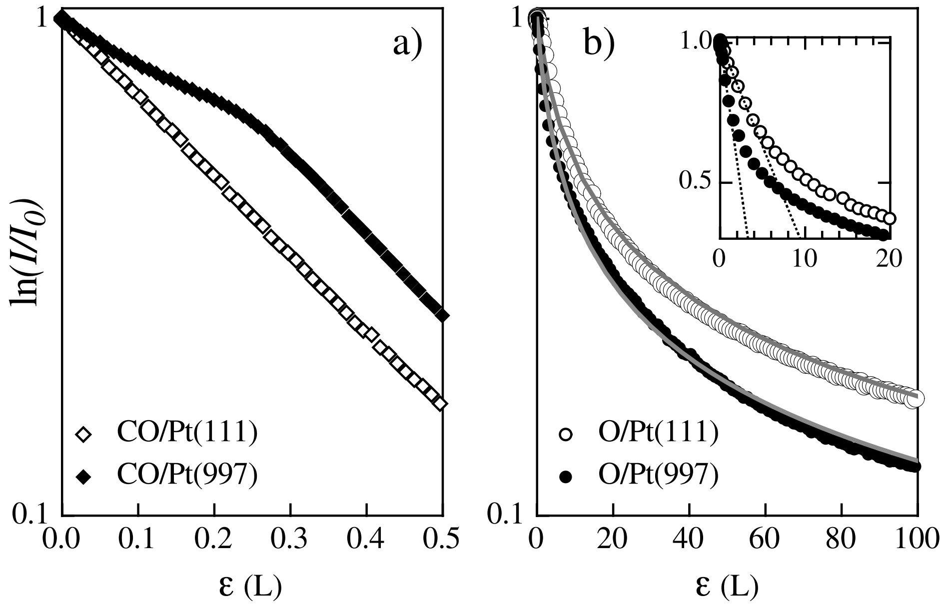

Figure 1.8: (a) Attenuation of the TEAS intensity I relative to the clean surface value I_0 during exposure to a background pressure of 2×10^{-8} mbar CO for Pt(997) at and Pt(111) at 340 K and 400 K, respectively. After saturation of the step sites around 0.2 L the slope of the Pt(997) at and Pt(111) curves is the same. (b) Same as (a) for 1×10^{-6} mbar O_2 exposure at 400 K. The solid lines are fits to the data. The inset shows a linear fit (dashed line) of the adsorption curves in the zero coverage limit.

measure of the in-plane reflectivity [see Ref. [3] and Fig. 1.7(b)], the quantity $1 - I/I_0$ is proportional to the probability of diffuse scattering. In the limit of high adsorbate dilution one has [3]:

$$1 - I/I_0 = \mathrm{n_s} \, \Sigma \, \theta \tag{1.7}$$

where θ is the adsorbate coverage, $\mathrm{n_s}$ the number of substrate atoms per unit area [1.5×10^{15} atoms/cm^2 for Pt (111)], and Σ the adsorbate cross-section for diffuse scattering. Σ generally depends on the energy of the probe particles and on their angle of incidence, but not on the surface temperature [11]. For CO on Pt(111), $\Sigma = 123$ Å^2 for a 63 meV He beam incident at $\theta_i = 40°$; at step sites the CO cross section takes on smaller values [3]. The CO/Pt(997) adsorption curve in Fig.1.8(a) shows an increase in slope around 0.2 L which is due to sequential occupation of the terrace sites after the step sites have been completely CO-saturated. Once the step sites have been filled, the Pt(997) and Pt(111) curves become parallel. In contrast to the CO case, the O/Pt(997) adsorption curve shows no abrupt slope change [Fig.1.8(b)]. In other words we do not observe any net disparity in the cross section for step and terrace adsorption of O, although sequential occupation of step and terrace sites by O is a well-established fact [12–18]. Differences between the CO and O cross section behaviors can be attributed to the different binding geometries at step sites (see Sec. 4).

In the high coverage limit the linear dependence of I/I_0 on θ breaks down. The overlap of the cross section of adatoms occupying neighbor sites as well as depolarization effects due to mutual interactions, and the possibility of multiple scattering events lead to a more complex $I/I_0(\theta)$ relationship. By considering a pure geometric overlap between the adsorbates cross sections and forbidden l-nearest-neighbor adsorption, for instance, one gets [3]

$$I/I_0 = (1 - l\theta)^{\frac{\mathrm{n_S}\,\Sigma}{l}} \,. \tag{1.8}$$

The fits in Fig.1.8(b) are based on this formula plus the assumption of Langmuir adsorption to model the dependence of the gas exposure ε on θ. To avoid relying on *ad hoc* assumptions, however, we prefer to limit ourselves to Eq. 1.7, which has the advantage of being independent of the system and which allows us to estimate the relative variations of the initial sticking coefficient of a given species between different samples. Consider the zero coverage limit: in this regime θ can be approximated by the sticking coefficient s_0 times ε; I/I_0 is then given by

$$I/I_0 = 1 - \Sigma\, s_0\, \varepsilon \,. \tag{1.9}$$

Taking the derivative of I/I_0 at $\theta = 0$ one gets Σs_0. To calculate s_0 one therefore needs to know Σ. In the case of oxygen adsorption on Pt(111) shown in the inset Fig. 1.8(b), for instance, by taking $\Sigma = 60$ Å^2, as it was measured by Peterlinz and Sibener for O/Ru(0001) [19], we calculate s_0=0.02 at 400 K, close to the 0.03-0.08 values found in the literature for background adsorption at 300 K [13, 14, 16, 20, 21]. It wouldn't be correct, however, to compare adsorption on different surfaces in the lack of a detailed knowledge of Σ in each case. Despite this, TEAS can be used very succesfully to detect changes in s_0 on the same surface as a function of any parameter, provided that the values of Σ remain reasonably constant over the parameter's range. Absolute s_0 values can then be extracted by comparison with TPD, King & Wells, and other techniques. In Sec. 4 we apply Eq. 1.9 to evidence the variations of the sticking coefficient of a vicinal Pt surface as the step sites are decorated by different amounts of Ag and Cu.

Metal structures characterization

In contrast to gas adsorption (Fig. 1.8), if we monitor the TEAS intensity during Ag deposition on a Pt surface, the ratio I/I_0 will not fall asymptotically to zero, but it will oscillate as a function of the Ag coverage. Ordered metal adlayers, due to the small

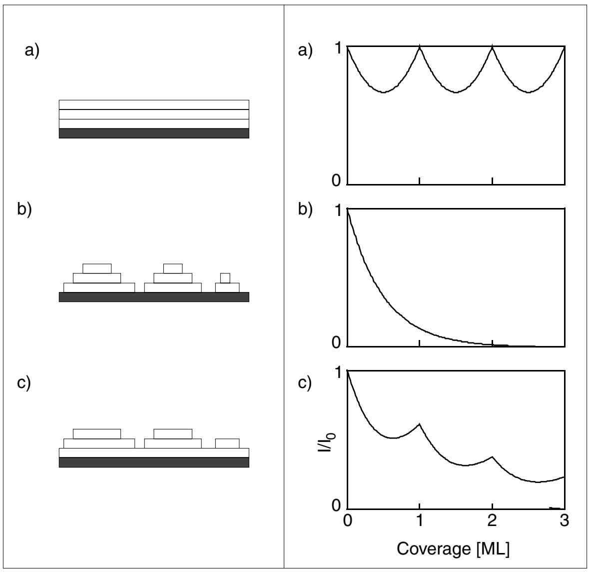

Figure 1.9: TEAS intensity as a function of coverage (right) for different growth modes (left): (a) layer-by-layer; (b) 3D; (c) imperfect layer-by-layer.

corrugation and to their rigidity, diffract the He atoms coherently, much in the same way as the substrate. The Debye temperature of the adlayer determines its reflectivity. A pseudomorphic monolayer of Ag on Pt, for instance, has a higher reflectivity than the Pt substrate.

Adisland edges, small isolated aggregates as well as dislocations in the metal adlayer constitute diffuse scattering centers. Given the high sensitivity of He scattering to the surface density of defects, TEAS is a powerful method to characterize the growth mode of metal structures on surfaces [22–24]. The TEAS intensity reflected from the sample during the growth of metal adlayers can be monitored continuosly during deposition. In the case of 2D layer-by-layer growth the surface defect density reaches a minimum each time a layer is completed; the TEAS intensity oscillates with a 1 ML period [Fig. 1.9(a)]. In the case of 3D growth the defect density increases monotonically during the deposition and the He intensity rapidly decays to zero (b). In the case of an imperfect layer-by-layer growth mode, the growth begins in a 2D- and continues in a 3D-fashion; we observe few intensity oscillations which are damped due to imperfect growth (b). This is what happens during epitaxial growth on flat crystalline surfaces [22]. On stepped surfaces, if the scattering geometry is chosen such that the He atoms reflected from adjacent terraces interfere constructively (the so called in-phase condition), we can monitor the average terrace defect density as if we were considering scattering from a flat surface. Moreover, as discussed in a recent paper [10], on vicinal surfaces the sensitivity to different surface sites shows substantial variations depending on the scattering geometry. By changing the scattering geometry we can select the regions of the surface we are looking at; this turns out to be particularly useful to characterize step decoration. Grazing incidence conditions (large θ_i values) greatly enhance the step sensitivity, while scattering angles closer to the surface normal probe the ordering of the entire surface. Thanks to this particular sensitivity it becomes possible to observe in real-time the formation of ordered 1D structures down to the monatomic limit.

TEAS characterization of 1D monatomic wire growth

We have mentioned in the introduction that vicinal surfaces can be used as nanotemplates for the growth of 1D monatomic wires exploiting step decoration. In this paragraph we show how the process of step decoration can be directly monitored and calibrated by TEAS measurements. We discuss some general features of the He reflectivity spectra in the particular case of Ag/Pt(997); similar arguments hold for other metals as well. Fig. 1.10 shows two deposition curves for Ag on Pt(997) at $\theta_i = 46.9°$ (a) and $\theta_i = 85.0°$ (b). The intensity in (a) oscillates with a period of one monolayer coverage, demonstrating in this case a layer-by-layer growth mode and serving as a precise calibration for the deposition rate. The contribution of the flat terraces to the reflected He intensity diminishes with increasing scattering angle while the step contribution increases. In (b) we observe a first peak at 0.13 ML and a pronounced shoulder at 0.25 ML. Since the He reflectivity in grazing conditions depends on the defect density at the step edges and because 0.13 ML is the nominal coverage of a monatomic wire on Pt(997), we attribute these peaks to the formation of the first and second Ag row along a Pt step edge [10], respectively.

The situation for $\Theta_{Ag} \geq 0.25$ ML is more complex. We do not observe further row peaks in the grazing incidence curve; however, this does not rule out the persistence of row-by-row growth. The averaging out of the He reflected intensity is due to desynchronization of the row growth on terraces that have different widths. Since for $T \leq 400$ K Ag adatoms are confined to their impact terrace (see inset in Fig. 1.11(a) and Sec. 2.2), the coverage on each terrace is proportional to the terrace width. Thus the rows on larger terraces are completed before those growing on smaller terraces. The simulation in Fig. 1.10 (c) qualitatively illustrates this effect for a terrace width distribution with standard deviation $\sigma = 3.6$ Å which is close to the STM determined value of 2.9 Å. In the simulation, we assume no interlayer mass transport and perfect row-by-row growth on each terrace; the intensity is obtained by weighting the fractional row coverage on each terrace by the statistical occurrence of the terrace width. As the adatom coverage approaches 1 ML, "resynchronization", as shown by the dotted line in Fig. 1.10(c),

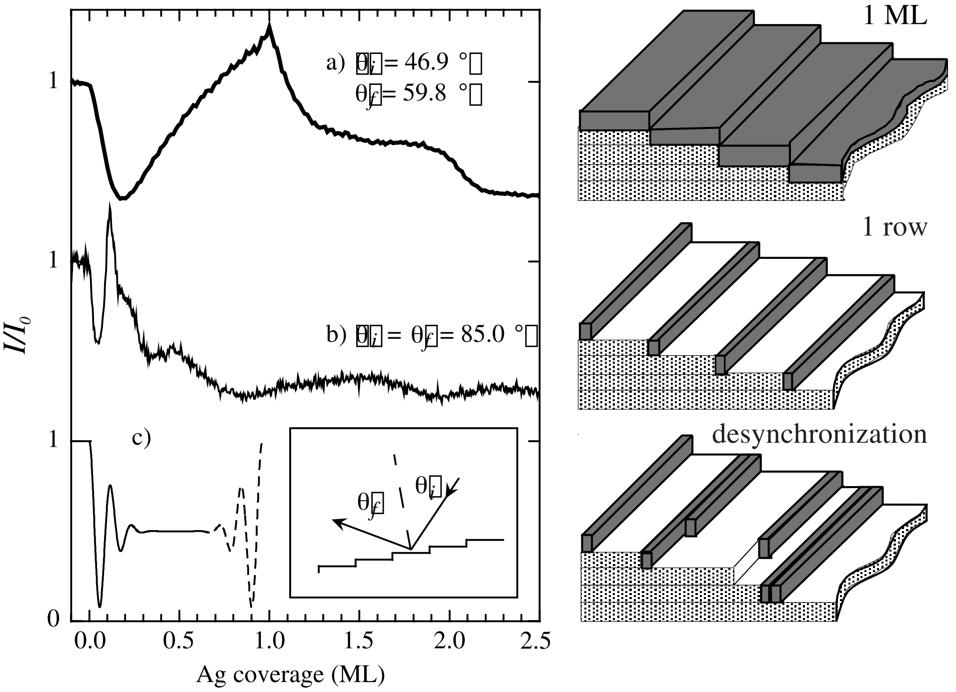

Figure 1.10: Normalized intensity of the reflected He-beam during deposition of Ag at $T =$ 300 K for different scattering geometries. (a) Small total scattering angle. (b) Large scattering angle (grazing conditions). The deposition rate is $F = 4 \times 10^{-3}$ ML/s for both curves. The He-beam wavelength λ_{He} is 1.01 Å. (c) Simulated He reflectivity in grazing incidence conditions showing the effect of the row growth desynchronization.

should occur. This is not the case for the Ag/Pt(997) system because the step edges of the growing monolayer are no longer smooth for $\Theta_{Ag} > 0.6 - 0.7$ ML (see Fig. 2.13). In contrast, resynchronization is observed on Pt(779), Fig. 1.11(b), which has the same terrace structure of Pt(997) but steps consisting of {100} instead of {111} microfacets.

If the He beam incidence angle is reduced slightly ($72° < \theta_i < 85°$) the reflected He intensity has a contribution from both the terraces and the steps [10]. A 4° variation in the total scattering angle with respect to the lower curve in Fig. 1.10 considerably changes the reflectivity of the surface. For $\theta_i = 83°$ a broad maximum appears around 0.5 ML (see Fig. 1.11). This maximum reflects the evolution of the terrace width distribution during the growth of the first monolayer. Due to the adatom confinement effects described above the standard deviation σ of the terrace width distribution reaches a minimum for $\Theta_{\mathrm{Ag}} = 0.5$ ML [25]; this process is analogous to a step debunching effect where the velocity of each step is proportional to the width of the terrace it has in front [26]. As a result, the better surface periodicity narrows the grazing incidence diffraction peak and increases its height. The 0.5 ML peak thus adds valuable information on the growth process, marking the presence of effective diffusion barriers across

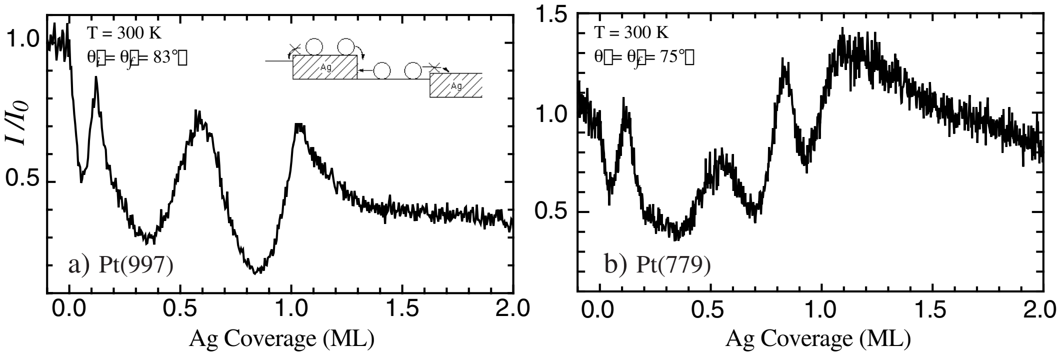

Figure 1.11: (a) TEAS intensity during Ag deposition on Pt(997) at 300 K, $\theta_i = \theta_f = 83°$, $\lambda_{He} = 1.08$ Å. The deposition rate is $F = 4 \times 10^{-3}$ ML/s. (b) Same as (a) for Ag/Pt(779) at $\theta_i = \theta_f = 75°$. The peak at ~ 0.85 ML is due to row growth resynchronization, as explained in the text.

heterosteps.

In Fig. 1.11 there is a third maximum at $\Theta_{\mathrm{Ag}} = 1$ ML. As discussed in Ref. [10] this maximum disappears at a more grazing incidence [see Fig. 1.10 (b)]; its intensity comes from the Ag covered terrace which has a higher reflectivity than bare Pt.

In summary, by analyzing the TEAS curves recorded at different angles of incidence we have a means to detect the formation of monatomic wires and the quality of the surface periodic pattern in real-time during the deposition process. As we will see in the following chapters, TEAS measurements allow us to conduct systematic growth studies to obtain uniform arrays of parallel 1D wires and to prepare samples with extremely well-defined wire coverages.

TEAS experimental setup

This section is dedicated to a brief description of the TEAS experimental apparatus. The conception of the instrument as well as the construction details are described in Refs. [8, 9, 25, 27]. The He spectrometer is schematically shown in Figs. 1.12 and 1.13. It consists of three principal modules:

- the He beam source (I-III in Fig. 1.12),

- the sample chamber (IV),

- the detection unit (V-VIII).

The He beam is created in the source by a supersonic expansion through a 10 μm nozzle [28, 29]. The stagnation pressure inside the nozzle can be varied up to 300 bar

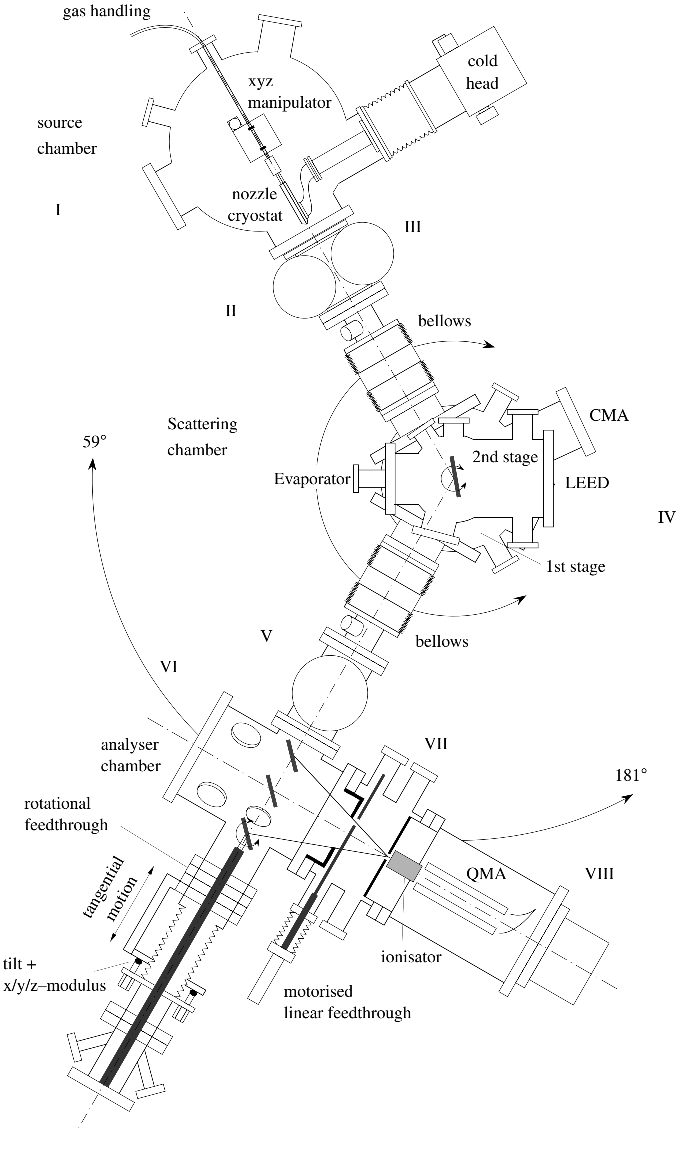

Figure 1.12: top-view of the TEAS spectrometer.

while a 6000 l/s diffusion pump coupled to a roots pump ensures a 10^{-6} mbar vacuum in the expansion chamber. Following the supersonic expansion the beam goes through two consecutive skimmers (ø 0.28 and 0.20 mm) positioned at the entrance of the two differentially-pumped stages II and III. Its angular divergence at the sample position (about 0.07°) is determined by a 0.23 mm wide slit at the exit of stage III. The He beam spot on the sample is about 1×5 mm^2. The nozzle temperature can be varied between 50 K and 350 K by the combined use of a helium cold head and a resistive filament. This temperature range allows to vary the energy of the He beam between 10 and 80 meV (1.5 to 0.5 Å). The kinetic energy broadening of the beam $\Delta E/E$ is 1.5%.

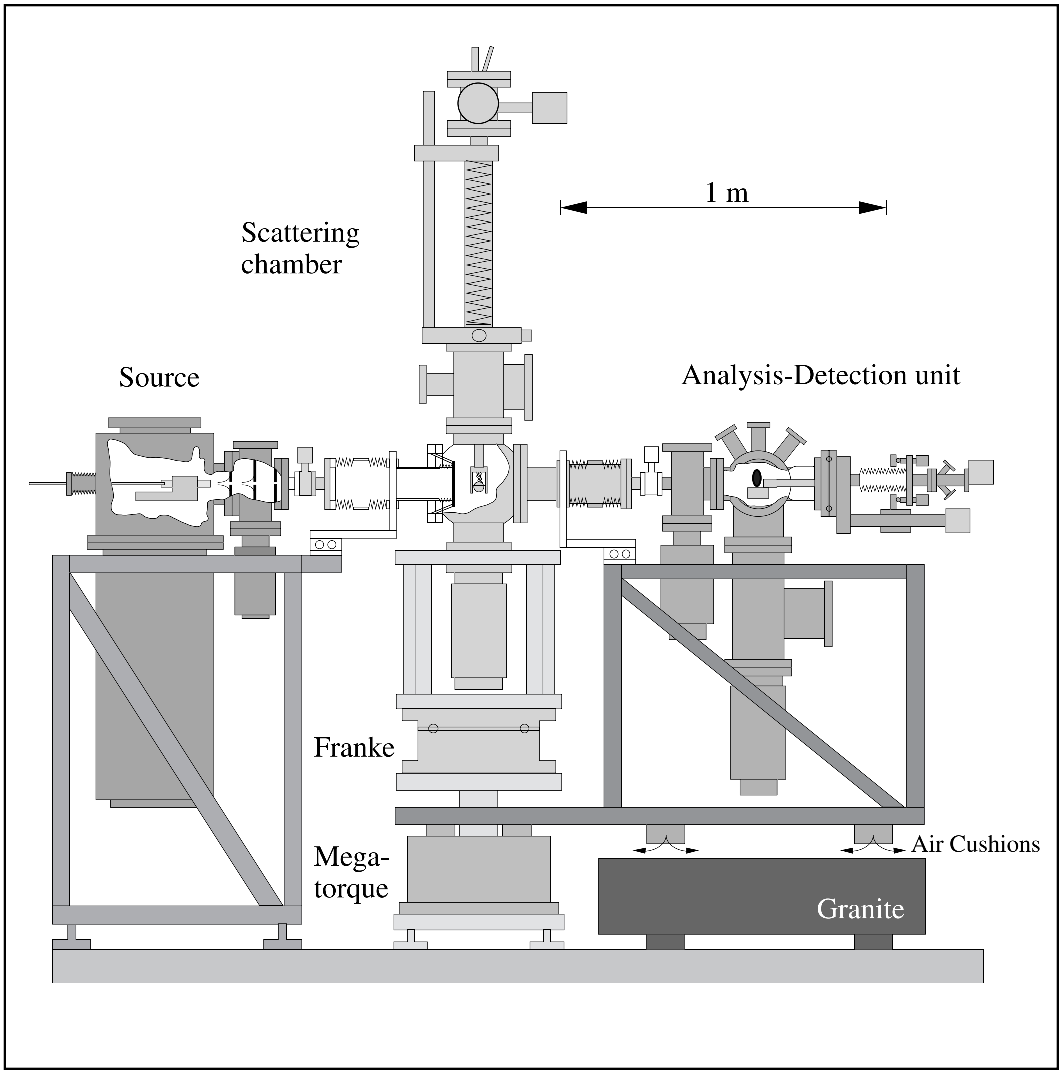

Figure 1.13: side-view of the TEAS spectrometer.

The sample or scattering chamber (IV) is kept under constant UHV conditions (base pressure 1×10^{-10} mbar) by two serial turbopumps. The He pressure due to the beam fluence is of the order of 2×10^{-9} mbar with negligible amounts of contaminants. The sample is positioned on a vertical manipulator with six degrees of freedom (x, y, z, and the *polar, tilt, azimuth* angles) to allow the precise adjustment of the scattering geometry. Its temperaure can be varied from 40 to 1100 K by a liquid He/liquid N_2 cryostat and by electron bombardment. The scattering chamber is equipped with the standard surface science tools, consisting in an ion sputter gun, a LEED, a cylindrical mirror analyzer (CMA) Auger spectrometer (Omicron, CMA 150), and Omicron e-beam metal evaporators. The whole chamber is mounted on a motorized rotary table that can rotate by ±30.5° from the position shown in Fig. 1.13 with a precision of 0.01°.

The UHV connection with the source and detection modules is ensured by two flexible bellows as shown in Figs. 1.12 and 1.13.

The detection unit consists of four differentially pumped UHV chambers (V to VIII). Its complexity stems from the particular design of the spectrometer which has been devised to perform a diffractive energy analysis of the He beam using a Pt vicinal surface (mounted in VI) as monochromator [8,9,25,27]. During the present work, however, no such analysis has been considered; a Pt(111) crystal has been employed as a mirror in VI to deflect the He beam into the detection stage (VIII). A differentially pumped stage (VII) separates the analyzer (VI) chamber from the detection unit in order to keep the background pressure of He atoms at a minimum. In stage VIII the He beam is ionized by electron bombardment, the ions are then extracted by electrostatic lenses and mass selected by a quadrupole mass analyzer. The details of the ionization unit are described in Ref. [30]. A channeltron device counts the number of ionized He atoms. The overall efficiency of the detector is of the order of $5 \cdot 10^{-6}$, the high intensity of the primary beam, however, ensures that the intensity of the direct beam is of the order of $5 \cdot 10^{6}$ counts/s. The dark counting rate is typically 30 counts/s. The whole detection unit is mounted on air cushions and glides over a micropolished granite table. It can rotate about the sample chamber axis to form an angle with the direction of the He beam at the source between 60° and 180° with an absolute precision of 0.005°.

The independent rotation of the scattering chamber and of the detection unit is one of the key features of this setup. It allows to choose the incident angle θ_i and reflection angle θ_f independently from any mechanical constraint. Its wide rotation range, moreover, gives access to the grazing scattering geometry that has been used to characterize the nanowire growth during this work. To ensure great manœuvrability and reproducibility of the scattering geometry all the rotary motions are controlled by a dedicated hardware and software network [8].

1.2 STM

STM owes its great popularity to its direct imaging capabilities coupled to the possibility of extracting information on the electronic structure of surfaces on a local scale [31, 32]. Compared to TEAS and other surface scattering techniques, which offer a reciprocal space image of the substrate, STM directly allows to visualize in real space the atomic structure of metal and semiconductor surfaces. On the other hand, the information provided by scanning probe techniques such as STM is inherently local and often limited to time snapshots of the surface. In this chapter we provide a basic introduction to the physics underlying tunneling microscopy and a brief description of the microscope employed in the experiments.

Principles

Figure 1.14 illustrates the basic principle of operation of an STM [33, 34]. A sharp metal tip is brought into close proximity ($\sim 5-10$ Å) to the (conducting) surface of a sample. The lateral tip position, x and y, as well as the vertical separation z between the tip and the surface are controlled with picometer precision by voltage signals applied

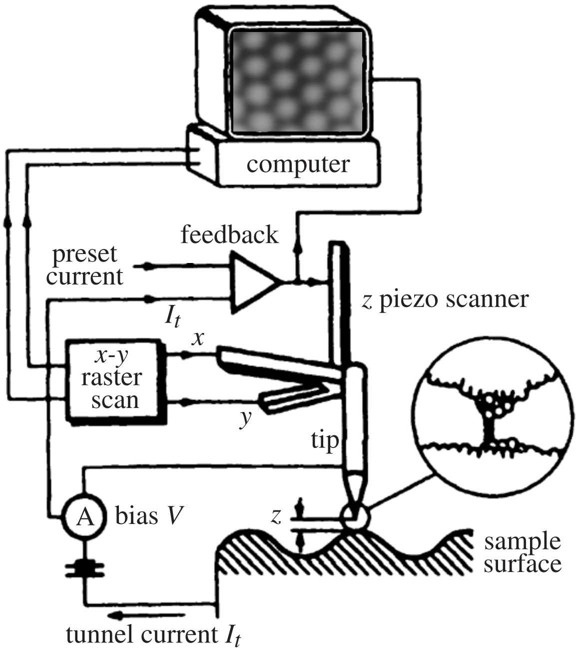

Figure 1.14: Schematic illustration of the basic principles and operation of a scanning tunneling microscope (Adapted from Ref. [32]). The circular inset shows an atomistic picture of the tip and sample structure.

to piezo-electric transducers. As on overlap between the tip and the sample electrons wave functions occurs, a bias voltage V applied to the sample (with respect to the ground and the tip) establishes a continuos tunneling current I across the vacuum region separating the two electrodes. The sign of V determines whether tunneling occurs from the tip occupied states to the sample empty states (positive V) or viceversa (Fig. 1.15). Once the sample and the tip are brought in thermodynamic equilibrium, their Fermi levels equalize. If a voltage V is applied to the sample, its energy levels will be rigidly shifted upward or downward by $|eV|$, depending on whether the polarity is negative or positive, respectively. Since states with the highest energy have the longest decay lengths into the vacuum, most of the tunneling current arises from electrons lying near the Fermi level of the negative-biased electrode. The tunnel current I depends exponentially on z, the individual atoms in the surface will give rise to current variations as the tip is scanned across the corrugated surface. In the constant-current mode of operation the current$I$, which is typically in the 0.5-5 nA range, is compared with a preset value I_0 in a feedback loop. The difference between I and I_0 is converted into a correction voltage and sent to the z transducer. In this way the tunneling current is kept constant by approaching or withdrawing the tip from the sample. Recording the feedback signal as a function of the tip position (x, y) over the substrate yields a 3D map of the surface topography. As we will see in the following, however, $z(x, y)|_{I,V}$ more correctly represents a surface of constant local density of electron states (LDOS) of the sample and therefore one has to be careful in interpreting it as an image of the position of the atomic nuclei of the surface. Note that a similar ambiguity exists also in the interpretation of

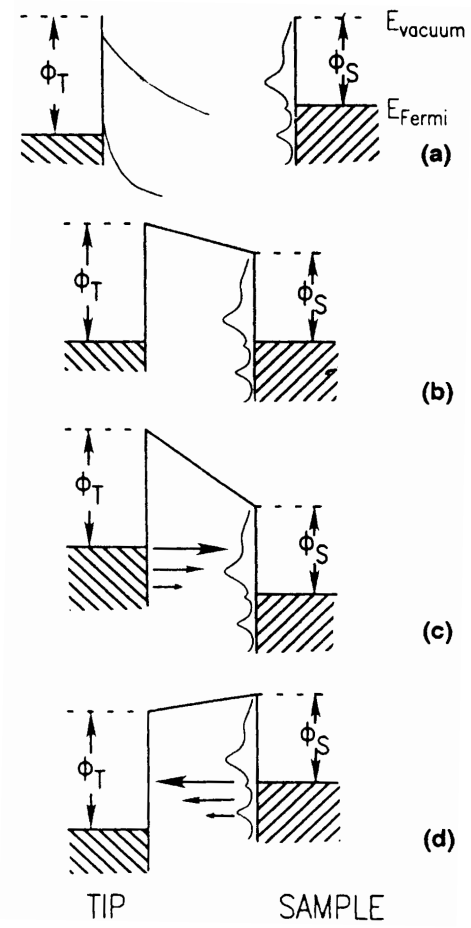

Figure 1.15: Energy level diagram of sample and tip: (a) separated sample and tip; (b) sample and tip in thermal equilibrium, without applied bias; (c) positive sample bias; (d) negative sample bias (from Ref. [35]).

the TEAS spectra discussed in Sec. 1.1.

A proper modelling of the tunneling process in an STM would require: the knowledge of the 3D electron potential in the vacuum region between the tip and the sample, the description of the electronic states of both the sample and the tip and the description of the spatial extension of the electron wave functions in the tunnel gap [32]. The poor symmetry of the system, the unknown geometry of the tip, and tip-sample interactions make this task a difficult one. Most of the existing theories are based on the "perturbative-transfer Hamiltonian" formalism introduced by Bardeen for tunneling between two parallel plates separated by an insulator [36]. By neglecting the interactions between the two electrodes, the tunnel current can be evaluated from the overlap in the gap region of the wave functions of the sample and tip, Ψ_μ and Ψ_ν, respectively, considered as separate systems [37]:

$$\begin{aligned} I(V) &= \frac{4\pi e}{\hbar}\sum_{\mu,\nu} |T_{\mu,\nu}|^2\,\delta(E_\mu - eV - E_\nu)\times \\ &\quad \Big(f(E_\mu - eV, T)\,[1 - f(E_\nu, T)] - f(E_\nu, T)\,[1 - f(E_\mu - eV, T)]\Big)\,, \end{aligned} \tag{1.10}$$

where

$$T_{\mu,\nu} = -\frac{\hbar^2}{2m_e}\int_{S_0} d\mathbf{S}(\Psi_\nu^*\nabla\Psi_\mu - \Psi_\mu\nabla\Psi_\nu^*)\,. \tag{1.11}$$

In Eq. 1.10 the summation goes over all quantum states μ and ν of the unperturbed sample and tip; the eigenvalues E_μ and E_ν are given with respect to the (common) Fermi level, f is the Fermi–Dirac distribution function, and T is the temperature. The delta function implies that tunneling is considered to be elastic, whereas the Fermi–Dirac functions take into account that tunneling occurs from filled to unfilled states. The integral 1.11 gives the tunnel matrix element $T_{\mu,\nu}$ and must be evaluated over any surface S_0 that lies entirely within the gap region. The main difficulty in this approach consists in evaluating $T_{\mu,\nu}$; Tersoff and Hamann have drastically simplified the problem by using as tip functions the solutions of the Schrödinger equation for a spherical potential wall (s-wave approximation) [38]. For low bias voltages the tunneling current becomes [39, 40]:

$$I(V,T,x,y,z) \propto e^{-2z\sqrt{\frac{2m_e\overline{\Phi}}{\hbar^2}}}\int_{-\infty}^{\infty} dE\,\rho_s(E,x,y,z)\,\rho_t(E-eV)\,(f(E-eV,T) - f(E,T))\,, \tag{1.12}$$

where $\overline{\Phi} = (\Phi_s + \Phi_t)/2$ is the average value of the tunneling barrier with respect to E_F

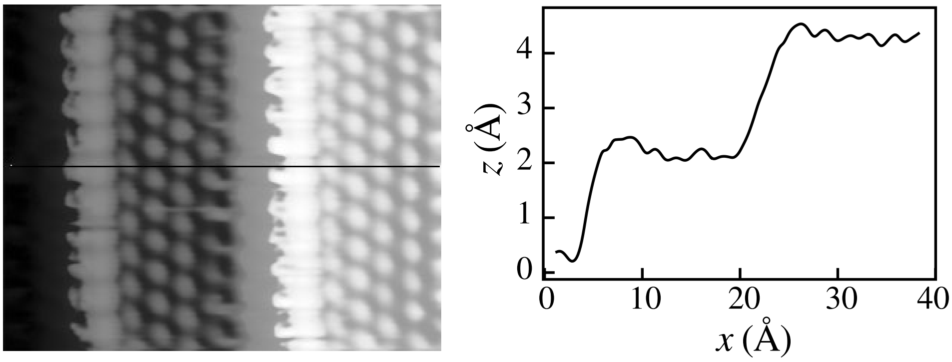

Figure 1.16: (a) Constant current STM image of three adjacent terraces on Pt(997); $I = 2.7$ nA, $V = 10$ mV. The image brightness is proportional to the z-coordinate. (b) z profile corresponding to the line scan shown in (a).

and

$$\rho_s(E, x, y, z) = \sum_{\nu} |\Psi_\nu(x, y, z)|^2 \, \delta(E - E_\nu) \tag{1.13}$$

is the LDOS of the sample surface at the position (x, y, z) of the center of the tip. If the measurements are performed at low temperature, the Fermi functions in Eq. 1.12 can be approximated by step functions, leading to

$$I(V, x, y, z) \propto e^{-2z\sqrt{\frac{2m_e\overline{\Phi}}{\hbar^2}}} \int\limits_0^{eV} dE \, \rho_s(E, x, y, z) \, \rho_t(E - eV) \, . \tag{1.14}$$

This approximation leads to two important results [32]: the first is that the tunnel current decays exponentially with increasing distance z between the tip and the surface. This implies that the tip apex atom dominates the tunneling process (for $\overline{\Phi} = 4$ eV, a 1 Å displacement in z implies a ten-fold variation in I), explaining the STM atomic-scale probing capabilities. The second result is that constant-current STM topographs can be simply interpreted as contours of constant $\rho_s(E_F)$ of the surface, since the largest contribution to the integral in Eq. 1.14 comes from the highest-lying energy states of the sample[1] and the tip electronic structure can be considered flat, i.e. ρ_t is taken to be constant. The atomic corrugation imaged by an STM, such as the one in Fig. 1.16, is therefore the modulation of a constant LDOS surface of the sample. Although the LDOS modulation has, in many cases, the same periodicity as the underlying atomic lattice, there are a number of instances where variations in the LDOS are caused by interference effects of the surface electron gas [41–43]. In the present work, however, all the constant-current images acquired can be simply interpreted as surface topographies.

---

[1] The states with the highest energy extend over longer distances into the vacuum

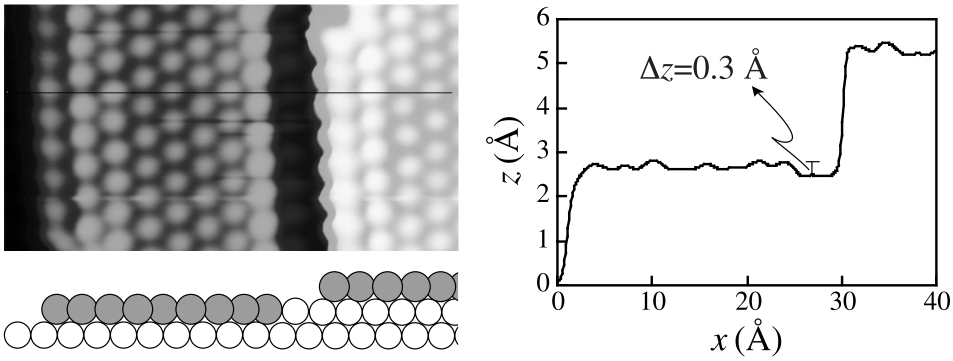

Figure 1.17: (a) Constant current STM image of Ag on Pt(997); $I = 4.1$ nA, $V = -6$ mV. The diagram represents a vertical cut through the surface evidencing Ag (grey) and Pt atoms (white). The line scan on the right shows the z-difference that allows to distinguish between Ag and Pt.

Figure 1.16(a) shows three adjacent Pt terraces separated by monatomic steps; the height of a single step is about 2.2 Å, in agreement with the theoretical value of 2.27 Å. The atomic corrugation on each terrace is 0.2 Å; such a vertical resolution, which is typical for most metal surfaces [32], cannot be accounted for by the Tersoff-Hamann theory presented above. Among the effects that have been suggested as the cause of the observed corrugation are the elastic deformation of the tip apex atoms due to attractive interaction between the tip and the sample [44], and the contribution of localized d_z states to the tunneling current [31, 45].

Chemical contrast

In performing epitaxial growth as well as chemisorption studies we are interested in obtaining elemental contrast with the STM between atoms or molecules of different species. The most elegant methods to achieve chemical sensitivity in STM rely on tunneling spectroscopy (STS) [46–48]; unfortunately, it is not always possible to use this technique for all kinds of adsorbates. Monolayer islands of Ag on Pt(997) analysed in this work, for instance, did not show any particular spectroscopic feature with respect to the substrate. Often, in the case of gas species such as atomic O, the main adsorbate-induced states lie too deep in energy ($\sim 5 - 7$ eV from E_F) to be detectable by STS.

Constant-current images, however, might contain enough information to allow to distinguish between different atomic species. A monolayer-high Ag island on Pt appears about 0.7 Å higher than a Pt monatomic step; the magnitude of this chemical contrast depends slightly on the tip structure, and does not depend on the bias or on the gap

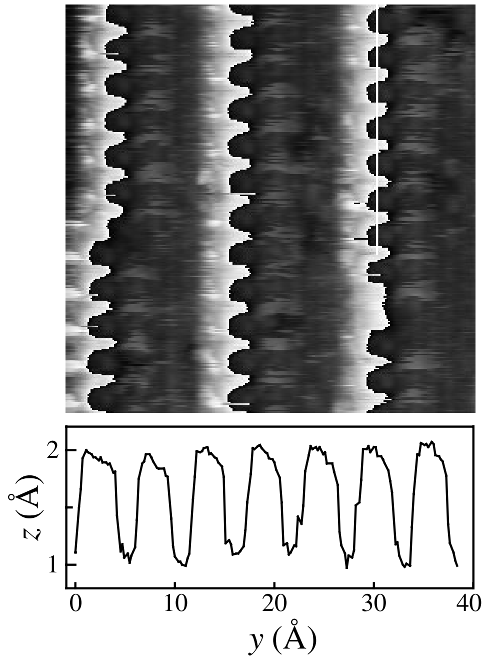

Figure 1.18: Top: O atoms adsorbed at the Pt(997) step edges are imaged as indentations on the Pt substrate. The greyscale has been artificially redistributed on each terrace to enhance contrast; $I = 6.4$ nA, $V = 9$ mV. Bottom: z line scan along the step edge.

width [49, 50]. This effect might be due to a smaller tunneling barrier above the Ag layer as suggested by a decrease in the work function Φ_s during Ag growth on Pt [51] or to a higher surface charge density in the compressed Ag islands with respect to the Pt substrate [50]. Figure 1.17 shows the height difference between Ag and Pt for a Ag layer growing at the base of the Pt steps.

Isolated adsorbates on metal surfaces generally induce pronounced changes in the LDOS near E_F and are therefore easily recognizable. Figure 1.18 shows O atoms adsorbed near the step edges of a Pt(997) surface; a local depletion of the LDOS near E_F induced by the O $2p$ resonance causes the O atoms to be imaged dark with respect to the surroundings. By modelling the tip and the sample as two adsorbed atoms facing each other on planar jellium-like electrodes, Lang [40, 52] has calculated the changes in the LDOS and the corresponding tip displacement at low bias voltage in the constant-current mode caused by C, O, Na, and S adsorbates. The results are shown in Fig. 1.19; it is seen that the Na $3s$ resonance and the S $2p$ resonance increase the LDOS at E_F, whereas for the electronegative C and O atoms the $2p$ resonances lead to a depletion of the LDOS at E_F. In the constant-current mode the adsorbates will consequentely appear as protrusions (Na, S) or as holes (C, O).

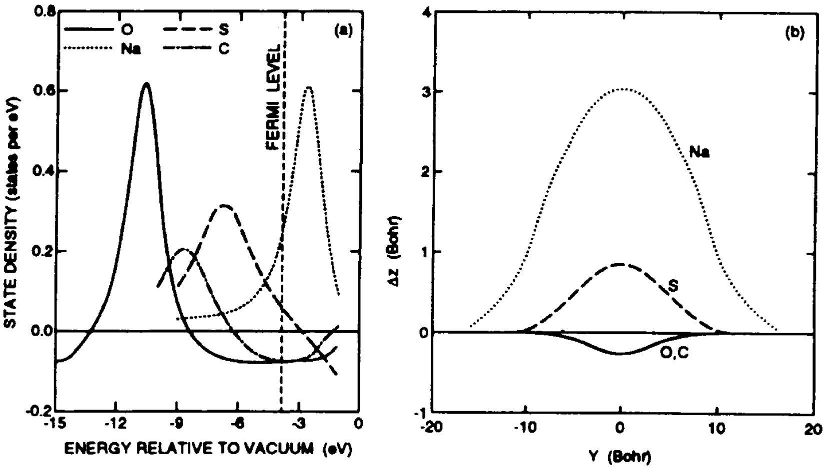

Figure 1.19: (a) Difference in eigenstate density between the adatom-metal system and the bare metal for Na, S, C, and O atoms. (b) The tip displacement versus lateral separation, Y, of the tip and adsorbate atoms (1 Bohr = 0.529 Å). From Ref. [40,52].

STM experimental setup

The STM images shown in this thesis have been acquired in a low-temperature STM built at the Institute de Physique Expèrimentale of the EPFL [53]. The experimental apparatus, shown in Fig. 1.20, consists in a single UHV chamber that contains the sample preparation stage and the microscope housing. The samples can be introduced into the UHV chamber through a load-lock system. They are subsequently transferred onto a manipulator for cleaning and preparation and eventually inserted into the microscope for analysis.

The sample (a replica of the Pt(997) crystal used in the TEAS experiments) is hat shaped and can be clamped onto a Mo sample holder leaving its surface entirely exposed. The electrical insulation necessary to apply the bias voltage V is assured by two thin sapphire rings placed between the Mo holder and the sample. Three feedthroughs at the bottom of the sample holder provide the contacts for a chromel/constantan thermocouple and the bias voltage. Once placed on the manipulator, the sample can be heated up to 1050 K by electron bombardment and cooled down to 40 K by thermal contact with a liquid helium cryostat. This temperature range allows to perform the usual annealing cycles required by the sample cleaning procedure (see Sec. 2.1) and to control the growth of low-dimensional structures via self-organization techniques [54]. The UHV chamber is equipped with an ion sputter gun, a CMA Auger spectrometer, and two Omicron e-beam evaporators. The Auger spectrometer (Omicron, CMA 150) is identical to the one used in the TEAS apparatus and has been used to cross calibrate the coverage of the metal adlayers in the TEAS and STM experiments. Variable

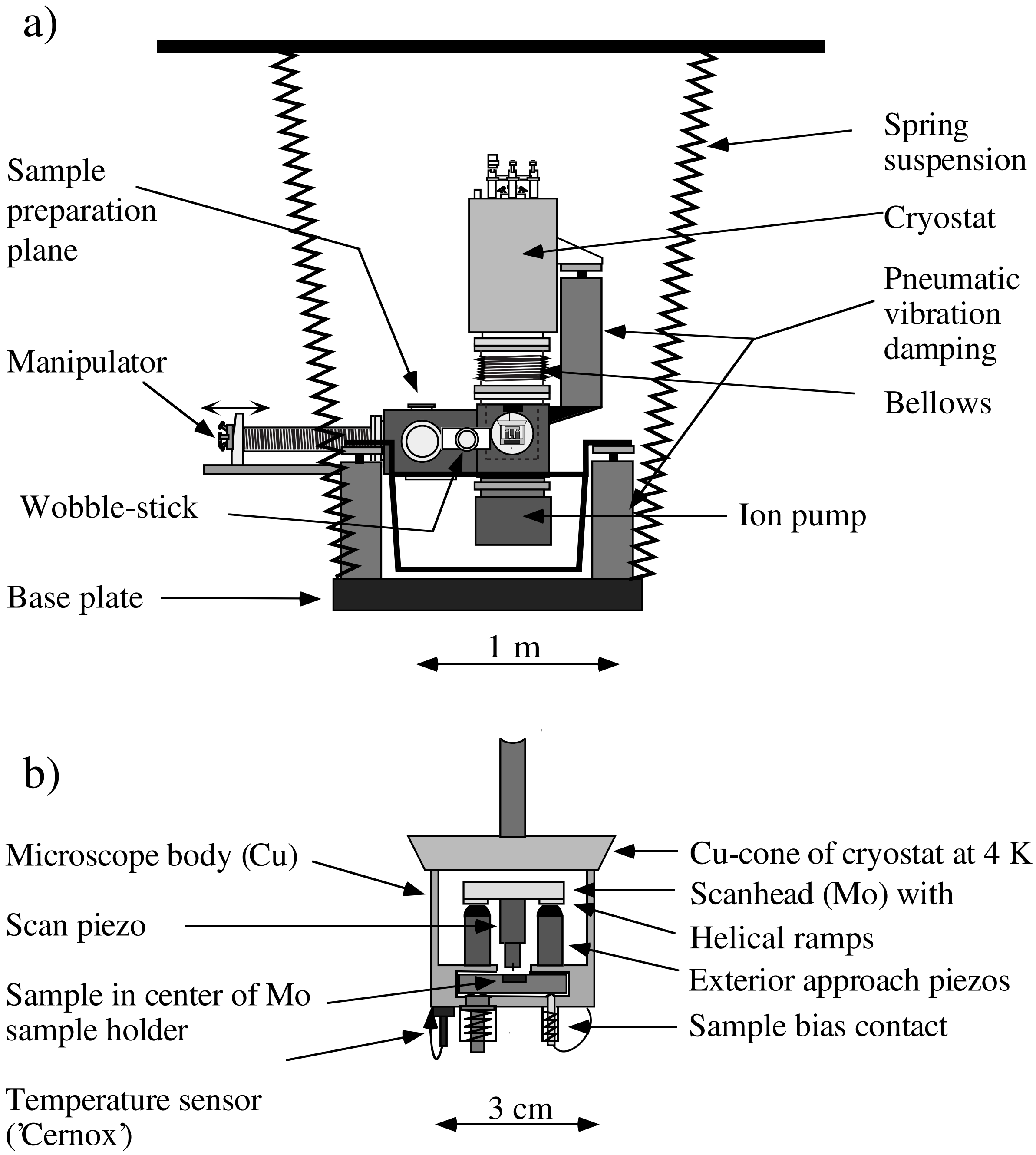

Figure 1.20: (a) Diagram of the UHV-chamber containing the sample manipulator and the 4K-STM. (b) The microscope housing and head. From Ref. [43]

leak-valves allow the backfilling of the UHV chamber with gas species for chemisorption experiments. The base pressure in the UHV system is 1×10^{-10} mbar or lower as the microscope cryostat is cooled to 77 K. After preparation, metal deposition or gas dosing, the sample is isothermally transferred into the microscope by means of a thermally insulated wobblestick.

The microscope body , shown in Fig. 1.20(b), is thermally coupled to a liquid helium - liquid nitrogen cryostat by mechanical contact with its upper Cu cone. The temperature of the microscope can thus be set to 8 K, 77 K or 300 K depending on the filling of the inner cryostat. In the present work the microscope has been exclusively operated at 77 K. The sample holder is inserted into a drawer in the microscope body and thermal contact is achieved by pressing it firmly against a polished Cu plate. Such a rigid coupling of the microscope-sample setup to the cryostat requires an efficient vibrational damping of the latter. This is achieved by three harmonic oscillators put in series, as shown in Fig. 1.20(a): a spring suspension of the base plate from the ceiling, plus two sets of pneumatic damping elements that decouple the cryostat from the chamber. To ensure a better sonic and electronic insulation the whole apparatus is housed into a metal-shielded sound-proof cubicle. A detailed discussion of the mechanical and electrical noise damping elements is reported in Refs. [43, 53].

The microscope is a "splitted beetle" design [53, 55]. The scan piezo with the W tip pointing downwards is shown in the center of Fig. 1.20(b); the scan piezo is mounted on a Mo disk that has three helical ramps on its underside. The coars approach of the tip to the sample surface is achieved by the inertial motion ("stick and slip" mechanism) of the Mo disk on three sapphire balls; these are mounted on top of three exterior piezos, of which two are shown in Fig. 1.20(b), glued to the microscope body. Once a tunneling current is detected, the coarse approach is stopped and scanning proceeds via the central piezo. This particular design has the advantage of providing good thermal contact between the microscope and the sample while maintaining the convenient coarse approach and lateral displacement typical of a beetle-type STM.

Chapter 2

1D Nanowires

The aim of this chapter is to study nucleation and growth of metals on densely stepped substrates in order to create arrays of 1D nanowires with tailor-made morphological characteristics. Metal epitaxy on the vicinal Pt(997) and Pt(779) surfaces has been investigated from the initial stage of step decoration to monolayer completion [23, 24]. The combination of two complementary experimental techniques such as TEAS and STM allows an extensive characterization of the epitaxial system: TEAS offers non-invasive, *in-situ*, macroscopic-scale, real-time monitoring of the wire growth at different temperatures, while STM gives access to atomic details that elude atom scattering probes. In this way we have successfully characterized the monatomic wire limit which is of particular relevance for the study of low-dimensional condensed matter properties.

Experimental work on nucleation at step edges was originally used as a method to obtain electron microscopy images of monatomic steps on rocksalt surfaces. The

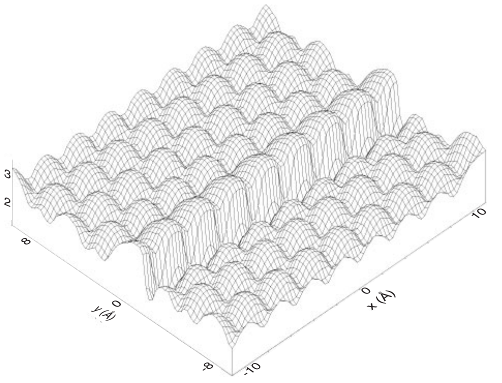

Figure 2.1: Potential energy map (in eV) experienced by a Co adatom above the Pt(997) surface [56].

	Co/Pt	Cu/Pt	Ag/Pt
E_T	-2.79	-2.17	-2.14
E_S	-3.79	-2.75	-2.68
ΔE	0.26	0.17	0.14 (0.17)$^{(a)}$
ΔH_S	0.59	0.46	0.39

Table I: E_T - binding energy in the middle of the terrace, E_S - binding energy at the step foot, ΔE - corrugation energy on the terrace, ΔH_S - Ehrlich-Schwoebel barrier [56]. $^{(a)}$ Experimental value from Ref. [57].

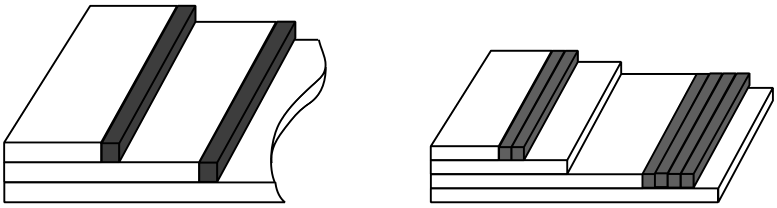

ideal row-by-row growth non-periodic pattern

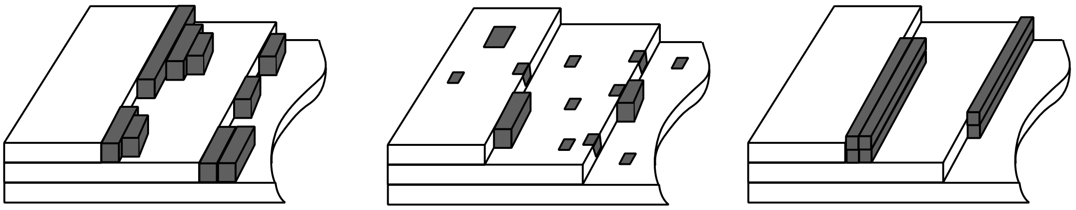

rough growth intermixing double adlayers

Figure 2.2: Different growth modes on a stepped substrate.

early studies by Bassett and Bethge [58, 59] showed that step ledges act as preferential nucleation sites for metal adatoms due to the increased coordination with respect to the terrace sites. Figure 2.1 shows the potential energy surface for a single Co adatom on Pt(997) calculated using a semi-empirical potential in a tight-binding scheme [56], as explained in more detail in Sec. 3.2. Values for Co, Cu, and Ag adsorption energies are reported in Table I. The adsorption sites at the bottom of the step edges are clearly favored over terrace sites, since the ratio $\frac{E_S}{E_T}$ is equal to 1.4.

With the rapid advancement of thin film deposition techniques in the last two decades the role of steps in homo- and heteroepitaxial growth has been extensively characterized. Initially, Molecular Beam Epitaxy on vicinal surfaces has been investigated to improve layer-by-layer growth on AlAs-GaAs interfaces, [60] but it was soon recognized that ordered stepped substrates can be employed as nanoscale templates for the growth of superlattices of quantum wires. [60–64] Studies of metal systems have shown that growth on stepped surfaces proceeds either as a smooth step-wetting process [65–69] or as nucleation of two-dimensional (2D) islands at step edges, [70, 71] provided that the adatom deplacement prior to nucleation is larger than the terrace width of the substrate.[1]

In Fig. 2.2 we show different scenarios of heteroepitaxy on a stepped substrate.

---

[1] It is interesting to point out that the influence of a monatomic step on the binding energy of adatoms is limited to the first and second row of adsorption sites. In the Co/Pt(997) case the adsorption energy for a single Co atom in the first row along the Pt steps is -3.79 eV while it increases to -2.86 eV in the second row, close to the value of the adsorption energy on the terrace (-2.79 eV) [56].

Besides the ideal case of smooth row-by-row growth, we distinguish: (i) wires of different widths due to interlayer crossing of the adatoms; (ii) formation of irregular 2D islands that wet the step edges; (iii) alloying; (iiii) formation of double layers structures. In preparing arrays of 1D wires for photoemission and magnetic dichroism experiments, we have focused on the conditions that favor the ideal case. A background in heteroepitaxial metal growth is not given here and the reader is referred to the extensive literature on the subject [57]. As a general trend we find that wire formation is limited at low temperature by slow edge-diffusion processes and at high temperature by heterostep-crossing and eventually by alloying between the metal adspecies and the substrate. We will determine the best deposition parameters that lead to the formation of smooth Ag, Cu, and Co wires.

This chapter is organized as follows: Sec. 2.1 presents the Pt substrate and the preparation methods; Secs. 2.2, 2.4, 2.3, and 2.5 deal with Ag, Cu, Co, and Ni growth, respectively.

2.1 The substrate

The basic requirement to grow self-organized patterns of regular wires by step decoration is a good template. By this we mean a sample whose steps are as straight and as evenly spaced as possible. We have chosen to work with Pt vicinal surfaces since repulsive interactions between adjacent steps suppress step meandering [72], resulting in remarkably straight steps and in a narrow terrace width distribution. For Pt(997) the average terrace width is 20 Å with standard deviation $\sigma = 2.9$ Å [73]. Figure 2.3 shows two STM images of a well-prepared Pt(997) surface after sputtering and annealing. In the present work we have employed two vicinal surfaces: Pt(997) and Pt(779). These two surfaces are alike, but for the step microfacets, which are $\{111\}$ for Pt(997) and $\{100\}$ for Pt(779) (Fig. 2.4). The study of two similar substrates allows to separate growth and chemisorption effects that might be dependent on the particular step geometry.

Although the average step separation as well as the kink density along the steps are determined by the crystal miscut, the cleaning procedure of the sample is fundamental in obtaining a regular periodic substrate. After 10 min. sputtering at 300 K with a 800 eV Ar^+ beam the stepped structure of the surface is completely lost (Fig. 2.5). It can be recovered by annealing the surface to high temperatures. To avoid uneven removal of material from the surface, however, the sample temperature is usually kept at $T = 750$ K during sputtering to allow sufficient mobility of the Pt atoms, and the ion beam is directed either normal to the surface or parallel to the steps. After the

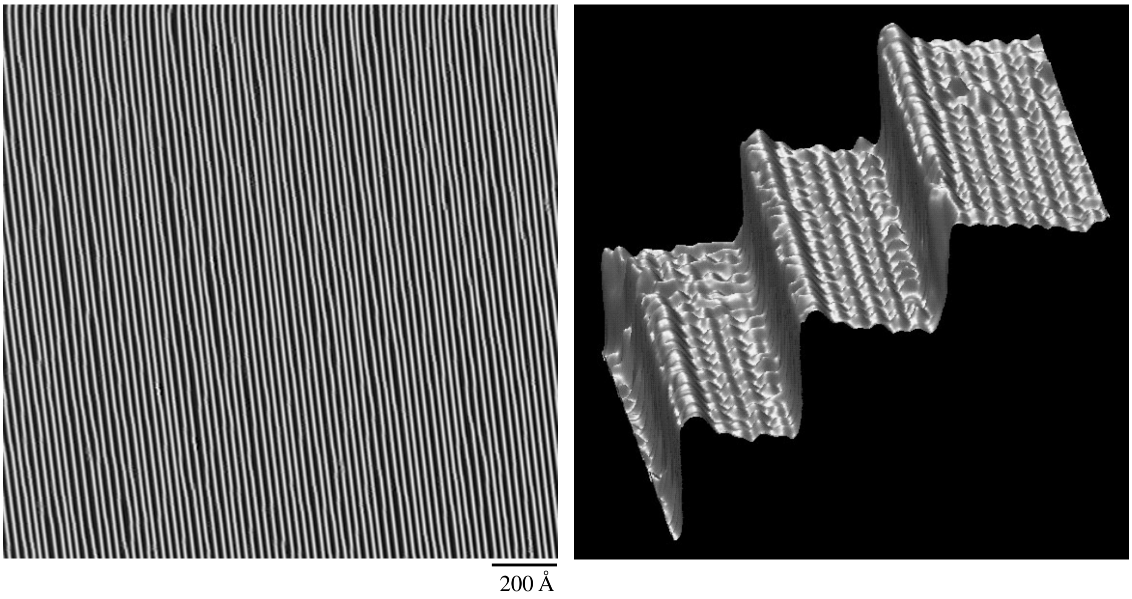

Figure 2.3: Left: STM $\partial z/\partial x$ image of the clean Pt(997) surface. Step down direction is from right to left. $I = 1.0$ nA, $V = 0.6$ V. Right: 3D close up of the Pt steps (the z scale has been exaggerated for better rendering), $I = 2.7$ nA, $V = 10$ mV.

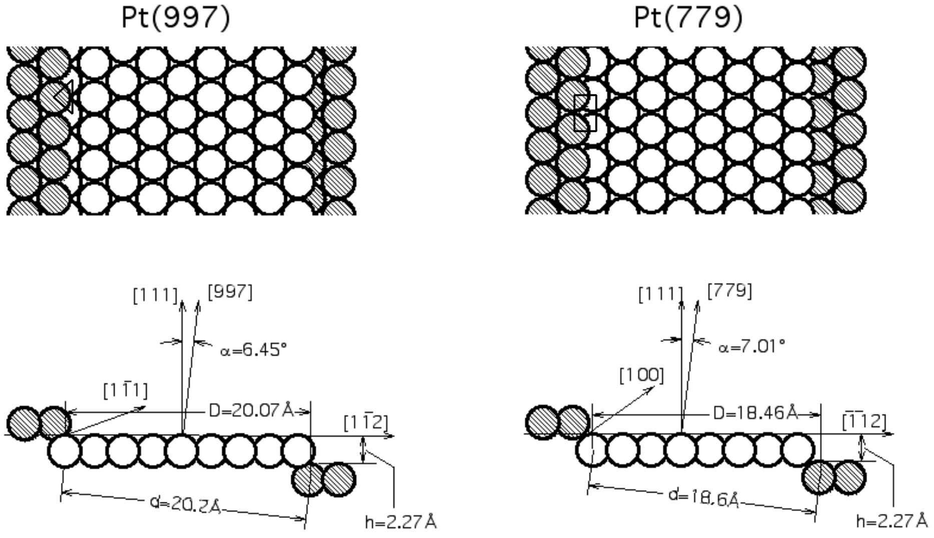

Figure 2.4: Hard-sphere models of the Pt(997) and Pt(779) substrates.

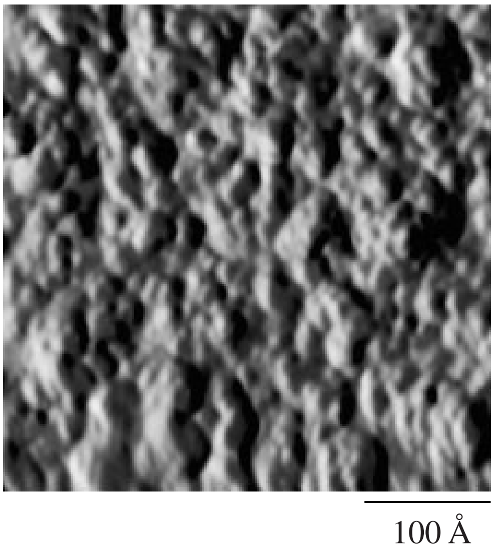

Figure 2.5: Pt(997) after 10 min. of cold sputtering at 300 K with a 800 eV Ar^+ beam at normal incidence.

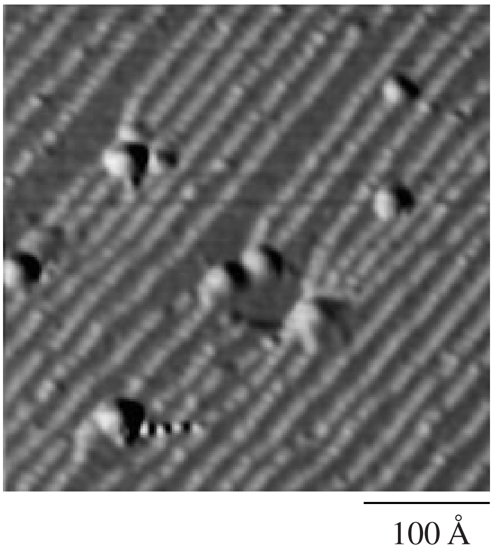

Figure 2.6: Pt(997) after annealing in the presence of contaminants.

deposition of metals, such as Co, that form alloys with Pt, sputtering is started at low temperature and continued at 750 K after a certain time. After repeated cycles of 800 eV Ar^+ sputtering at 750 K the surface is annealed to 850 K, followed by a brief exposure to 1×10^{-7} mbar oxygen and by a flash to $T > 1000$ K to remove residual contaminant. Care has to be taken in cooling the sample at a slow enough rate ($<$ 40 K/min) until 500 K in order to allow equilibration of the step morphology. Annealing in the presence of impurities might result in step pinning during the cool down of the surface, as it is shown in Fig. 2.6. The surface periodic pattern is eventually checked by He diffraction (see Fig. 1.4) or by STM.

2.2 Ag

As Ag grows pseudomorphically on Pt(111) in a wide range of temperatures without intermixing with the substrate [49, 74], Ag/Pt(997) is regarded as a model system in our study of metal chain formation. We have shown in Sect. 1.2 that Ag and Pt are chemically distinguishable by STM due to a positive height difference between the first Ag layer and a Pt step. In images like Fig. 2.3 (left panel), however, it is virtually impossible to detect small amounts of adatoms at step edges. To analyze the initial stages of row growth we have to reduce our field-of-view to less than 200 × 200 Å^2. Figure 2.7 is taken after deposition of 0.03 ML Ag at 340 K. Two incomplete Ag rows are visible attached to the lower step edge of two adjacent steps (see arrows). In the inset, a constant current image of the same spot shows the STM contrast between Ag and Pt. At 340 K the Ag adatoms impinging on the surface can rapidly migrate to step sites where they start diffusing along the Pt step edges. With increasing Ag coverage they will meet other Ag atoms and accommodate in stable 1D aggregates. Similarly to the process of 2D island formation on flat surfaces [57], the length of the stable 1D nucleus will generally depend on the sample temperature and on the deposition rate. Eventually the incomplete atomic rows coalesce and form a continuous row along the Pt step edge as shown in Fig. 2.8. From images like Fig. 2.8 taken at $T \geq 300$ K we note further that the first Ag row wets the Pt step in a perfect pseudomorphic way. This means that the Ag wire is a true 1D structure whose length is ultimately limited by the kink density of the substrate. Therefore the sample miscut determines not only the average separation between the wires but also their longitudinal coherence.

Ag wire growth *vs* T

In order to characterize the growth scenario, we have conducted a systematic study of the wire formation vs substrate temperature. This is most easily done by TEAS measurements at grazing incidence which provide information on the order and size distribution of the adwires. Figure 2.9 shows TEAS curves recorded at $\theta_i = 85°$ during sub-monolayer Ag deposition at different temperatures. As discussed in Sec. 1.1, the peak at $\sim$ 0.13 ML corresponds to the completion of the first Ag row. The temperature evolution of this peak shows that monatomic row growth occurs for 150 K $\leq T \leq$ 550 K. Although this result depends on the particular system under examination, it shows that step decoration can be exploited to obtain monatomic wires for a wide range of temperatures. However, even in the allowed temperature range, the "quality" of the monatomic wires can vary and the growth scenario for $\Theta_{\mathrm{Ag}} > 0.13$ ML might change

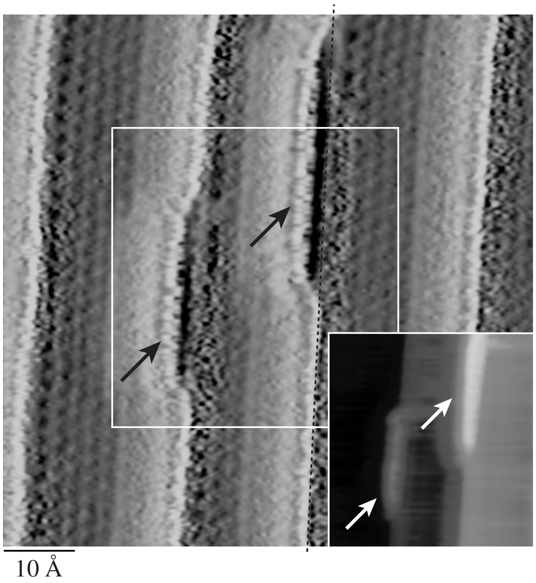

Figure 2.7: $\partial z/\partial x$ image of the row formation process at T = 340 K. Step-down direction is from right to left, one of the Pt step edges is marked by a dotted line. Two Ag 1D aggregates (indicated by the arrows) are attached to the lower step edges. $\Theta_{\mathrm{Ag}} = 0.03$ ML, $F = 3 \times 10^{-3}$ ML/s, $I = 4.6$ nA, $V = 6$ mV. Inset: constant current detail showing the STM contrast between Ag and Pt.

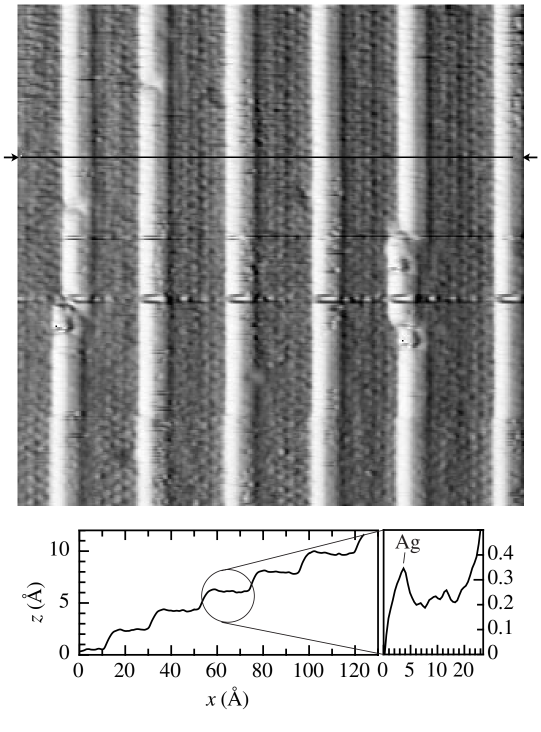

Figure 2.8: $\partial z/\partial x$ image of single monatomic Ag wires decorating the Pt step edges. Ag is distinguishable from Pt because of its larger apparent height as shown in the constant current line scan at the bottom and by the luminosity contrast along the steps. $\Theta_{\mathrm{Ag}} = 0.13$ ML, $F = 3 \times 10^{-3}$ ML/s, $T = 400$ K, $I = 2.85$ nA, $V = 5$ mV

as well. The dependence of row growth on the deposition rate F has been investigated at 300 K: He curves measured for 3×10^{-4} ML/s $\leq F \leq 2 \times 10^{-2}$ ML/s do not show any marked difference, although we cannot exclude a different low temperature behavior. In the following, Ag growth is analyzed starting from low temperature. On Pt(111) single Ag adatoms are mobile above 50 K; Ag dimers on the same surface are immobile and stable up to 110 K [75]. Therefore for 50 K $< T <$ 110 K Ag adatoms can diffuse on the terrace until they meet a second adatom and form a stable dimer without attaching to a step. On the other hand, because the terrace width of Pt(997) is small compared to the mean free path of Ag adatoms at 110 K ($\approx$ 100 Å as inferred by the mean island density measured by Brune *et al.* in Ref. [75]), most adatoms can migrate to step sites even at lower temperatures. But step attachment is not the only necessary condition to form a 1D wire. At $T <$ 150 K Ag adatoms do not have enough thermal energy to accommodate into the minimum energy configuration which is the pseudomorphic decoration of a Pt step: they migrate to a step but stick to the first site of contact. Thus, the wire formation is kinetically hindered by slow edge- and corner-diffusion processes. Figure 2.10 shows such a situation following deposition at 120 K, where Ag islands grow attached to the step edges with an irregular contour.

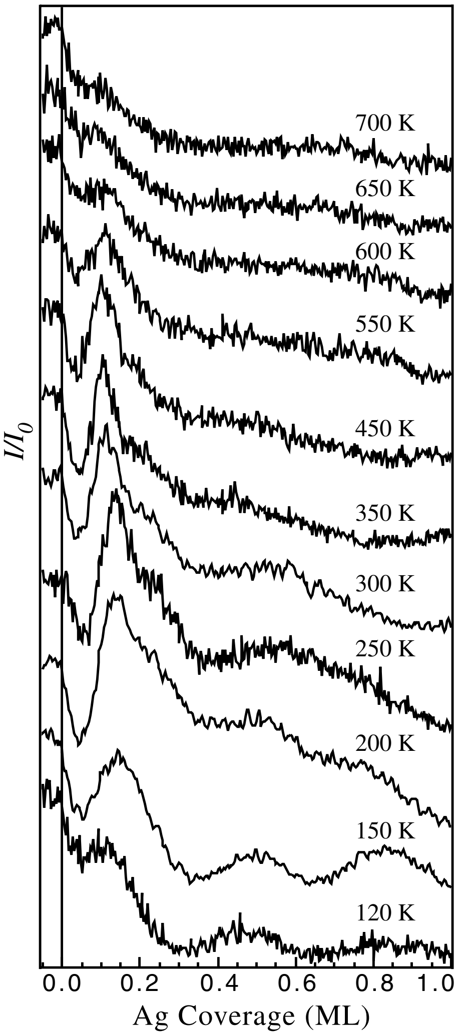

Figure 2.9: TEAS intensity during deposition of Ag at different temperatures; $\theta_i = \theta_f = 85°$, $\lambda_{He} = 1.01$ Å, $F = 3 \times 10^{-3}$ ML/s for all curves. The sequence shows the temperature evolution of the peak at $\sim 0.13-0.17$ ML that corresponds to the formation of the first Ag row.

We now proceed to examine row growth in the temperature range: 150 K $\leq T \leq$ 550 K. As we demonstrated in Sect. 2.2, Fig. 2.7 and Fig. 2.8, row growth proceeds via incorporation of adatoms in 1D stable nuclei attached to the step edges. Perfect row

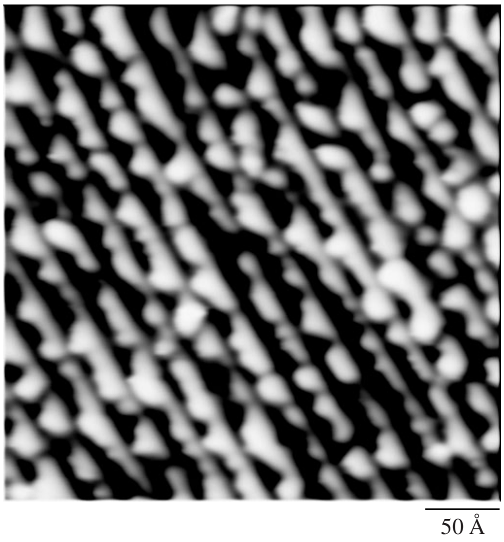

Figure 2.10: STM constant current image taken after deposition of 0.5 ML of Ag at 120 K, $F = 3 \times 10^{-3}$ ML/s, $I = 1.1$ nA, $V = 0.1$ V.

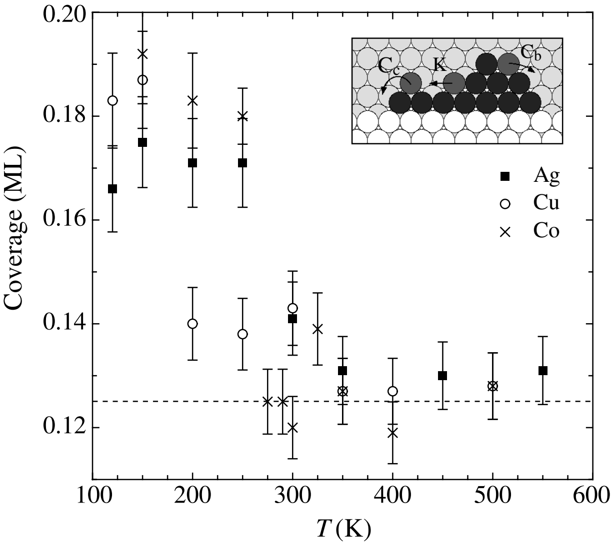

Figure 2.11: Coverage *vs* deposition temperature corresponding to the first He reflectivity maximum in Fig. 2.9 for Ag, Fig. 2.18 in Sect. 2.3 for Cu, and Fig. 2.20 in Sect. 2.4 for Co. The coverage is calibrated with the procedure outlined in Sec. 1.1 at 300 K. Inset: edge diffusion processes.

growth implies that all Ag atoms migrating to the steps are incorporated in the growing row. However, a plot of the coverage corresponding to the first row peak (Fig. 2.9) *vs* deposition temperature shows that this occurs only for $T > 250$ K as coincidence with the nominal monatomic row coverage of 0.125 ML is attained (see Fig. 2.11). This implies that at $T \leq 250$ K the Ag-Ag edge and corner trapping diffusion barriers are still effective in preventing Ag adatoms that stick to a Ag covered step to migrate to the bare Pt step sites. The rate-limiting processes for wire smoothing are most likely kink breakup, corner breakup and corner crossing of Ag atoms attached to Ag decorated steps (indicated by K, C_b, and C_c respectively in the inset in Fig. 2.11). Density-functional calculations for the Al/Al(111) system have indeed shown kink and corner breakup as well as corner crossing to have the highest barriers among low-symmetry diffusion processes [76]. The above can be considered to be relevant in the general case for wire formation as the same trend is observed for Cu although with a lower temperature threshold. Another way to rearrange 2D islands attached to the step edges into a perfect row is adatom 2D evaporation from the step to the terrace and subsequent recondensation. Evaporation of Ag atoms from 2D Ag islands on Pt(111) has been shown to set in with temperatures exceeding 110 K [54] and to lead to a dense 2D gas phase of Ag adatoms on large terraces at $T > 300$ K [77]. We conclude that in terms of

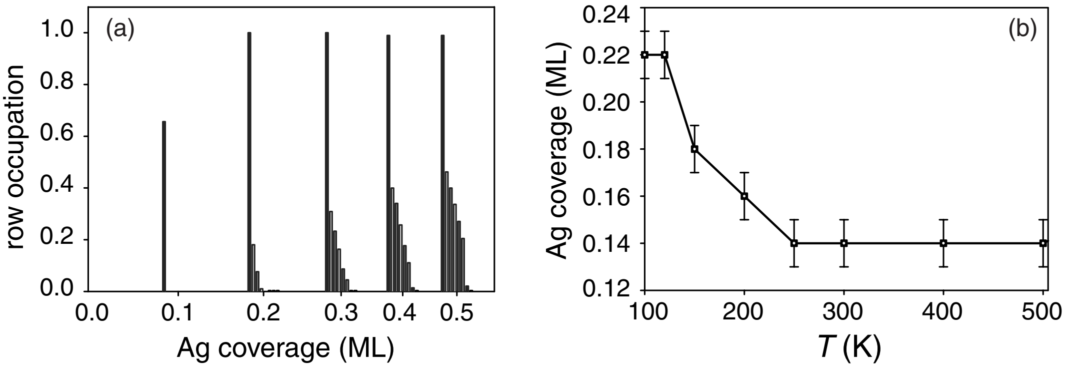

Figure 2.12: (a) Ag row occupation on Pt(997) *vs* coverage determined within the KMC simulation at 300 K for an atom flux equal to 10^{-3} ML/s. Rows are numbered from left to right. (b) Ag coverage *vs* temperature leading to the first row completion. The error bars characterize the uncertainty of the statistical distribution of adatoms (Adapted from Ref. [78]).

1D character the most regular Ag monatomic wires are grown above 250 K, as shown in Fig 2.8.

Using the semiempirical potentials mentioned in the introduction to describe the Pt-Ag and Ag-Ag interactions, F. Picaud *et al.* [78] have performed Kinetic Monte Carlo simulations to model the kinetics of the row growth process. The observed growth dependence on temperature, coverage, and deposition flux is successfully interpreted by the calculations, whose results are shown in Fig 2.12(a) and (b). The small deviations from the experimental parameters are discussed in Ref. [78].

Increasing the temperature to obtain smooth wires has its limits. Although Ag has a higher surface free energy than Pt, intermixing confined to the topmost layer of the surface occurs for $T \geq 600$ K [49]. As shown by Röder *et al.* in Ref. [49], diffusion of Ag into the first Pt layer proceeds via the step edges; roughening of the Ag-Pt interface at the step edges increases the defect density seen by TEAS. Accordingly, the first row peak in Fig. 2.9 gradually decreases in intensity and finally disappears as the temperature rises to more than 600 K. The upper limit for wire growth is evidently determined by the surface alloying temperature of the system. One must be careful, though, that intermixing at step edges might be effective even before that alloying takes place homogeneously on the terraces. In Sect. 2.2 we will see that it might also be desirable to stay far below the alloying temperature to maintain the wire pattern uniformity by avoiding diffusion of adatoms across different terraces.

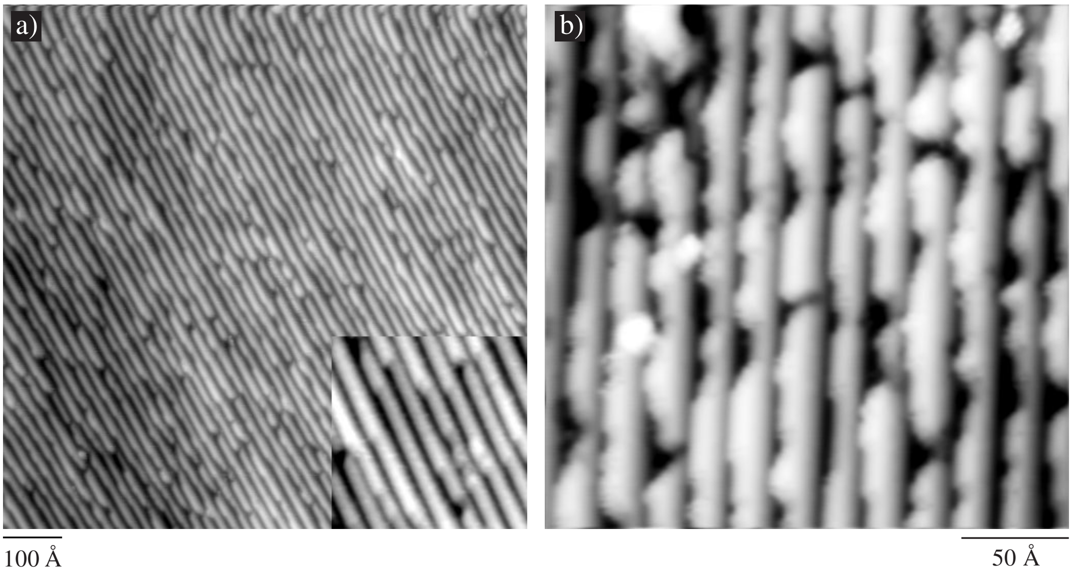

Figure 2.13: (a) Constant current image of 0.5 ML Ag deposited at T = 230 K, $F = 3 \times 10^{-3}$ ML/s, I = 1.3 nA, V = 0.1 V; the inset shows the Ag edges in more detail. A tip broadening effect enlarges the apparent width of the Ag stripes. (b) Constant current image of 0.85 ML Ag deposited at T = 230 K, $F = 3 \times 10^{-3}$ ML/s, I = 5.3 nA, $V = -7$ mV; the Ag edges are rough compared to the inset in (a).

Ag wire growth *vs* coverage

As the coverage increases to more than a single monatomic wire per terrace, Ag can either grow row-by-row or form rough stripes, corresponding to a Stranski-Krastanov growth mode in 1D. The latter growth mode has been observed, e.g., by Mo and Himpsel for Cu on a stepped W(110) surface [79]. We find that, up to 0.5-0.7 ML, the Ag stripes, although not perfectly continuos, have smooth edges [see Fig. 2.13(a)], but that for higher coverages the Ag edge becomes rough, as already mentioned in Sec. 1.1. The roughening of the Ag edge is evident from the comparison of Fig. 2.13(a) and Fig.2.13(b) taken after deposition of 0.5 and 0.85 ML Ag, respectively, at 230 K. We point out the analogy between Ag growth on Pt(111) and on Pt(997): on Pt(111) a transition from 2D layer-by-layer growth to 3D growth is observed above a critical coverage [74]; on Pt(997) we observe a transition from 1D row-by-row growth to rough 2D growth above 0.5 ML.

Roughening of the Ag edge can either be of kinetic or of thermodynamic origin. In the first case the process that limits the reshaping of the rough Ag stripe into a smooth one might be the progressive closing of diffusion channels as the stripe edge approaches the lower terrace. Ag adatoms on the upper terrace are confronted to a strong repulsive barrier from the the Pt-Ag heterostep (see inset in Fig. 1.11 in Sec. 1.1) [74]. Such a repulsion can enhance diffusion barriers along the stripe edge and limit rearrangement by evaporation and recondensation. Moreover, the diffusion barriers along the Ag stripes and across the stripe corners might become larger due to an increasing outward relaxation of the stripe edge atoms caused by the strain accumulated as the Ag stripes grow wider. Since diffusion is generally slower along $\{111\}$ than along $\{100\}$ faceted steps [76, 80, 81] we expect Ag stripes grown on Pt(779) to remain smooth up to higher coverages with respect to the stripes grown on Pt(997). Preliminary measurements indicate that this is indeed the case for Ag/Pt(779 (see Fig. 1.11(b)).

Thermodynamics could also play a role in the observed roughening near monolayer completion. The minimization of the misfit strain energy between the Pt substrate and the Ag adlayer might lead to the formation of irregular structures where Ag atoms are less compressed compared to straight stripes. At present we have no means to rule out kinetic vs thermodynamic arguments; the persistence of rough growth up to 430 K implies large rearrangement barriers if the state of the system is determined by kinetic limitations.

Periodic patterns of Ag wires

Besides the 1D character of wires grown by step decoration, their uniformity and their spatial distribution on the surface are other important issues. This is especially true if one wants to prepare samples for investigation by integral probes such as in, e.g., photoemission or photoabsorption spectroscopy experiments. It is clear that the average spacing (or density) of the wires is determined by the miscut angle and that the width of the spacing distribution is determined by the accuracy and the homogeneity of the miscut. The same is true for the wire thickness, however, only when the adlayer coverage on each terrace is proportional to the terrace width, i.e. in the absence of interlayer diffusion.[2] Assuming that our substrate is ideal, in order to grow uniform wires of the same (average) thickness we have to work at substrate temperatures that do not allow the Ag atoms to cross neither the bare Pt steps nor the Ag decorated ones (heterostep crossing, see Fig. 2.14).

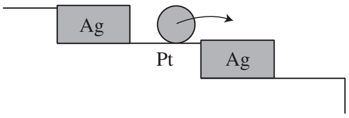

Figure 2.14: Heterostep crossing.

The temperature at which interlayer diffusion becomes significant can be determined by TEAS. As discussed in Sec. 1.1, the TEAS measurements taken at $\theta_i = \theta_f = 83°$ show a peak at ~ 0.5 ML coverage that is due to terrace

---

[2] Interlayer diffusion is defined here as the diffusion of adatoms across adjacent terraces.

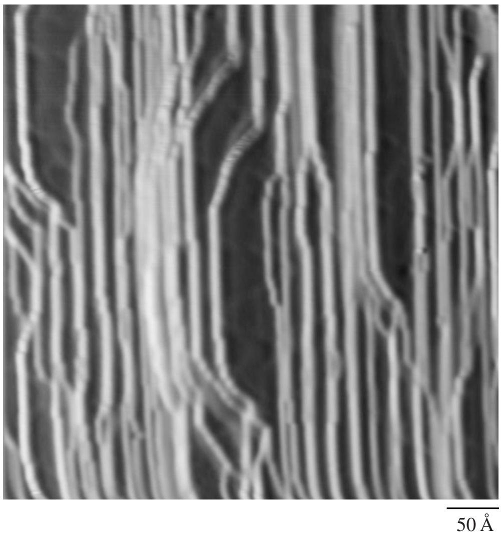

Figure 2.15: $\partial z/\partial x$ image taken after deposition of 5 ML Ag at $T = 430$ K. Faceting results from Ag atoms crossing the Ag-Pt lateral interface at steps causing step bunching. Note that the Ag facets are not wider than $\sim$ 80 Å. $I = 1$ nA, $V = 0.62$ V.

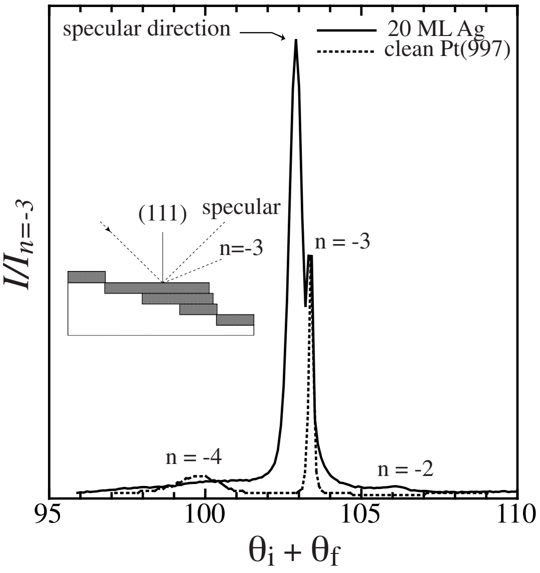

Figure 2.16: Diffraction pattern of 20 ML Ag deposited on Pt(997) at $T = 450$ K (solid line) compared to that of the bare Pt(997) surface (dotted line). The intensity in the specular direction is due to facetting of the Ag adlayers. Both curves are arbitrarily normalized to the $n = -3$ peak. During the scan $\theta_i = 58.0°$ is kept fixed, while θ_f varies; $\lambda_{He} = 1.01$ Å.

confinement of adatoms (see Fig. 1.11 in Sec. 1.1). The intensity of this peak in the Ag case decreases for $T > 400$ K, indicating that Ag adatoms eventually acquire enough thermal energy to overcome the heterostep barriers. The analysis of the STM topograph shown in Fig. 2.15 and the TEAS data in Fig. 2.16 confirm this conclusion. At coverages larger than 1 ML, Ag atoms diffusing across adjacent terraces can give rise to step bunching and faceting. Since the formation of (111) facets disrupts the periodicity of the surface, the diffraction pattern of the reflected He beam is also modified with respect to that of a vicinal (997) surface. In particular, Fig. 2.16 shows the comparison between a spectrum taken after deposition of 20 ML Ag at 450 K (solid line) and one of the clean Pt(997) surface (dotted line). At non-grazing angles of incidence, specular reflection arises from the scattering of He atoms by flat (111) facets; the clean Pt(997) diffraction spectrum includes only the $n \neq 0$ diffraction orders, the signature of the periodic structure of the surface.

If we define the threshold temperature at which heterostep crossing becomes active as the temperature where crossing takes place once per second, we can estimate the diffusion barrier E_h for this process as

$$E_h = \ln(\nu_0)\ \ k_B\ T \tag{2.1}$$

where k_B is the Boltzmann constant and ν_0 is the usual prefactor. By taking $\nu_0 = 6\times10^{12}$ as in Ref. [76], and $T = 400$ K we calculate E_h to be 0.9 eV for diffusion of Ag atoms across Pt-Ag step boundaries. We note that even higher temperatures for crossing the Pt-Ag border are required on Pt(111), where the large barrier for heterostep crossing has been attributed to the binding energy difference of Ag/Pt(111) with respect to Ag/1 ML Ag/Pt(111) and to compressive strain in the Ag layer [74].

From the results presented in this section we conclude that the optimal temperature range for patterning Pt(997) with Ag nanowire arrays is between 250 K and 400 K.

2.3 Cu

Cu growth on Pt(997) is first compared to the flat (111) surface and subsequently analyzed in terms of the wire growth. The growth of Cu on Pt vicinal substrates appears to be quite different with respect to the (111) surface. Holst *et al.* reported in a TEAS-STM study of Cu on Pt(111) [82] no oscillations in the He scattering reflectivity during growth at 340 K. They attributed the oscillation damping to incomplete coalescence of the first layer Cu islands and to the formation of a dislocation network at Θ_{Cu}= 2 ML. On Pt(997), in contrast, we found oscillations in the deposition curves at least up to 4 ML in the same temperature range, with damping occurring only for $\Theta_{Cu}\geq$ 2 ML. Figure 2.17 shows the He intensity during Cu deposition at 350 K: the first maximum corresponds to the formation of the first Cu row at 0.13 ML. This is confirmed by the grazing incidence curves in Fig. 2.18 which show the first row peak as a function of growth temperature. The reason why the first row formation gives rise to an intensity maximum in the non-grazing geometry, in contrast to the Ag case, is probably due to a bending of the He-surface scattering potential near the step edges induced by Cu atoms. The second maximum in Fig. 2.17 corresponds to the monolayer completion and serves as a coverage calibration for the deposition curves. Its intensity is larger than the bare Pt signal (I_0) because the higher Debye temperature of (bulk) Cu with respect to Pt enhances the elastic scattering from the surface layer. Damping of the monolayer oscillations occurs only after deposition of the second layer, suggesting that the first Cu layer is complete and

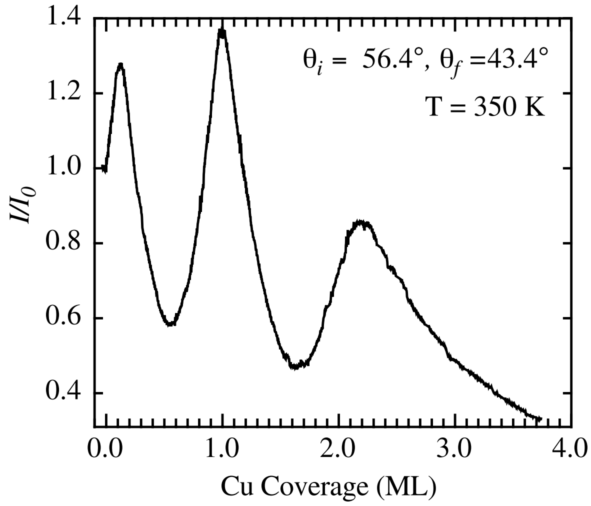

Figure 2.17: TEAS normalized intensity of the $n = -3$ peak during deposition of Cu. The second maximum reflects the completion of the first Cu adlayer and is used to calibrate the deposition rate for the curves reported in Fig.2.18. $\lambda_{He} = 1.01$ Å, $F = 1.7 \times 10^{-3}$ ML/s.

pseudomorphic with respect to the substrate. The better layer-by-layer growth mode on Pt(997) with respect to the (111) surface is related to its very short terrace width that renders second layer nucleation less likely. Also the formation of the (13×13) fcc-hcp dislocation network observed for Θ_{Cu}= 2 ML on Pt(111) [82,83] is presumably suppressed on Pt(997), explaining the persistance of the oscillations in the He curves for Θ_{Cu}> 1 ML.

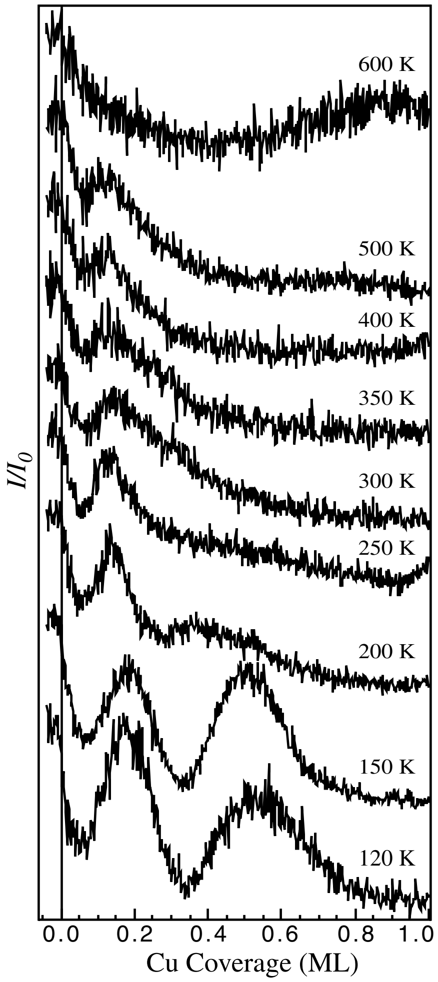

Figure 2.18: TEAS intensity during deposition of Cu at different temperatures; $\theta_i = \theta_f = 83°$, $\lambda_{He} = 1.01$ Å, $F = 1.7 \times 10^{-3}$ ML/s. The peak at $\sim 0.13 - 0.18$ ML corresponds to the formation of the first Cu monatomic row.

From the analysis of the grazing incidence curves taken during Cu deposition we see that row growth occurs down to $T = 120$ K and presumably even at lower temperatures. However, at $T = 120$ K the first row peak in Fig. 2.18 is broad and centered around 0.18 ML, indicating slow edge diffusion. In the case of Cu, the transition to smooth row growth happens between 150 K and 200 K (see also Fig. 2.11), i.e. at lower temperature than for Ag. On the other hand, Cu row growth seems to degrade earlier than in the Ag case. The intensity of the first row peak normalized to the bare Pt signal is already considerably diminished at 350 K with respect to the low temperature value, while it is constant up to 500 K in the Ag case. The reduced row reflectivity is attributed to Cu-Pt mixing at the step interface. Dynamic work function measurements indicate the onset of intermixing between Cu and Pt(111) at 500 K. [84] Since intermixing is favored at step sites, it is likely to set in earlier on Pt(997). At $T = 600$ K the row peak disappears completely; Cu deposition results in alloy structures, in agreement with experiments on Cu/Pt(111). [84]

For $\theta_i = 83°$ (Fig. 2.18) the 0.5 ML peak is clearly visible below 200 K. As in Sec. 2.2, we attribute the suppression of this peak at $T \geq 200$ K to the onset of heterostep crossing by Cu atoms. Therefore Cu seems to be more mobile on Pt than Ag, in terms of both edge and interlayer diffusion. Assuming the same prefactor as in the Ag case and taking $T = 200$ K in eq. (2.1), the diffusion barrier across the Pt-Cu boundary at steps is estimated to be ~ 0.5 eV.

2.4 Co

The possibility of growing monatomic wires of Co is extremely interesting to address the question of magnetism in 1D structures. The step decoration method, although it creates supported wires which are not completely decoupled from the substrate, is particularly useful since it allows a continuum of choices from the monatomic limit to larger structures. The growth of Co chains of monatomic and multi-atomic width is reported in Secs. 2.4 and 2.4, respectively. In Sec. 2.4 we discuss the Co-Pt interface corresponding to 1 ML Co coverage. Although a lot of interest has been dedicated to thin Co/Pt layered structures due to the pronounced perpendicular magnetic anisotropy that makes this system a good candidate for high-density magneto-optical devices [85–89], relatively few studies [90–92] reported an atomic-scale analysis of the Co-Pt interface. Details of the interface atomic structure, such as strained layers, stacking faults, steps and intermixing can give sizable contributions to the magnetic anisotropy, favoring or inhibiting its perpendicular component [85, 87, 89, 91, 93–97]; given that the separation of such contributions is still controversial, it would be useful to measure anisotropy-related quantities on well defined Co/Pt interfaces

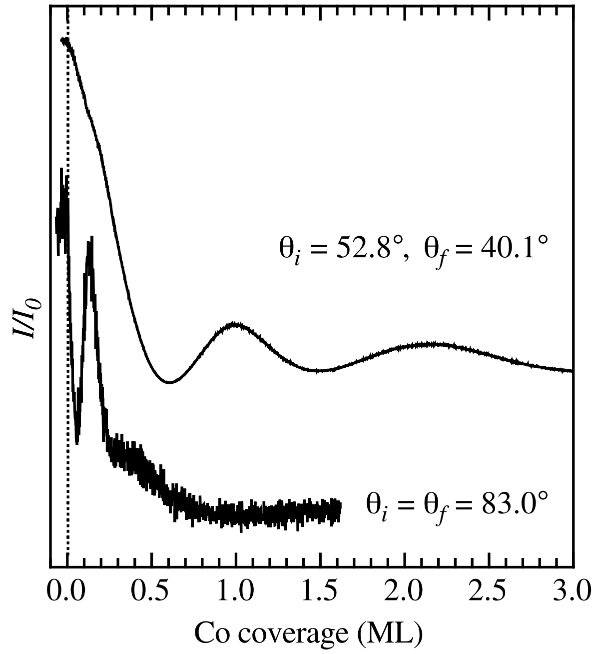

Figure 2.19: Normalized TEAS intensity during deposition of Co at $\theta_i = 52.8°$, $\theta_f = 40.1°$ (top) and $\theta_i = \theta_f = 83.0°$ (bottom). The He beam wavelength λ_{He} is 1.03 Å, the deposition rate is 1.6×10^{-3} MLs^{-1} for both curves. The upper curve is recorded at $T = 250$ K while the lower one is recorded at $T = 300$ K.

whose differences are well known, such as Co on flat and vicinal Pt(111) surfaces. In order to characterize the Co/Pt interface on a stepped substrate we have investigated the monolayer structure by STM and TEAS. As expected from the strong lattice mismatch and from the negative intermixing enthalpy between Pt and Co, the monolayer film reveals a partially dislocated structure with a small degree of alloying even below room temperature (RT). The work presented here constitutes to our knowledge the first study of Co nucleation on a densely stepped Pt surface. Also no data exist in the literature for Co deposition on Pt below RT.

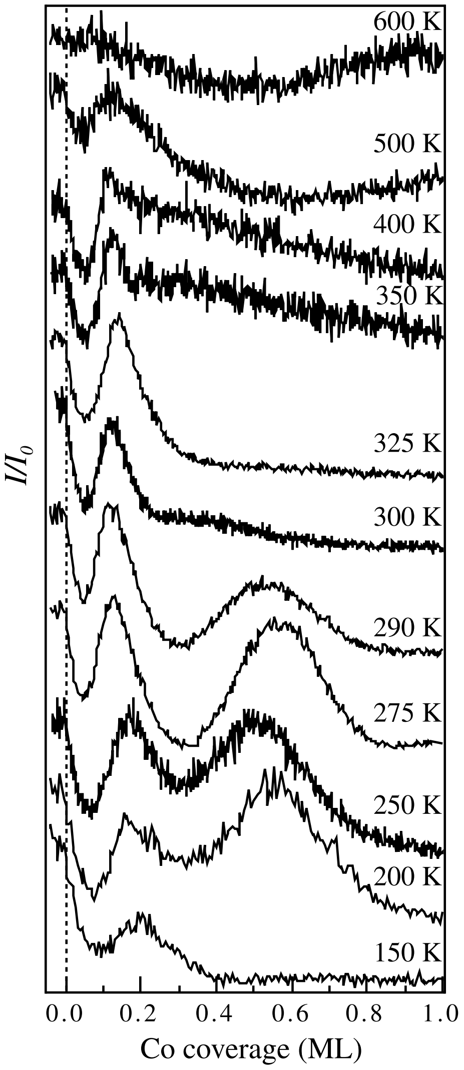

Figure 2.20: TEAS intensity in grazing incidence conditions during Co deposition at different temperatures; $\theta_i = \theta_f = 83°$, $\lambda_{\mathrm{He}} = 1.01$ Å. The first peak around 0.13-0.20 ML corresponds to the monatomic decoration of the Pt steps by Co atoms. The deposition rate is between 1.6×10^{-3} and 4.2×10^{-3} MLs^{-1} for all curves.

As shown in a previous STM study [90], Co on Pt(111) nucleates in a spatially homogeneous way at RT and it grows in a quasi-layer-by-layer mode up to 3 ML. After 3 ML, three-dimensional growth with hcp stacking sets in. A number of depressions are observed in the first Co layer that are attributed to non-specified misfit dislocations. For $T \geq 300$ K Co induces a reconstruction of the Pt(111) surface in the form of Pt fcc and hcp domains. The reconstruction has been attributed to Co atoms incorporated in the first Pt layer by a strain-relief process. Post-deposition nucleation of dendritic islands removes the Pt reconstruction. A recent STM study suggests that the dendrites mainly consists of Pt atoms that have been replaced in the underneath layer by Co atoms [92]. Surface X-ray diffraction measurements [91] confirm that Co grows quasi-layer-by-layer in the first layers, but, contrary to Ref. [90], suggest that Co grows with its own lattice spacing already from the first layer at RT. On Pt(997), on the other hand, our measurements clearly show that up to $T \approx 350$ K Co grows in a strained fashion forming domains with the lattice spacing of the underlying Pt layer. These domains are separated by two different kinds of dislocations in the form of hcp-fcc stacking faults and of what we attribute to Co inclusions in the Pt layer.

Growth of Co monatomic chains

Fig. 2.19 shows two TEAS curves for Co deposition on Pt(997) at $\theta_i = 52.8°$, $\theta_f = 40.1°$ (top) and $\theta_i = \theta_f = 83.0°$ (bottom). The upper curve has two maxima which we attribute to the completion of the first and second Co monolayer, respectively. As we have done for Ag and Cu we use the first maximum to calibrate the coverage scale. This calibration yields a coverage of 0.13 ML for the first peak in the grazing incidence curve (bottom), as expected for a single monatomic row decorating each step of the Pt(997) surface.

To determine the influence of growth kinetics on Co row formation, a series of TEAS deposition curves was recorded at grazing incidence for different temperatures (Fig. 2.20). We note that no influence of the deposition rate on the growth-mode was observed for rates between 3×10^{-4} MLs^{-1} and 6×10^{-3} MLs^{-1} at $T = 250$ K. By following the temperature evolution of the intensity maximum around 0.13-0.20 ML in Fig. 2.20, we observe that the first Co row decorates the Pt steps between 150 and 500 K. However, as discussed in Sec. 2.2, the formation of a true one-dimensional atomic chain cannot be inferred by the sole presence of this intensity maximum. At 150 K the first row peak is quite broad and centered at 0.2 ML. As in the case of Ag and Cu at 120 K (Secs. 2.2 and 2.3) we conclude that the growth mode is rough because of kinetically inhibited edge-smoothening. Rough growth implies that the adatoms attaching to Co already decorating the Pt step edges are not mobile enough to migrate to the remaining bare Pt sites. To find the threshold at which smooth row growth occurs, we have plotted in Fig. 2.11 the coverage corresponding to the first intensity maximum in Fig. 2.20 vs substrate temperature; one can see that only for $T > 250$ K the first peak corresponds to the monatomic row nominal coverage of 0.13 ML which is expected for fast diffusion of the Co adatoms.

The STM image in Fig 2.21, taken after deposition of 0.07 ML Co at 250 K, shows atomically-resolved Co monatomic chains decorating the Pt step edges. Co rows grow on the lower step edge side, as in most cases of step decoration in metal systems [66, 67, 70, 98, 99], but contrary to Fe on Cu(111) [100]. A few protrusions can also be seen on the Pt terraces in Fig 2.21; we suggest that these protrusions, that are ~ 0.3 Å higher than the surrounding Pt atoms, represent small inclusions of Co in the Pt layer. At

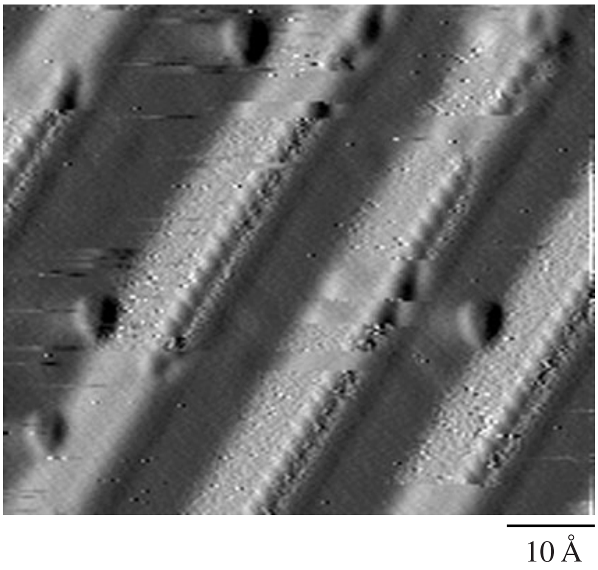

Figure 2.21: $\partial z/\partial x$ image taken after deposition of 0.07 ML Co at 250 K. Atomically-resolved Co chains decorate the step edges. Step down direction is from right to left. The protrusions on the terraces might be due to Co atoms incorporated in the Pt layer. $I = 1.0$ nA, $V = 0.1$ V.

present, however, we cannot definitively assign these features to Co atoms embedded in the Pt layer as our Auger sensitivity to contaminants is $\sim 1\%$ of a ML, close to the observed coverage of such features. Further support for moderate intermixing between Co and Pt at low temperature will be given in Sec. 2.4.

In the high temperature range, step decoration is limited by the onset of alloying between Co and Pt. X-ray diffraction and LEED studies [91, 101, 102] of Co films on Pt(111) have shown that alloying sets in at 550 K. In agreement with these measurements we do not observe step decoration at 600 K (see Fig. 2.20) and the ratio between the Co and Pt Auger peak intensities decreases accordingly.

Growth of Co stripes

We now describe Co growth beyond the monatomic chain limit. Particular attention is paid to those growth conditions that allow to prepare samples with uniformly spaced arrays of regular Co stripes. The fabrication of stripes with regular smooth edges is important in order to address the transition from 1D to 2D behavior in, e.g., magnetism studies without dealing with geometrically complex growth patterns. Although raising the substrate temperature might be effective in smoothening the Co stripes, one has to take care that the Co atoms remain confined to their adsorption terraces. Only in this case, in fact, the periodic arrangement of the substrate will be preserved and the average width of the Co stripes can be taken to be $w\Theta_{\mathrm{Co}} \pm \sigma\Theta_{\mathrm{Co}}$ where w is the average terrace width, σ the standard deviation of the terrace width distribution, and Θ_{Co} is the Co coverage.

We start from the analysis of Fig. 2.20 for $\Theta_{\mathrm{Co}} \geq 0.13$ ML. As discussed in Sec. 1.1, the desynchronization of the row growth on terraces having different widths suppresses the reflection maxima due to chain formation apart from the first one. The second maximum centered at $\sim 0.5 - 0.6$ ML, due to terrace confinement of Co atoms (see Sec. 1.1), indicates however that regular structures form parallel to the step edges. For $T < 200$ K edge diffusion is too slow to allow rearrangement of the Co adatoms in regular stripes and no half-monolayer peak is observed in Fig. 2.20. Deposition in this temperature range is likely to produce connected Co islands with irregular triangular shapes attached to the Pt steps as has been observed by STM for the Ag/Pt(997) system at $T = 120$ K (Sec. 2.2). In agreement with our results, Rusponi *et al.*, in a yet unpublished STM study of Co nucleation on Pt(111) [103], have found that Co islands grow randomly ramified at $T = 130$ K and that the mobility-driven transition to compact-shaped clusters starts between 160 and 200 K. As the substrate temperature increases, smoothening occurs and we assist to the formation of regular parallel stripes. Figure 2.22(a) is an STM image recorded after deposition of 0.6 ML Co showing that Co growth at $T = 250$ K conserves the original step pattern, forming regular stripes that run parallel to the Pt steps. Note that, depending on the tunneling parameters and tip

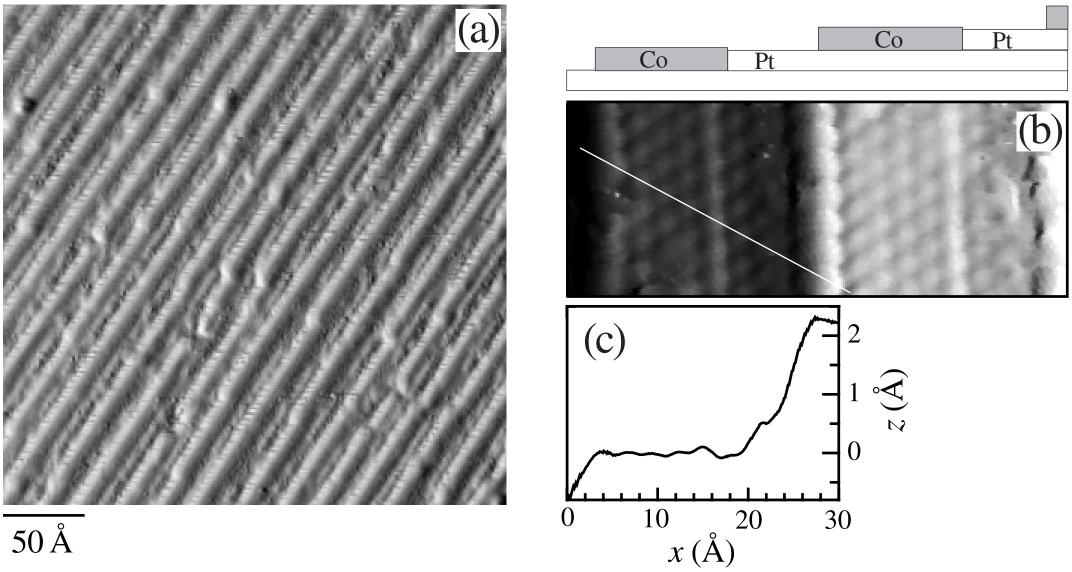

Figure 2.22: (a) STM $\partial z/\partial x$ image of 0.6 ML Co deposited at $T = 250$ K; step down direction is from right to left; $I = 1.0$ nA, $V = 0.1$ V. (b) Detail of two adjacent terraces, $I = 4.0$ nA, $V = 1$ mV; the drawing shows the corresponding vertical cross section. (c) Line scan showing the height difference between Co and Pt.

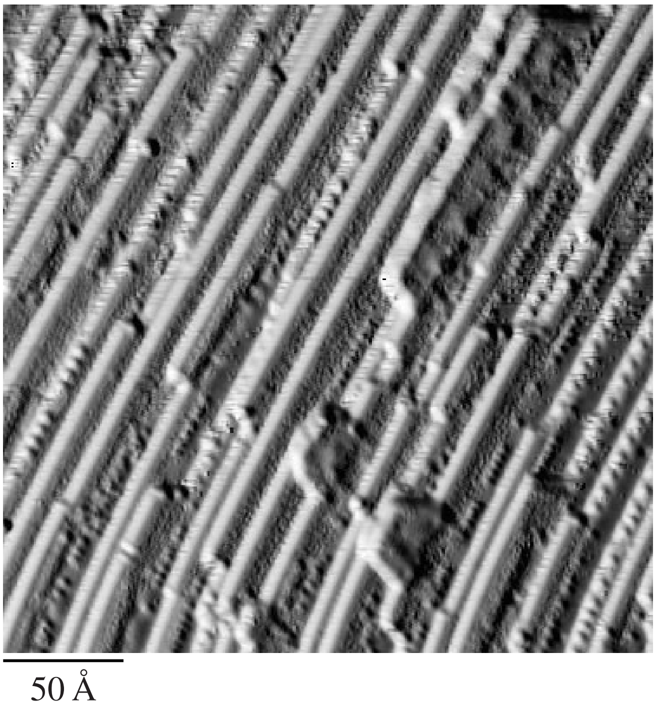

Figure 2.23: $\partial z/\partial x$ image of 0.6 ML Co deposited at $T = 385$ K. Formation of double layer Co islands. $I = 1.0$ nA, $V = 0.1$ V.

conditions, Co can be imaged a few tenths of Å higher or lower than Pt [90,92,103]; in the present work the Co layer is found to be in most cases 0.2-0.4 Å higher than Pt as in (b). Due to the finite tip size, atoms on the lower step edge side are often distorted or not imaged at all; this effect is evident in the line scan reported in (c), where the rising edge extends itself over more than one lattice spacing.

The half monolayer peak in Fig. 2.20 suddenly disappears between 290 and 300 K. Such a net transition has a counterpart in the Co growth mode. Co adatoms at $T \geq 300$ K have enough thermal energy to cross the Pt-Co boundary at steps, thereby disrupting the high step periodicity that is the origin of the half monolayer peak. Fig. 2.23 shows such an effect following 0.6 ML Co deposition at 385 K. Irregular step bunching is also observed indicating that Co tends to form bilayer islands. The temperature at which Co atoms can cross over the Co-Pt lateral interface at steps gives us an estimate for the diffusion barrier of such a process. By taking $\nu_0 = 10^{13}$ and $T = 300$ K in Eq. 2.1, we estimate E_h to be of the order of 0.7 eV.

In contrast to the deposition of Co on Pt(111) [90,92,103], we do not observe the formation of dendrite-like islands above 300 K; reconstruction and exchange processes between Co and Pt are nonetheless not excluded and will be discussed in Sec. 2.4. The fabrication of periodic arrays of Co regular stripes is limited at low temperature by

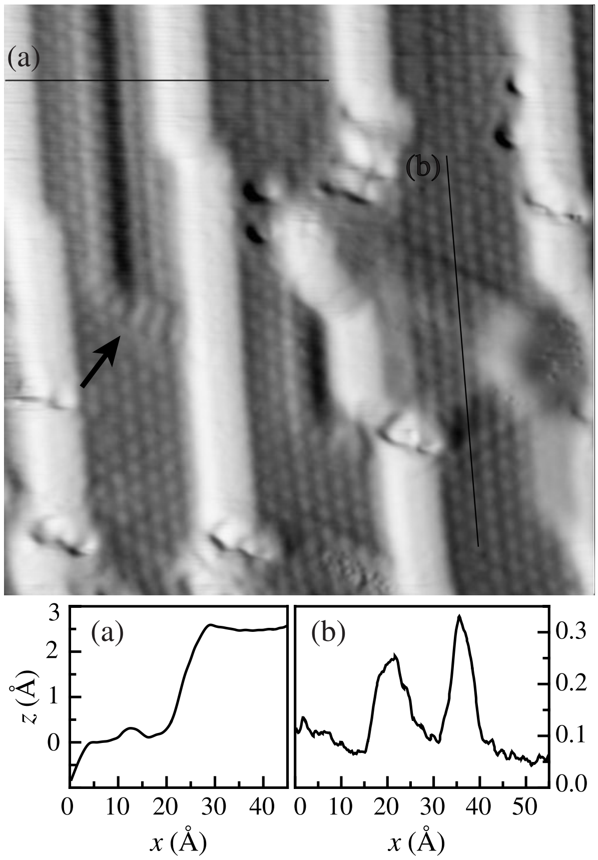

Figure 2.24: $\partial z/\partial x$ image of 1 ML Co deposited at $T = 250$ K; $I = 1.0$ nA, $V = 8$ mV. Two different dislocated domains (a) and (b) [see the corresponding line scans at the bottom] are clearly visible.

slow diffusion processes and at high temperature by the migration of Co atoms across adjacent terraces, a process which is active already at 300 K.

1 ML Co

When a complete Co layer is formed, dislocations develop on part of the surface; this is evident already at 250 K. The dislocation pattern consists of fcc-hcp stacking-faults that run parallel to the step edges [(a) in Fig. 2.24] and of triangular shaped structures whose arms intersect the steps at an angle of ±60° [(b) in Fig. 2.24]. Since the dislocations do not form an ordered superstructure they do not give rise to additional diffraction peaks in the He spectrum, contributing only in lowering the reflectivity of the Co monolayer.

The arrow in Fig. 2.24 evidences the transition between fcc and hcp domains along the dislocation (a). The formation of stacking-faults is attributed to a strain-relief mechanism arising from the 9.7 % lattice mismatch between Co and Pt. However, in terms of strain relief one would expect the domain boundaries to be perpendicular to the steps because strain is supposedly higher along atomic rows running parallel to the step edges than along the short perpendicular ones. The formation of domain boundaries parallel to the step edges can be attributed to the presence of a lateral interface between Pt and Co. Since Pt-Co heterobonds are stronger than Co-Co bonds at the step edges (see chapter 3), the first Co row is probably shifted towards the Pt step with respect to an ideal pseudomorphic overlayer; as a result of this shift the amount of strain in the direction perpendicular to the substrate steps can be increased in a considerable way and give rise to dislocations.

The analysis of the triangular structures (b) is not conclusive. Recent tight-binding calculations [104] indicate that the optimal structure of a Co monolayer on Pt(111) conssists of a superlattice of alternating fcc-hcp equilateral triangular regions, separated by local line defects extending over two contiguous atomic rows. This suggests that the observed triangular dislocation in Fig. 2.24 is a domain boundary between fcc and hcp regions. On the other hand, the stacking transition between the exterior and the interior of the triangle is not as evident as for (a). In alternative, since Co atoms appear higher in the STM images than Pt atoms (see Fig. 2.22), the positive height difference between the triangle sides and the rest of the terrace could be attributed to Co atoms on top of Co incorporated in the Pt underlying layer.

Co incorporation upon deposition at 300 K was reported by Lundgren *et al.* in Ref. [92] and low-temperature intermixing has been reported for similar systems such as Pt/Ni [105, 106]. Supporting evidence (see also Fig. 2.21) for exchange processes between Co and Pt below RT is given in Fig. 2.25: a Co island on the lowest terrace on the left has nucleated on top of 1 ML Co at 250 K. Its height difference with respect to the Co atoms on the adjacent terrace (which preserve the Pt interlayer spacing) is 0.3 Å, the same value measured for the protrusions found on the terraces. This suggests that the protrusions in Fig. 2.25 are actually Co atoms on top of incorporated Co, as sketched at the bottom.

We now discuss the Co-Co spacing in the monolayer film. He scattering on a vicinal surface, in addition to the diffraction peaks due to the step periodic structure, gives rise to a modulation of the diffracted beam due to the atomic corrugation of each terrace (Sec. 1.1, Fig. 1.5). Knowing the He beam wavelength, the angular position of the maximum of the modulating envelope allows us to determine the lateral lattice constant of the topmost layer of the surface. The dotted line in Fig. 2.26 shows the $n = 6$ diffraction peak (Eq. 1.2) in coincidence with the maximum of the envelope function due to the Pt atomic corrugation. From its position we calculate (Eq. 1.6) a spacing between neighboring atomic rows running along the $[1\bar{1}0]$ direction (parallel to the steps)

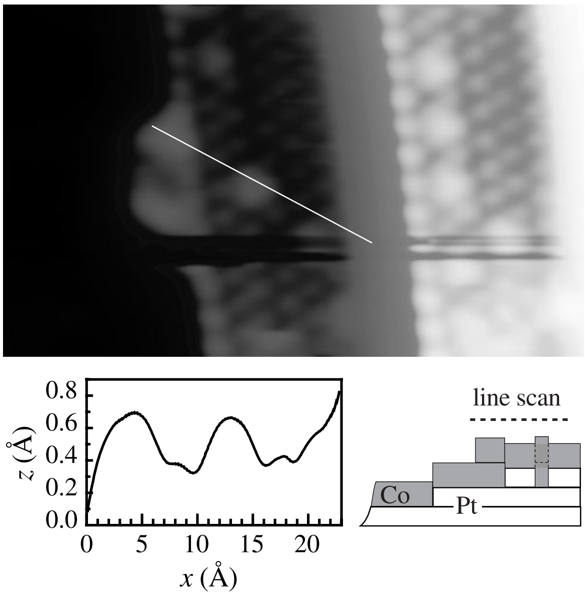

Figure 2.25: Image of 1 ML Co taken at $T = 250$ K; $I = 6.0$ nA, $V = 4$ mV. A Co island nucleating on top of the first Co layer is visible attached to the middle step. The height of the Co island is the same as that of the protrusions on the terrace, suggesting that the latters result from Co atoms incorporated in the Pt substrate, as depicted in the drawing. The horizontal lines in the lower half of the STM image are due to a tip instability.

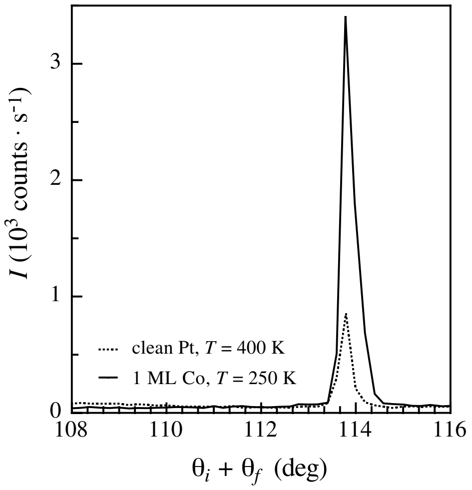

Figure 2.26: First-order Bragg peak relative to the terrace atomic structure measured for clean Pt at 400 K (dotted line) and 1 ML Co at 250 K (solid line). The incidence angle is kept fixed while the reflection angle is varied. The Bragg incidence and reflection angles corresponding to the peak are 34.8° and 79.0°, respectively, measured with respect to the (111) direction; $\lambda_{\mathrm{He}} = 0.98$ Å.

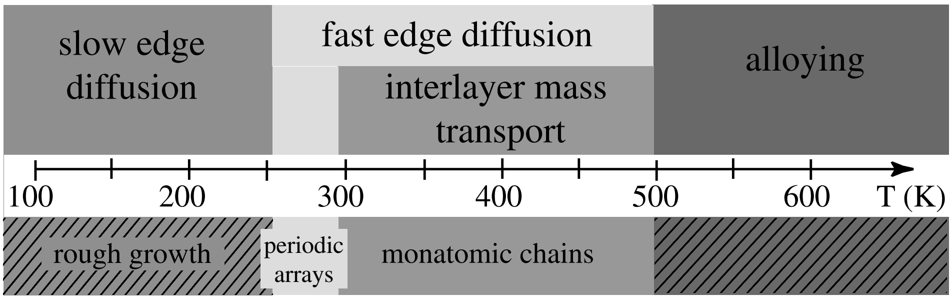

Figure 2.27: Diagram representing different Co growth modes on Pt(997) as a function of the substrate temperature. Although the temperature scale refers to the Co/Pt(997) system, this description applies to other metals such as, e.g., Ag and Cu.

of 2.39 ± 0.05 Å, which is very close to the theoretical value of 2.40 Å. The thin solid line is a spectrum recorded after deposition of 1 ML Co at 250 K. If the Co lattice spacing did not coincide with the Pt one, the modulating envelope would shift and the peak shown in Fig. 2.26 would be quenched. The presence of the peak after Co deposition is an indication that at least part of the Co layer is in registry with the Pt substrate (the observed increase in intensity is due to temperature effects and to the larger corrugation of the He-Co potential with respect to the He-Pt one). We conclude that large portions of the first Co layer at this temperature have the same lattice spacing as the Pt substrate, in agreement with the calculation for the Co/Pt(111) system reported in Ref. [104].

In conclusion, we have found that the decoration of the Pt steps by Co atoms takes place in a wide range of temperatures: from 150 to 500 K, when alloying sets in. However, for $T \leq 250$ K slow edge-diffusion limits the smoothening of the Co chains. At 300 K Co atoms have enough thermal energy to cross the Co-Pt lateral interface at the steps thereby allowing the formation of double layer Co stripes and the breaking of the original periodic step patterns. The temperature window for the growth of a regular periodic pattern of Co wires is therefore limited to a narrow interval between 250 and 300 K when edge diffusion is fast enough to have perfect row-by-row growth and interlayer crossing is still inhibited. These results are summarized in Fig. 2.27. There is some evidence for Co incorporation (the order of 0.01-0.02 ML) into the Pt top-layer already at 250 K. At monolayer completion strain causes the formation of stacking faults at 250 K; most of the Co layer is however in registry with the Pt substrate at this temperature. Heating above 300 K results in the formation of bilayer Co islands.

2.5 Ni

Having gone through the preceding paragraphs, one might think that growing 1D structures by step decoration is a viable process for any combination of substrate and deposited materials. It is not so, as the Ni/Pt(997) case demonstrates. Intermixing between Ni and Pt takes place in the topmost surface layer already at 150 K. The adislands at this temperature have a rough 2D character and substantial alloying occurs at the step edges, as shown in Fig. 2.28(a). It is therefore not possible to find a temperature range where adatom diffusion is fast enough to lead to row-by-row growth prior to alloying. Ni, as Co, is highly miscible with Pt in the bulk; in the Co case, however, Co films on Pt are kinetically stabilized because the activation energy needed for interdiffusion is relatively high. Exchange processes between Ni and Pt, on the other hand, seem to have a very low energy threshold. Field-ion-microscope observations have shown that Pt atoms exchange with Ni already at 105 K on a Ni(110) surface overcoming an activation barrier of 0.28 eV [105, 107].

Intermixing proceeds mainly via the substrate steps: at 150 and 200 K most Ni atoms are imaged as protrusions along the step edges and only a few protrusions are visible on the terraces [Fig. 2.28(a) and (b)]. The line scan reported in Fig. 2.29 shows that the periodicity of the Ni atoms at the step edges is 5.5 Å, i.e., two Pt lattice constants. We have therefore a one-dimensional alloyed phase of alternated Pt and Ni atoms at the step edges. The existence of such an ordered phase might be considered as the 1D analogue of the $NiPt_3$ alloyed phase in the bulk, where Ni atoms do not have Ni nearest neighbors. Given the presence of the Pt surface layer, however, the Ni/Pt ratio is not equal to 1:3, but rather to 1:6 (counting only the nearest neighbors). Incorporation

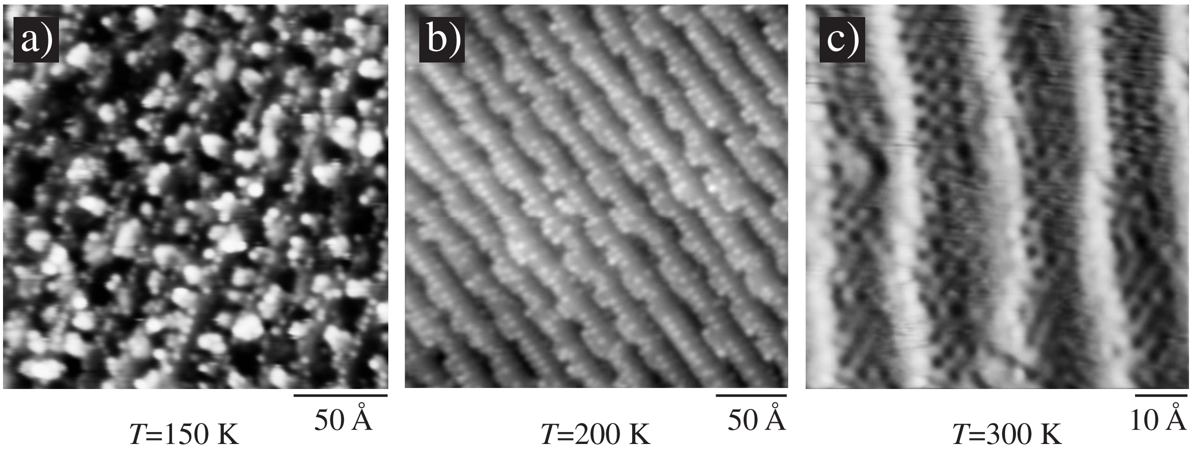

Figure 2.28: 0.2 ML Ni deposited on Pt(997) at 150 K (a), 200 K (b), 300 K (c). Ni atoms are imaged as protrusions ~ 0.4 Å higher than Pt. Step down direction from right to left.

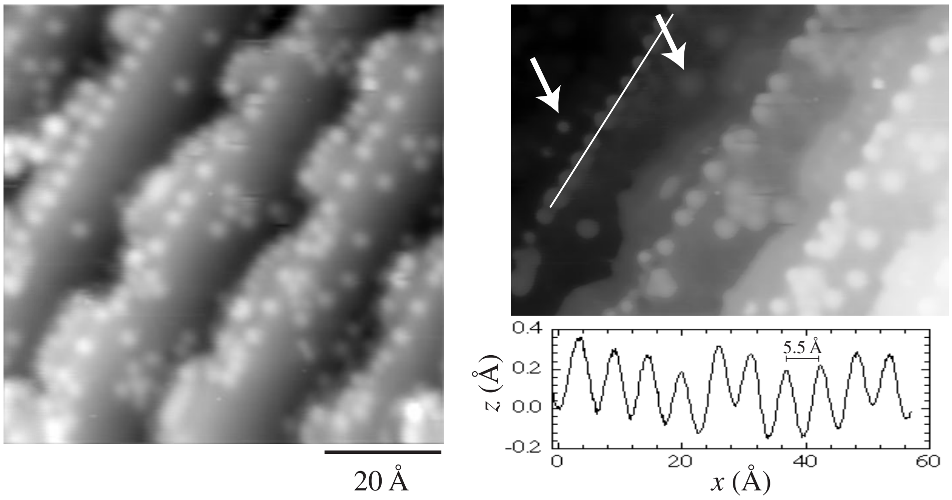

Figure 2.29: Detail of Fig. 2.28(b); subtraction of a plane parallel to the (111) terraces (right image) evidences that Ni atoms (arrows) are imaged as protrusions about 0.4 Å higher than Pt. The line scan evidences the 2 × 1 structure at the step edge.

in terrace sites might occur directly upon impact or as a slow process with respect to incorporation at step sites. It is also likely that the alloyed steps block further diffusion into the terraces. A close look at Fig. 2.29 reveals that the adislands decorating the step edges consist of both Pt and Ni atoms. The arrows in the image at right point two Ni atoms, both surrounded by Pt: one is part of an island decorating the step, the other is incorporated in the adjacent terrace. So while Ni atoms are incorprated into the Pt layer, Pt atoms are probably expelled into the islands that decorate the step edges.

At 300 K the surface is completely alloyed [Fig. 2.28(c)] and Ni atoms seem to form a 2 × 2 ordered structure. This result is completely at variance with the only study of Ni growth on Pt(111) found in the literature, a photoelectron diffraction analysis which concluded that Ni grows layer-by-layer at RT occupying hcp sites [108]. The alloyed phase at 300 K is similar to that observed by STM for Mn on Cu(100) and Cu(111), where Mn atoms are incorporated in the Cu layer forming a $c(2\times2)$ and a $(\sqrt{3}\times\sqrt{3})\mathrm{R}30^\circ$ ordered superstructure, respectively [109–111]. *Ab initio* total-energy calculations have shown that the observed buckling of the Mn atoms in the alloyed phase on Cu(100) is essentially due to an increase of the Mn local magnetic moment that accompanies relaxation, i.e. loss of coordination [109, 112]. Although Ni atoms have a much smaller magnetic moment than Mn, a similar explanation for the buckling of Ni atoms observed in Fig. 2.28(c) merits further investigation since it implies a long-range ferromagnetic or antiferromagnetic order of the alloyed phase. Even more interesting would be the possibility of studying the magnetic properties of the 1D Ni-Pt alloy observed at the step edges.

Chapter 3

Bimetal Wires

Epitaxy of multicomponent metal films is a widely studied subject because of its relevance for technological applications in the areas of catalysis, microelectronics and material science [93, 113]. Understanding the interplay between heteronuclear metal-metal bonds, surface geometric structure and overlayer morphology is a prerequisite for fabricating mixed-metal compounds with tailored structural and electronic properties. Interfaces between different materials in multicomponent systems constitute a natural test ground for such investigations. The morphological and elemental composition characteristics of interfaces, defined in terms of roughness and sharpness, respectively, can critically influence the physical behavior of most low-dimensional systems. Interfaces between magnetic and non-magnetic materials are of particular interest because of their influence on the magnetic anisotropy of thin films [94, 114–116] and on the electronic transport properties of multilayered devices [117–120]. Ag/Co superlattices exhibit giant magnetoresistance properties [121] and bulk immiscibility of the two constituents. As a consequence they have been the object of numerous studies that investigated the connection between structure and transport properties [89, 119, 122]. In order to have a high magnetoresistance effect and a sizeable current to work with, the most convenient superlattice geometry would be a film of contiguous stripes of magnetic and non-magnetic materials with the current flowing perpendicular to the lateral interfaces between the stripes. Such a geometry raises growth concerns that have not found a solution yet.

In this Section we investigate the character of lateral one-dimensional Ag-Co interfaces on a stepped Pt substrate. This is rather an interesting and general combination of elements: Co and Ag are immiscible in the bulk and have different atomic sizes. While Ag is not miscible in bulk Pt, Co is and therefore we can expect the two elements to interact in dissimilar ways with Pt. The presence of surface steps makes it possi-

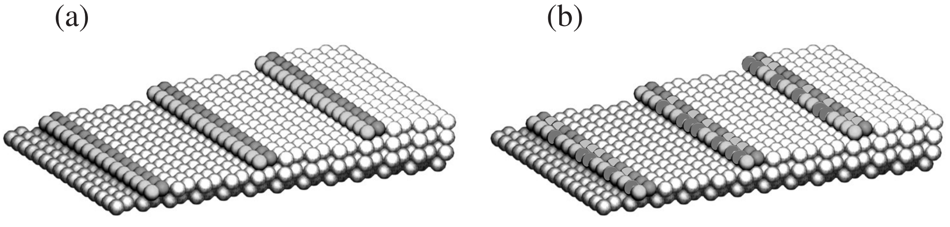

Figure 3.1: (a) Growth of two ordered rows of different metals on Pt(997). (b) Mixed rows.

ble to investigate the formation of lateral interfaces between the three metals. Linear monatomic chains of either Ag or Co are obtained by step decoration of the Pt(997) surface as described in the previous chapter. Subsequent deposition of Co or Ag leads to the formation of a Ag-Co interface which can be either sharp or disordered depending on the order of evaporation and on the surface temperature. In particular, we will show that general surface energy arguments commonly used to explain different growth modes in thin film epitaxy can be adapted to the 1D case reported here. Finally, our results are compared with equilibrium energy calculations at 0 K and with a thermodynamic model of row formation which support the experimental data. The calculations have been performed by F. Picaud, C. Ramseyer, and C. Girardet in Besançon with the collaboration of C. Barreteau, D. Spanjaard, and M.C. Desjonquères in Orsay, France, and are reported in more detail in Ref. [56].

3.1 Ag/Co wires

We have shown in Sec. 1.1 that by means of TEAS we can control in real-time the step decoration process for Ag and Co separately. We can now take advantage of this fact to deposit precisely a monatomic row along the Pt step edges in order to form a true 1D interface of Co (Ag) atoms. By subsequent deposition of Ag (Co) we can then study how growth evolves, whether ordered structures will form or intermixing between the two metals will prevent ordering on the atomic scale. Figure 3.1 depicts the situation where two different metals form two separated rows (a), and when they intermix forming a disordered phase (b). Fig. 3.2(a) shows the He reflectivity curves recorded in grazing incidence conditions during deposition of Ag and Co at 150, 200 and 250 K.[1] In the following, this deposition sequence will be referred to as $Ag^{I}Co^{II}$. First a single row of Ag has been deposited on the surface as it is evidenced by the peak at ~ 0.17 ML; then Ag deposition has been stopped and after a few seconds we have started evaporating Co. If the Co evaporator shutter is kept close, the He beam intensity remains constant

---

[1] Temperatures higher than 250 K have not been investigated to reduce Co/Pt intermixing.

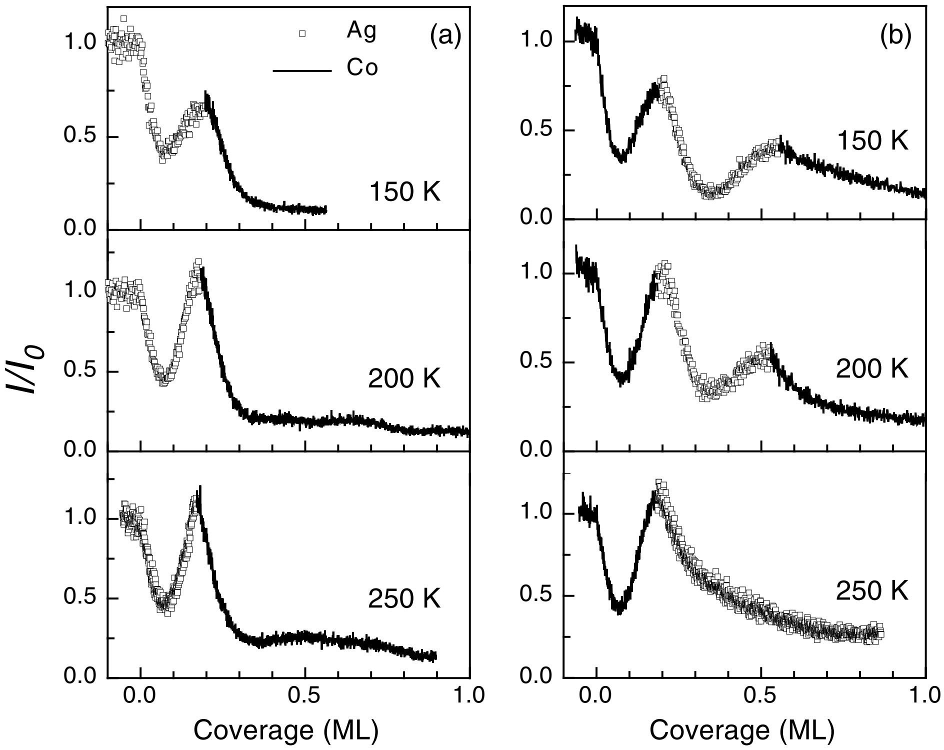

Figure 3.2: (a) TEAS reflectivity recorded during deposition for the $Ag^I Co^{II}$ sequence; $\theta_i = \theta_f = 83°$. Deposition of Ag is stopped after completion of a monatomic row and Co is subsequentely evaporated on the surface. (b) Same as (a) for the $Co^I Ag^{II}$ sequence. Ag is deposited after completion of a Co monatomic row; the formation of ordered stripes is inferred from the presence of the peak at ~ 0.6 ML at $T = 150$ K and $T = 200$ K.

after Ag deposition, indicating that no structural changes take place in the Ag row. The rapid decrease in intensity during Co evaporation shows that the defect density on the surface augments; at 200 and 250 K we would expect to observe the Co peak at ~ 0.5 ML as in Secs. 1.1 and 2.4 if Ag and Co formed ordered atomic rows parallel to the Pt step edges.[2] Since this is not the case we conclude that the Ag-Co overlayer is disordered. In the Ag/Pt(997) and Co/Pt(997) cases at $T \geq 200$ K the mobility is sufficiently high for both Ag and Co atoms to rearrange into regular stripes parallel to the Pt steps (Secs. 2.2 and 2.4); disorder in the Ag-Co case therefore is not likely to be due to a roughening of the step edges, but rather to intermixing of the two species, in agreement with the results of Secs. 3.2 and 3.3. We now discuss the reversed situation where Co is deposited first, indicated as $Co^I Ag^{II}$ [Fig. 3.2(b)]. We stop deposition at a coverage corresponding to a monatomic Co row and subsequently start evaporating Ag. At 150 and 200 K we observe the development of the peak at ~ 0.6 ML, as expected

---

[2] The 0.5 ML peak is observed for Co/Pt(997) below 290 K and for Ag/Pt(997) below 400 K.

from ordered Ag growth on Pt(997). This case is quite different from the previous one as we have indications of ordered structure formation. Supported by the calculations reported in Sec. 3.2, we suggest that the most stable configuration is that of the Co atomic row being in contact with the Pt steps while the Ag rows align themselves at the Co boundary without considerable intermixing. As the temperature rises, though, intermixing can occur even in this configuration. The binding energy values calculated for alloying of Co and Ag (3.82 eV/atom) are in fact close to those of the most stable $Co^{I}Ag^{II}$ configuration (3.68 eV/atom). Accordingly, at 250 K no peak is observed in the $Co^{I}Ag^{II}$ case. Note that in Fig. 3.2(b) Ag deposition has been stopped at around 0.6 ML and further Co has been deposited on the surface. This was done in the hope of growing an ordered superlattice of alternated Co and Ag rows, a task that turned out to be unfeasible by the measurements in (a) relative to the $Ag^{I}Co^{II}$ case.

Surface-confined mixing of Ag and Co has been observed on Ru(0001) [123] and on Mo(110) [124]. In both cases intermixing has been attributed to a strain-relief mechanism which compensates the strain of opposite sign imposed by the substrate on the two overlayer metals [125]. On Pt(997), as on Ru(0001), Co is under tensile strain while Ag is under compressive strain; in contrast to Ref. [123, 124], however, strain-relief is unlikely to be at the origin of interdiffusion in our case, at least below 250 K. The different behaviour of the $Co^{I}Ag^{II}$ and $Ag^{I}Co^{II}$ configurations cannot be explained in terms of strain since mixing would occur in both cases. A qualitative understanding of our results can be presented in terms of surface and interface energies of Pt, Co and Ag. It is well known from thin film epitaxy that layer-by-layer growth requires an adsorbate with a smaller surface energy to be deposited on a substrate with a higher surface energy, the interface energy being small to avoid intermixing [126]. If the surface energy of the substrate is smaller than that of the deposited material segregation can occur. The above argument holds for two dimensional films, but it can be extended to one-dimensional interfaces. In our case, since Ag that has a smaller surface energy with respect to Co [127], thermodynamics favours the $Co^{I}Ag^{II}$ over the $Ag^{I}Co^{II}$ configuration. Following the analogy with 2D systems, a more detailed analysis can be done in terms of the first and second derivatives of the surface energy with respect to the adlayer coverage, as described by Christensen *et al.* [128]. The first derivative of the surface energy is the segregation energy, while the second derivative determines the sign of the interaction between the deposited adatoms in the host matrix. If the segregation energy is negative the deposited material stays at the surface layer; if it is positive the deposited material will eventually diffuse into the substrate. Christensen *et al.* have calculated these derivatives for all combinations of transition and noble metals consid-

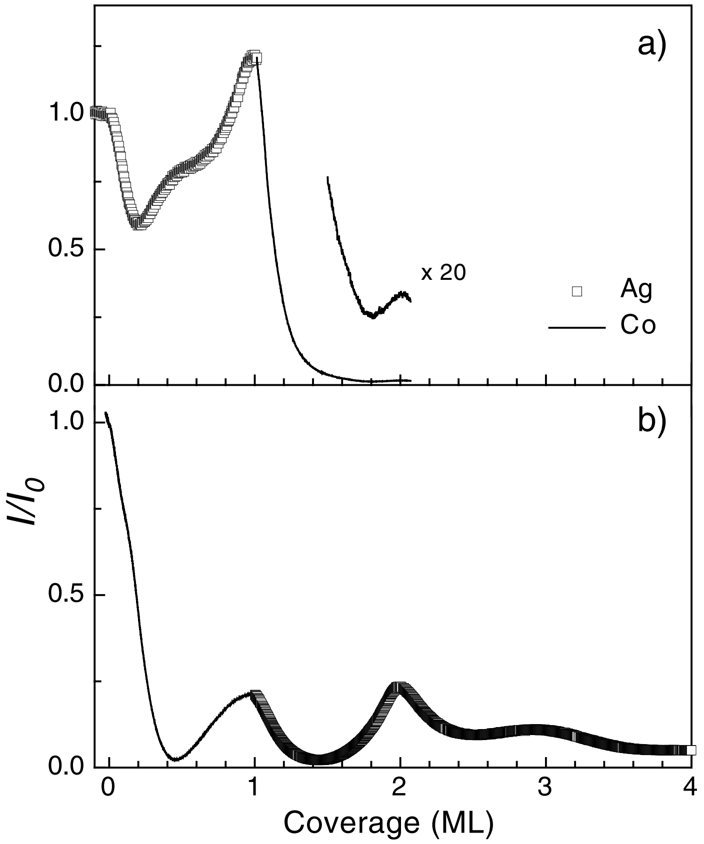

Figure 3.3: TEAS reflectivity in non-grazing incidence conditions, $\theta_i = 60.5°, \theta_f = 47.2°$. (a) Deposition of 1 ML Ag and subsequentely 1 ML Co at 225 K. (b) Reversed order of Ag and Co deposition at 200 K.

ering deposition on close-packed flat surfaces. The segregation energy for Co deposition on Ag results to be 0.33 eV/atom, while Ag deposited on Co yields -1.16 eV/atom [128], again favouring the $Co^I Ag^{II}$ over the $Ag^I Co^{II}$ configuration. Moreover, the calculated Co/Pt binding energy is 20 - 30 % larger than the Ag/Pt one, depending on the adsorption site (Table 3.3). In Sec. 2.4 we have suggested that, as a result of the strong Co-Pt interaction, Co atoms might diffuse in the Pt surface layer in moderate quantities (0.01-0.02 ML) already at 250 K. The stronger tendency of Co to bind with Pt with respect to Ag is certainly another factor that makes the $Co^I Ag^{II}$ configuration the most stable one. Further discussion of this point is reported in Sec. 3.2.

Comparison between 1D and 2D growth

To stress the analogy between 1D and 2D systems, we have repeated the measurements reported in Fig. 3.2 for Ag and Co monolayer films. Figure 3.3 shows the reflected intensity of the He beam recorded during deposition of 1 ML Ag followed by 1 ML Co

[Fig. 3.3(a)] and deposition of 1 ML Co followed by more than 2 ML Ag [Fig. 3.3(b)] in non-grazing incidence conditions. The coverage scales have been calibrated separately for the two metals, as described in Sec. 1.1. In this scattering geometry the He reflectivity depends on the overall surface (mostly terrace) order. At monolayer completion, in the case of layer-by-layer growth, the density of diffuse scatterers is at a minimum, therefore the oscillations in Fig. 3.3 have a period of 1 ML. The relative intensities of the monolayer peaks depend on the corrugation of the He-overlayer potential, on the Debye temperature and on the ordering of the overlayer. The first peak in Fig. 3.3(a) corresponds to the formation of a pseudomorphic Ag single layer on the Pt substrate with excellent ordering. The following Co monolayer peak is barely visible, and it is a factor 40 less intense compared to the situation where Co is deposited first, suggesting that the Co-Ag interface is disordered. Reversing the deposition order, we see in Fig. 3.3(b) that the He-beam intensity during Ag evaporation recovers, at monolayer completion, the initial 1 ML Co value and even further oscillations can be detected. We conclude that Ag grows layer-by-layer on the Co film for the first two layers, as it does on the bare Pt(997) surface [25].

In conclusion, the $Co^{I}Ag^{II}$ configuration has been shown to be the most stable in the case of decoration of Pt steps by monatomic Co and Ag rows as well as in the case of single monolayer films of Co and Ag on Pt. General thermodynamics arguments commonly applied in the description of thin film epitaxy can therefore be extended, at least in some cases, to 1D linear interfaces.

3.2 Calculation of the equilibrium structure at 0 K

The experimental observations described above will be analyzed in two steps. The first is the calculation of the total energy of the system considering only the interactions between Pt, Ag, and Co atoms, which yields the most stable configuration at 0 K. The second is the introduction of temperature effects in a mean field Ising model which essentially takes into account the entropy contribution to the free energy of the system. Kinetic effects have not been considered because it is extremely time-consuming to perform Monte-Carlo simulations of metal atom mixtures due to the number of diffusion processes involved in the calculations. Moreover, since the time interval between successive Ag and Co deposition is large compared to that of typical diffusion processes in the temperature range investigated here, we expect kinetics effect to play only a minor role.

The potential used to model the interactions between adatoms and between the

	Pt	Co	Cu	Ag
r_0 (Å)	2.77	2.51	2.55	2.89
λ (eV)	2.9135	0.2361	0.7776	1.9994
p	6.9662	8.2732	5.9935	6.2177
ϵ (eV)	3.9653	0.7918	1.2952	2.5096
q	3.2087	1.8493	2.4055	2.9138
α	0.93365	0.8570	0.9097	0.9518

Table 3.1: Potential parameters of Eq. 3.1 for Pt, Co, Cu, and Ag.

adatoms and the substrate is a N-body semi-empirical potential based on the second moment approximation in the tight-binding scheme [56, 129–138]. It is written as the sum of site energies E_i which are composed of a repulsive pairwise contribution and of a non-additive attractive part; the potential energy of the i^{th} atom in the presence of its neighbors j in a homogeneous system is given by[3]

$$E_i = \lambda \sum_j e^{-p\left(\frac{r_{ij}}{r_0}-1\right)} - \epsilon \left(\sum_j e^{-2q\left(\frac{r_{ij}}{r_0}-1\right)} \right)^{\alpha}, \quad \text{with} \quad r_{ij} < r_c\,. \tag{3.1}$$

The repulsive (λ, p) and attractive (ϵ, q, α) parameters are obtained by a least mean square fit of bulk and surface properties of the crystal, namely the experimental values of cohesive energy, bulk modulus, shear elastic constants [139], and the surface energies of low index surfaces [140] ((111), (100) and (110) in cubic crystals). r_0 is the nearest neighbor distance between metal atoms and r_c corresponds to a cut-off distance. This distance is taken to be $2r_0$, beyond which all the parameters converge to the infinite cut-off value. The optimized values of the potential parameters are given in Table 3.1 for Pt, Co, Ag and Cu. Note that α remains close to unity ($\alpha \simeq 0.8 - 0.9$) for most species, indicating that the potential in Eq. 3.1 is not far from being pairwise. Nevertheless it would be an error to assume that metals could be modelled by strictly pairwise potentials [129].

To generalize Eq. 3.1 to the case of hetero-atomic systems one usually takes the arithmetic averages for the distances r_0 and r_c and geometric averages for the parameters p, q, λ and ϵ calculated for the different atomic species. The exponent α can change from metal to metal and is approximated as α_X for XX interactions and α_{Pt} for the X-Pt interactions, and as $\sqrt{\alpha_X \alpha_Y}$ for X-Y interactions. This assumption however is not crucial since all the α parameters are quite close to each other ($\alpha = 0.9 \pm 0.05$). Finally,

---

[3] The exponent α in the second moment approximation is usually taken to be 1/2. For transition metals it can sometime be considered as an additional parameter [56, 130].

	Co^IAg^{II}	Co/Ag ordered alloy	Co/Ag disordered alloy	Ag^ICo^{II}
E	-62.44	-62.26	-61.15	-58.86
	Co^ICu^{II}	Co/Cu ordered alloy	Co/Cu disordered alloy	Cu^ICo^{II}
E	–60.22	–58.66	-57.97	-57.26

Table 3.2: Total energy (in eV) of equimolar alloys Co/Ag and Co/Cu on Pt(997) [from Ref. [56]].

the contribution to the variations of the binding energies due to the substrate relaxation and to the adsorbate-induced perturbation of the substrate have been found to be small and have been neglected.

The potential energy surface of a single adatom on Pt(997) is obtained by minimizing the potential energy E_i of the adatom at the position (x_i, y_i, z_i) with respect to z_i. A typical energy map obtained with this method is drawn in Fig. 2.1. By adding atoms adiabatically one can calculate the equilibrium structure which yields the minimum potential energy of the system. In the Ag, Co, Cu cases investigated by F. Picaud *et al.* in Ref. [56], this invariably leads to commensurate (1×1) adlayer structures, which agree well with the data presented in Sec. 2 at least on a short range scale. We now consider the situation for which an equimolecular mixture of atoms of two different metals is adsorbed on the Pt(997) surface. A set of $N/2$ atoms of A species and $N/2$ atoms of B species is adsorbed along the step of the Pt(997) surface and the minimum energy is determined for every arrangement of A and B species in the sites. The calculations have been performed for $N = 16$; periodic boundary conditions are applied along the rows to eliminate edge effects. The results are reported in Table 3.2. The energy values are given for a system formed by 8 Co atoms and 8 Ag (or 8 Cu) atoms which are restricted to occupy the first two rows closest to the lower step edge. Four types of atomic configurations are considered (X=Ag or Cu): Co^IX^{II} when the Co atoms and X atoms occupy the first and second row, respectively; CoX ordered alloy; CoX disordered alloy (an average is taken over many configurations); X^ICo^{II} where the X atoms and the Co atoms occupy the first and second row, respectively. The most stable structure is obtained when the Co atoms occupy the first row close to the step and the Ag atoms are trapped behind them, forming a second row, in analogy with the Co^IAg^{II} case described in Sec. 3.1. The least stable geometry corresponds to the case where the first row sites are occupied by Ag atoms while the Co atoms are all in the second row sites. All the other configurations in which the Co and Ag atoms lie randomly within the first two rows close to the step edges lead to intermediate adsorption energies. These results indicate that the most stable structures are those for which most Co atoms are bound to Pt, given that the Co-Pt bond is stronger than the Ag-Pt one. The interactions between Ag atoms, Co atoms, and between Ag and Co atoms are very similar and they do not provide selectivity in the random or ordered lateral arrangements of the binary mixture.

3.3 Stability of heterowires at finite temperature

The calculations presented above corroborate the TEAS results reported in Sec. 3.1 showing that the $Co^I Ag^{II}$ configuration is indeed favored over all the others, whereas the $Ag^I Co^{II}$ configuration is unstable with respect to alloying. However, at $T \neq 0$, disordered configurations might prevail over the $Co^I Ag^{II}$ one. To investigate this point further, F. Picaud *et al.* have devised a thermodynamic approach based on the mean-field Ising model [56]. The analysis is limited to the arrangement of an equimolecular binary mixture of atoms A and B occupying completely three rows of lattice sites adjacent to a Pt step and interacting through very similar lateral interaction potentials $V_{AA} \simeq V_{BB}$. The third row acts as an atom bath which can supply atoms A or B to the first two rows in order to reach thermodynamic equilibrium. In the nearest neighbor interaction approximation and in the mean field approach, the free energy per adatom can be written as [56]

$$\frac{F}{N} = \Big[\Big(b(3) - b(1)\Big)M_1 + \Big(b(3) - b(2)\Big)M_2 + 2\eta M_1(M_1 + M_2)\Big] + k_B T f(M_1, M_2), \quad (3.2)$$

where

$$\begin{aligned} b(\ell) &= \frac{1}{2}\Big[V_{A-Pt}(\ell) - V_{B-Pt}(\ell)\Big] \\ \eta &= \frac{V_{AA} + V_{BB} - 2V_{AB}}{4} \\ M_\ell &= \theta_\ell^B - \theta_\ell^A \end{aligned} \quad (3.3)$$

and $l = 1, 2, 3$ defines the row number, θ_l^X the coverage of the atomic species X in the lth row. The term $f(M_1, M_2)$ is a function of the order parameters M_1 and M_2, only, and is given by

$$\begin{aligned} f(M_1, M_2) = {} & \frac{1 - M_1}{2}\ln(\frac{1 - M_1}{2}) + \frac{1 + M_1}{2}\ln(\frac{1 + M_1}{2}) + \frac{1 - M_2}{2}\ln(\frac{1 - M_2}{2}) + \\ & + \frac{1 + M_2}{2}\ln(\frac{1 + M_2}{2}) + \frac{1 - M_1 - M_2}{2}\ln(\frac{1 - M_1 - M_2}{2}) + \\ & + \frac{1 + M_1 + M_2}{2}\ln(\frac{1 + M_1 + M_2}{2}) \,. \end{aligned}$$

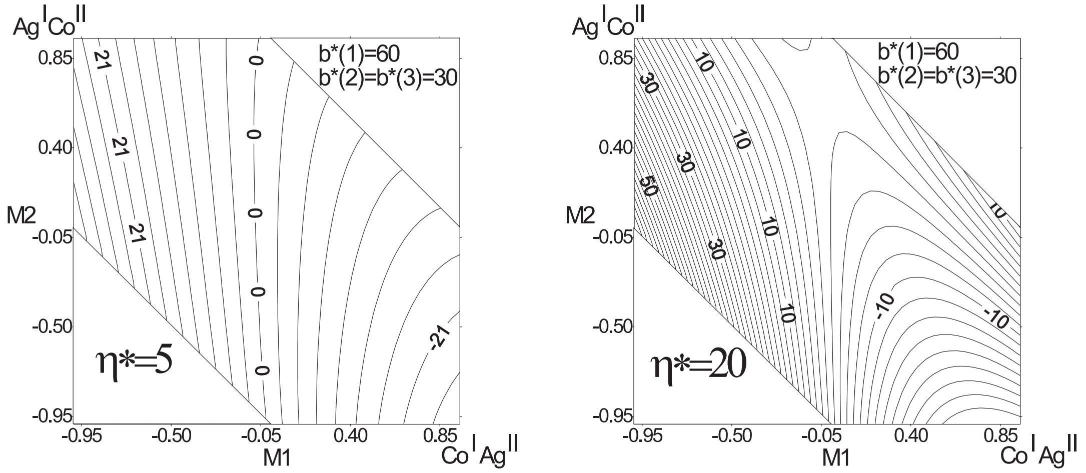

Figure 3.4: Reduced free energy maps for different values of η^* as a function of the molar fractions M_1 and M_2 of metal atoms in the first and second row. The $Co^I Ag^{II}$ configuration corresponds to $M_1 = 1$, $M_2 = -1$, whereas $Ag^I Co^{II}$ corresponds to $M_1 = -1$, $M_2 = 1$.

The values of the adsorption energies occurring in Eq. 3.2 for Ag and Co have been calculated as described in Sec. 3.2 and are reported in Table 3.3. The solutions leading to minima for $\frac{F}{N}$ in Eq. 3.2 can be discussed in a general way by drawing the reduced free energy map per adatom $\frac{F^*}{N} = \frac{F}{Nk_BT}$ as a function of M_1 and M_2 for various values of parameters $b(1)^*, b(2)^*, b(3)^*$ and η^* reduced by the thermal energy k_BT . Since $b(2)^* \simeq b(3)^*$, due to the short range influence of the step, the important parameters result to be $b(1)^* - b(3)^*$ and η^*. The former characterizes the influence of the potential increment at the step and the latter describes the difference between hetero (V_{AB}) and homo (V_{AA} and V_{BB}) interactions which is the driving force leading to the order/disorder transition in alloys. In Fig. 3.4, we report the free energy map at $T = 220$ K *vs* the molar fractions M_1 and M_2 in the first two rows for a value of $b(1)^* - b(3)^* = 30$ which is characteristic of the Co/Ag system. For small values of η^* (low tendency to alloying between Ag and Co), the lowest free energy (-500 meV) is obtained when $M_1 = 1$ and $M_2 = -1$, i.e. in the $Co^I Ag^{II}$ configuration. When η^* increases up to 20 (higher tendency to alloying), two minima occur. In the deepest well (-540 meV) the first row is formed mainly by Co atoms ($M_1 = 0.9$) while the second row contains exclusively Ag atoms ($M_2 = -1$). The shallower well (-40 meV) corresponds to a situation where the first row is occupied by a mixture of Ag and Co atoms ($M_1 = -0.15$) with a slight predominance of Ag atoms,

	1^{st} row	2^{nd} row
Co	-4.20	-3.38
Ag	-3.15	-2.80
Cu	-3.12	-2.71

Table 3.3: Adsorption energy (eV) per adatom as a function of its position with respect to the step.

while the second row is filled by Co atoms only ($M_2 = 1$). The estimated value of η^* from the potential given in Eq. 3.1 for the Co/Ag mixture is equal to 12.

Based on these results, we draw the following conclusions: when Co is deposited first, it forms a stable row along the Pt step and additional deposition of Ag results in a pure Ag second row. On the contrary, when Ag is deposited first, the Co atoms tend to occupy first row sites leading to instability of the $Ag^I Co^{II}$ phase. Since no energy barrier separates this configuration from the mixture phase, the system directly evolves into a disordered state. The TEAS data presented in Sec. 3.1 are therefore nicely described by the thermodynamic model.

Chapter 4

Chemical activity of Pt and Ag/Pt steps

Understanding and controlling the interplay between composition, structure, and chemical activity of heterogeneous metal surfaces is a fascinating subject and a key to many catalytic processes [113, 141]. Here we focus on the activity of Pt steps with respect to atomic and molecular chemisorption. We show that the peculiar properties of the step sites, which are due to the breaking of the terrace symmetry, are ultimately related to a change of the electronic band structure of the Pt edge atoms. The adsorption of O_2, H_2, and CO on Pt(997) and Pt(779) is investigated as a function of the Ag coverage decorating the Pt step edges by means of TEAS and STM.

We demonstrate that O_2 molecules dissociate from a molecular precursor on the upper side of the Pt step edges, where the two dissociation products are found two lattice constants apart. Dissociation at the steps proceeds by elongation of the O_2 molecule across bridge sites, as for terrace O_2 [142–144]. The increased dissociation rate observed at the step edge is attributed exclusively to the so-called *electronic effect*, ruling out any influence of the step geometry in favoring a particular steric approach to dissociation. Trends in the reactivity of transition metal surfaces are governed by the coupling of the adsorbate bonding and antibonding states to the metal d-bands. A local change of the hybridization of the Pt d-states would therefore modify the dissociation properties at the Pt step edges. To confirm this hypothesis we have decorated the Pt steps with Ag monatomic wires. Although Ag does not physically block the Pt active sites, the reactivity of the Pt steps is decreased by a factor of ten as a single row of Ag atoms decorates the step edges. This phenomenon is strictly local; Ag deposited away from the Pt step edge does not influence the initial dissociation rate.

A single Ag monatomic wire (coverage 0.13 ML) decorating the step sites is found to decrease strongly the sticking coefficient of molecular species that undergo dissociation during adsorption, such as O_2 and H_2, but to have a minimal influence on CO adsorption which is non-dissociative. Thus the specific chemisorption properties of Pt step sites can be selectively modified with respect to different molecular species by decoration with Ag. In terms of binding energy, Pt step sites remain favored over terrace sites for O and CO regardless of Ag decoration of the Pt step edges, whereas we have indications that atomic H is driven away from the steps.

TEAS is employed to monitor the Ag deposition process and to measure the relative variations in the O_2, CO, and H_2 adsorption rates for different coverages of Ag as described in Sec. 1.1. The STM images have been acquired at 77 K after dosing the samples at the temperatures specified in the text. The gas species were dosed by backfilling the UHV chambers at pressures in the $10^{-7} - 10^{-6}$ mbar range for O_2 and H_2, $10^{-8} - 10^{-7}$ mbar for CO.

In Sec. 4.1 we present an introductory view of chemisorption on transition metal surfaces. The concepts introduced there will help the interpretation of the experimental results reported in this chapter. Sec. 4.2 treats O and CO chemisorption at Pt steps; Sec. 4.3 focuses on O_2 dissociation, while Sec. 4.5 compares the effect of Ag-Pt bonding at the steps on the adsorption of different molecular species.

4.1 Chemisorption on metal surfaces

The aim of this paragraph is to derive a few simple formulae that relate the chemical reactivity of a given surface to its electronic structure. A conceptual framework is provided in which the results of Secs. 4.3-4.5 can be interpreted and understood. For an overview on the subject the reader is referred to Refs. [145–148].

In introducing the relevant quantities that define the interaction between an atom or a molecule and the surface, we briefly review the problem of a single electron interacting with two atoms A and B forming an AB molecule. In the LCAO (Linear Combination of Atomic Orbitals) approximation [149] the one-electron wave function ψ_{AB} is written

$$\psi_{AB} = c_A\psi_A + c_B\psi_B \tag{4.1}$$

where each of the atomic orbitals ψ_A and ψ_B are solutions of the atomic one-electron equation

$$\mathcal{H}_A\psi_A = (-\frac{\hbar^2}{2m}\nabla + v_A)\psi_A = E_A\psi_A\,. \tag{4.2}$$

Assuming that the effective one-electron potential for the AB molecule is the sum of the atomic potentials, $v_{AB} = v_A + v_B$, the one-electron hamiltonian of the molecule reads

$$\mathcal{H}_{AB} = \mathcal{H}_A + v_B = \mathcal{H}_B + v_A \tag{4.3}$$

and we have

$$\mathcal{H}_{AB}\psi_{AB} = E\psi_{AB} \,. \tag{4.4}$$

By minimizing the energy of the AB state $E = \langle\psi_{AB}|\mathcal{H}_{AB}|\psi_{AB}\rangle / \langle\psi_{AB}|\psi_{AB}\rangle$ with respect to c_A and c_B, the values of E are given by the solutions of the equation

$$(H_{AA} - E)(H_{BB} - E) - (V - ES)^2 = 0 \,, \tag{4.5}$$

where

$$\begin{aligned} H_{AA} &= \langle\psi_A|\mathcal{H}_{AB}|\psi_A\rangle \approx \langle\psi_A|\mathcal{H}_A|\psi_A\rangle = E_A \,, \\ V &= \langle\psi_A|\mathcal{H}_{AB}|\psi_B\rangle \,, \\ S &= \langle\psi_A|\psi_B\rangle \,. \end{aligned}$$

Given that we consider $v_{AB} < 0$ everywhere in space, a positive overlap S (equal phases of ψ_A and ψ_B) corresponds to a negative (attractive) interaction matrix element V and *vice versa*. Typically S will be small and to first order in S we have:

$$E_\pm = \frac{1}{2}(E_A + E_B) \mp \sqrt{V^2 + (\frac{E_A - E_B}{2})^2} - VS \,. \tag{4.6}$$

For hetero-nuclear diatomic molecules ($E_A \neq E_B$) whose eigenvalues are well separated compared to the coupling matrix element ($|V| \ll |E_A - E_B|$) one gets the approximate expression

$$E_\pm = \begin{cases} E_A - \frac{V^2}{E_B - E_A} - VS \\ E_B + \frac{V^2}{E_B - E_A} - VS \end{cases} \quad \text{with } E_B > E_A \,. \tag{4.7}$$

This are the well-known bonding and antibonding solutions to Eq. 4.4, which are represented in Fig. 4.1.

If the AB molecule has one valence electron on each atom taking part in the bond, the strength of the AB bond can be estimated from Eq. 4.6 [146] and reads, neglecting many-body effects, as

$$\Delta E = 2E_+ - E_A - E_B = -2SV - \sqrt{4V^2 + (E_A - E_B)^2} \,. \tag{4.8}$$

Working in analogy with the procedure outlined above for a diatomic molecule, we look now for an estimate of the bond strength in the case of molecules or atoms bound to a metal surface.

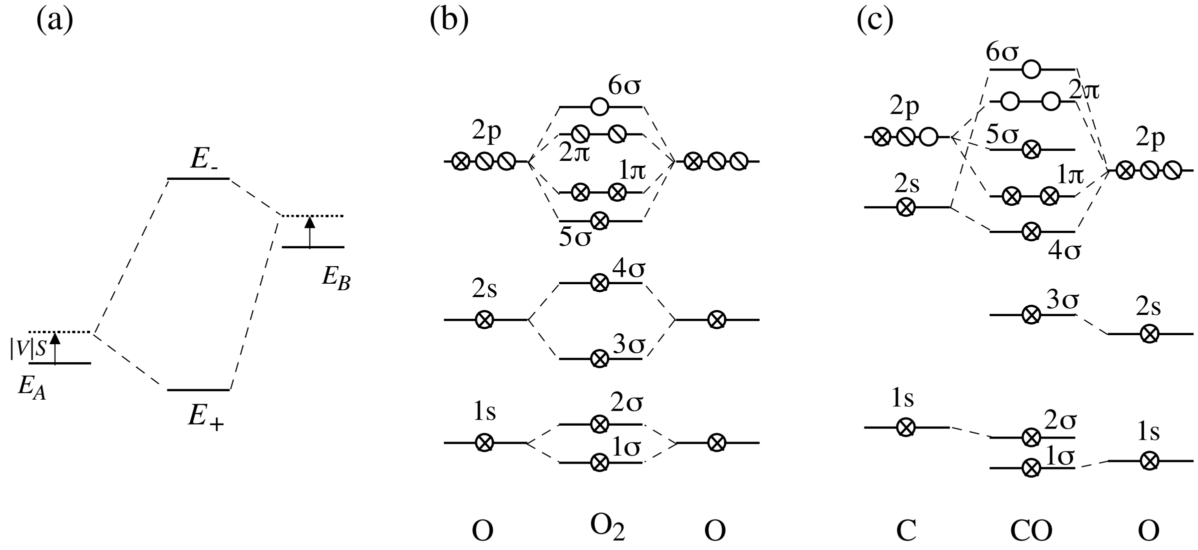

Figure 4.1: (a) Formation of bonding and antibonding molecular levels in a diatomic molecule. Note that, according to Eq. 4.7, both states are shifted up by an amount $-|V|S$ due to Pauli repulsion between the two atomic states (adapted from Hammer and Nørskov [146]). (b) O_2 levels; in the homonuclear notation the 1π, 2π levels are called $1\pi_u$ and $1\pi_g$, respectively. (c) CO levels; to underline its antibonding character the 2π orbital is often designated as $2\pi^*$ (from Zangwill [147]).

The Newns-Anderson model

Consider the interaction between an adsorbate with a single valence state $|a\rangle$ with energy E_a and a metal surface with one-electron band states $|k\rangle$ with energy E_k. When the adatom is brougth close to the metal the two sets of states are coupled by the matrix elements $V_{ak} = \langle a|\mathcal{H}|k\rangle$, where $\mathcal{H}$ is the Hamiltonian of the combined system. As in Eq. 4.1, we can expand the solutions $|i\rangle$ of $\mathcal{H}$ into a linear combination of the separate adsorbate and surface system: $|i\rangle = c_{ai}|a\rangle + \sum_k c_{ki}|k\rangle$. Since there is an infinity of metal states it is not worth trying to solve the energy problem by optimization of the c coefficients as in the molecular case. Instead, we consider the projection of the density of states (DOS) on the adsorbate state:

$$n_a(E) = \sum_i |\langle i|a\rangle|^2 \delta(E - E_i) \tag{4.9}$$

where the sum is over the eigenstates of $\mathcal{H}$. A comparison between $n_a(E)$ and the density of states of the unperturbed adsorbate species tells us how the adsorbate states interfere with the substrate states. After some mathematics, one finds [146, 150]

$$n_a(E) = \frac{1}{\pi} \frac{\Delta(E)}{(E - E_a - \Lambda(E))^2 + \Delta(E)^2}, \tag{4.10}$$

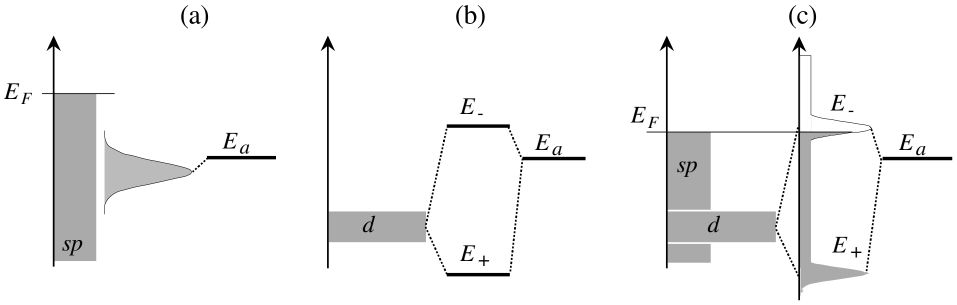

Figure 4.2: (a) Local DOS of an adsorbate on a free electron-like *sp*-metal; (b) splitting of the adsorbate state due to interaction with a narrow band metal. (c) Two step model for adsorption on a transition metal surface.

where

$$\Delta(E) = \pi \sum_k |V_{ak}|^2 \delta(E - E_k)\,, \tag{4.11}$$

and

$$\Lambda(E) = \frac{1}{\pi} \int dE' \frac{\Delta(E)}{E - E'}\,. \tag{4.12}$$

The adsorbate DOS broadens from a sharp, bound state, delta function centered at E_a into a Lorentzian line shape with width $\Delta(E)$ shifted to an energy E determined by the condition $E = E_a - \Lambda(E)$. This equation can be solved graphically for some choice of V_{ak}. The broadening of the adsorbate induced level is given by the finite lifetime of an electron in the adsorbate state: if the level lies in an energy band of the substrate, there is a certain probability for the electron in that state to leave the adatom region and propagate inside the substrate.[1] This probability is given by the Golden Rule type expression in Eq. 4.11. The occupancy of the adsorbate resonance and the characteristics of the surface bond depend on the relative position of the resonant level energy and the metal Fermi level. We discuss two limiting cases for $n_a(E)$.

Weak chemisorption: if $\Delta(E) \approx \Delta_0 =$ const. as for an adsorbate level in the middle of an *sp*-band of a simple metal like Al, we have $\Lambda(E) = 0$ in Eq. 4.12 and $n_a(E)$ is a Lorentzian of width Δ_0 centered around E_a. In reality, the position of the adsorbate resonance is shifted down in energy compared to E_a due to the additional effective one-electron potential originating from the solid surface potential barrier [151]. Figure 4.2(a) represents $n_a(E)$ in this limit.

---

[1] Note that it is no longer meaningful to speak of purely "atomic" or purely "metallic" states in the vicinity of the adsorbate and in the energy region of E_a.

Strong chemisorption: this case is typical for transition metals when considering the interaction with the d-bands. For narrow metal bands the problem simplifies into the two levels problem of Eq. 4.7, and we have sharp bonding and antibonding states forming above and below E_a and ϵ_d, where ϵ_d is the centroid of the d-band [Fig. 4.2(b)]. If the bandwidth of the metal d-states is small compared to the hopping matrix element V_{ad}, one has $\Delta(E) \approx \pi|V_{ad}|^2\delta(E-\epsilon_d)$ and $\Lambda(E) \approx |V_{ad}|^2/(E-\epsilon_d)$. The shift of the adsorbate level determined by the $E = E_a - \Lambda(E)$ condition is therefore given by Eq. 4.7 substituting $E_B = \epsilon_d$ and $V = V_{ad}$.

Trends in chemisorption energies

Considering adsorption on transition and noble metals, we can imagine that bonding proceeds in two steps [145, 146]. First the adsorbate valence state interacts with the metal sp-bands. This will give rise to a single resonance as in Fig. 4.2(a). Then the coupling to the d electrons is switched on, causing the resonance to split into a state which is bonding with respect to the adsorbate and metal d states and another which is antibonding [Fig. 4.2(a)]. This is a good approximation, e.g., to what happens to the O p-derived resonances as O adsorbs on a transition or noble metal surface. The degree of filling of the bonding and antibonding resonances determines the balance of the binding energy of the adsorbate-metal system. On Ag, for instance, both states are filled, whereas the antibonding state is only partially filled on Pt, resulting in a stronger O-Pt bond with respect to the O-Ag one. The same reasoning applies for molecular chemisorption. In the CO case, for instance, one has to take into account the coupling of both the 2π and 5σ states (see Fig. 4.1) to the d states. Due to their different symmetry, they interact with different d orbitals and the two interactions can be treated independently [146], as in Fig. 4.3.

Although it provides most of the absolute binding energy, the contribution from the coupling to the metal sp-states varies little among transition metals [145,146]. The main trends in chemisorption energies are therefore given by the coupling to the d-states. This is true for both atomic and molecular chemisorbed species, and it determines the trends in chemisorption energies across the periodic table. Since, to a first approximation, the total energy of the system is given by the sum of the occupied one-electron energy levels, and assuming that the introduction of the d-state coupling alters the adsorbate levels in a negligible way, we can isolate the contribution to the bonding energy due to the d electrons by considering only the one-electron eigenvalues determined in the Newns-Anderson model. In analogy with Eq. 4.8 the d coupling contribution is given by $\Delta E_d = 2(E_+ + fE_-) - 2(E_a + \epsilon_d)$, where the factor 2 accounts for the spin degeneracy

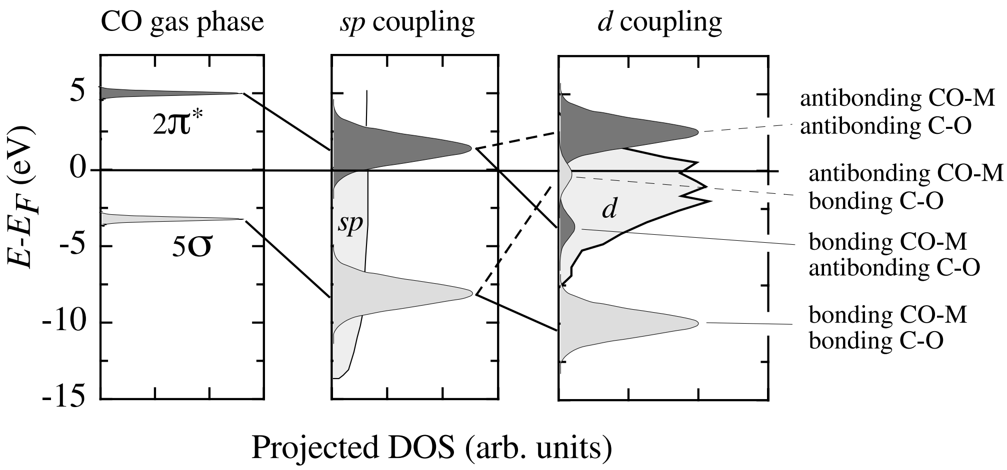

Figure 4.3: Schematic representation of the two-step model for CO adsorption on a transition metal surface (adapted from Hammer *et al.* [152]). Note that the filling of the CO $2\pi^*$ orbital gives a bonding contribution to the adsorbate-metal (M) system, but weakens the C-O intramolecular bond.

and f represents the filling of the d-band. From Eq. 4.6 one has

$$\Delta E_d = -(1-f)(\sqrt{4V_{ad}^2 + (\epsilon_d - E_a)^2} - (\epsilon_d - E_a)) - 2(1+f)VS\,. \tag{4.13}$$

This equation can be further simplified by assuming[2] $S = -\alpha V_{ad}$ and by considering a weak coupling V_{ad} relative to the energy difference $|\epsilon_d - E_a|$:

$$\Delta E_d = -2(1-f)\frac{V_{ad}^2}{|\epsilon_d - E_a|} + 2(1+f)\alpha V_{ad}^2\,. \tag{4.14}$$

Equation 4.14 is an important result since it relates in a simple way the trends in chemisorption energies and dissociation barriers observed in the transition metal series to the electronic structure of the adsorbate-metal system (Fig. 4.4). The first term in the above expression represents the hybridization energy gain with the d-states which is non-zero until both the bonding and antibonding resonances become occupied, i.e. until the d-band is not completely filled. The second term is always repulsive and it represents the cost paid to the overlap of the adsorbate and metal states. The main factors influencing the ΔE_d contribution to the binding energy are:

- the filling of the d-bands, f;
- the strength of the adsorbate d-bands coupling, given by V_{ad};
- the position of the d-band with respect to the Fermi level, ϵ_d.

---

[2] Partially justified by the fact that both S and V decay exponentially with increasing adsorbate-substrate distance [146].

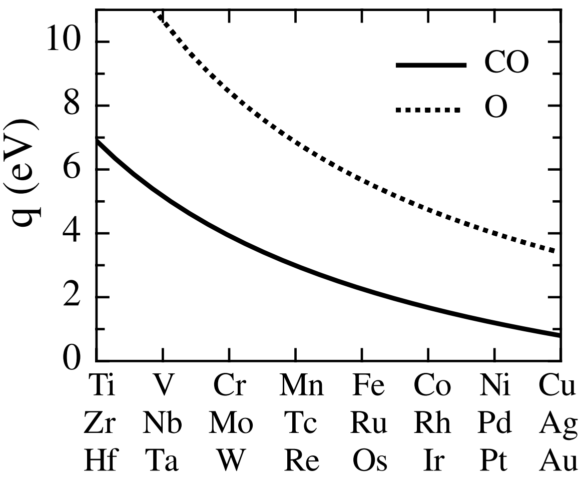

Figure 4.4: Heat of adsorption of CO and O on polycristalline transition metal surfaces (data are averages from Toyoshima and Somorjai [153]).

The first factor explains why early transition metals with fewer d electrons form stronger chemical bonds [Fig. 4.4(a)]. To a greater d-band occupation corresponds an increased filling of the antibonding resonance, which weakens the adsorbate-metal chemical bond. The size of the coupling matrix element increases down the groups of the periodic table due to the increasing extension of the $3d$, $4d$, $5d$ states. This drives up the orthogonalization energy between adsorbate and metal d-states and it explains why, e.g., Au is the least reactive among the noble metals [154]. The position of ϵ_d determines the ability of the d electrons to participate in bonding to the adsorbate, the interaction being stronger for ϵ_d closer to E_a after renormalization with the sp-states [146, 155]. In the case of CO, for instance, the binding energy increases if ϵ_d moves towards the Fermi level resulting in a more effective hybridization of the d-states with the 2π (or $2\pi^*$) CO levels[3] [152, 156]. The value of ϵ_d near a given metal atom will depend on the chemical and geometrical characteristics of the surroundings. This is central in interpreting the results of Secs. 4.2-4.5. Just to mention one effect, consider CO adsorption on a Pt stepped surface as treated by Hammer *et al.* in Ref. [152]: the value of ϵ_d increases as the coordination of the substrate atoms decreases. This happens due to the narrowing of the Pt d-bands caused by the loss of coordination, as it is schematized in Fig. 4.5. The ϵ_d upshift for metals having $f > 0.5$ like Pt, results from the need to preserve the degree of filling of the d-band. As a result, the CO binding energy is larger on kink and step sites than on terrace sites (Fig. 4.6). The former result is quite general and can be extended to most transition metal surfaces where preferential adsorption at defect

---

[3] Assuming that the 2π-derived antibonding resonance remains empty, which is realistic since the 2π renormalized CO level is usually higher than the Fermi level.

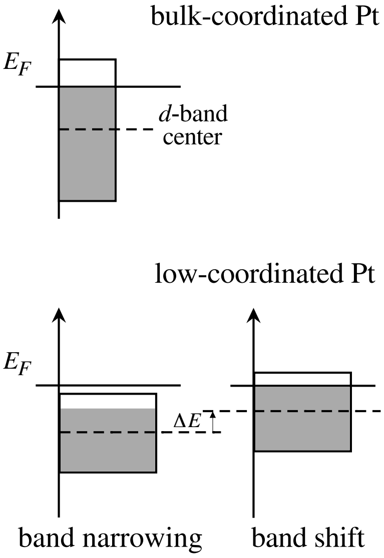

Figure 4.5: Narrowing of the d-DOS due to a decrease of coordination of the surface atoms at edge sites.

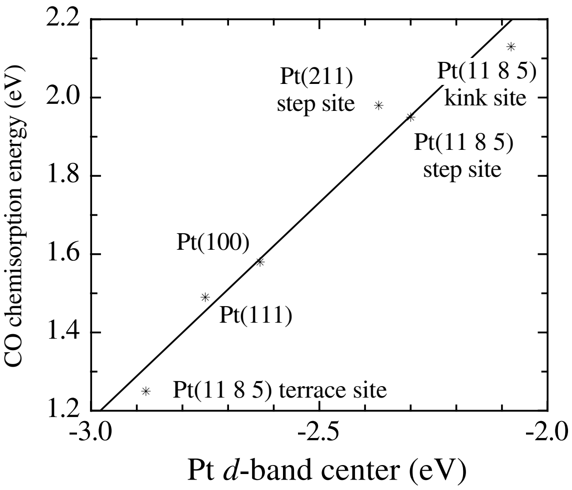

Figure 4.6: Calculated CO binding energies on Pt vicinal surfaces for different adsorption sites as a function of the position of ϵ_d with respect to the Fermi level (values from Ref. [152]).

sites is a well-established fact. In applying Eq. 4.14 one can take into account only the adsorbate levels (with their degeneracy) that after sp renormalization result closer to ϵ_d. As an example we consider the case of the O_2 molecule adsorbed on Pt. The binding energies of the 1π and 2π (or π and π^*) levels of the free molecule are 16 and 12 eV, respectively. Once (physisorbed) on the surface, the net surface to molecule charge transfer will cause an upward shift of the center of gravity of the 1π and 2π resonances of about 7-8 eV [157, 158], and the two levels will be situated at 8-11 and 4-5 eV from the Fermi level, respectively [159]. The Pt d-bands do not extend more than 8 eV down from the Fermi level. Then, only the interaction with the antibonding 2π levels can be considered, since the 1π levels do not superpose to a large extent with the Pt d-band. Also for CO the main contribution to Eq. 4.14 comes from the 2π antibonding orbitals which couple stronger to the d-bands with respect to the 5σ level [156]. The fact that the O_2 and CO interaction with the metal d-states passes mainly through their antibonding orbitals is extremely relevant when considering dissociative adsorption on transition metal surfaces.

Trends in dissociation barriers

Most of the concepts developed in the last paragraph are also useful in understanding the facility with which molecules interacting with a transition metal surface may or may not break intramolecular bonds. It is not necessary to stress here the fact that the ability

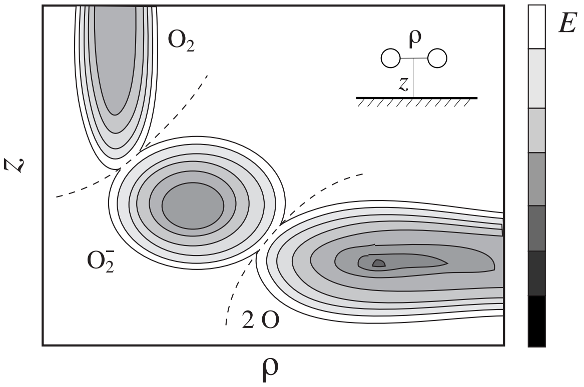

Figure 4.7: Simplified PES for O_2 dissociative adsorption on Pt.

to break bonds and stabilize intermediates is what determines the catalytic properties of solid surfaces [141]. In general, many a factor concur in the dissociation process. An exact description would require a complete knowledge of the potential energy surface (PES) of the adsorbate for every degree of freedom of the system. In Fig. 4.7 we have drawn a simplified PES for the O_2/Pt system based on Refs. [160] and [161]. The variation of the potential energy of an O_2 molecule is represented as a function of the vertical distance from the surface and of the intramolecular separation. Starting from a large molecule-surface separation, dissociation proceeds through a molecular precursor chemisorbed state, labelled O_2^-. Changes of the electronic configuration of the system are marked by dashed lines, which correspond to the saddle points of the activation barriers separating different adsorption states. It is clear that the O_2 dissociation rate will depend on the energy of the saddle point (transition state) between the O_2^- and the O states. Such a picture, however, is incomplete: the orientation of the molecule with respect to the surface lattice, its internal energy, the corrugation of the surface, all represent additional dimensions in the PES [148] that should be incorporated in its representation. Here we concentrate on the dependence of the dissociation activation barriers on the electronic structure of the surface. This is partially justified by the fact that the probability for a molecule in thermal equilibrium at a temperature T above the surface to overcome the activation energy barrier E_{act} for dissociation is proportional to $e^{-E_{act}/kT}$. The strong E_{act} dependence ensures that, unless limited by entropy, the minimum energy path between different adsorption states on the surface will be favored over most of the remaining alternatives. To interpret the experimental trends in dissociative sticking observed on different transition metal surfaces, one can therefore concentrate on determining the contribution of the d-states to the minimum value of E_{act} [146].

Since there is no conceptual difference in estimating the variations of E_{act} due to the metal d-states contribution from the arguments of the preceeding paragraph, one finds Eq. 4.14 to hold also in estimating the d electron contribution to E_{act}. For molecules such as H_2, O_2, CO, the valence levels that interact more strongly with the metal d-bands are typically the anti-bonding molecular levels because they are partially filled and hence they lie near the Fermi level where also the d-states are situated [145]. The filling of the anti-bonding molecular levels such as the 2π states in the O_2, CO case, weakens the intramolecular bond favoring dissociation. Empty d-states, a high lying d-band and a large matrix element contribute to lower the dissociation barrier. More detailed density-functional calculations [154, 155] support this view: H_2, for instance, has no dissociation barrier on Ni and Pt, and an increasingly larger one on Cu, Au, and Al. Further experimental confirmation comes from the fact that CO dissociates only on the elements situated in the periodic table to the left of Fe, Ru, and Re in the transition metal series; an increase in chemisorption energy therefore corresponds to a decrease of the dissociation barrier. In Sec. 4.3 we provide a direct demonstration of the d-band structure – dissociation rate relationship by analyzing H_2 and O_2 adsorption on Pt steps whose reactivity has been modified by the addition of controlled amounts of noble metals such as Ag and Cu.

4.2 O and CO adsorption at Pt steps

Due to the unsaturated valences of low-coordinated edge atoms described above, steps on Pt(111) bind O_2, CO molecules and O atoms more strongly than terrace sites [12, 13, 15–18, 20, 144, 162, 163]. At $T \gtrsim 100$ K oxygen adsorbs dissociatively on Pt [13, 16, 20, 144]; Fig. 4.8(a) shows the Pt(997) surface after 1.2 L O_2 dosing at 350 K: the black depressions that are observed along the step edges represent O atoms occupying near-edge fcc sites [Fig. 4.8(b)], in agreement with the results of Feibelman *et al.* [162]. The step sites are completely saturated with a 2×1 periodic structure, whereas very few O atoms can be seen on the terraces. Since at $T \geq 200$ K the O atoms resulting from dissociation are free to move about on the surface [164] they tend to occupy the energetically most favored adsorption sites. Clearly, O atoms prefer step sites over terrace sites, a behavior which is fully accounted for by density-functional calculations: the O binding energy is 5.28 eV on fcc terrace sites, 5.66 eV on near-edge fcc sites at {111} steps, and 5.85 eV on edge bridge sites at {100} steps [162]. Although these values might be overestimated, the relative differences can be considered to be correct [165].

Depending on the interaction among the adsorbates, preferential step adsorption might lead to sequential site filling [141] or to a rearrangement of the adatoms in favor of

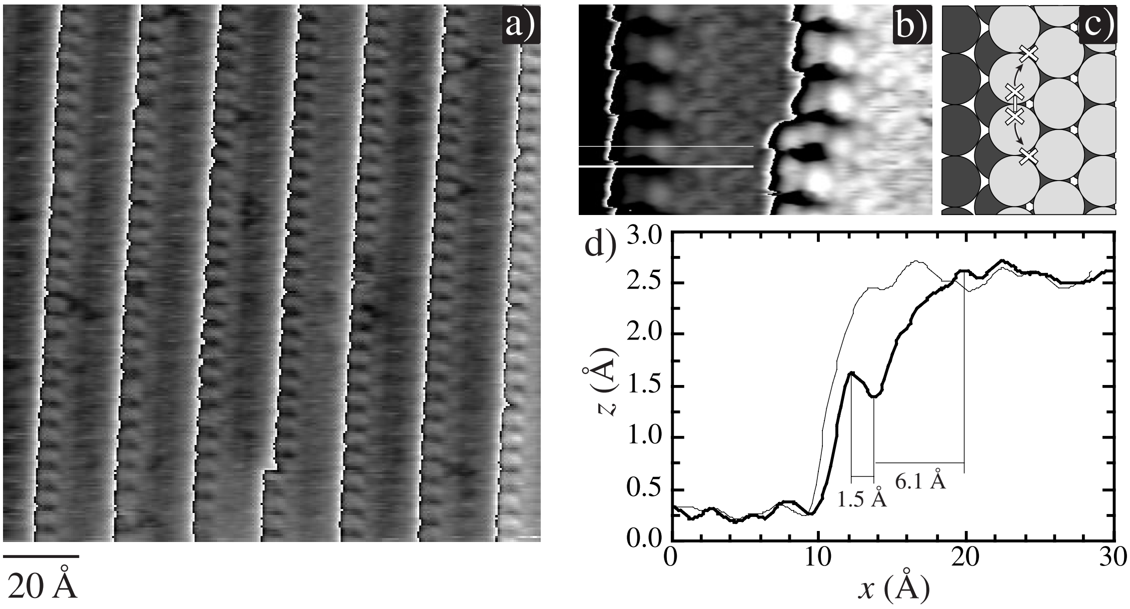

Figure 4.8: STM image of Pt(997) following exposure to 1.2 L O_2 at 350 K. The O atoms are imaged as dips along the step edges and on terraces. The grayscale has been redistributed on each terrace for better contrast. Step down direction is from right to left. (b) Close up of the Pt steps showing the O atoms in near-edge fcc sites. (c) Diagram of the O_2 molecular precursor in bridge position at the step edge and of the two dissociation products. (d) Comparative z line scans over O and Pt atoms, as shown in (b). The 6.1 Å distance between the O-induced minimum and a terrace atom on its right corresponds to O occupying near-edge fcc sites.

terrace sites in case repulsive interactions prevail over the extra binding energy provided by the steps [166]. In Fig. 4.9 we show the O uptake curve measured by TEAS for two different scattering geometries on Pt(997) and Pt(779). As discussed in Sec. 1.1, the grazing incidence condition $n = 0$ is selectively sensitive to adsorption at step sites whereas the more normal $n = -3$ condition is sensitive to both terrace and step coverage. Saturation of the $n = 0$ intensity around 1 L O_2 indicates that step sites are filled by O atoms much faster than terrace sites on both surfaces. Figure 4.8(a) and Fig. 4.9 therefore demonstrate a sequential site filling process: the sites with the largest bonding energy are filled first and the thermodynamic equilibrium between step and terrace sites is largely in favor of the formers. No oxygen reorganization is observed at high step coverage due to adsorbate-adsorbate interactions, as suggested by Hammer and Nørskov for NO on Pd(211) [166].

CO adsorption also leads to preferential occupation of the step sites [3, 12, 167], as shown in Fig. 4.10(a) and (d). The CO molecules occupy mostly edge on-top sites [Fig. 4.10(b)], but we observe also bridge sites, in agreement with other studies [152,167]. Molecules occupying on top sites are found two lattice constant (5.54 Å) apart due to

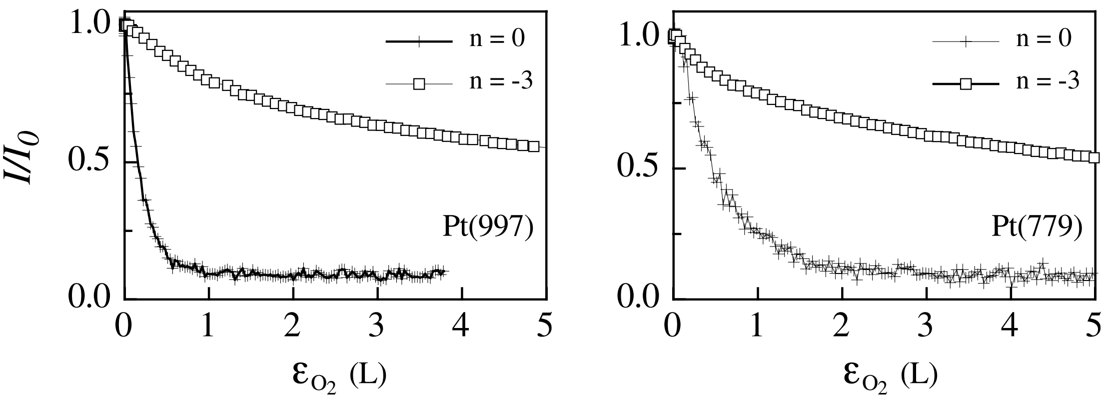

Figure 4.9: TEAS intensity during O_2 dosing of Pt(997) [left] and Pt(779) [right] at 400 K. The intensity in the $n = 0$ curve ($\theta_i = \theta_f = 83.0°$) decays due to O adsorption at the step edges; the decay of the $n = -3$ curve ($\theta_i = 55.6°$, $\theta_f = 44.2°$) depends mainly on the O terrace coverage and only weakly on O adsorption at step sites.

repulsive interaction between nearest neighbors. Repulsion between adsorbed CO is also responsible for the increased mobility of the admolecules observed at 77 K at high CO coverage in Fig. 4.10(d) [168].

A temperature programmed desorption (TPD) experiment performed by TEAS also evidences the stronger bonding of CO molecules at step sites: in Fig. 4.11 (right panel) we report the He intensity recorded while heating the surface at a 60 K/min constant rate

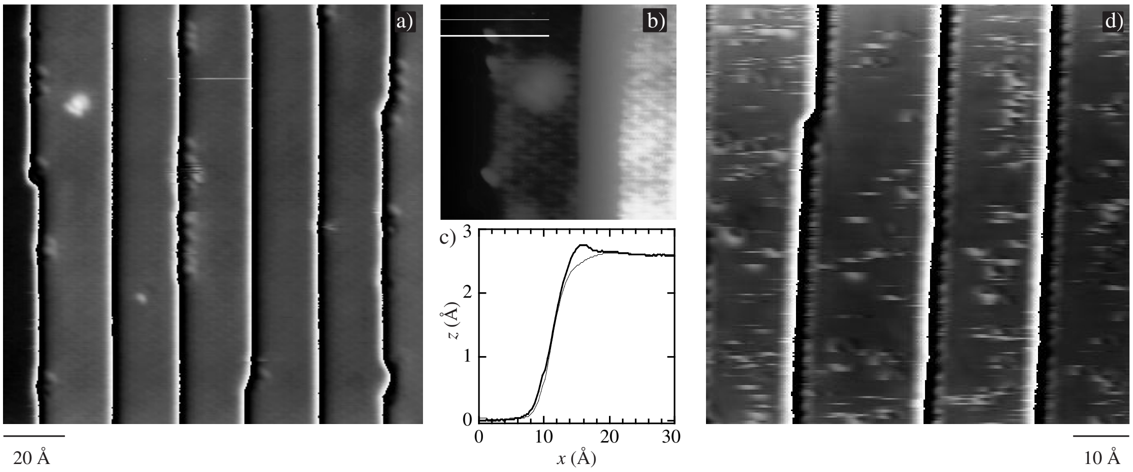

Figure 4.10: (a) CO (white dots) adsorbed at the step edges of Pt(997). Step down direction as in Fig. 4.8. (b) Atomic detail showing CO molecules occupying edge on-top (top left), terrace (center), and a kink on-top positions (bottom left). (c) z profiles over CO and Pt atoms corresponding to the line scans shown in (b). (d) CO-saturated Pt(997) steps. Molecules on the terraces are still mobile at 77 K and are imaged as white streaks due to the STM tip motion.

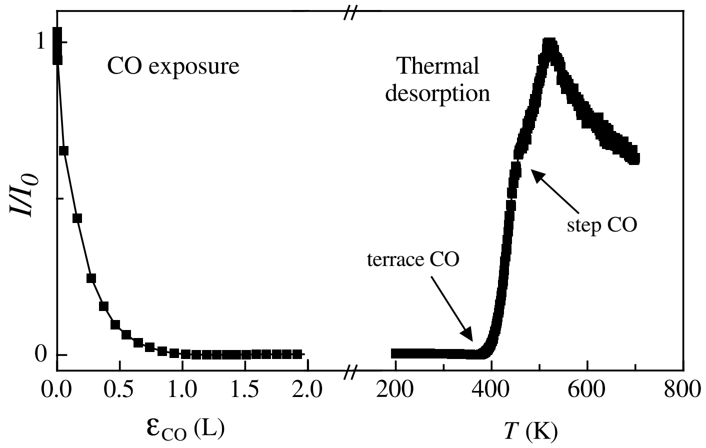

Figure 4.11: Left panel: CO dosing of Pt(997) at T = 200 K at a background pressure of 1×10^{-7} mbar CO. Right panel: TEAS signal recorded immediately after dosing by ramping the substrate temperature to cause CO desorption. The decrease in intensity observed above 500 K is due to the temperature-dependent Debye-Waller factor.

after having saturated the surface with CO at 200 K. Desorption starts around 340 K; at 455 K we observe a change of slope in the curve which is due to the progressive decrease in terrace coverage and to the beginning of step desorption. This result is in full agreement with TPD spectra recorded by mass spectrometry in other studies [167]. Similar curves for O show the same behavior shifted to 600 and 750 K for terrace and step desorption, respectively.

At this stage, it is clear that the binding energy of O and CO at surface steps is larger than on terrace sites, in agreement with the arguments presented in Sec. 4.1. In dealing with surface chemical reactions, however, the ability to make bonds is as important as that of breaking bonds. In the following paragraph we turn our attention to the role played by step sites with respect to O_2 dissociation.

4.3 O_2 dissociation on Pt stepped surfaces

Dissociation of O_2 on Pt is a fundamental step in many oxidation reactions that involve Pt as a catalyst. Due to the relevance of Pt and, in general, of transition-metal catalyzed reactions, the O_2/Pt(111) system has been extensively studied as a model for surface chemisorption. O_2 dissociation proceeds by sequential population of physisorbed and chemisorbed precursor states [13, 20, 142–144, 158, 161, 169]. Three chemisorbed molecular states have been identified on Pt stepped surfaces by TDS, EELS, and STM [16–18, 143, 144], corresponding to a fcc- and a bridge-bonded terrace species

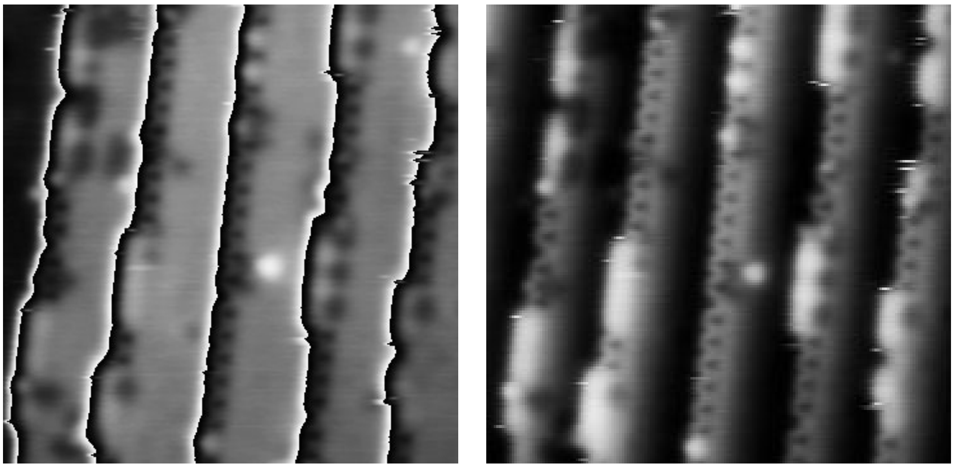

Figure 4.12: STM image showing O atoms following dissociation at 140 K, below the onset of O thermal mobility. O_2 dissociation involves exclusively the Pt upper edge atoms. In the left panel the grayscale has been redistributed on each terrace for better contrast; step down direction as in Fig. 4.8. In the right panel we show the same image without any processing. The bright stripes decorating the step edges are monatomic Ag wires, which can also be observed (with poorer contrast) in the left panel.

and a bridge-bonded step species [143, 144]. The terrace molecular species are stable only below 100-120 K, whereas molecules at step sites are stable until 150 K [16, 144]; heating or dosing the surface above this temperature results either in dissociation or in fast O_2 desorption. Ho and coworkers have shown that it is possible to dissociate terrace-chemisorbed molecular species with the STM by inelastic tunneling of electrons, by UV irradiation, or by thermal heating [144]; in agreement with a previous study, the dissociation products occupy fcc sites one to three lattice constants apart [164]. Although an increase in oxygen dissociative adsorption with respect to flat surfaces has been observed in various studies [12, 13, 16], there is a lack of detailed knowledge on the dissociation process at Pt steps. The prominent role played by structural defects in surface reactions, as well as the relevance of the O/Pt system underline the interest of the present study.

To observe where O_2 actually dissociates on a Pt stepped surface we have lowered the adsorption temperature to 140 K. Below 190 K the mobility of O atoms on Pt(111) is completely inhibited on a day timescale [164]; the spatial distribution of the dissociated O atoms allows therefore to identify the active sites in the dissociation process. At 140 K the O_2 molecular precursors on the flat terraces are short-lived; adsorption either results in dissociation or in O_2 desorption [16–18, 143, 144]. Because of the short terrace width of our samples, however, the adsorbed molecular species can scan all the available sites prior to desorption or dissociation.[4] The distribution of the O atoms in Fig. 4.12 shows that O_2 dissociation is largely promoted at the step edges with respect to the terrace sites, where very few O atoms can be observed. As in Fig. 4.8, an exposure to 1.2 L O_2 is sufficient to saturate almost all the Pt step sites; the independence of the dissociation rate at the step sites on the sample temperature is indicative of a process with a very low activation barrier. Since very few O atoms are observed on the lower side of the steps, we conclude that the bond breaking process involves only the Pt atoms that are situated at the upper step edges. After dissociation, the two O atoms end up in near-edge fcc sites, indicating that the O-O bond is stretched in the $(1\bar{1}1)$ direction, parallel to the steps.

Based on these observations we propose the following model for dissociation from a molecular chemisorbed state: the O_2 precursor binds in a bridge position at the Pt edge sites with its axis parallel to the step edge, as demonstrated by Stipe *et al.* [143] [see sketch in Fig. 4.8(c)]; a shift of the molecule in the direction perpendicular to the step accompanied by a simultaneous elongation of the O-O bond accomplishes the dissociation process, resulting in two O atoms situated two lattice constant apart. Note that no O atoms end up on the lower terrace. A point that remains open is whether, in dissociating, the O_2 molecule moves inwards or outwards with respect to the upper terrace. In the first case the O atoms would gain in coordination with Pt but would interact repulsively with each other, thereby increasing the transition state energy barrier. In the second case the O atoms would end up directly in the most favored adsorption sites, but at the expense of a temporary loss of coordination with the substrate. The scenario proposed here is remarkably similar to that devised by Eichler and Hafner for O_2 dissociation on terrace sites starting from a molecule adsorbed on bridge position [142]. It follows that the O_2 dissociation path results to be similar at step sites and on terrace sites. The geometrical configuration of the step sites does not play a role in favoring O_2 dissociation. In this respect, the oxygen case is remarkably different from N_2 and NO dissociation at the steps of a Ru(0001) surface. DFT-GGA calculations [170, 171] show that for N_2 and NO on Ru(0001) the dissociated atoms are found on different terraces. This is dictated by the need to mini-

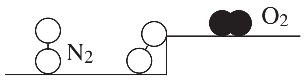

Figure 4.13: Different steric approach of N_2 and O_2 molecules to the step edge.

---

[4] A conservative estimate of the mean free path of O_2 molecules on Pt(111) at 140 K can be calculated by taking a 10^{13} s^{-1} prefactor and a 8 kcal/mole desorption barrier as determined by Winkler *et al.* [16] and by assuming the diffusion barrier to be $\sim$ 3 kcal/mole. The estimate exceeds the Pt(997) terrace width by orders of magnitude.

mize the interaction energy between the adsorbates and by steric factors, since the N_2 and NO precursors have the molecular axis perpendicular to the surface (see Fig. 4.13). O_2 dissociation is further discussed in the following paragraph.

4.4 Adsorption and dissociation at Ag-decorated Pt steps

In the preceding section we have ruled out the influence of step geometry[5] on O_2 dissociation on Pt. To explain the peculiar reactivity of step sites we then have to look for

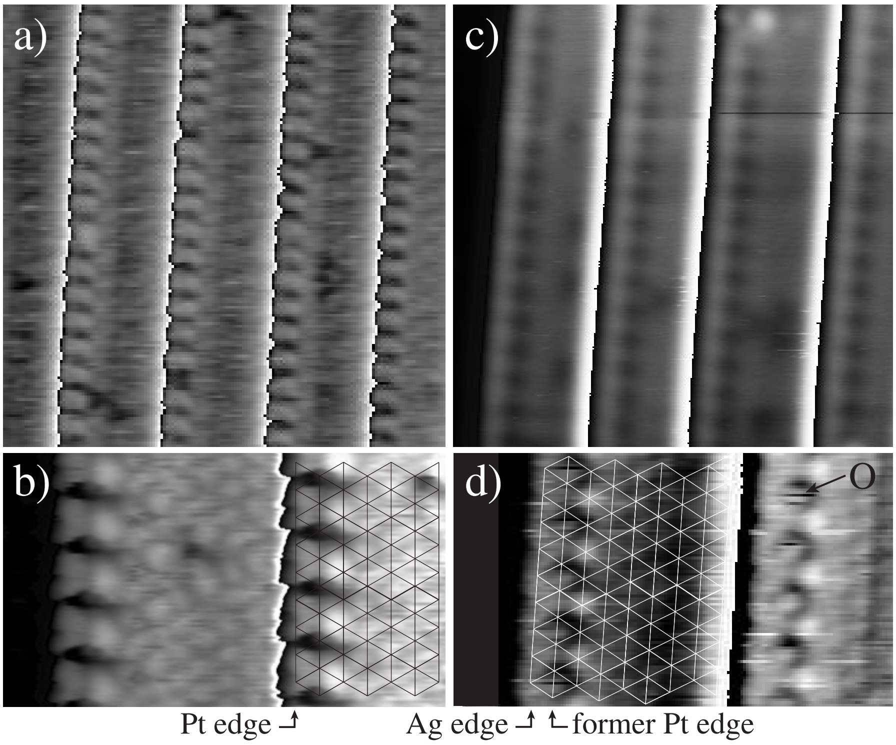

Figure 4.14: Comparison between O adsorption on Pt steps and on Ag-decorated Pt steps. Step down direction is from right to left in all images. (a) STM image of Pt(997) after exposure to 1.2 L O_2 at 350 K. (b) Atomic detail of the Pt steps. The grid represents Pt lattice sites. (c) O adsorption on a Ag-modified surface after exposure to 19 L O_2 at 350 K; a monatomic Ag row decorates each Pt step, the O atoms are visible near it, to the right. (d) Atomic detail of the Ag-decorated Pt steps: O atoms are imaged as "sombreros" occupying the former Pt near-edge fcc sites. O chemisorption causes an enhancement of the electron density on the adjacent terrace atoms; this effect is visible on both lower panels as bright dots to the right of the O atoms.

---

[5] "Geometry" is intended here purely as "shape" factor influencing the steric approach of a molecule to the dissociative state.

a purely electronic effect. According to the model presented in Sec. 4.1, the height of the dissociation barrier is determined by the relative position in energy of the adsorbate states and metal d-bands, by the degree of filling of the molecule-surface anti-bonding states, and by the size of the coupling between the adsorbate and the metal d-states [155]. The first two factors are largely determined by the position of the center of the metal d-bands, ϵ_d, relative to the Fermi level. The upshift of ϵ_d due to the low coordination of Pt step atoms explains the enhanced reactivity of the Pt steps. By inducing changes in the ϵ_d value in a local way, we are able to isolate the *electronic effect* that is at the origin of O_2 enhanced dissociation on Pt steps. In the following we show that we can reduce the step reactivity in a controlled way by decorating the step edges with Ag monatomic wires. As Ag decorates the steps, the Pt edge atoms become 9-fold coordinated as their terrace counterparts; hybridization with Ag, however, is not complete, due to the energy difference between the Ag and the Pt d-bands. ϵ_d results therefore in between the pure Pt step and terrace values. Altogether, we expect to find a decrease of the dissociation ability of Pt step atoms, which remain however more active than terrace atoms. In Fig. 4.14 we compare O adsorption on pure Pt steps and on Ag-decorated Pt steps. To produce the images shown in (c) and in (d) a monatomic Ag row was deposited at 400 K as described in Sec. 2 and O_2 was subsequently introduced in the vacuum chamber as the sample reached 350 K. Ag is imaged as the bright stripe along the steps, while O atoms are imaged black. We see that most O atom lie aligned to the right of the Ag row; a close comparison between images (b) and (d) evidences that the preferred adsorption sites are still the near-edge fcc with respect to Pt only. This is further confirmed by the line scans shown in Fig. 4.15. Hence (Ag-decorated) Pt step sites are still favored over terrace sites. However, if we look at the O_2 exposures needed to obtain the images in (a), (b) and in (c), (d), we note a large discrepancy: 15 times more O_2 has been dosed on the Ag-decorated sample in order to obtain a coverage similar to the bare Pt one. Hence the dissociation rate on the two surfaces is drastically

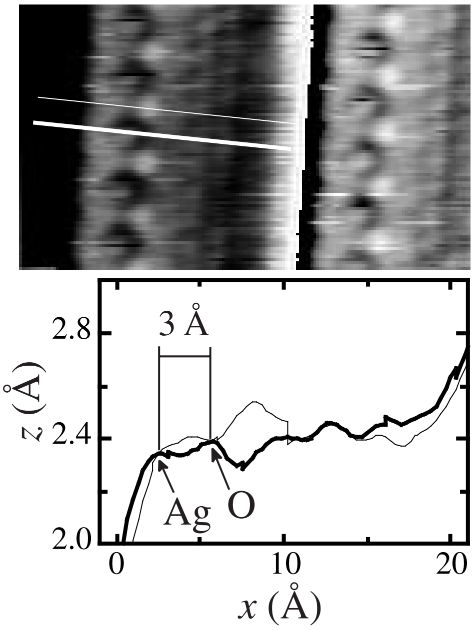

Figure 4.15: Line scans over Ag-decorated Pt steps.

different.

To probe the variation of the oxygen dissociative sticking coefficient due to Ag step decoration, we have measured the decay of the TEAS intensity for a He beam diffracted from the oxygen-exposed samples for various Ag coverages. The results are shown in Fig. 4.16 for Pt(997) and Pt(779); the slope of the TEAS curves diminishes with increasing Ag coverage. As described in Sec. 1.1, in the limit of low adsorbate coverage, the normalized TEAS intensity, I/I_0, can be described as $I/I_0 = 1-\Sigma s_0 \varepsilon$, where Σ is the adsorbate cross section, s_0 the sticking coefficient, and ε the gas exposure. To calculate the relative variation of the dissociation rate we take the value $\mathrm{d}(I/I_0)/\mathrm{d}\varepsilon|_{\varepsilon=0}$ for each curve and divide it by the clean Pt values. This procedure is correct inasmuch the value of Σ is not affected by the presence of Ag. A check done by comparing the relative s_0 variation obtained with TEAS and STM for a clean surface and an Ag-decorated sample (see, e.g., Fig. 4.14) has led to consistent results, supporting our analysis. The largest difference (a factor 10) in the slope of the curves is obtained for clean Pt and the situation where a single row of Ag atoms decorates the Pt steps. As shown in Fig. 4.17, the ratio $s_{0-Ag/Pt}/s_{0-Pt}$ decreases linearly with the Ag coverage up to complete decoration of the Pt steps by a single line of Ag atoms. From then on, $s_{0-Ag/Pt}/s_{0-Pt}$ varies slowly until it drops abruptly as the first Ag monolayer is completed. This behavior indicates that Ag locally modifies the reactivity of the Pt edge atoms, an effect that is limited to the Pt atoms in direct contact with Ag. Thickening of the Ag wires results in terrace site blocking, reducing the total O saturation coverage of the substrate, as evidenced by the asymptotic values of I/I_0 for large O_2 exposures in Fig. 4.16. The initial linear variation with Ag coverage can be understood considering a one-dimensional line of sites where the dissociation rate is proportional to the probability of finding an Ag-free region of the step edges. Since the Ag atoms condense into 1D chains (see Fig. 2.7 in Sec. 2.2), the dissociation rate is proportional to $(1-\Theta_{\mathrm{Ag}})$, where Θ_{Ag} is the fractional coverage of an Ag row decorating the step edge, (see the solid line in the inset in Fig. 4.17) and not to $(1-\Theta_{\mathrm{Ag}})^2$ as it would be the case for random dispersion of single Ag atoms. Ag deposition beyond one monatomic wire does not reduce $s_{0-Ag/Pt}/s_{0-Pt}$ strongly; the slow decrease that we observe until monolayer completion can be explained by taking into account the fraction of O_2 molecules that desorb directly upon impinging on the growing Ag layer [172]. It is interesting to note that the few Pt atoms that remain exposed on an almost completely Ag-covered surface have the same reactivity as a Pt substrate with only the Pt steps decorated by Ag, meaning that the O_2 dissociation process requires only interaction with a few Pt atoms.

It might be asked if Ag completely blocks dissociation at the step edges and if

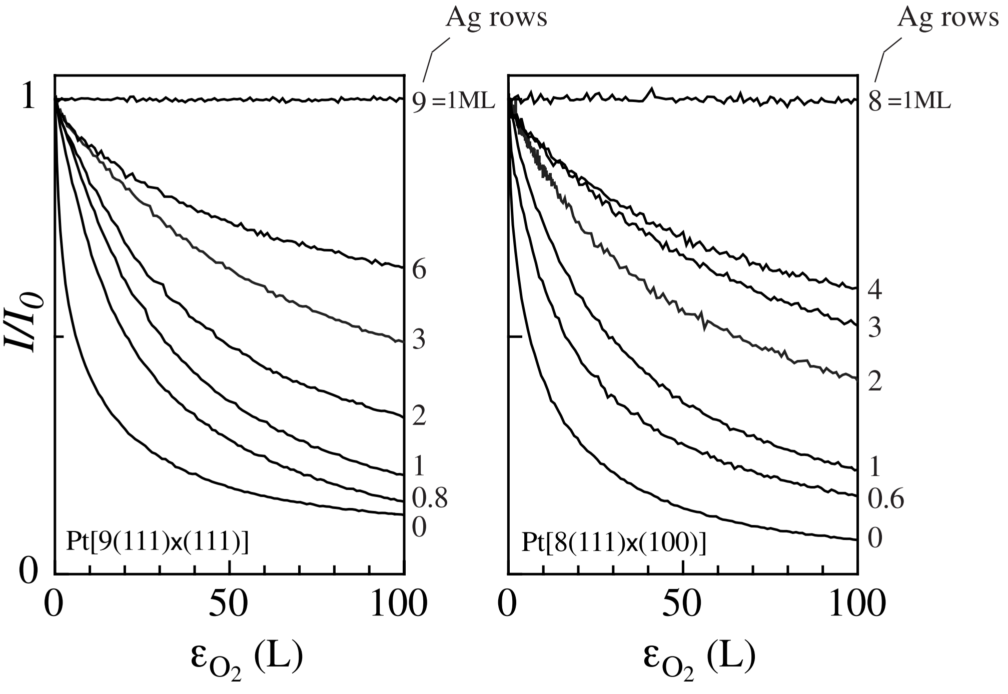

Figure 4.16: TEAS intensity as a function of O_2 exposure for different coverages of Ag monatomic wires, indicated on the right. The He beam incidence and reflection angles are 55.6° and 44.2° for Pt(997) [left], and 56.6°, 42.5° for Pt(779) [right], respectively. The He beam energy is 22 meV.

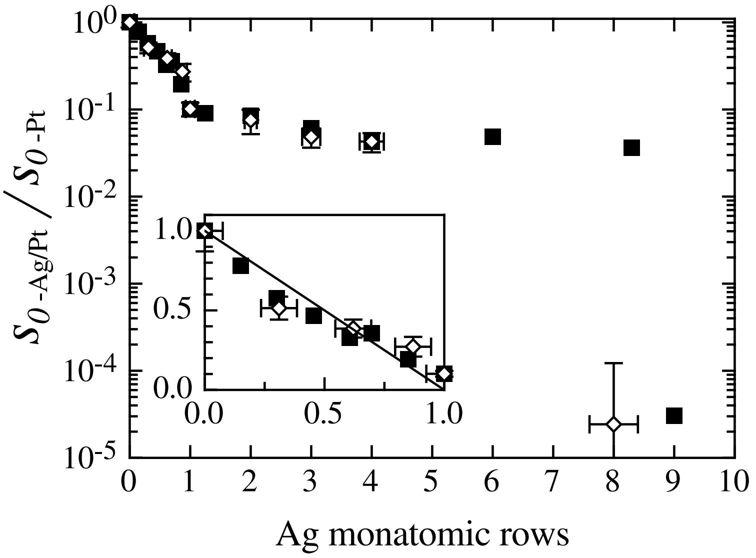

Figure 4.17: Variation of the O_2 dissociation rate with respect to the Ag-free step value for Pt(997) [full squares] and Pt(779) [open diamonds]. The solid line in the inset represents the $(1 - \Theta_{Ag})$ function (see text).

the O atoms observed in Fig. 4.14 actually come from terrace dissociation. This is not so, as revealed by Fig. 4.12. At the temperature below the onset of O thermal diffusion, O atoms are found dissociating on Ag-decorated steps with a higher probability with respect to terrace sites. Note also that $s_{0-Ag/Pt}/s_{0-Pt}$ *vs* Θ_{Ag} varies in the same way for the (997) and (779) surfaces, i.e., for the {111} and {100} steps; although a direct comparison of the two types of steps is not possible due to the incertitude in Σ, hybridization with Ag has an equal weight on the dissociation rate.

We showed above that by modifying the local chemical environment of the Pt atoms at the step edges we can investigate the factors that determine the reactivity of Pt step sites. Our results can be easily interpreted by the model proposed in Sec. 4.1 and support the conclusion that O_2 dissociation is enhanced at Pt steps due to the particular structure of the Pt *d*-bands at low coordinated sites. Finally, we demonstrated that we can vary the reactivity of a surface with a high density of defects in a controlled way. In the following section this point will be further developed.

Adsorption on terraces

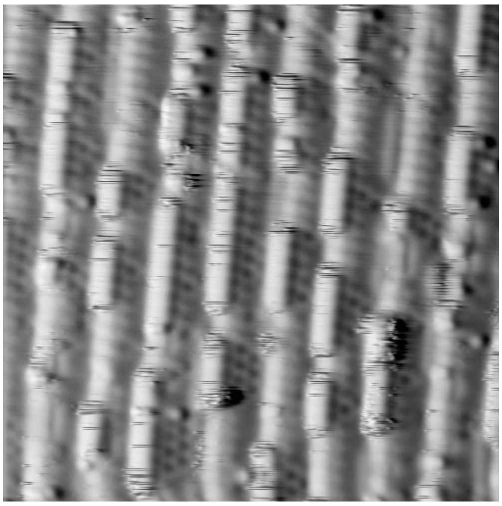

Figure 4.18: O $p(2{\times}2)$ patches on Pt(997) with partial Ag decoration.

A common belief is that once the step sites have been completely O-saturated, their reactivity becomes negligible and that adsorption proceeds subsequently as on a flat surface [141,173]. Here we argue against this point by showing that a reduction of the step reactivity induced by Ag step decoration (which we showed to be a local effect limited to the Pt atoms in direct contact with Ag) reduces the adsorption rate on Pt terraces. Consider O adsorption on a clean Pt stepped surface. On Pt terraces, the O saturation coverage is 0.25 ML, which corresponds to a $p(2 \times 2)$ structure of the O atoms. Such a structure can be easily observed by STM, as shown in Fig. 4.18 for a Pt(997) surface with partially Ag-decorated steps. However, surface scattering techniques such as LEED or TEAS provide a better tool to investigate its order on a large scale, due to the additional diffraction peaks originating from the O superstructure. Figure 4.19(a) shows the diffraction spectra recorded from Pt(779) and from Pt(779) plus a monatomic

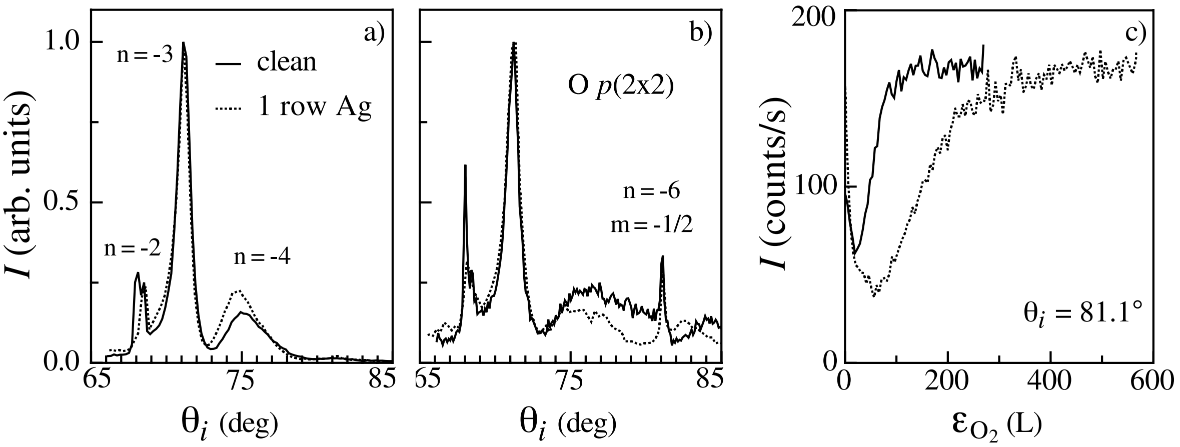

Figure 4.19: (a) TEAS diffraction pattern for the clean and Ag-decorated Pt(779) surface. The total scattering angle is fixed at $\chi = 123.5°$, $\lambda_{He} = 0.98$ Å. (b) Half-order diffraction peak originating from the O $p(2 \times 2)$ structure at saturation O coverage on clean and Ag-decorated Pt(779). (c) Intensity of the $m = -1/2$ peak as a function of O_2 exposure for the clean and Ag-decorated surface at 400 K. In the latter case the exposure has to be increased by a factor 3 in order to reach saturation.

Ag row. Dosing O_2, a diffraction peak corresponding to the periodicity of the 2×2 superstructure appears at $\theta_i = 81.1°$. We note that the 2×2 pattern forms independently of Ag. If we monitor the intensity on the peak at 81.1° during O_2 dosing, however, we see that saturation is reached on a much longer scale (at least a factor 3) for the Ag-decorated surface, indicating a reduced O filling of the terrace sites. Inhibition of the step reactivity thus reduces the overall adsorption rate on the whole surface.

Two arguments could be invoked to explain how steps influence adsorption on terraces: the first is that O atoms dissociating at the steps migrate to terrace sites leaving room for other molecules to dissociate. The second is that dissociation on O-saturated sites is still active. The first argument depends on the difference in adsorption energy between step and terrace sites, ΔE_{ts}. If the O atoms adsorbed at step and terrace sites are in equilibrium with each other, the terrace coverage Θ_t is related to the step coverage Θ_s by the following relationship [174]:

$$\Theta_t = \frac{e^{-\Delta E_{ts}/kT}}{e^{-\Delta E_{ts}/kT} + (\frac{1}{\Theta_s} - 1)}. \qquad (4.15)$$

Figure 4.20 shows how Θ_t evolves as a function of Θ_s for $\Delta E_{ts} = 0.57$, 0.38, 0.25 eV at 400 K. The first

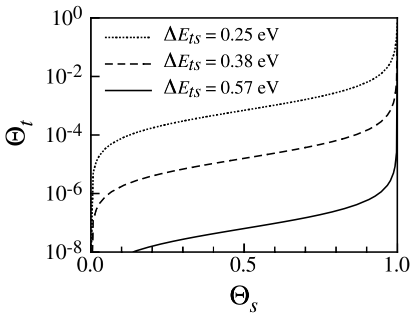

Figure 4.20: Coverage of terrace sites *vs* coverage of step sites, as in Eq. 4.15.

two values correspond to the calculation done by Feibelman for {100} and {111} steps, respectively [162]. Such values would exclude an efficient transfer of O atoms from step to terrace sites, which becomes relevant only for $\Delta E_{ts} \leq 0.25$ eV. Values of ΔE_{ts} estimated experimentally range about 0.35 eV [175]. The second option looks more realistic, expecially in light of the results by Zambelli *et al.* [21], who observed enhanced O_2 dissociation in the proximity of chemisorbed O atoms on Pt(111) terraces. Occupied step sites could therefore augment dissociation on nearby terrace sites.

We obtained further confirmation of the reactivity of saturated step sites by comparing the O_2 exposure that leads to the formation of the O $p(2 \times 2)$ pattern on Pt(779) and on Pt(111), analogously to what we did in Fig. 4.19(c) for Pt(779) and 1 row Ag/Pt(779). The intensity due the O $p(2 \times 2)$ diffraction peak on Pt(111) saturates at ~ 800 L O_2, a factor ~ 8 more slowly than on the stepped surface. If the O-saturated steps on Pt(779) did not participate in the dissociation process, we would expect that about the same amount of O_2 is needed to obtain the $p(2 \times 2)$ pattern on both surfaces, since step saturation is complete after only ~ 2 L (see Fig. 4.9). We conclude that, in the general case of adsorption on stepped surfaces, one cannot neglect the role of the steps, even after saturation (blocking) of all step sites by the adsorbing species.

4.5 Selective reactivity of decorated steps

As we have discussed in the preceeding sections, bonding with another species can induce significant changes in the band structure of a metal. Novel and interesting modifications in the reactivity of metal compounds are obtained in this way [113]. Thanks to the combined use of TEAS and STM and to the ability to deposit controlled amounts of material near specific adsorption sites, we have the opportunity here to investigate the local reactivity of bimetal surfaces with respect to different adsorbed species. We let the surface structure unaltered and observe how a change in the chemical identity of the step atoms affects the chemisorption process. This allows us to isolate the contribution of a second metal to the reactivity of step sites towards O_2, H_2, and CO. The results for O_2 have been already presented in Sec. 4.4.

In Fig. 4.21(a) we show the comparison between CO adsorption on a clean and Ag-decorated Pt(997) surface. The CO case is particularly interesting because, contrary to O_2, CO does not dissociate on Pt. As in the O case, CO still adsorbs preferentially at the former Pt edge sites after Ag step decoration and not on terrace sites. No perceivable displacement is observed with respect to the adsorption sites on clean Pt. If they were allowed to choose between Ag-decorated and Ag-free steps, CO molecules would go for

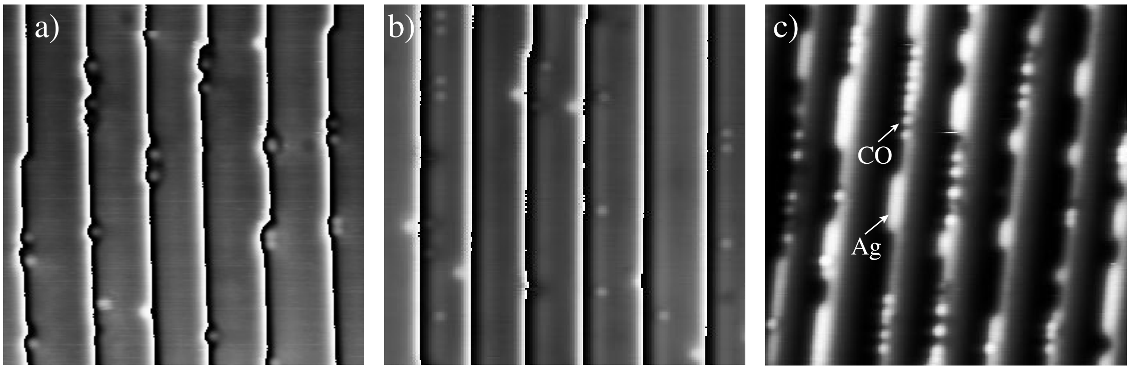

Figure 4.21: (a) CO (white dots) adsorbed at the step edges of Pt(997). Step down direction is from right to left. (b) CO adsorption after decoration of the Pt steps with a monatomic Ag row: most CO molecules are found at the right of the Ag row, on Pt edge sites. (c) CO adsorption after partial decoration of the Pt steps with Ag: CO prefers to bind to Ag-free steps.

the latter ones, as in Fig. 4.21(c). This behavior is similar to that of O atoms. The CO adsorption rate *vs* Ag coverage, however, is markedly different from that of O. Observe Fig. 4.22(a): the slope of the CO TEAS curves does not change significantly between the clean and Ag-decorated surface; I/I_0 approaches zero at the same CO exposure in both curves. Hence, CO sticking on a Pt stepped surface is not affected by Ag step decoration. An early study by Davies *et al.* [176] had found similar results on CO/Ag/Pt(553) although the morphology of the Ag overlayer had been incorrectly characterized.

Since CO does not dissociate upon adsorption on Pt, step sites do not "boost" the CO adsorption rate as for O and H.[6] To confirm the hypothesis that a modification of the step environment largely influences the sticking of molecular species that dissociate upon adsorption, we have repeated the same experiment as in Fig. 4.21(a) dosing H_2 on a clean and Ag-decorated Pt(779) surface (b). The H_2 dissociative sticking on 1 row Ag/Pt(779) is decreased by a factor of four. By decorating the Pt step edges with Ag we have therefore obtained a surface where the adsorption rate of molecular species that chemisorb molecularly or dissociatively can be modified in a selective way.

Contrary to O and CO that still bind to Pt step sites after Ag decoration, H atoms seem to be pushed away from the steps by the presence of Ag. By monitoring the TEAS intensity at grazing incidence (step sensitivity condition) we see that I/I_0 does not decrease due to H_2 dosing on the Ag-decorated steps [Fig. 4.23(a)]. A comparison

---

[6] Note also that the CO sticking coefficient on a flat Pt surface is already close to 1 at room temperature [20].

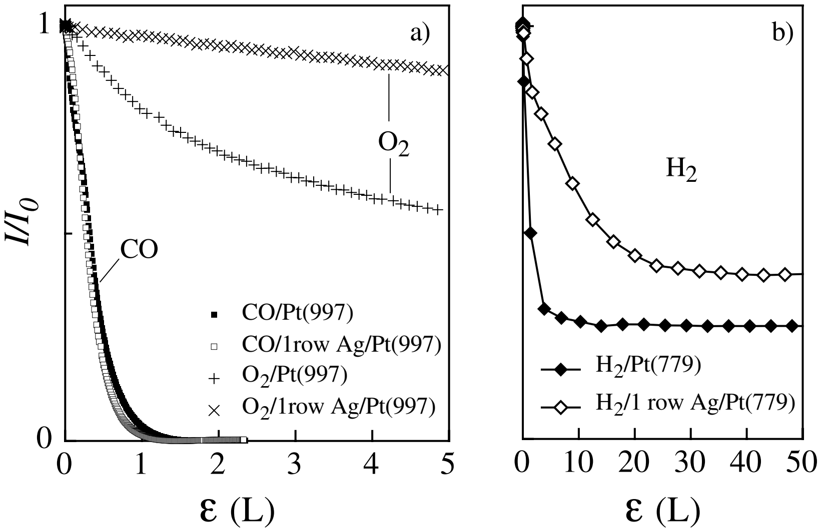

Figure 4.22: (a) Non-grazing TEAS intensity as a function of gas exposure for O_2 at 400 K, and CO at 340 K on clean and on 1 row Ag/Pt(997). $\theta_i = 55.6°$, $\theta_f = 44.2°$. (b) Same as (a) for H_2 dosing at 315 K on Pt(779) and on 1 row Ag/Pt(779). $\theta_i = 56.6°$, $\theta_f = 42.5°$. The slow decay of the TEAS intensity for O_2 and H_2 in the presence of Ag indicates that the dissociation rate is considerably reduced with respect to clean Pt.

with O and CO shows that Ag slows down O step adsorption considerably [Fig. 4.23(b)], whereas CO step adsorption is more or less unvaried [Fig. 4.23(c)]. In the H_2 case, Ag not only decreases the adsorption rate but it seems to forbid occupation of the former Pt step sites on the surface.

The results for CO adsorption are in line with the widespread opinion that the noble metal atoms on transition metal surfaces act as mere "site-blockers" for the reactant species [176, 178–182]. However, the strong decrease in the dissociation rate of O_2 and H_2 caused by Ag decoration of the Pt step edges shows that this picture is not complete. Neither can noble metals be always considered as site-blockers (in particular with respect to defect sites as shown here), nor can they be considered as inert. A comparison between our results and those by Besenbacher *et al.* on CH_4 dissociation on a Au-alloyed Ni(111) surface [183] shows that this is especially true for substrates with a high density of defects. Group IB metals are often employed as diluents in catalysts containing transition metals as the active components [178, 180, 183]. Given the high number of surface defects in the small crystallites used in actual catalysts and the likely nucleation of noble metal atoms at surface sites, considerable attention should be given to this effect.

Not all noble metals modify adsorption at Pt steps in the same way. We report in

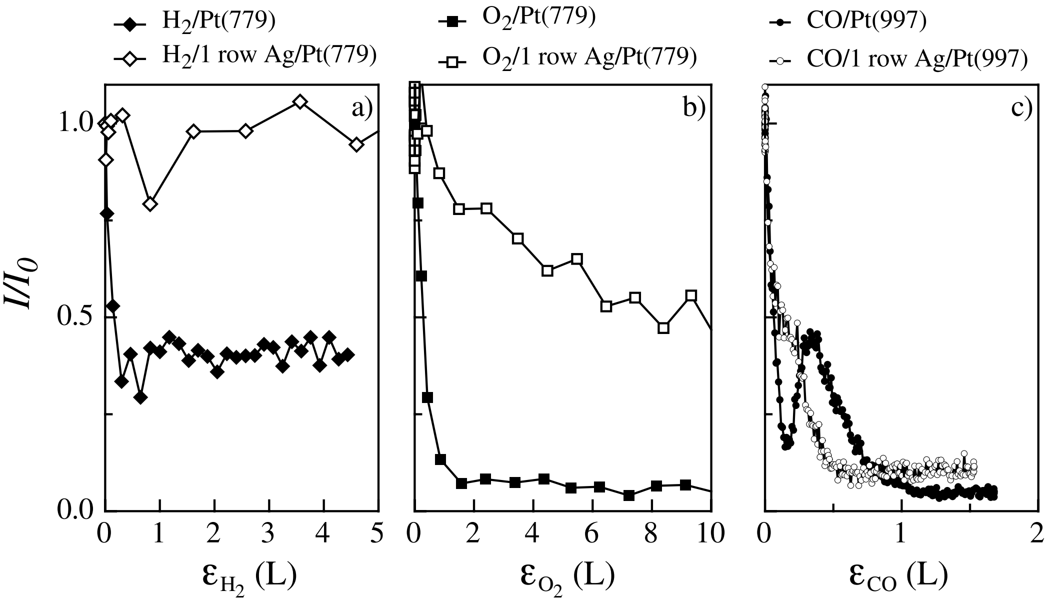

Figure 4.23: TEAS curves in grazing incident conditions, $\theta_i = \theta_f = 83°$. (a) H_2 dosing on Pt(779) at 400 K, 1×10^{-7} mbar H_2. (b) O_2 dosing on Pt(779) at 400 K, 1×10^{-7} mbar O_2. (c) CO dosing on Pt(997) at 340 K, 1×10^{-8} mbar CO. The full dots peak at 0.5 L is due to the completion of 1 row CO at the steps, as for metals (see Sec. 2), and Xe [177]. The comparison between panel (a) and Fig. 4.22(b) suggests that Ag selectively inhibits H adsorption at the steps.

Fig. 4.24 the TEAS curves measured during O_2 exposure of Pt(997) whose steps have been decorated by a monatomic row of Cu atoms. Compared to the clean Pt(997) curve there is no appreciable difference in the initial O adsorption rate. There is however a change of slope around 6 L which we attribute to inhibition of the O atoms exchange between step and terrace sites due to the stronger bonding of O on Cu with respect to Pt [146]. It is also evident that O adsorption on 1 ML Cu/Pt(997) proceeds much faster than on a clean Pt surface, whereas negligible O adsorption is found on 1 ML Ag/Pt(997) [Fig. 4.16].

Proposals of further experiments and conclusions

Up to now we have considered adsorption of single species. The next step would involve the study of surface reactions between different admolecules. We present here an overview of what could be done following the main lines of the experiments presented above.

Pt is well known as a model catalyst for the CO oxidation reaction. Many studies have pointed out that defect sites might have an influence on the CO_2 production

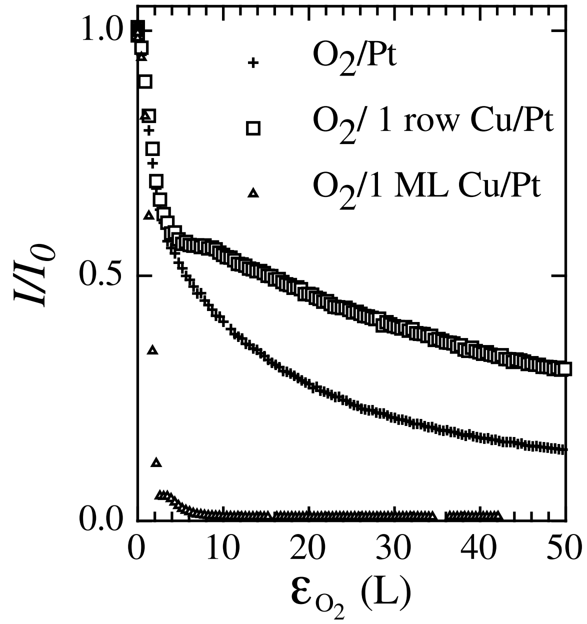

Figure 4.24: Non-grazing TEAS intensity as a function of O_2 exposure for clean Pt(997), 1 row Cu/Pt(997), and 1 ML Cu/Pt(997) at 350 K. $\theta_i = 54.8°$, $\theta_f = 41.9°$.

rate [12, 163, 184]. Xu *et al.* have found that the most favorable reaction sites at high CO coverage for the oxidation of CO involve CO species adsorbed on (111) terrace sites adjacent to O species adsorbed on step sites [184]. A clear distinction between geometrical and electronic factors influencing the reaction rate could not be made. In principle, this can be achieved by comparing reaction rates near Ag-decorated steps, as for the situation imaged in Fig. 4.25. Unfortunately, the fixed 77 K temperature of our STM did not allow us to do so, nor is TEAS able to distinguish between O and CO adsorption.

Pt(111) is also an excellent catalytic surface for the water formation reaction. The kinetics of water formation is however complex [185] and the role of specific adsorption sites is not fully clarified [186–188]. We report the preliminary results of a simple experiment which can be used to shed some light on the subject. We have pre-dosed Pt(111), Ag-free and Ag-decorated Pt(997) and Pt(779), with different O coverages; subsequent exposure to H_2 leads to water formation and desorption. The TEAS intensity is monitored during both O adsorption and H_2 dosing. Due to the extremely high reaction rate between H and O adsorbed on Pt [189], H_2 dosing is very efficient in removing O from the surface. The short residence time of H on Pt at 400 K due to thermal desorption ensures that there is very few residual H on the surface. The TEAS signal I/I_0 can therefore be considered to depend only on the presence of adsorbed O.

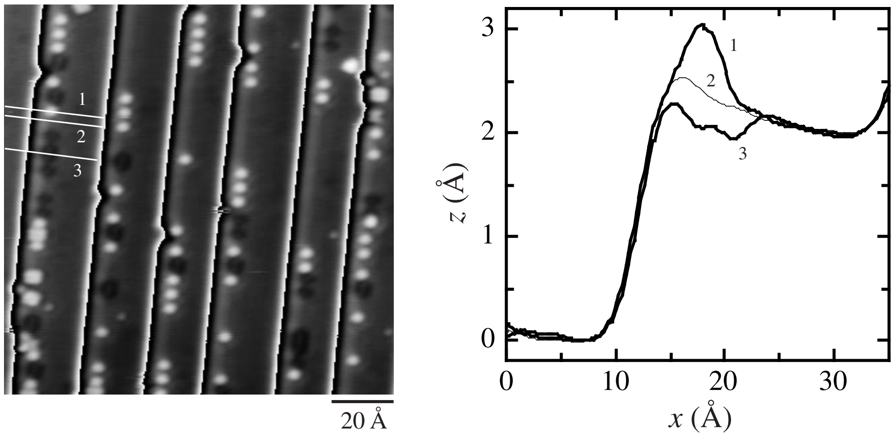

Figure 4.25: Co-adsorption of O and CO at Ag-decorated steps. At $T \leq 150$ K the CO_2 production reaction is thermally inhibited [184].

The $1 - I/I_0$ value after O_2 dosing is taken to be proportional to the O coverage, an assumption that is valid at least in the low coverage limit [3]. Then we expose the O-covered surface to H_2 and we measure how much hydrogen is needed to react away all the oxygen. By comparison of the TEAS curves in grazing and non-grazing incidence, we find that O at step sites is removed last. This is a consequence of the strong O-Pt bond at the step sites, which results in a slower H_2O reaction rate compared to terrace sites. Steps, on the other hand, favor the H adsorption on the surface, which is a prerequisite for the reaction to occur. The overall reaction rate is eventually determined by the competition between step-enhanced adsorption and step-reduced water formation. By decorating the steps with Ag we reduce the step-enhanced adsorption (Secs. 4.3 and 4.5) while (most likely) increasing the water formation rate at the steps (due to the weaker O-Pt bonding at the Ag-decorated steps). We are then able to determine which of the two effects is the most relevant one. Figure 4.26 reports the reagent exposure ε_{H_2} for given $1 - I/I_0$ coverages of O. By comparing the linear fits in the low coverage limit, we see that the addition of Ag to the step edges slows the reaction down by a factor of about 3 ± 0.2 for both surfaces. Hence, we suggest that, despite a local reduction effect, the presence of defect sites on Pt increases the H_2O overall formation rate due to the enhanced adsorption rate of the reagents.

In conclusion, we have conducted an atomic-scale study of the reactivity of specific adsorption sites on a Pt surface. We have found that O_2 dissociate preferentially on the upper edge of Pt steps due to the peculiar electronic configuration of step sites only. Decoration of the step sites of a Pt vicinal surface with monatomic Ag chains leads to a selective modification of the reactivity of the substrate towards dissociative and non-dissociative chemisorption. The dissociation rate of O_2 (H_2) at the Ag-decorated step sites sites is ten (four)-fold reduced with respect to pure Pt steps. This behavior is exclusively attributed to local *electronic effects* due to Ag binding with Pt next to the specific adsorption sites and not to site-blocking. In the dissociative case, adsorption on terrace sites is found to be dependent on the step reactivity even after step saturation by the adsorbed species. The CO adsorption rate is not affected by Ag. Furthermore, we showed that the controlled modification of the chemical identity of specific adsorption sites on a given surface can lead to a better understanding of their individual reactivity.

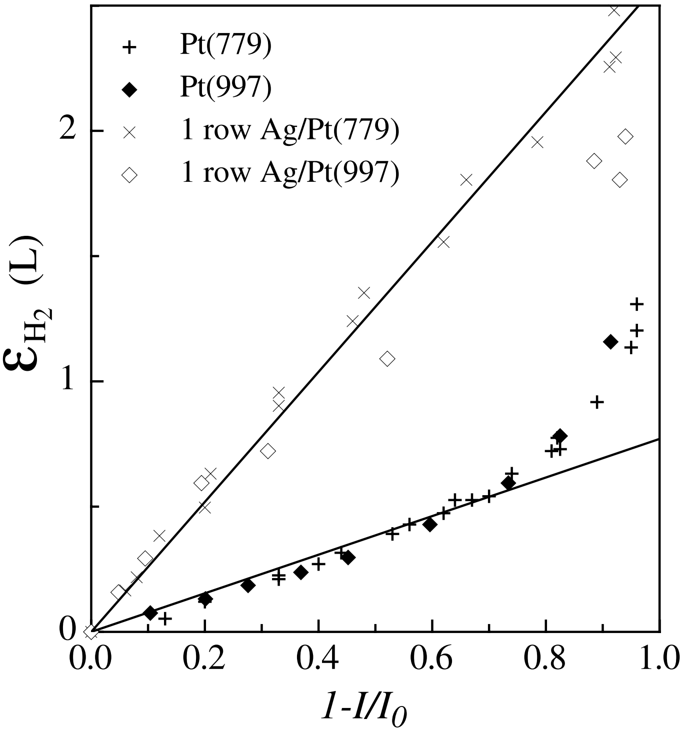

Figure 4.26: H_2 titration of O adsorbed on Pt(779) and Pt(997). The O coverage is given by the decrease in reflectivity $1 - I/I_0$ caused by O adsorption. The solid lines are fits to the Pt(779) data.

Chapter 5

Electronic states of Co and Cu monatomic wires

The electronic properties of low-dimensional metal systems are in many ways different from those of the bulk constituents. This is most evident when electrons are severely confined in one or two dimensions [42,65,190–194]. In our one-dimensional chains grown on vicinal surfaces we cannot speak properly of electron confinement since the chain states are inevitably coupled to the metal substrate states. Nevertheless, we show in this chapter that distinct electronic states show up in valence band photoemission spectra as Cu and Co monatomic chains are deposited on Pt(997). In particular, Co spectra indicate that the $3d$ Co band is exchange-split in one-dimensional systems, demonstrating the presence of magnetic moments that are localized near the Co atoms [195].

To investigate the electronic structure of Cu and Co nanowires, we introduce first angle-resolved photoemission spectroscopy (ARPES). ARPES is the method of choice to probe the occupied electronic states of any material. The technique is based on the analysis of the interaction of electromagnetic radiation with a macroscopic portion of the sample, about 0.5 mm^2 in size. We thereby justify the care taken in chapter 2 to obtain substrates with a uniform distribution of regular wires over large spatial extensions.

The photoemission process is described on a general footing in Sec. 5.1. Core level photoemission is also treated in this chapter to introduce the basics of x-ray magnetic circular dichroism (XMCD), a technique based on x-ray core level absorption, which we will employ in Chapter 6 to investigate the magnetic behavior of Co wires.

Since ARPES and XMCD require a tunable source of polarized light in the UV - soft x-ray range and an extremely intense photon beam to achieve sensitivity to submonolayer amounts of material, the experiments described in Secs. 5.2 and 6 have been carried out at synchrotron facilities. These measurements have been conducted in collaboration with the group of C. Carbone and W. Eberhardt from the Institut für Festkörperforschung of the Forschungszentrum Jülich. An elementary introduction to synchrotron radiation is presented in the following paragraph.

Some useful properties of synchrotron radiation

Synchrotron radiation is emitted by charged elementary particles - typically electrons - moving close to the speed of light as their trajectory is deflected by a bending device. The latter can be either a single bending magnet or a periodic array of magnets (wiggler or undulator). A discussion of the physics underlying the radiation process is outside the scope of this thesis and it is left to the extensive literature on the subject (see, e.g., Refs. [196–198]). Here we just mention the main characteristics that make synchrotron light an extremely valuable probe for condensed matter studies:

- *Tunable emission spectrum* with a bandwidth that depends on the characteristics of the bending device. The central frequency of the emitted photons, being an increasing function of the radiating particles energy and of the strength of the bending magnetic field, can be varied with continuity. This makes synchrotron radiation the only tunable photon source in the UV and soft x-ray region (10-1000 eV), which is the relevant spectral range for valence band and core level atomic excitation processes.

- *High intensity*; the power emitted by a single electron increases very rapidly with its energy and with the strength of the bending field.

- *High collimation*; because of the relativistic velocity of the electrons the radiation is emitted in a narrow cone tangential to their curved trajectory. Together with the elevated intensity, the high degree of collimation determines the extraordinary brightness of synchrotron radiation (defined as the number of photons emitted by a radiative source per unit time, solid angle, and area in 0.1% bandwidth). The high brightness allows to concentrate under a well-defined angle a large number of photons on a small sample area, increasing the sensitivity of the experiment.

- *High degree of polarization*; the type of emitting device and the direction of emission determine the polarization vector.

The peculiar properties of synchrotron radiation allow to control the photon energy, direction, and polarization parameters in photoemission and photoabsorption experiments. The high brightness of synchrotron light pushes the sensitivity of emission and absorption spectroscopies, such as ARPES and XMCD, to only a few percent of a monolayer of material.

5.1 The Photoemission process

Principles

The emission of electrons resulting from light absorption is the base of both photoemission and photoabsorption spectroscopies. It is treated here on a general footing, while specific aspects relative to ARPES and XMCD are examined separately. In the photoelectric effect, an electron in a bound state of a solid is excited into an unbound (free-electron) state by absorption of a photon of energy $\hbar\omega$. From the unbound state the electron can escape the solid yielding a measurable photocurrent. Neglecting many-body effects, the final energy of the excited electron is given by the energy conservation relationship

$$\varepsilon_f = \hbar\omega + \varepsilon_i\,, \qquad (\varepsilon_i < 0) \quad (5.1)$$

where ε_i is the energy of the bound state; both ε_f and ε_i are measured with respect to the Fermi level E_F. There will, of course, be no photoeffect below the threshold for ionizing the least-bound electron from an outer shell. As the electron escapes the solid, its kinetic energy is given by $\varepsilon_{kin} = \varepsilon_f - \Phi$, where Φ is the work function of the material. Figure 5.1 illustrates the photoexcitation process of electrons in core or valence states in a solid.

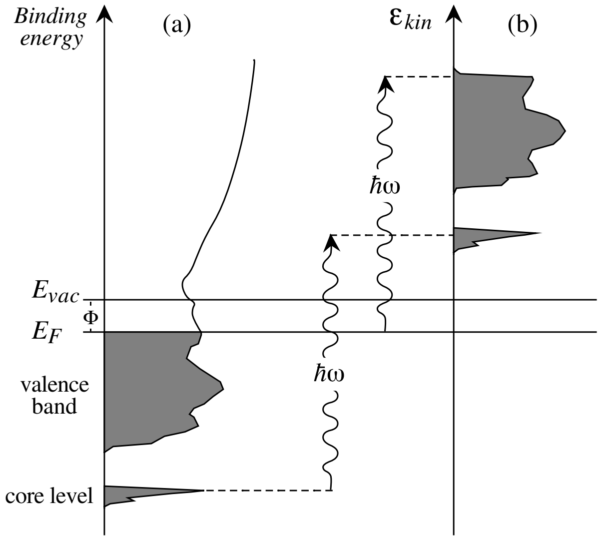

Figure 5.1: Schematic illustration of the photoemission process. The energy $\hbar\omega$ of the incoming photon is transferred to an electron in a bound state so that the photon is annihilated and the electron excited. The density of electronic states in the solid (a) is reflected in (b) modulated by the final density of states (adapted from Ref. [199]).

The absorption of a photon beam of intensity I penetrating into the solid is described by the exponential law

$$I = I_0 e^{-\mu x} \quad (5.2)$$

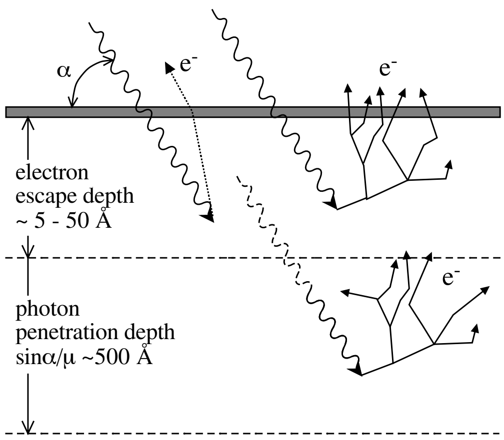

Figure 5.2: Penetration depth of photons and escape depth of photoelectrons. Inelasting scattering of the primary photoelectrons (dotted line) results in an electron cascade (solid lines).

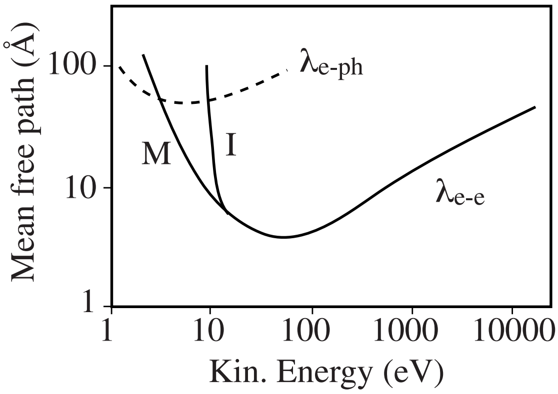

Figure 5.3: Energy dependence of the escape depth of excited electrons showing the mean free path as a function of kinetic energy for metals (M) and insulators (I), for electron-electron (λ_{e-e}) and electron-phonon (λ_{e-ph}) scattering. (Adapted from Ref. [199]).

where x is the penetration length and μ is the (energy-dependent) radiation absorption coefficient. μ is related to the absorption cross section σ by the atomic volume density of the sample $\mathrm{n_v}$ (atoms/cm^3) according to $\mu = \mathrm{n_v}\sigma$. In a metal, for photons in the UV or soft x-ray range the penetration depth $1/\mu$ is about 500 Å. However, the probing depth range of the various spectroscopies that rely on the photoelectric effect is actually determined by the short mean free path of the photoelectrons generated inside the solid, as illustrated in Fig. 5.2. Electron-electron, electron-plasmon, and electron-phonon interactions can inelastically scatter the photoelectrons on their way to the surface. The relative importance of the scattering mechanism depends on the kinetic energy of the electrons and follows a universal curve (with small variations depending on the material) which is shown in Fig. 5.3. Photons in the 10-1000 eV range produce primary photoelectrons with a mean free path of the order of 10 Å. Photoemission spectroscopy is therefore inherently surface sensitive. The inelastic scattering of the primary electrons results in an electron cascade constituted by the so-called secondary electrons. The fraction of secondaries that escape the surface has a smaller energy than predicted by Eq. 5.1: it represents the smooth low-energy tail of a photoemission spectrum, which is easily distinguisheable from the more structured primary region. As we will see later on, in ARPES only the primary electron spectrum is considered, whereas in x-ray absorption spectroscopy (XAS) all electrons escaping the sample are counted.

For most practical purposes, photoemission can thus be thought to occur in three-steps:[1]

- photon absorption in the solid with consequent primary photoelectron excitation from a bound to an unbound state;
- electron transport to the surface;
- escape from the surface, i.e. passage of the electron through the surface potential.

On a first approximation, the number of both primaries and secondaries escaping the surface is proportional to the absorption cross section σ. To interpretate ARPES and XAS spectra we need therefore to relate σ to the electronic structure of the sample.

The absorption cross section

Consider a monochromatic photon beam incident on the sample; the associated electromagnetic field can be described by a vector potential of the form

$$\mathbf{A}(\mathbf{r},t) = \mathbf{A}(\mathbf{r})e^{-i\omega t} \tag{5.3}$$

where $\hbar\omega$ is the photon energy. The transition probability per unit time that an electron, upon absorption of a photon, is excited from an initial state Ψ_i of energy E_i to a final state Ψ_f of energy E_f is given by the Golden Rule expression [204, 205]

$$P_{i\to f} = \frac{2\pi}{\hbar}\sum_f \left|\langle\Psi_f|H'|\Psi_i\rangle\right|^2 \delta(E_f - E_i - \hbar\omega)\,. \tag{5.4}$$

where the summation is carried over the various experimentally-indistinguishable symmetry-degenerate final states, and H' is the interaction Hamiltonian. Note that the delta function accounts for energy conservation as anticipated in Eq. 5.1. To first order in $\mathbf{A}$, i.e. considering only one-photon processes,

$$H' = -\frac{e}{2mc}\big(\mathbf{P}\ \mathbf{A} + \mathbf{A}\ \mathbf{P}\big) \tag{5.5}$$

where m is the electron mass and $\mathbf{P} = \sum_{l=1}^{N}\mathbf{p}_l$ is the electron momentum operator for the N electrons of the system. The differential cross section for the absorption process is then proportional to Eq. 5.4 summed over all possible initial states and reads

$$\frac{\mathrm{d}\sigma}{\mathrm{d}\Omega} \propto \sum_{i,f} \left|\langle\Psi_f|\,\mathbf{P}\ \mathbf{A} + \mathbf{A}\ \mathbf{P}\,|\Psi_i\rangle\right|^2 \delta(E_f - E_i - \hbar\omega)\,. \tag{5.6}$$

---

[1] A more formally correct representation of the photoemission process is discussed in Refs. [199–203].

Equation 5.6 contains the essential physics behind photoemission and allows to relate the electronic structure of the sample to σ, which is a measurable quantity.

With a few assumptions the transition matrix element can be further simplified. By making use of the commutator $[\mathbf{A}, \mathbf{p}] = i\hbar\nabla \cdot \mathbf{A}$, and choosing a gauge such that $\nabla \cdot \mathbf{A} = 0$, H' reduces to $(e/mc)\,\mathbf{A}\,\mathbf{P}$.[2] Moreover, if the wavelength of the incident radiation is large compared to the electronic shells typical dimensions, $\mathbf{A}$ can be considered as a constant in the integral involving the $\mathbf{A}\,\mathbf{P}$ operator (dipole approximation). The matrix element in Eq. 5.6 then reads

$$M_{if} = \mathbf{A} \cdot \langle \Psi_f | \, \mathbf{P} \, | \Psi_i \rangle \, . \tag{5.7}$$

Until now no assumption has been made on the initial and final states appearing in the above expressions. Since the aim of emission and absorption spectroscopies is that of gathering information on Ψ_i and Ψ_f, respectively, we need to relate the excitations observed in the experimental spectra to specific characteristics (energy and quantum numbers) of the initial and final states.

Single particle and many-body effects

Atoms and solids are complicated many-body systems of electrons all interacting with each other. In general, Ψ_i and Ψ_f have to be considered as N-electrons wave functions of the system under investigation. There are several levels of accuracy in approximating the correct many-body wave functions. A fairly good description of Ψ_i and Ψ_f can be obtained in the *configuration interaction* scheme [200, 206, 207], where any of the Ψ is expressed as a sum of Slater determinants [149] with properly chosen one-electron (Hartree-Fock) basis functions, each determinant describing a different configuration of the N-electron system. This approach is particularly useful when the ground state of an atomic system is described as a bonding combination of different configurations, e.g. the $3d^8 4s^2$, $3d^9 4s$, $3d^{10}$ states for Ni atoms in the metal [206, 207]. The mixing of the various configurations into either the final or the initial states can affect the observed intensity of a given final state appreciably, depending on the matrix element 5.7. In Ni core and valence band photoemission spectra [208] as well as in x-ray absorption [45], for instance, peaks corresponding to the transitions between different configuration states of both the initial atom and the final ion are observed at different energies.

---

[2] The $\nabla \cdot \mathbf{A} = 0$ condition is rigorously valid only in an uniform medium. We neglect here the fact that a strong spatial dependence in the vector potential can be induced by the discontinuity at the sample surface, expecially if ω is close to the plasma frequency of the solid [199].

A simpler, but more widely used approximation is that where $\Psi_i(N)$ and $\Psi_f(N)$ are factorized into antisymmetrized products of single-particles Hartree-Fock wave functions, i.e. they are represented by just a single Slater determinant. The basis set generally differs for $\Psi_i(N)$ and $\Psi_f(N)$ to account for the rearrangement of the electrons in the final ion state. By assuming a strong *one-electron* character for the photoemission process [200], the initial N-particle state can be written as the product of an "active" single-particle state ϕ_i times the Slater determinant of the remaining $N-1$ electrons $\Psi_i(N-1)$:

$$\Psi_i(N) = \mathcal{T}\{\phi_i, \Psi_i(N-1)\} \tag{5.8}$$

where $\mathcal{T}$ is a proper antisymmetrizer operator. If the photoelectron decouples rapidly from the $N-1$ remaining electrons after excitation with respect to their relaxation time (*sudden* approximation) we can write a similar expression for $\Psi_f(N)$:

$$\Psi_f(N) = \mathcal{T}\{\phi_f, \Psi_f(N-1)\}\,. \tag{5.9}$$

The matrix element then becomes

$$M_{if} = \mathbf{A} \cdot \langle \phi_f | \, \mathbf{p} \, | \phi_i \rangle \, \langle \Psi_f(N-1) | \Psi_i(N-1) \rangle \tag{5.10}$$

where the sum over the single-particle momentum operators $\mathbf{p}_l$ coincides with the sum over the initial states in Eq. 5.6 and has been left out. The last term represents an overlap integral over $N-1$ electrons between the final ion wave function and the initial "passive" electrons in the presence of the "active" electron. The energy relative to the initial and final states can be expressed as

$$E_i = \varepsilon_i + E^i_{N-1}\,, \quad E_f = \varepsilon_f + E^f_{N-1}\,. \tag{5.11}$$

Here ε_i and ε_i represent single-particle Hartree-Fock levels, E^i_{N-1} and E^f_{N-1} the energies of the initial and final $(N-1)$-electron states, respectively. Energy conservation implies

$$\varepsilon_f = \hbar\omega + \varepsilon_i + (E^i_{N-1} - E^f_{N-1})\,. \tag{5.12}$$

The $\Delta\varepsilon_r = E^i_{N-1} - E^f_{N-1}$ term represents the relaxation energy that is gained by the readjustment of the $(N-1)$ electrons into eigenstates of the final ion hamiltonian. This energy is effectively passed on to the photoelectron, shifting up ε_f by an amount $\Delta\varepsilon_r$ (see Fig. 5.4). In molecules and solids the relaxation energy is larger with respect to isolated atoms due to the charge flow from the neighbors towards the ion that carries the hole (extra-atomic relaxation). In the end, the ARPES-measured binding energies

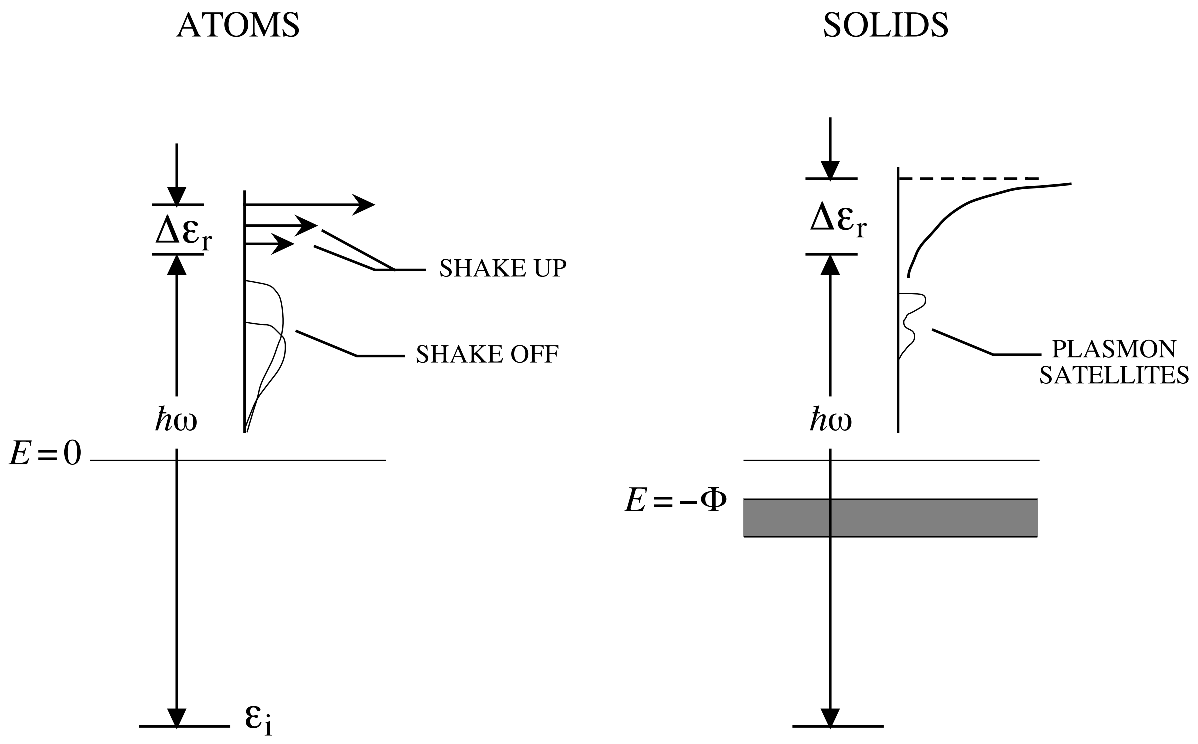

Figure 5.4: Energy levels diagrams for core level excitations. Left panel: atomic photoionization showing the main line shifted by $\Delta\varepsilon_r$, shake-up and shake-off satellites. Right panel: Solid state photoemission; note that the relaxation energy is larger with respect to the atomic case due to the valence band electrons additional screening of the photohole (adapted from Gadzuk, in Ref. [199]).

are actually hole-state energies, i.e. the difference between the total energy of a system with N electrons and one with $N-1$ electrons. If the final state with $(N-1)$ electrons has s excited states with wave functions $\Psi_f^s(N-1)$ and energy $E_{N-1}^{f,s}$ greater than the ion ground state, the transition matrix element in Eq. 5.10 must be calculated by summing over all possible excited final states. For strongly correlated systems, the overlap integral in Eq.5.10 is non-zero for at least some of the s excited states; in this case the energy of the excited states of the emitting atom is taken away from ε_f giving rise to additional peaks (*satellites* or *multi-electrons* excitations) in the photoemission spectrum. Satellite features, therefore, appear always at a lower ε_f with respect to the peak representing the ionic ground state (*main line*). The spectrum of the satellite peaks is discrete in case the final ion excitation is a transition to a bound state (multiplet and *shake up* transitions) or continuos if a second electron is excited above the vacuum level (*shake off*). Processes analogous to shake-ups and shake-offs are also expected to occur during core-level emission from metals, where the form of the DOS curve above the Fermi energy provides a continuos range of allowed excitation energies (creation of electron-hole pairs across the Fermi surface), rather than the discrete set available in atoms or molecules [200]. Many-body effects in valence band spectra of solids are generally strongly reduced on metals with wide bands formed by well delocalized states. In this case the screening of the photohole is almost perfect and therefore the final state energy equals the initial state one-electron energy. Significant correlation effects are nonetheless expected for narrow bands and more localized states. Satellites due to core hole - valence hole correlation effects will indeed be observed in the XAS spectra of Co in Sec. 6.4. Further many-body effects observed in metals are the creation of plasmon excitations during the formation of a core hole (*intrinsic* plasmon losses) and plasmon created during the photoelectron escape from the material (*extrinsic* plasmon losses) [208]. A pictorial view of many-body excitation losses observed in photoemission spectra of atoms and solids is reported in Fig. 5.4.

The simplest approximation which allows a more intuitive picture of photoemission is that of considering the N electrons as non-interacting. This approach is often sufficient to interpret the photoemission spectra of metals. In the independent-electron approximation the $(N-1)$ electrons overlap integral in Eq. 5.10 is equal to 1 and $E^f_{N-1} - E^i_{N-1} = 0$. The problem is reduced to the transition between two single-particle levels. The measurement of the kinetic energy of the photoelectrons directly yields the energy of the single-particle occupied levels and the transitions are restricted by selection rules that facilitate the mapping of the electronic structure of the sample. The direction of the polarization vector $\boldsymbol{\epsilon}$, for instance, enters in Eq. 5.10 by writing $\mathbf{A} = \mathrm{A}\boldsymbol{\epsilon}$ and it determines the orbital symmetry of the states involved in the transition. If the initial and final states are represented by ϕ_{n,l,l_z,s_z} states, we have the well-known dipole selection rules: $\Delta l = \pm 1$ (parity), $\Delta l_z = 0, \pm 1$ (angular momentum conservation), $\Delta s_z = 0$ since the spin does not enter in the Hamiltonian H'. For core levels which are described in the $j-j$ coupling scheme (ϕ_{n,l,j,m_j} notation), these rules become: $\Delta j = 0, \pm 1$ (parity), $\Delta m = \pm 1$ for circularly polarized light, and $\Delta m = 0$ for linearly polarized light. These rules will be employed in Chapter 6 to identify the transitions in the XAS spectra of Co.

Valence band photoemission

Band electrons in a solid are completely characterized by a set of quantum numbers such as energy E, momentum $\mathbf{k}$, point-group symmetry, [3] and spin. ARPES spectra

---

[3] Point-group symmetry quantum numbers are related to the crystal symmetry operations. They are analogous to the angular momentum in atoms and molecules which is related to the rotational symmetry.

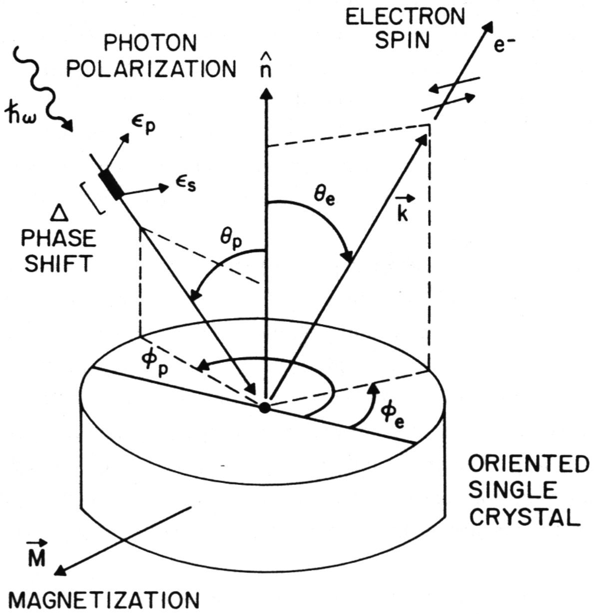

Figure 5.5: Diagram showing the experimental parameters of a fully-characterized photoemission experiment (from Ref. [203]).

allow, under certain assumptions, to determine the quantum numbers of the occupied electronic states by analysing the kinetic energy, the angular directions, and the spin of the primary electrons emitted by the sample due to photoexcitation with a polarized monochromatic photon beam of known energy [199–203]. Figure 5.5 shows the relevant parameters in a typical ARPES experiment. In the independent particle approximation, by measuring the kinetic energy of the photoexcited electrons, Eq. 5.1 directly allows us to calculate the energy of the occupied states of the sample. This is already a good piece of information. Figure 5.6 shows an ARPES spectrum of Pt(997) taken at photon energy $\hbar\omega = 122$ eV. This value determines the energy of the most inner bound state that can be excited. Analysing the kinetic energy of the emitted electrons, excitations of the Pt levels show up as peaks in the measured photoelectron current. Note that the core electrons yield sharp transition lines whose position is typical of each element, whereas the valence band states yield a continuos spectrum; a simple energy analysis is sufficient to define the core levels in a solid due to their atom-like character. For a complete characterization of band states, however, one needs to measure both the energy and the momentum components of the electrons with respect to the crystallographic axis. The 3D (2D, 1D) periodicity of the bulk (surface) electron potential V in a solid is responsible for the **k**-selection rules that allow to determine the momentum of the occupied band states in angle-resolved photoemission. Considering ϕ_i and ϕ_f as Bloch states, the momentum components of the excited electron inside the crystal $\mathbf{k}_f$ are equal to the

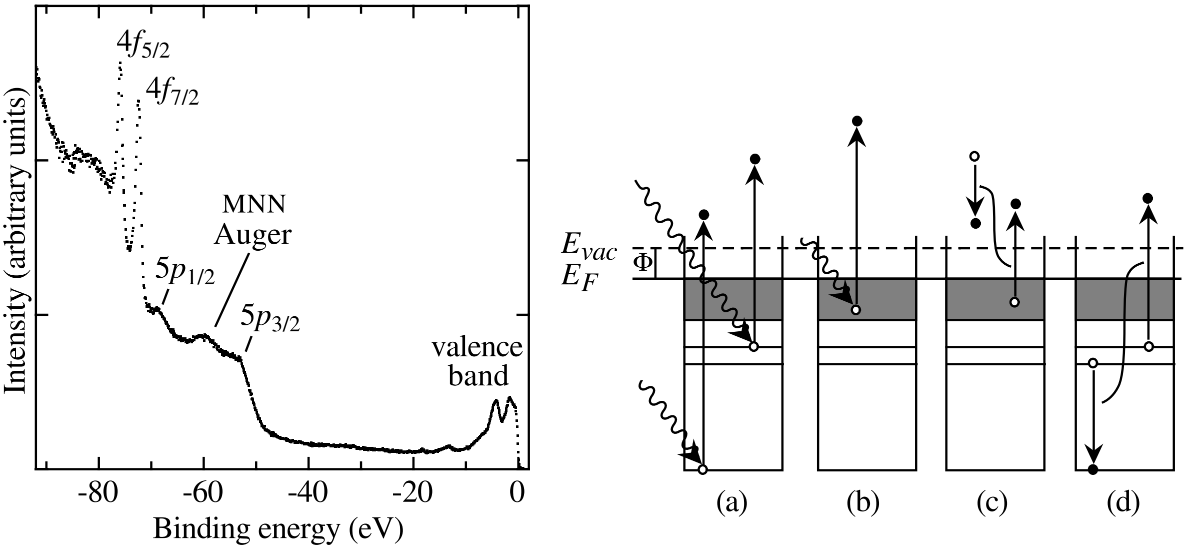

Figure 5.6: Left panel: Normal emission ARPES spectrum of Pt(997) taken at $\hbar\omega = 122$ eV. The assignement of the transitions is made by comparison with tabulated values of the Pt levels [208]. The background of the secondary electrons increase exponentially approaching the photon energy. Right panel: diagrams showing (a) core level transitions; (b) valence band transitions; (c) Secondary emission; (d) Auger transitions. Auger peaks can be identified as their kinetic energy is independent on the photon energy.

momentum of the initial state $\mathbf{k}_i$ modulo a reciprocal lattice vector $\mathbf{G}$.[4] As the electron escapes a 3D crystal, it is refracted by the work-function barrier at the surface. Only the momentum component parallel to the surface $\mathbf{k}_{||}$ modulo $\mathbf{G}_{||}$ is conserved, which can easily be determined in the direction specified by the detector's angles defined in Fig. 5.5 by the relationship $k_{||} = \sqrt{(2m/\hbar^2)\varepsilon_{kin}}\sin\theta_e$. To determine the vertical component of $\mathbf{k}_f$ one needs to know or assume a dispersion relation for the final states $E(\mathbf{k}_f)$ and then use energy conservation. The knowledge of $\mathbf{k}_{||}$, however, is sufficient to completely determine the band structure of 2D or 1D systems such as ultrathin films and nanowires. In confined 1D electron systems the electronic band structure becomes quantized in the transverse direction and the continuum of energies remains only in the longitudinal direction. It is difficult to obtain truly confined 1D states, however, since bulk states are able to couple to wire states relatively easily by projection in the directions perpendicular to the wires [93]. Even if there is no true confinement for Co

---

[4] Momentum conservation can be easily proved by making use of commutator rules for $\mathbf{p}$ such that the matrix element in Eq. 5.10 becomes proportional to $\mathbf{A} \cdot \langle\phi_f|\,\nabla V\,|\phi_i\rangle$ and by expanding V in Fourier series in $\mathbf{k}$-space. The photon momentum can be negliged for $\hbar\omega \lesssim 1000$ eV; simultaneous conservation of energy and momentum in the scattering event is ensured by the crystal lattice which provides momentum in multiple amounts of $\mathbf{G}$.

and Cu wires on Pt(997), one would expect to observe a uniaxial dispersion behavior along the wires for our system. Unfortunately, the characterization of the Co and Cu wire bands in **k**-space could not be satisfactorily carried out in our experiments due to the superposition of Pt and Co (or Cu) dispersion. Further discussion of this point is reported in Sec. 5.2.

ARPES experimental setup

The ARPES experiments presented here have been performed at the BESSY storage ring in Berlin at the TGM 5 undulator beamline [209]. The experimental setup is sketched in Fig. 5.7. The sample is mounted on a manipulator that allows to rotate the azimuthal and polar emission angles with respect to the detector, which is fixed and forms an angle of 30° with the photon beam. The preparation of Co and Cu wires on Pt(997) was done *in situ* by evaporating Co and Cu at 300 K with the procedure described in Sec. 2. The surface periodicity was checked by LEED, while Co and Cu coverages have been calibrated with a quartz-microbalance. The energy analysis of the photoemitted electrons was performed with a 90°-spherical electron analyzer (energy resolution $\sim$ 250 meV) by applying a voltage ramp to the sample while the analyzer potentials are kept constant. The angular acceptance of the electron analyzer is $\pm 1^\circ$. The synchrotron radiation coming from the storage ring was linearly polarized in the scattering plane (*p*-polarized) and it was monochromatized by a toroidal grating monochromator prior to entering the sample chamber. The probed sample area is of the order of 0.5 mm^2. The

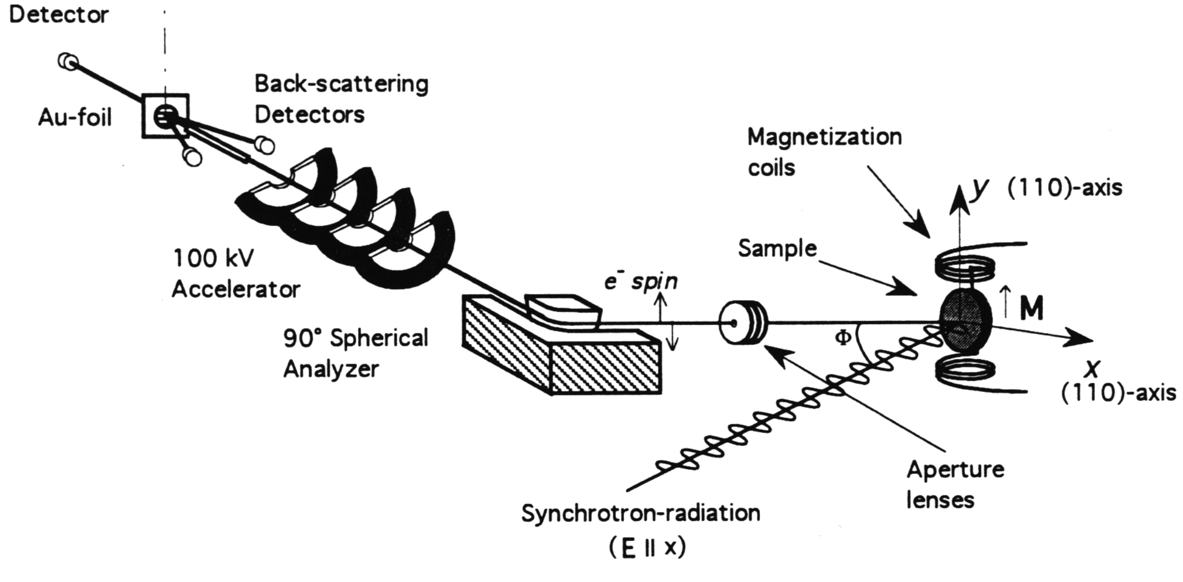

Figure 5.7: Experimental setup at BESSY TGM 5 beamline (from Ref. [210]).

Au foil and the back-scattering detectors that are visible in Fig. 5.7 allow to measure the transverse spin of the electrons by Mott scattering [211]. For ferromagnetic systems, spin-resolved ARPES spectra would evidence the in-plane remanent spin-polarization of valence band states.

5.2 Cu and Co chain states

Cu and Co 3d *vs* Pt 5d photoionization cross sections

Considering the small coverage of Cu or Co that corresponds to a monatomic chain array on Pt(997), one serious problem encountered in the experiment was the isolation of Cu and Co chain-induced states from the Pt background in angle-resolved photoemission spectra. In order to identify the Cu and Co 3*d* *vs* the Pt 5*d* contributions to the valence-band photoemission, we have made use of the difference in the photon energy dependence of the 3*d* and 5*d* photoionization cross sections. Figure 5.8(a) shows the photoemission spectra of clean Pt(997) and of 0.12 ML Co on Pt(997) taken at a photon energy of 40 eV: the two spectra are nearly the same, rendering the identification of Co states impossible. In order to increase the sensitivity to Cu and Co over Pt, we take advantage of the Cooper minimum [212]

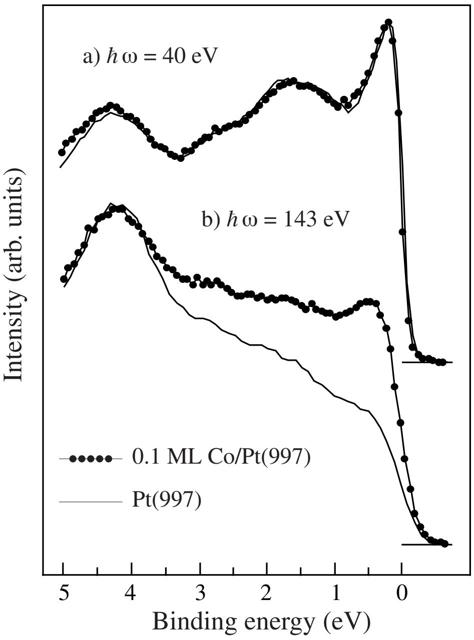

Figure 5.8: Photoemission spectra of clean Pt(997) and of 0.12 ML Co on Pt(997) taken at a photon energy of 40 eV (a) and 143 eV (b).

in the Pt 5*d* cross section.[5] The Pt 5*d* cross section rises to a maximum around $\hbar\omega = 50$ eV and then drops to a broad minimum starting at around 150 eV [213, 214]. The minimum in the cross section is a general occurence for orbitals with nodes in their wave functions [212]; for 3*d* orbitals the cross section merely increases and then decreases with energy.[6] At 150 eV the ratios of Cu and Co 3*d* to Pt 5*d* emission is about 15 [213,214]. This factor is responsible for the enhancement of the Co contribution in the photoemission spectrum reported in Fig. 5.8(b) taken at $\hbar\omega = 143$ eV. The chain-induced states that show up in Fig. 5.8(b) following Co deposition have therefore a prevalent 3*d* character.

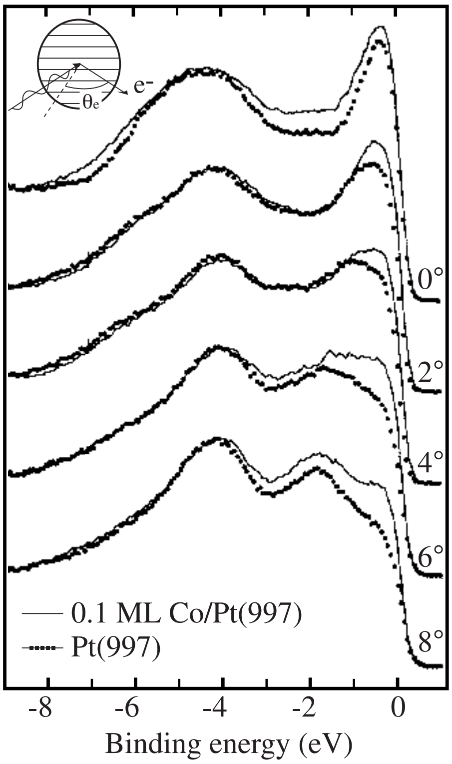

Figure 5.9: Photoemission spectra of 0.10 ML Co on Pt(997) taken at $\hbar\omega = 122$ eV for different emission angles θ_e in the direction parallel to the steps (see diagram).

Even if high photon energies allowed to distinguish between Cu, Co and Pt states, following the chain-induced states band dispersion with $\mathbf{k}_{||}$ proved to be a difficult task. Figure 5.9 shows a series of spectra taken between 0° and 8° from normal incidence along the direction parallel to the wires for 0.10 ML Co on Pt(997): although emission features due to Co can easily be identified, no clear-cut Co dispersion behavior can be isolated from that of the Pt bands.

Cu chain-induced 3d states

Figure 5.10 shows the development of Cu 3*d* states with increasing Cu coverage. Already at coverages below 0.1 ML we observe the formation of a single Cu 3*d* state at a binding energy of 2.3 eV. No Cu-derived states can be found close to the Fermi level because the *d*-band is entirely filled in Cu and the photoemission cross section for *sp* states is very small in this photon energy range. The Cu 3*d* peak shifts to a higher binding energy above 0.17 ML and reaches 2.7 eV at 2.0 ML. The evolution of the Cu 3*d* state on Pt(997) reflects changes in the electronic structure due to the modification

---

[5] Emission from *sp* states gives a much smaller contribution with respect to *d* states.

[6] The number of nodes in the radial wave function is $n - l - 1$, hence 3*d* orbitals do not have nodes.

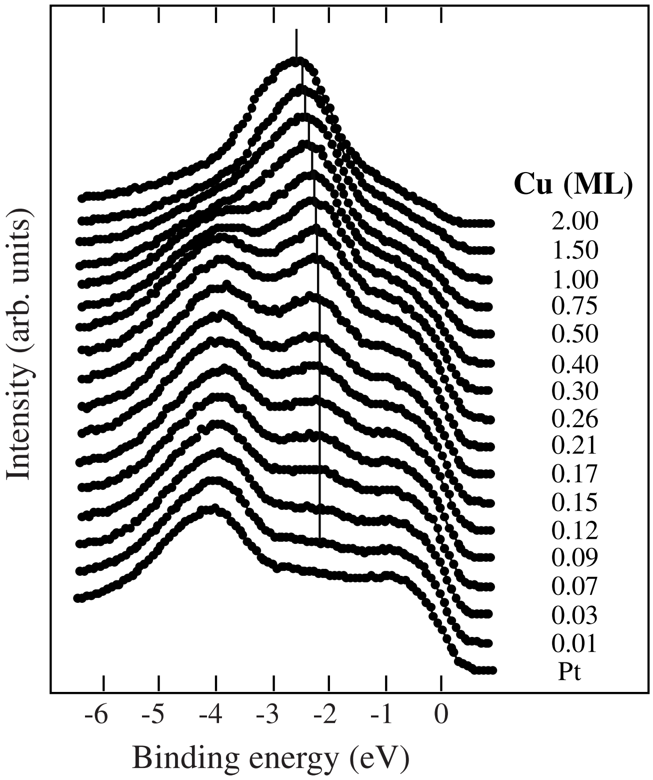

Figure 5.10: Photoemission spectra taken at a photon energy of 122 eV at normal emission displaying the evolution of Cu states on Pt(997) with increasing Cu coverage.

of the bonding configuration of Cu atoms. The observed shift starts around 0.17 ML, in correspondance with the transition from a 1D to a 2D wire structure. Contrary to what we observe here, for systems with 2D islands or 3D cluster growth, increasing the coverage in the submonolayer regime does not lead to observable changes in the electronic structure because the atomic coordination already resembles that of a monolayer or of the bulk, respectively [215,216]. For Cu on Pt(111), where growth proceeds in large 2D islands [82], Shek *et al.* [217] have shown that the Cu 3*d* peak is found already at 2.6 eV for coverages lower than 0.1 ML. A calculation of the binding energy corresponding to the 3*d* band centroid reported in the same paper yields 2.24 eV for a Cu atom embedded in a Pt surface and 2.47 eV for a Cu adatom on Pt. For an ordered Cu_3Pt surface, Schneider *et al.* [218] have reported a photoemission peak due to Cu states at 2.4 eV. These values can be compared with the value of 2.3 eV for the chain states reported here, which obviously corresponds to low-coordinated Cu atoms.

Co chain-induced 3d states

Figure 5.11 shows the evolution of the Co 3*d* states with Co coverage. Clearly the spectra differ from those of Cu, reflecting differences in the electronic states of Co and

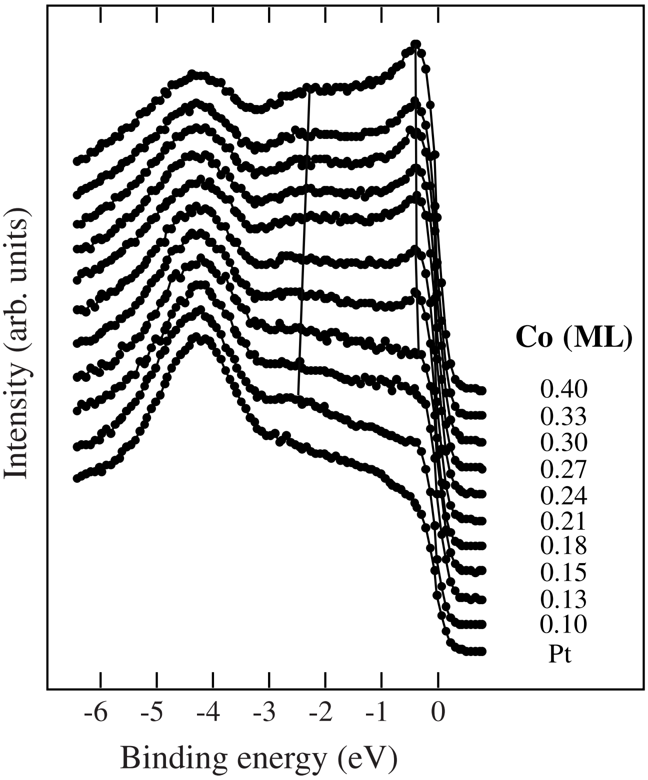

Figure 5.11: Photoemission spectra taken at a photon energy of 122 eV, 4° off normal emission, displaying the evolution of Co states on Pt(997) with increasing Co coverage.

Cu chains. Two features become more evident with increasing coverage: one close to the Fermi level and the other approximately at 2.4 eV. In order to isolate the contribution due to the Co chain-induced states, a difference spectrum between 0.10 ML Co and clean Pt is plotted in Fig. 5.12 together with the spectrum of a Co monolayer. The spectra have been normalized to the amplitude of the Pt peak at $\sim$ 4 eV. In contrast to the single peak observed for the Cu chains, we observe two peaks for the Co chains, located at 0.3 and 2.4 eV. It is very unlikely that one of the two Co peaks represents a Co-Pt interface state. If that were the case, a similar feature would be observed also for Cu, whose electronic structure differs from that of Co mainly in the energetic position of the bands. We therefore attribute the double peak structure observed in Figs. 5.11 and 5.12 to the exchange splitting of the Co 3*d* bands. In ferromagnetic materials, electrons in unfilled bands tend to maximize the total spin number due to the positive sign of the exchange interaction (see Sec. 6.2). As a result, the minority (e.g. spin down) electrons are pushed up in energy to avoid double occupancy of the same electronic states. This causes the exchange splitting between up and down spin bands which shows up in the photoemission spectra of Co valence band states. A schematic picture of the exchange-split Co 3*d*-band is drawn in Fig. 5.13. In the Cu case the *d*-band is entirely filled and

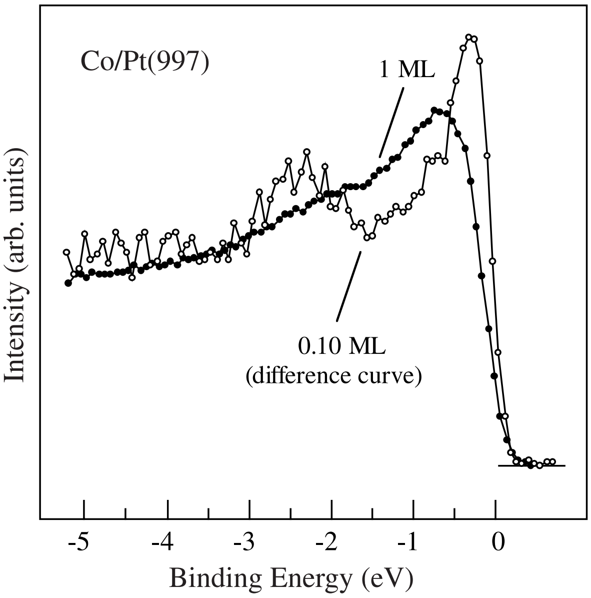

Figure 5.12: Difference spectrum for 0.10 ML Co evidencing the Co chain-induced states in comparison with a photoemission spectrum of 1 ML Co (not a difference spectrum); $\hbar\omega = 122$ eV.

no such effect can be observed (see Fig. 5.10).

Exchange splitting is the key to magnetism since it creates a spin unbalance that produces the magnetic moment. There is actually an approximately linear correlation between the $3d$ magnetic splitting and the local magnetic moment per atom in transition metals. Averaging the exchange energy over different symmetries and $\mathbf{k}$ values one gets that the $3d$ moment is of the order of $1\mu_B$ per electron volt exchange splitting [93].

The magnitude of the exchange splitting depends on the atomic coordination of the system. Starting from a single $3d$ atom and going towards the bulk, the splitting will be reduced as the d levels broaden and hybridize with the sp-states (Fig. 5.13). We therefore expect our 1D chain states to have a larger splitting compared to Co film and bulk states. The magnitude of the exchange splittings in Fig. 5.12 cannot be safely compared without spin analysis, since the broad feature close to the Fermi level observed in the 1 ML spectrum could consist of contributions from states of different spin character and symmetry. However, we estimate that the exchange splitting for the chain-induced Co states is large (≈ 2.1 eV) compared to typical values for Co thin films (1.4-1.9 eV) [219, 220] and for bulk Co (≈ 1.4 eV) [219, 221]. This suggests in turn that the local magnetic moments in Co monatomic chains are considerably larger with respect to the Co films and bulk values. The larger values of d-exchange splitting for monatomic metal chains were predicted in a pioneering theoretical study of the electronic structure of Ni and Fe wire arrays by Weinert and Freeman published in 1983 [222]. Our data represent the first experimental proof of their predictions based on arrays of 1D monatomic chains. More sophisticated calculations taking into account the presence of the Pt substrate also confirm the results presented here [223].

The presence of a splitted band in the spin-integrated Co spectra does not imply the existence of long-range magnetic ordering. The observed splitting testifies only that the Co atoms in the chain structures have large local magnetic moments, but it doesn't tell anything about their alignment. To probe the magnetic ordering one needs to perform spin-resolved measurements. If the Co chains were ferromagnetic we would expect the remanent magnetization to show up in two spin polarized states 2.1 eV apart. With the experimental setup described in Sec. 5.7 it is possible to measure the in-plane spin polarization. The electrons that go through the energy analyzer shown in Fig. 5.7 are accelerated to 100 keV and scattered by a thin Au foil. The electron spin polarization results in a right-left asymmetry measured in the backscattered photocurrent [211]. Figure 5.14 shows the spin-resolved and spin-integrated spectra of 0.1 ML Co on Pt(997) taken at 100 K following the application of a magnetic field H_0 in the direction perpendicular to the wires. The arrows indicate the direction of the applied field with respect to the drawing in Fig. 5.7. Similar results are obtained if H_0 is applied parallel to the wires. It is evident that the Co chain-induced states are not spin-polarized. In the absence of an external magnetic field, the different orientation of the atomic magnetic moments results in mixed spin polarization of either of the peaks observed in Figs. 5.11 and 5.12. We conclude that the Co chains are not ferromagnetic at this temperature. It is also possible that the easy magnetization direction of the wires is out-of-plane (which is not accessible with our experimental setup) and that the absence of in-plane remanence did not allow to detect any spin-polarized state. The measurements presented in Sec. 6.3, however, reveal that the in-plane and out-of-plane directions perpendicular to the wires are almost equally favored. The absence of ferromagnetism at finite temperature is consistent with the predictions for a 1D Ising chain with nearest

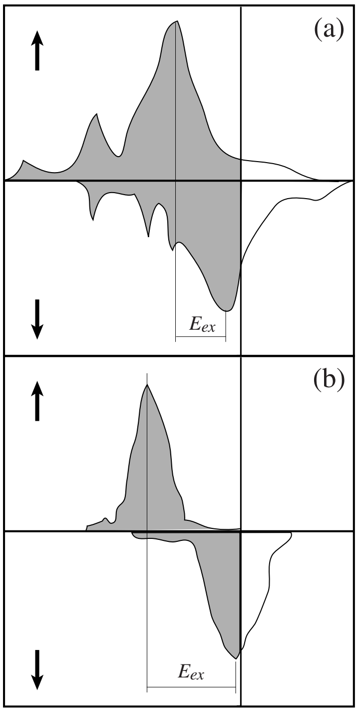

Figure 5.13: (a) Schematic d density of states for bulk Co. (b) The narrower bandwidth due to a reduction of the atomic coordination results in the enhancement of the exchange splitting.

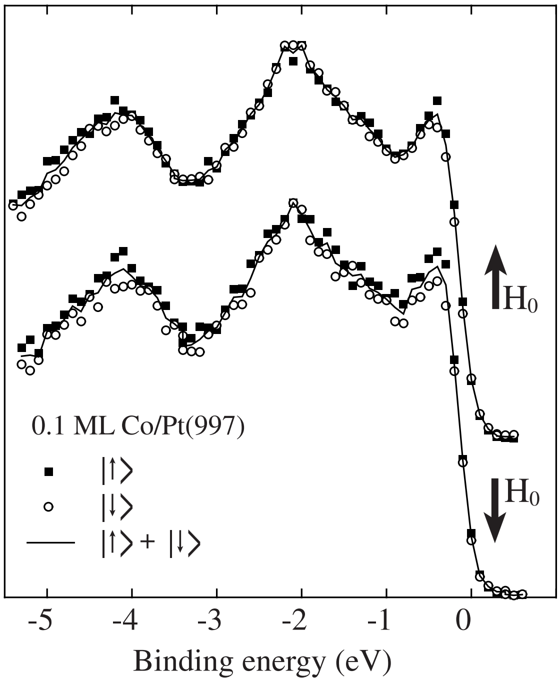

Figure 5.14: Spin-resolved and spin-integrated spectra of Co monatomic chains at 100 K, normal emission, $\hbar\omega = 92$ eV, for two opposite directions of the applied field. The arrows in the kets indicate the spin direction with respect to the direction of the applied field (in-plane, perpendicular to the wires).

neighbor interactions [224, 225] for which the existence of long range magnetic order is not allowed at $T > 0$ K. The coupling between real atoms, however, could be incorrectly described by the Ising model [222]. From the data presented in this chapter, we cannot exclude a ferromagnetic behavior below 100 K. The Curie temperature of a magnetic system, in fact, decreases strongly with its dimensions [226]. The XMCD data reported in Sec. 6 will clarify this point, demonstrating that Co monatomic chains on Pt(997) are superparamagnetic and that their blocking temperature is below 10 K.

Chapter 6

Magnetism of Co monatomic wires

Fundamental magnetic properties like the spontaneous magnetization, the anisotropy, and the temperature dependence of ordered magnetic states in low-dimensional systems deviate substantially from those observed in bulk elemental systems [93, 227]. In this chapter we present the results of the magnetic dichroism experiments on 1D arrays of Co monatomic wires grown on Pt(997) performed at the European Synchrotron Radiation Facility (ESRF) in Grenoble. This study constitutes the first experimental investigation on the magnetism of 1D structures in the monatomic limit. In the preceding chapter we have shown that Co monatomic wires display a large magnetic exchange splitting value. Spin-resolved photoemission spectra did not show any long-range magnetic order down to 100 K. The x-ray magnetic circular dichroism (XMCD) measurements reported here allow a more specific and complete characterization of the magnetic behavior of the Co wires. The XMCD technique is introduced in Sec. 6.1. In Sec. 6.2 we discuss the long range magnetic order of the (supported) 1D wires and we show that the Co monatomic wires behave superparamagnetically in the investigated temperature range (10-300 K) and that the blocking temperature is reached at around 5 K. Strong anisotropy effects are expected for 1D structures. A simple model introduced in Sec. 6.3 shows how the magnetocrystalline anisotropy can be related, through the electronic structure, to the size and dimensions of the system. XMCD measurements taken with the magnetic field applied in the in plane and out of plane directions show that the peculiar symmetry of the monatomic Co wires is reflected in a nearly uniaxial anisotropy. Coupling effects between the Co chains and the Pt substrate can affect the magnetic anisotropy and are also discussed in this section. Finally, in Sec. 6.4 we analyze the XMCD spectra as a function of the Co coverage. Applying the dichroism sum rules (Sec. 6.1) we show that the orbital magnetic moment of the Co monatomic wires is largely enhanced with respect to a Co monolayer film. The measurements reported in this chapter are the result of a joint experiment with the group of C. Carbone and W. Eberhardt of the IFF-FZ Jülich.

6.1 XMCD spectroscopy

Synchrotron radiation in the soft x-ray range allows access to the strong dipole-permitted (core $2p \rightarrow$ valence $3d$) excitations in transition-metal ferromagnets, and (core $3d$, $4d \rightarrow$ valence $4f$) in rare-earth magnetic materials. X-ray absorption experiments with polarized light in this energy range allow therefore to extract a great deal of information on the magnetic state of such systems. After the first practical demonstration of x-ray magnetic dichroism (XMD) using linearly polarized light in 1986 [228], XMD with the "C", i.e. using circularly polarized light, has been developed both experimentally [45, 229–236] and theoretically [206,237–244] into a powerful quantitative magnetometry tool. XMCD is element-specific, has sub-monolayer sensitivity, and can be used to measure magnetization loops. It allows to identify the moment orientation in ultrathin films of magnetic materials and, unique among surface-sensitive magneto-optical techniques, to determine separately the spin and orbital magnetic moments of a given element together with their anisotropies.

The absorption of polarized light by a magnetized sample depends on the orientation of the magnetization **M** relative to the light polarization direction. XMCD is defined as the difference in the absorption coefficients for parallel and antiparallel orientation of the magnetization direction of the sample with respect to the helicity of the circularly polarized exciting light. The photon absorption process has been treated in some detail in Sec. 5.1. For $3d$ transition metals the dipole selection rules allow the following transitions:

- K: $1s \rightarrow 4p_{1/2}$
- L_2: $2p_{1/2} \rightarrow 3d_{3/2}$, $4s$
- L_3: $2p_{3/2} \rightarrow 3d_{3/2,5/2}$, $4s$,

where the subscript indicates the total angular momentum quantum number j. The properties of $3d$ electrons are probed by excitation of $2p$ core electrons to unfilled $3d$ states; our attention is therefore exclusively dedicated to the L_2, L_3 absorption edges. The energies corresponding to the L_2 and L_3 main lines for a number of transition metals are reported in Table 6.1. Figure 6.1(a) shows the L_2, L_3 adsorption edges of a 15 ML thick Co film on Pt(997) obtained by measuring the current of the excited photoelectrons

Element	L_3 (eV)	L_2 (eV)
Mn	640	650
Fe	707	721
Co	779	794
Ni	854	871
Cu	933	953
Pt	11561	13271

Table 6.1: X-ray absorption energies [245].

as a function of the energy of the incident photons, as described in Sec. 6.1. The dashed line schematizes the contribution due to $p \to s$ transitions; in practice the exact form of the s background is not known, even if smoothed step functions are commonly used in the literature [233] to take it into account. The $p \to d$ channel, however, largely dominates the spectrum. The sum of the L_2, L_3 line intensities after the correction for the s transitions is proportional to the number of holes in the $3d$ Co band.

Following Stöhr [236], a qualitative understanding of the physics underlying XMCD can be given in the following way: right (R) or left (L) circularly polarized photons are absorbed and transfer their angular momentum ($\Delta m = \pm 1$, respectively) to the excited photoelectron. If the photoelectron originates from a spin-orbit split level, e.g. the $p_{3/2}$ level, the angular momentum of the photon can be transferred in part to the spin through the spin-orbit coupling.[1] R polarized photons transfer the opposite momentum to the electron than L polarized photons, and hence one obtains large transition matrix elements between final states of opposite spin polarization in the two cases. In other words, for a given initial state, R and L polarized photons will excite photoelectrons having opposite spin polarization. Since the $p_{3/2}$ (L_3) and $p_{1/2}$ (L_2) levels have opposite spin-orbit coupling ($l + s$ and $l - s$, respectively), the spin polarization will be opposite at the two edges, L_3, L_2. The magnetic properties enter in the transition of the excited photoelectron to an unfilled $3d$-state of the valence band. In the absence of a net magnetization, the number of excited electrons for a given light polarization would be the same for any of the L_3, L_2 edges because the total spin polarization for both the $p_{3/2}$ and $p_{1/2}$ manifolds is equal to zero. Suppose now that the $3d$ band is exchange split; the empty states have predominantly minority character. The favored transitions are those that involve the initial states with predominant minority spin character. As we will

---

[1] The $\Delta S = 0$ selection rule of dipole transitions holds only in the $L - S$ coupling. In the $|nljm\rangle$ base that is used to represent spin-orbit split states, the single particle spin eigenvalue s_z is not a good quantum number. Its expectation value $\langle jm|s_z|jm\rangle$ yields the spin polarization of each state $|jm\rangle$.

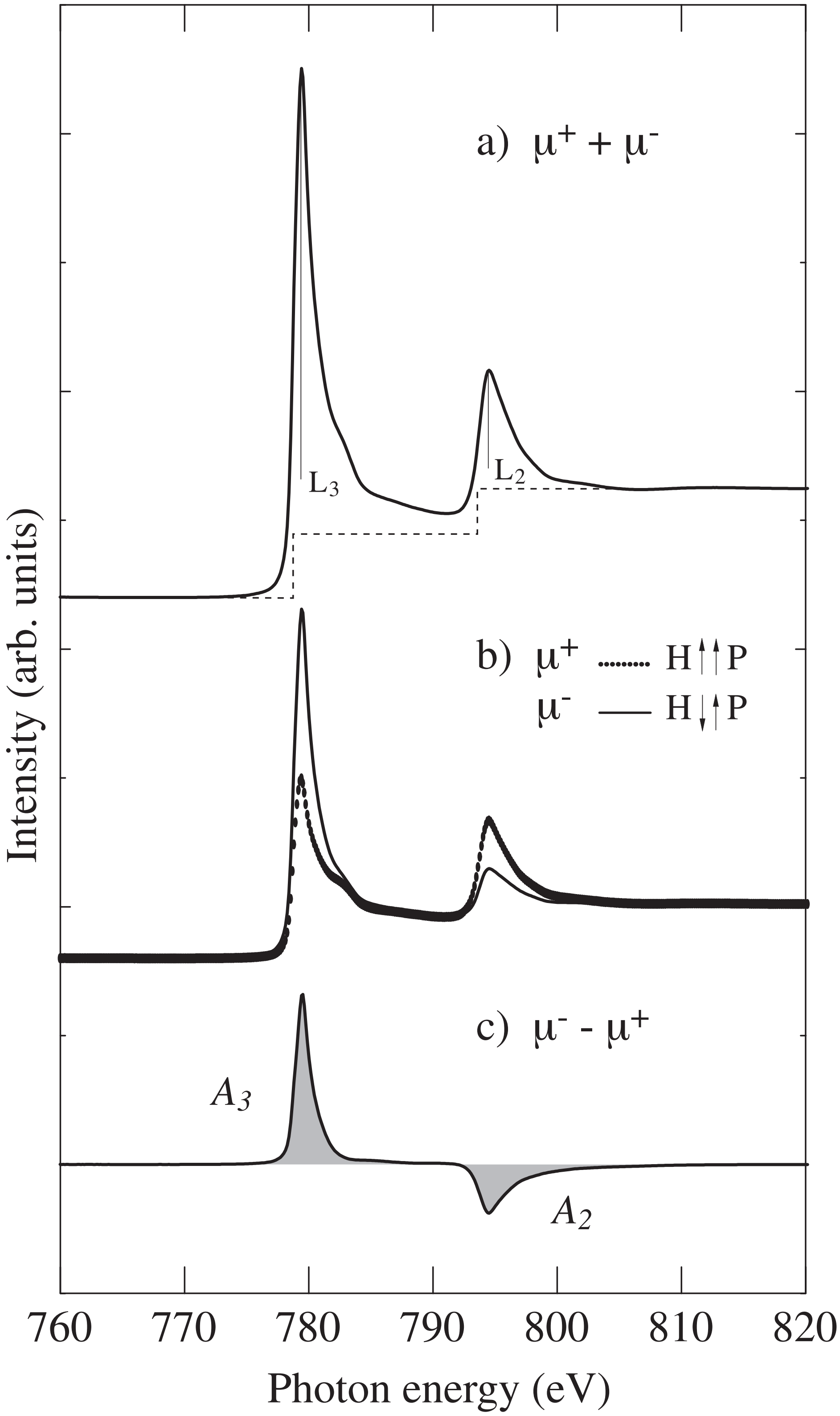

Figure 6.1: Absorption spectra of a 15 ML Co film on Pt(997). $T = 300$ K, $H = 7$ Tesla. (a) Sum spectrum; (b) R, L spectra; (c) XMCD spectrum.

show later, these are the L_3 transitions for antiparallel and the L_2 transitions for parallel direction of the magnetization with respect to the photon spin. The exchange split final states therefore act as a filter for the spin of the excited photoelectron. The quantization axis of the filter is given by the magnetization direction which, for maximum dichroism effect, needs to be aligned with the photon spin direction. The photon helicity or photon spin is taken to be positive (negative) when it is parallel (antiparallel) to the light propagation direction, corresponding to R (L) polarization. For a given orientation of the magnetization **M** with respect to the photon helicity **P** one has

$$\begin{array}{ccc} I_{\mathrm{L}_3^-} & > & I_{\mathrm{L}_3^+} \\ \mathbf{M} \uparrow\downarrow \mathbf{P} & & \mathbf{M} \uparrow\uparrow \mathbf{P} \\ I_{\mathrm{L}_2^-} & < & I_{\mathrm{L}_2^+} \end{array}$$

where I_{L_x} is the intensity of the line at the L_x edge, and the sign indicates the relative orientation of **M** and **P**. This result is clearly shown in the x-ray absorption spectra in Fig. 6.1(b): the solid line refers to the $\mathbf{M} \uparrow\downarrow \mathbf{P}$ configuration whereas the dotted line refers to the $\mathbf{M} \uparrow\uparrow \mathbf{P}$ configuration. The corresponding absorption coefficients are called μ^+ and μ^-, respectively. The XMCD spectrum (c) is obtained by taking the difference $\mu^+ - \mu^-$ of the two spectra shown in (b). From the above reasoning it follows that the XMCD signal is proportional to the imbalance between the minority and majority $3d$ states above the Fermi level of the element under consideration, which in turn is proportional to the element magnetization.

Similarly, if the d valence shell possesses an orbital moment, it will act as an orbital momentum filter for the excited photoelectrons [236]. By using appropriate sum rules [238, 240, 241] we will see how the orbital and spin contribution to the magnetic moment can be extracted from a XMCD spectrum such as the one shown in Fig. 6.1(c). The following paragraphs are devoted to a more quantitative understanding of the x-ray abosorption process and associated XMCD.

Single particle models

In calculating soft x-ray core-level absorption and XMCD spectra in $3d$ transition metals, two simple atomic models have been devised [237, 239], besides more complex band structure calculations [244]. The first one, the so-called *Erskine-Stern* model [237], is based on the single-particle model of optical transition from a core state of prescribed symmetry into valence-band states with symmetry corresponding to allowed dipole transitions. Only the core states are treated relativistically (spin-orbit split levels) and we

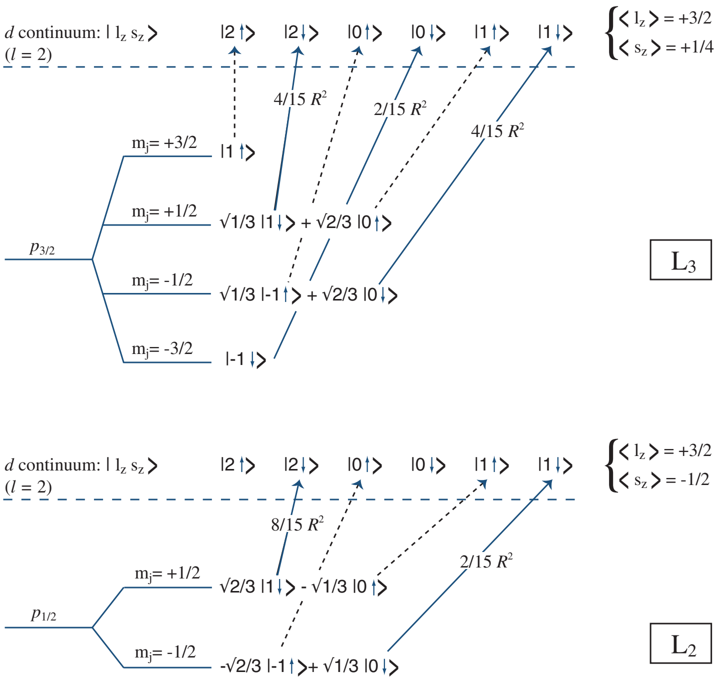

Figure 6.2: Absorption of a right circularly polarized photon ($\Delta l_z = +1$) by $p_{1/2}$, $p_{3/2}$ electrons. In the Erskine - Stern model one considers only the transition to final states with $\downarrow$ spin (solid lines). The square transition matrix elements are taken from Ref. [239].

make the assumption that the empty valence-band states are exclusively of minority character. We treat here the case relevant for the L$_3$, L$_2$ edges.

From the dipole approximation discussed in Sec. 5.1 it follows that the absorption coefficient μ is proportional to the square of the matrix element

$$\langle \phi_f | \boldsymbol{\epsilon} \cdot \hat{\mathbf{r}} | \phi_i \rangle \,. \tag{6.1}$$

The initial $2p$ states are split by the spin-orbit interaction into two levels, which in the $|jm\rangle$ base are given by $|\frac{1}{2}\, m\rangle$ and $|\frac{3}{2}\, m\rangle$, degenerate with respect to $m =$ -$\frac{1}{2}$, $\frac{1}{2}$ and $m =$ -$\frac{3}{2}$, -$\frac{1}{2}$, $\frac{1}{2}$, $\frac{1}{2}$, respectively (see Fig. 6.2). Since the spin-orbit interaction is neglected in the final states, the latter can be described in the $|l_z s_z\rangle$ representation or equivalently in the spherical harmonics $Y^{s_z}_{l,l_z}$ representation. The $\boldsymbol{\epsilon}$ $\cdot\hat{\mathbf{r}}$ operator can be expressed as

$$\boldsymbol{\epsilon} \cdot \hat{\mathbf{r}} = \sqrt{\frac{4\pi}{3}}(\epsilon_z Y_{1,0} + \frac{-\epsilon_x + i\epsilon_y}{\sqrt{2}} Y_{1,1} + \frac{\epsilon_x + i\epsilon_y}{\sqrt{2}} Y_{1,-1}) \,, \tag{6.2}$$

where for R and L circular polarization only the middle and last term survive, respectively. To calculate the matrix element 6.1 it is therefore sufficient to express the initial $|jm\rangle$ states as superposition of $Y^{s_z}_{l,l_z}$ states and to integrate over the spherical coordinates r, θ, and ϕ. This is done here as an example for a transition from the $|\frac{3}{2}\frac{1}{2}\rangle$ initial state to the $Y^{\downarrow}_{2,2}$ final state for R polarization. With the use of the Clebsch-Gordan coefficients one has $|\frac{3}{2}\frac{1}{2}\rangle = \frac{\sqrt{2}}{\sqrt{3}}Y^{\uparrow}_{1,0} + \frac{1}{\sqrt{3}}Y^{\downarrow}_{1,1}$. Since the dipole operator does not act upon the spin, only the spin down component $Y^{\downarrow}_{1,1}$ gives a non-zero contribution to the transition rate, which is then proportional to

$$\left| R \iint \sin\theta\, d\theta d\phi\; Y^{\downarrow *}_{2,2}(\theta,\phi)\,\sqrt{\frac{4\pi}{3}}\Big(-\epsilon_x + i\epsilon_y\Big) Y_{1,1}(\theta,\phi)\,\frac{1}{\sqrt{3}} Y^{\downarrow}_{1,1}(\theta,\phi)\right|^2 = \frac{4}{15}R^2\,, \quad (6.3)$$

where $R = \int dr\, r^2 R_p(r) R_d(r)$ is the integral of the $2p$ and $3d$ radial wave functions, and $|\epsilon_{x,y}| = 1$. The $1/\sqrt{2}$ factor that appears in Eq. 6.2 has been omitted to be consistent with Ref. [239]. A similar calculation can be carried out for all the possible transitions between the initial $p_{3/2}$ and $p_{1/2}$ and the final d levels. For the spin-orbit split states, the radial integral and the phase space are almost unchanged, and hence the ratio of the intensity of different transitions can be determined from the angular parts of the integral alone, that is, purely from angular momentum considerations. The values of the transition matrix elements 6.1 as a function of R are reported in Fig. 6.2 for the case of R polarized light. For the L_3, L_2 edges, by summing incoherently over the entire manifold of the unoccupied $d^{\downarrow}$ states, one obtains [239]:

$$\mathrm{L}_3 \quad (p_{3/2} \to d^{\downarrow}) \quad \begin{cases} \mu^+ + \mu^- = \frac{16}{9}R^2 \\ \mu^+ - \mu^- = -\frac{4}{9}R^2 \end{cases}$$

$$\mathrm{L}_2 \quad (p_{1/2} \to d^{\downarrow}) \quad \begin{cases} \mu^+ + \mu^- = \frac{8}{9}R^2 \\ \mu^+ - \mu^- = \frac{4}{9}R^2\,. \end{cases}$$

The model therefore predicts the L_3 and L_2 asymmetries $(\mu^+ - \mu^-)/(\mu^+ + \mu^-)$ to be -1/4 and 1/2, respectively; the two values coincides with the expectation value of the spin $\langle s_z\rangle$ in the final states considering all the available transitions (to $d\downarrow$ and $d\uparrow$ states) from the $p_{3/2}$ and $p_{1/2}$ manifolds, respectively. The final states expectation value of the orbital momentum $\langle l_z\rangle$ is, in this model, equal for both the initial levels. The L_3 to L_2 ratio for the total cross section $(\mu^+ + \mu^-)$ and for the XMCD cross section $(\mu^+ - \mu^-)$ are 2:1 and -1:1, respectively. This result explains the larger intensity of the L_3 edge relative to the L_2 edge and the opposite sign of the dichroic contribution observed in the experimental spectra. The analysis of Fig. 6.1 reveals, however, that these ratio values are not correct. In fact, considering the final d states as equally probable, the intensity ratio are determined only by the degeneracy (population) of the initial states.

The symmetry between the final states is removed if valence-band spin-orbit coupling is included, as shown in Fig. 6.3. In a model where both the initial and final states are treated relativistically [239], spin-orbit splitting will enhance the $j = 5/2$ over the $j = 3/2$ character near the top of the d band (3rd Hund's rule for a more than half-filled

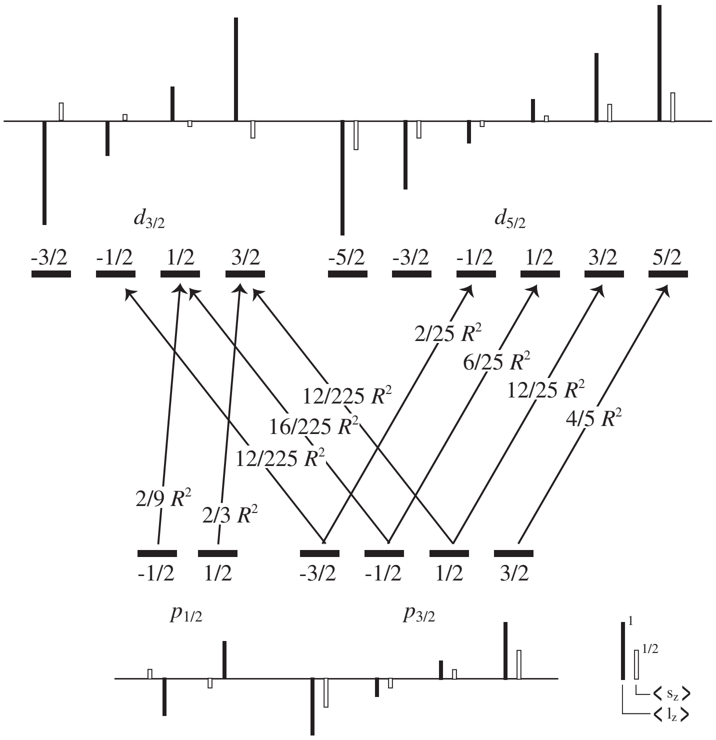

Figure 6.3: Dipole-allowed $p \to d$ transitions for right circularly polarized light ($\Delta m = +1$) in the fully relativistic model. The bars represent the expectation values of the l_z, s_z operators in each of the $|jm\rangle$ state.

d shell). There are therefore more empty states with $j = 5/2$ rather than $j = 3/2$ character. Since the $j = 5/2$ states can only be accessed by L_3 transitions, the intensity of the L_3 edge will be favored over L_2, and the -1:1 XMCD ratio will shift in favor of L_3. This is actually observed in the Co spectra shown in Fig. 6.1 where the L_3 to L_2 XMCD ratio is $\sim$ 2:1. In Sec. 6.4 we will see that this ratio varies considerably with the Co coverage reflecting changes in the hybridization of the Co 3d states. Note also that the inclusion of spin-orbit splitting in the final states removes the l_z degeneracy, opening the possibility of having a non-zero orbital contribution to the magnetic moment per atom, as will be discussed in Sec. 6.3.

Relativistic band structure calculations [239, 246, 247] refine considerably the results presented above, but are not treated in detail here because of their complexity. Many-body dynamical effects of the type mentioned in Sec. 5.1 have also been taken into account to explain the appearence of satellite peaks both in the x-ray absorption (XAS) and in the XMCD spectra of Ni [206,248]. We will see in Sec. 6.4 that electron correlation effects are active also for Co as demonstrated by the presence of satellite peaks in both XAS and XMCD spectra.

Sum rules

Three important magneto-optical sum rules [238, 240–242] relate the XAS and XMCD data to the element-specific orbital and spin magnetic moments, and to the anisotropy terms of the spin and charge densities in the unit-cell. We will expound here the results derived from the orbital moment and spin moment sum rules [238, 240, 241], which will be employed in the analysis of our data. The derivation has been carried out for electric dipole transitions in a localized model, considering a single ion in an arbitrary crystal-field symmetry. Hybridization of the final states is only allowed for intra-shell orbitals, i.e. there is no mixing of the d states with sp-like states. The sum rules have been tested by band-structure calculations [249, 250] and have been verified experimentally [233].

The first rule relates the shell-specific ground-state expectation value of the orbital angular momentum operator L_P (P is the direction specified by the incident photon beam) to the integral of the XMCD absorption spectrum taken over the complete core level edge ($\mathrm{L}_3 + \mathrm{L}_2$ in our case) of a magnetically oriented ferromagnetic or ferrimagnetic material [238, 240]. In the case of L_3, L_2 transitions, one calculates the d-shell orbital momentum expectation value as

$$\frac{1}{2n_h}\langle L_P\rangle = \frac{\int_{\mathrm{L}3+\mathrm{L}_2} dE(\mu^+ - \mu^-)}{\int_{\mathrm{L}3+\mathrm{L}_2} dE(\mu^+ + \mu^- + \mu^0)}\,, \tag{6.4}$$

where n_h is the number of holes in the d shell (a LDA calculation yields $n_h = 3$, 2.60, 2.55 for atomic, surface, and bulk Co, respectively [250]), and the denominator term is the normalization to the unpolarized (isotropic) absorption spectrum (μ^0 is the absorption coefficient for linearly polarized light and is usually taken to be the average between μ^+ and μ^-).

The second rule relates the XMCD signal to the shell-specific ground-state expectation values of the total spin S_P operator and of the intra-atomic magnetic dipole operator T_P [241]:

$$\frac{2}{3n_h}\Big(\langle S_P\rangle + \frac{7}{2}\langle T_P\rangle\Big) = \frac{\int_{\mathrm{L}_3} dE(\mu^+ - \mu^-) - 2\int_{\mathrm{L}_2} dE(\mu^+ - \mu^-)}{\int_{\mathrm{L}3+\mathrm{L}_2} dE(\mu^+ + \mu^- + \mu^0)}\,. \tag{6.5}$$

The term containing $\langle T_P\rangle$ arises from the multipole expansion of the spin density: the largest (monopole) term after integration over the atomic volume, corresponds to the isotropic magnetic spin moment; the next higher (quadrupole) term reflects the lowest-order anisotropic spin distribution in the atomic cell and it gives rise to the intra-atomic magnetic dipole moment $\mu_D = -7\mu_B\langle T_P\rangle$, where $\mu_B = e\hbar/2m_e$ is the Bohr magneton [236].[2] First principle calculations [244] show that the $7\langle T_P\rangle$ term in Eq. 6.5

---

[2] The magnetic dipole operator is defined as $\mathbf{T} = \mathbf{S} - 3\hat{\mathbf{r}}(\hat{\mathbf{r}}\cdot\mathbf{S})$, and it represents the anisotropy of the

can be safely neglected for atoms in cubic symmetry, but that its contribution might be of the order of 10 % of $\langle S_P \rangle$ for atoms at surfaces and interfaces.

In performing the integrals in Eq. 6.5, some ambiguity exists in the choice of the L_3, L_2 integration limits, because the intensity of the two edges might superpose to a certain extent. According to Ref. [233], the cutoff in our calculations is chosen at the onset of the L_2 edge. If one wants to determine absolute $\langle L_P \rangle$, $\langle S_P \rangle$ values, one has to remove the $2p \rightarrow 4s$ contribution from the measured $(\mu^+ + \mu^-)$ data while integrating the isotropic absorption spectrum in Eqs. 6.4 and 6.5. This implies that some assumption on the form of the s background has to be made. Also, the experimental absorption coefficients μ^{exp} are related to the theoretical values by

$$\mu^{exp} = C \cos^2\alpha \; \mu \, , \tag{6.6}$$

where C is the degree of circular polarization of the exciting light and α is the photon incident angle with respect to the sample magnetization direction. Moreover, in the derivation of 6.4 and 6.5, the sample magnetization is supposed to be completely saturated, which might not always be the case in an experiment.

If we consider the $\langle L_P \rangle / \langle S_P \rangle$ ratio, on the other hand, the above contributions cancel out and the comparison between theory and experiment becomes straightforward. The orbital and spin magnetic moments are related to the expectation values of the L_z, S_z operators by

$$\begin{aligned} \mu_L &= -\mu_B \langle L_z \rangle & (6.7) \\ \mu_S &= -2\mu_B \langle S_z \rangle \, , & (6.8) \end{aligned}$$

where z is the direction of the spin quantization axis. If $\langle T_P \rangle$ can be neglected with respect to $\langle S_P \rangle$, the μ_L/μ_S ratio becomes:

$$\frac{\mu_L}{\mu_S} = \frac{2}{3} \frac{A_3 - A_2}{A_3 + 2A_2} \, , \tag{6.9}$$

where the notation with $A_i \geq 0$ defined in Fig. 6.1 has been used instead of the integrals appearing in 6.4 and 6.5.

---

spin distribution in the unit cell due to the crystalline field and/or to the spin-orbit interaction [241]. Since the sp contribution to the spin density is negligible [251], the spin operator $\mathbf{S}$ can be expressed only by the sum of its d-orbital projected components: $\mathbf{S} = \sum_i \mathbf{s}_i$. In materials with lower than cubic symmetry (typically monolayers and low-dimensional structures) the d electron density deviates strongly from spherical symmetry [236,251]; due to the small spin-orbit coupling, the charge distribution is not significantly altered if the spin is rotated by an external magnetic field. As a consequence the anisotropy of the spin density is related to that of the charge density [236].

XMCD experimental setup

The XAS and XMCD measurements reported in this chapter have been conducted at the ID12B beamline [252] of the ESRF. The beamline has been especially designed for polarization-dependent x-ray absorption studies. A grating spectrometer ensures the monochromaticity of the photon beam, while either R or L circular ($C = 0.85$) polarization can be obtained by the longitudinal phasing of the undulator magnetic arrays. The sample has been prepared *in situ* in UHV conditions with the procedure described in Sec. 2. The Co coverage has been calibrated by means of a quartz microbalance. From the preparation chamber the sample could be transferred into the measurement chamber without breaking the vacuum. The base pressure in the two stages was $< 4 \times 10^{-10}$ mbar and $< 1 \times 10^{-10}$ mbar, respectively. In the XMCD chamber a cryomagnet produces a variable ±7 Tesla magnetic field collinear with the photon beam originating from the electron storage ring. The sample is inserted in the magnet bore on a variable-temperature (10 - 300 K) manipulator which can be rotated over 180° (Fig. 6.4) with respect to the incident light direction. By rotating the sample, the magnetic field **H** could be oriented either normal or parallel (70°) to the surface. The in-plane orientation of the Co wires with respect to **H** could be further adjusted prior to the sample insertion in the XMCD chamber.

The XAS spectra were taken in the electron yield (EY) mode by measuring the drain current of the photoexposed sample. All spectra have been normalized by the photocurrent emitted by a gold mesh positioned before the sample which serves as a

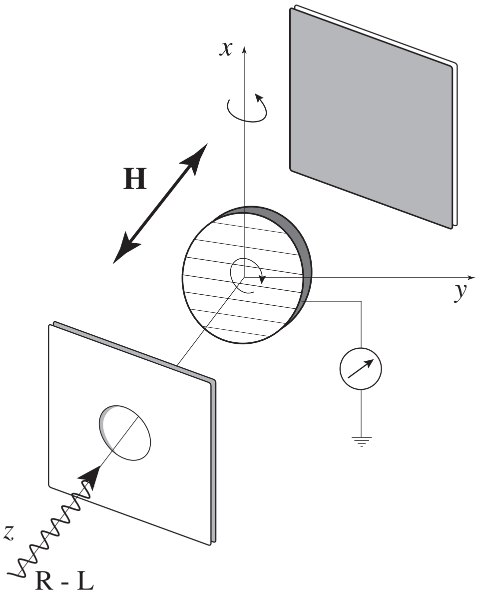

Figure 6.4: Schematic setup of the experiment at beamline ID12B, ESRF.

measure of the incident photon flux. The XMCD signal was obtained by subtraction of consecutive XAS spectra taken with reversed helicity-magnetic field orientation. Due to the very small coverage of the Co wires, the measured signal was often disturbed by a varying background. In this case the subtraction of the XAS spectra was not reliable and some data have been rejected.

6.2 Magnetism of Co monatomic wires

Introduction: magnetism in one dimension

A fundamental question arises when the dimension of structures made of bulk magnetic materials are drastically reduced in size: what type of magnetic order exists at finite temperature? The answer has far reaching consequences both on the theoretical understanding of magnetism and on magneto-recording technologies.

From a theoretical point of view, the magnetic behavior of condensed matter systems is usually described either in terms of localized moments (Heisenberg model) or in terms of itinerant electrons belonging to exchange split bands (Stoner model) [253, 254]. The Heisenberg model is particulary suited for treating the thermal properties of a magnetic system and to explain the formation of magnetic domains and the like. On the other hand, it does not take into account the delocalization of the valence electrons in a metal which is responsible, among other things, for the observed non-integer values of the magnetic moments. The itinerant or Stoner model has the advantage of being consistent with general band theory and it describes fairly well the transport properties of magnetic materials; however, dealing with states that are extended over the whole crystal, it cannot describe the spatial dependence of the magnetization. Unfortunately, neither of the two models has succeded in building a comprehensive theory of magnetic phenomena based on realistic physical assumptions. Workers in magnetism usually stick to one model or another depending on their favored perspective. That is to say that we don't know which framework is best suited to predict the magnetic behavior of our Co wires deposited on Pt. Moreover, different models lead to contradictory predictions regarding the existence of long-range magnetic order in 1D structures. Before introducing the experimental results, some of the model predictions are discussed below.

Consider first isolated (free standing) atomic chains. "The one- [and two-] dimensional isotropic Heisenberg model with interactions of finite range can be neither ferromagnetic nor antiferromagnetic at nonzero temperature." This statement was rigorously proved by Mermin and Wagner [225] for 1D and 2D spin lattices with periodic boundary conditions. As it is, it excludes any long range magnetic order for systems which can be described by the Heisenberg Hamiltonian

$$H = -\sum_{i,j} J_{ij}\mathbf{S}_i \cdot \mathbf{S}_j - g\mu_B \mathbf{H} \cdot \sum_i \mathbf{S}_i\,, \tag{6.10}$$

where i, j are lattice point labels, J_{ij} represents the exchange interaction between the spin i and j, $\mathbf{H}$ is an external field, and g is the Landé factor. However, it takes only a tiny modification of this Hamiltonian such as, e.g., the introduction of dipolar coupling or an arbitrarily small anisotropy of spin-orbit origin, to obtain a ferro- (or antiferro-) magnetic 2D system [255]. The Ising model, which can be regarded as a particular anisotropic version of Eq. 6.10, does give stable ferromagnetism in 2D, but it predicts zero magnetization at zero applied field for a 1D system. This result, which is often cited in conjunction with studies of low-dimensional magnetic structures, is actually correct only in the thermodynamic limit, i.e. for structures made of a large number of atoms. Consider a chain consisting of N spins described by the Ising Hamiltonian $H = -J\sum_{i=1}^{N-1} S_{z\,i}S_{z\,i+1}$, with $J < 0$ (ferromagnetic coupling). The ground state energy of the system is $E_0 = -J(N-1)$ and corresponds to the situation where all spins are aligned. The lowest lying excitations are those in which a single break occurs at any one of the N sites, as shown below:

$$\begin{array}{ll} \uparrow\uparrow\uparrow\uparrow\uparrow\uparrow\uparrow\uparrow\uparrow\uparrow\uparrow\uparrow\uparrow\uparrow\uparrow & \text{ground state} \\ \uparrow\uparrow\uparrow\uparrow\uparrow\uparrow\uparrow\uparrow\uparrow\downarrow\downarrow\downarrow\downarrow\downarrow\downarrow & \text{lowest excited state}\,. \end{array}$$

There are $N-1$ such excited states, all with the same energy $E = E_0 + 2J$. At temperature T the change in free energy due to these excitations is $\Delta G = 2J - k_B T \ln(N-1)$. For $N \to \infty$ we have $\Delta G < 0$ at any finite temperature T and it is clear that the ferromagnetic (ground) state becomes unstable against thermal excitations. For $(N-1) < \mathrm{e}^{2J/k_B T}$, however, the argument does not hold any more.

At this point one could argue that considering the magnetic moments as being localized at lattice sites is not a correct microscopic description of the system. The spin and orbital magnetic moments -which add up to give the atomic magnetic moment- cannot be considered as point vectors. Rather, they should be treated as distributions of spin and charge density varying across the unit cell. This can be done in the framework of band theory, but a word of care should be spent here. Two famous theorems [256, 257] forbid the existence of magnetic ordering for a system of N electrons described by 1D or 2D Bloch states interacting through the Coulomb and exchange interactions. As pointed out by Freeman [222], however, these theorems cannot be applied to real atoms arranged in 1D or 2D lattice structures. Real atoms, in fact, are 3D objects and so are the spin and charge distributions, no matter the dimensionality of the lattice. Indeed, local spin density calculations [222] carried out in 3D space for arrays of monatomic Ni and Fe chains show that these structures are ferromagnetic at 0 K. Moreover, they are characterized by large values of the exchange splitting (see Sec. 5) and of the magnetic moments compared to bulk systems (1.07 μ_B *vs* 0.6 μ_B for Ni, 3.36 μ_B *vs* 2.2 μ_B for Fe, and 2.2 μ_B *vs* 1.7 μ_B for Co). Given that the exchange interaction is short ranged, such results are not expected to show a strong dependence on the chain length.

So far for the free standing wires. In the experiments, however, we can only deal with wires deposited onto a surface. The redistribution of the electron density due to hybridization with the substrate can lead to substantial changes in the magnetic behavior of the supported wires. To take into account these effects the Heisenberg model is certainly inadequate, and state of the art *ab initio* calculations [223] are expected to give more reliable results which can be compared with the experiments. Pastor and Dorantes-Dávila [258] have calculated in a tight-binding approach that one of the major effects due to the presence of a metallic substrate is on the magnetic anisotropy of the wires. Their results predict a strong magnetic anisotropy reduction (from 10 to 1 meV/atom) in passing from free-standing wires to Pd(110)-supported wires, accompanied by a rotation of the easy axis of magnetization from the longitudinal to the transverse direction perpendicular to the substrate. In experiments similar to ours, where a magnetic material is deposited onto a non-magnetic stepped substrate, coupling between adjacent stripes and/or with the substrate gives rise to different magnetic behaviors. Fe stripes formed by connected triangular-shaped islands on a stepped Cu(111) surface exhibit a pronounced temperature- and time-dependent magnetic behavior and out-of-plane anisotropy [100, 259], while Fe stripes more than 20 atoms wide on vicinal W(110) show a relaxation-free magnetization with in-plane easy axis across the stripes and ferromagnetic coupling between adjacent stripes [98, 260]. None of these studies, however, has addressed the monatomic chain limit.

Co wires magnetization *vs* applied field

The investigation of the magnetism of the Co chains is based on the dichroism effects at the Co $L_{3,2}$ absorption edges. Figure 6.5 shows the μ^+ and μ^- absorption spectra and relative dichroic signal for an array of Co monatomic chains on Pt(997) deposited at 275 K. The intensity of the Co signal is considerably reduced with respect to the 15 ML Co film shown in Fig. 6.1. The Co $L_{3,2}$ edges are superimposed onto a strong background due to the EXAFS (extended x-ray absorption fine structure) oscillations following the Pt $N_{3,2}$ threshold. As the substrate structures do not present a dichroic effect, they are cancelled out by taking the difference between the two spectra for oppositely polarized

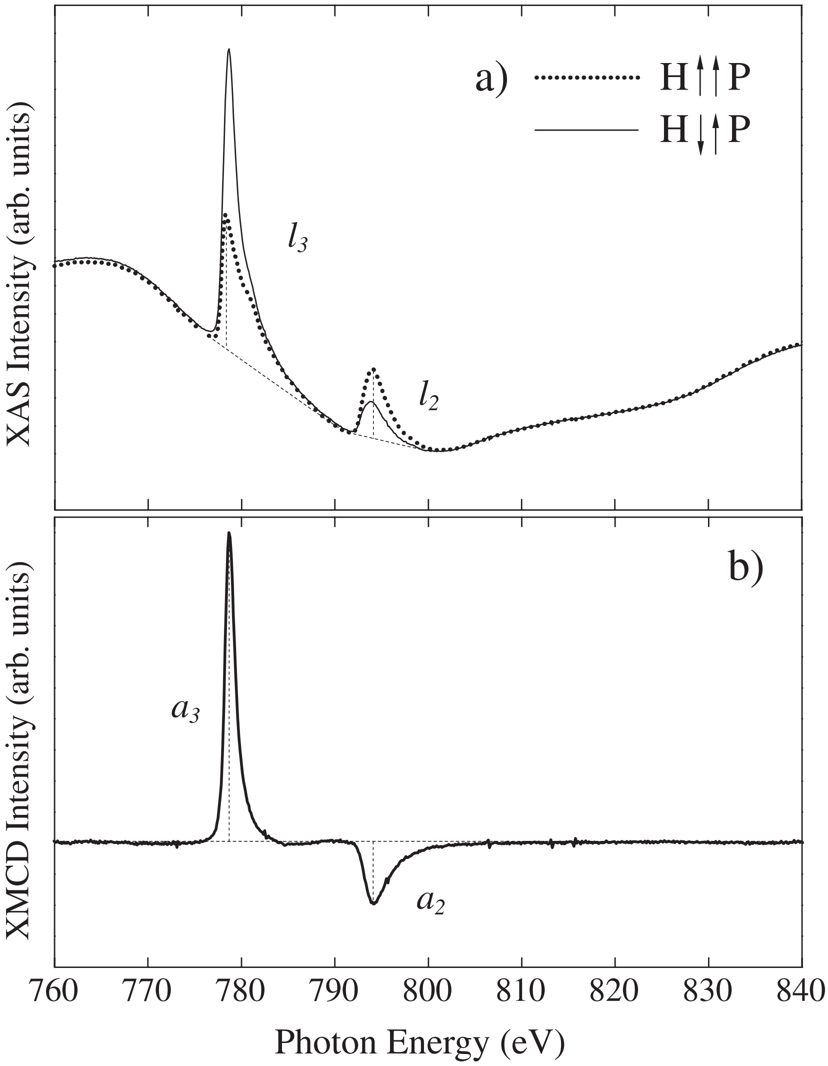

Figure 6.5: (a) Co x-ray absorption spectra for parallel (dotted line) and antiparallel (solid line) alignment of the light polarization **P** and **H**-field induced magnetization perpendicular to the surface. The measurements were performed at $T = 8\ K$ in a 7 Tesla magnetic field for ~ 0.13 ML Co coverage. (b) Dichroism signal obtained by subtraction of the absorption spectra shown above.

radiation. The magnitude of the dichroic signal is essentially proportional to the magnetization **M** of the Co atoms on the surface (see Sec. 6.1). A linear combination of the A_3, A_2 areas or of the L_3, L_2 peak intensities is usually taken in the literature as a measure of **M**. Here we take a linear combination of the peak intensities of the μ^+ and μ^- absorption spectra, $l_3^\pm$ and $l_2^\pm$, after the subtraction of a linearly interpolated background:

$$M \propto \frac{(l_3^+ - l_3^-) - (l_2^+ - l_2^-)}{l_3^+ + l_3^- + l_2^+ + l_2^-}\,. \tag{6.11}$$

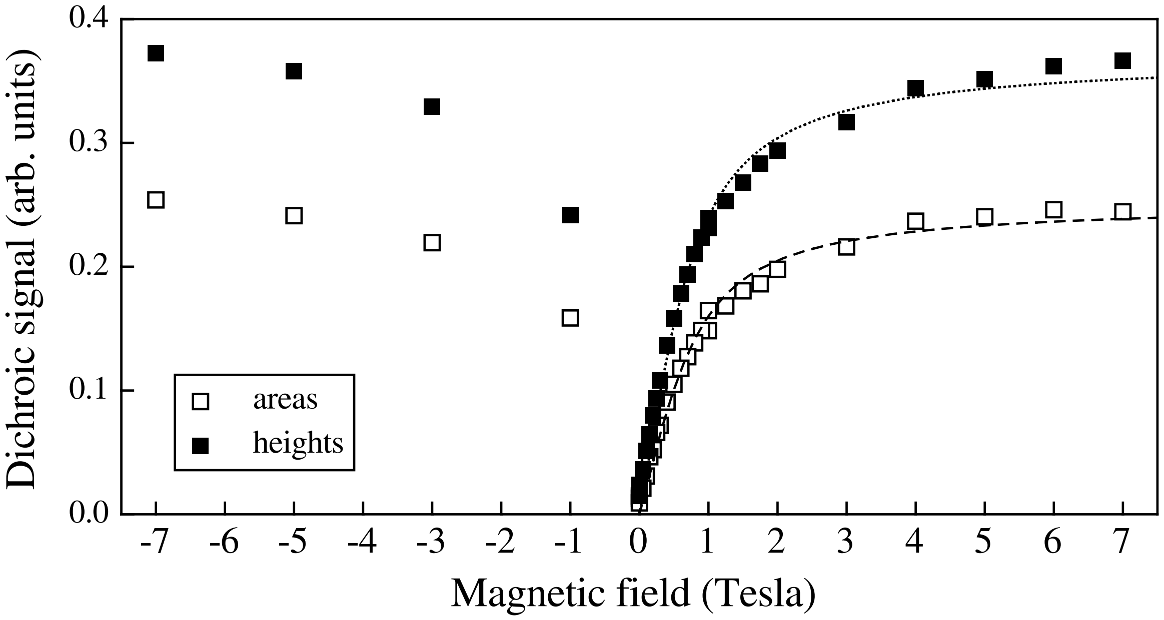

Figure 6.6: (a) Dichroic signal as a function of the applied magnetic field in the direction perpendicular to the Pt(997) surface for 0.13 ML Co at 10 K. The data sets are calculated by taking the peak intensities (■) and the peak areas (□).

The l values are taken after renormalization of the μ^+, μ^- spectra at a common background value around 775 eV. This correction is usually small, as shown by the non-renormalized spectra reported in Fig. 6.5, but it is sometimes necessary to account for fluctuations of the x-rays intensity. The values of the dichroic signal calculated with Eq. 6.11 for a series of spectra relative to 0.13 ML Co at 10 K are shown in Fig. 6.6. For each value of the magnetic field we have switched from R to L polarization and recorded a full spectrum. Full and open squares correspond to the dichroic signal calculated from the peak intensities $l_{3,2}$ and from the peak areas after subtraction of the linear background shown in Fig. 6.5(a). A Langevin fit (lines) shows that, besides a proportionality factor, the two data sets differ only by 3 % of the fitting parameter. The experimental curve shows a gradual increase of the magnetization with increasing field strength and absence of magnetization in field-free conditions (see also Fig. 6.7). At the largest applied field the saturation of the dichroic signal indicates that the Co moments are basically aligned along the field directions and thus give evidence for a significant (ferro)-magnetic coupling between the atomic moments. As discussed below, for non-interacting paramagnetic moments the magnetization expected in the present experimental conditions would be significantly smaller. The observed behavior is therefore qualitatively analogous to the one of a superparamagnetic system above the blocking temperature, characterized by a sizable magnetization at high field and low magnetic

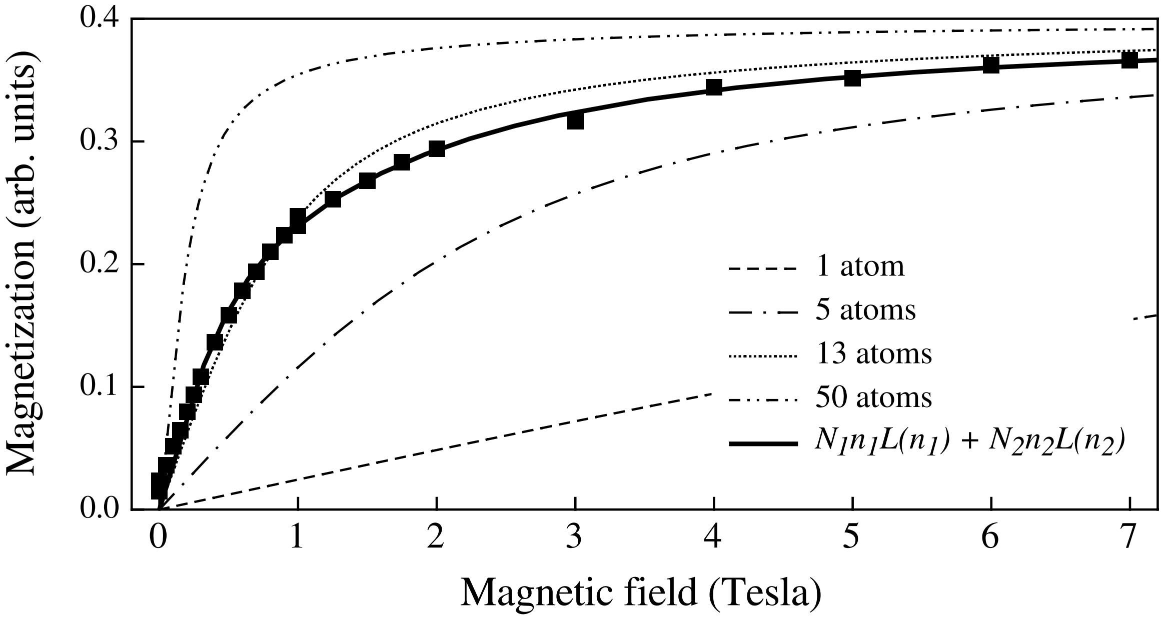

Figure 6.7: Superparamagnetic response of an array of monatomic Co wires at 10 K to a magnetic field (■) in comparison with the response of 1, 5, 13, and 50 atom ensembles modelled with a Langevin function (dashed and dotted lines). The solid line is a fit with two Langevin functions.

susceptibility. A superparamagnetic ensemble is constituted by particles whose atoms are ferromagnetically coupled, but whose total magnetic moments do not have a fixed direction in space due to random thermal fluctuations. The macroscopic behavior of the system is that of a paramagnet except for the values of the particle moments which are much larger than those measured in paramagnetic systems. Below the so-called blocking temperature the particle momentum cannot fluctuate anymore and the system behaves like a ferromagnet. Over the whole temperature range investigated in this work (10 - 300 K) the Co wire ensemble displays a superparamagnetic behavior, showing that the blocking temperature for such a system is lower than 10 K. Assuming a Langevin function to describe the superparamagnetic behavior of the monatomic wires, an average size of the superparamagnetic spin-blocks corresponding to $n \sim$ 10-15 Co atoms can be estimated from the curves in Fig. 6.7. These values are calculated assuming the magnetic moment per Co atom to be $\mu = 2.2\ \mu_B$, as extimated in Refs. [222] and [223] for Co monatomic chains. If we take $\mu = 1.7\ \mu_B$ as in bulk Co then n becomes ~ 20. Linear combinations of the $l_{3,2}^{\pm}$ data different from Eq. 6.11 yield identical results. We point out, however, that the n value is not directly related to the average length of the Co wires, which is unknown. A better fit of the data can be obtained considering a distribution of wires having different lengths. The solid line in Fig. 6.7 is a fit obtained with the sum of two Langevin functions:

$$M \propto N_1 n_1 L(n_1 \mu H/K_B T) + N_2 n_2 L(n_2 \mu H/K_B T)\,, \tag{6.12}$$

where N_i is the density of wires consisting of n_i atoms, and $N_2 = 1 - N_1$. The fitted values N_1, n_1, and n_2 in this case are not independent from each other and hence they have little physical meaning. Nonetheless the fit shows that realistic models of the system should consider a size distribution of the wires. This fact can have significant consequences for the dependence of the magnetization on the sample temperature: long wires might have a higher blocking temperature than short wires and also the *intra*-wire Curie temperature could be size-dependent. Further experiments are programmed to investigate this point.

Interactions between the wires, either of dipolar origin or mediated by the substrate, cannot be excluded in principle. It is well known that diluted alloys of Pt and Pd with the magnetic $3d$ elements present “giant” moments, due to the induced polarization of the non-magnetic host [261]. Also, a weak moment is induced in the Pt interface layers in Pt/Co film structures [91]. The present results, however, do not give direct evidence for coupling effects between the wires, although the size of the paramagnetic spin blocks might represent the interacting moments both within and among Co wires and also on Pt sites. Actually the anisotropic superparamagnetic response of the system, which favors a magnetization perpendicular to the monatomic wire axis (see Sec. 6.3), indicates that the magneto-crystalline anisotropy prevails over the dipole-dipole interactions within and among the quantum wires.

6.3 Magnetic anisotropy

The magnetic anisotropy energy (MAE) is the change in the free energy of a crystal which is due to the rotation of the magnetization. Although small compared to the exchange interaction (typically $10^{-5} - 10^{-6}$ *vs* 1 eV/atom in bulk Co, Fe, Ni), the MAE plays a fundamental role in determining the properties of ferromagnets. The exchange interaction is invariant under a rotation of the quantization axis of the spin, i.e. it is totally isotropic. Without anisotropy, all ferromagnets will just behave as superparamagnets. The MAE determines the preferred orientation and the stability of the magnetization of ferromagnetic single domain particles. Thus the understanding of the magnetic anisotropy is both of scientific and technological importance.

Generally the MAE consists of two contributions: the *shape* anisotropy [254], due to the magnetostatic *self-energy* originating from the classical interaction among magnetic dipoles, and the *magnetocrystalline* anisotropy, due to the spin-orbit interaction. The latter couples the isotropic spin moment to the orbital motion of the electrons, which is related to the lattice structure of the material.[3] From a phenomenological point of view, the MAE for a uniaxial system is usually expressed as $E_a = -K \cos^2\theta$, where θ denotes the angle between the magnetization direction and the principal axis of the system, and K is an effective anisotropy constant defined in J/m^3 or eV/atom. For low-dimensional structures such as thin films and layered systems, it is customary to distinguish between volume anisotropy (K_v), and surface or interface anisotropy (K_s/t, where t is the thickness of the magnetic layer), which contains all the thickness dependent contributions:

$$K = K_v + K_s/t\,. \tag{6.13}$$

For a Pt-capped Co film on Pt(111) McGee *et al.* [88] have measured $K_v = -5.3 \times 10^{-5}$ eV/atom and $K_s = 4.8 \times 10^{-4}$ eV/atom. Between 6 and 8 Co ML the easy axis turns from perpendicular to in-plane [88, 262], as expected from Eq. 6.13, since K_v and K_s have opposite sign. Already from an approximate relation as Eq. 6.13 one can see that the size and dimensionality of a magnetic system can have a drastic influence on the magnitude of the MAE and on the preferred direction of the magnetization. In fact, the ability to grow thin epitaxial films has led to materials with novel magnetic properties which can be tailored by an appropriate choice of thickness, substrate-overlayer elements, degree of intermixing, and other factors.

In the low thickness limit ($t \leq 10$ ML), Co/X(111) layered structures (X = Pt [88, 262], Pd [85], Au [95, 232], Cu [95]) all display perpendicular anisotropy. At larger t the easy axis turns in-plane because the shape anisotropy (which is proportional to the film volume) overcomes the magnetocrystalline contribution. The phenomenological picture, however, is not so clear cut. Co-Pt multilayers grown on (100), (110), and (111) Pt substrates have different orientations of the easy axis [87]; (111) $CoPt_3$ thin films display either a perpendicular magnetic anisotropy or almost no anisotropy depending on the local chemical composition of the layers [263]. For the Co/Cu system the presence of surface steps causes the easy axis to be in-plane in the direction parallel to the step edges [264]. Decoration of the step edges with Cu atoms leads to a 90° switch of the easy axis [265]. Fe films on stepped Pd [266] and Ag [267] surfaces reveal a uniaxial anisotropy with the easy axis perpendicular and parallel to the step edges, respectively, indicating that substrate-overlayer hybridization has a large influence on the MAE. Two

---

[3] *Magnetoelastic* effects are also included in this term since they are essentially due to strain-induced modifications of the magnetocrystalline anisotropy.

things emerge from the studies mentioned above: first, the magnetic anisotropy is largely dependent on the structural (size, dimensionality, roughness, strain) and chemical (e.g. Co-X bonding) details of a given system; second, the separation of such contributions is still controversial. It is clear that the global approach represented by Eq. 6.13 does not allow to make much progress in this direction and that we need a more detailed microscopic description.

The shape anisotropy is fairly well understood both in its origins and in its consequences [254, 268, 269]. Although it is of primary importance in determining, e.g., the formation of magnetic domains, estimates of its contribution [255, 270–272] show that this term is several orders of magnitude too small to explain most of the experimental results on low dimensional magnetic structures, and that the magnetocristalline anisotropy (MCA) is apparently dominant. From now on, we restrict our description to the MCA, neglecting other contributions to the MAE. Calculations of the MCA are very demanding since they require the subtraction of two large numbers, in the order of eV for the total energies of the different magnetization directions, to obtain energies of the order of $10^{-4}-10^{-6}$ eV. Moreover, correlation between theory and experiments is often hampered by the lack of a precise correspondance between the atomic scale structure of the model systems and the real ones. One way out of this conundrum is to study low-dimensional magnetic structures with a well defined symmetry and in a fully characterized atomic environment. As will be discussed below, thin films and magnetic nanostructures show an enhancement of the MCA up to $10^{-4} - 10^{-2}$ eV/atom [88, 232, 273]; comparison between theory and experiment becomes possible since this energy range is nowadays within the accuracy of *ab initio* electronic structure calculations [251,258,274–276]. The investigation of the magnetic anisotropy of structures made of very few atoms arranged in 1D chains is therefore expected to shed further light on the subject and to lead to a direct comparison with theoretical models [223, 258].

Magnetocrystalline anisotropy in low-dimensional structures

The physical origins of the magnetocrystalline anisotropy are still largely debated by theoreticians [251, 258, 274, 275, 277–279] and constitute an expanding experimental research field [236]. The idea that the MCA originates from the spin-orbit interaction is due to van Vleck [280] and dates back more than 60 years ago. Only recently, though, Bruno [277] has put the basis for a perturbative treatment of the spin-orbit coupling which allows to derive the anisotropy constants from the unperturbed tight binding band structure. This treatment has the advantage of providing intuitive physical insights over *ab initio* methods and will be briefly outlined here in addition with some further developments [236, 279]. The reason to do so is to motivate our XMCD experiments and to provide a unitary context in which our results can be interpreted.

Let's start by supposing that the origin of the magnetocristalline interaction is entirely due to the spin-orbit interaction (SO)

$$H_{so} = \xi \, \mathbf{S} \cdot \mathbf{L} \,, \tag{6.14}$$

where ξ is the spin-orbit constant.[4] Since for $3d$ transition metals ξ is between 30 and 80 meV [279,281], which is small compared to the d bandwidth of a few eV, we can treat Eq. 6.14 as a perturbation of the Hamiltonian that describes the $3d$ electron states. The anisotropy energy is then given by

$$E_a = E_{so}(\hat{\mathbf{S}}_z) - E_{so}(\hat{\mathbf{S}}_x) = \Delta E_{so} \,, \tag{6.15}$$

where $E_{so}(\hat{\mathbf{S}})$ represents the spin-orbit correction to the unperturbed Hamiltonian for a given direction $\hat{\mathbf{S}}$ of the magnetization. For parity reasons the lowest-order contribution to the SO induced change in the total energy is second order:

$$E_{so}(\hat{\mathbf{S}}) = \xi^2 \sum_{o,u} \frac{|\langle o|\mathrm{S}\hat{\mathbf{S}} \cdot \mathbf{L}|u\rangle|^2}{\epsilon_o - \epsilon_u} \,, \tag{6.16}$$

where o and u represent occupied and unoccupied states, respectively. For the limiting case of strong exchange splitting (which is a good approximation for Co), we may consider that the spin-up band is almost fully occupied, and all empty states belong to the spin-down band, as in Fig. 6.8. We can thus exclude the effects of the empty spin-up states in Eq 6.16, obtaining

$$E_{so}(\hat{\mathbf{S}}) \approx E_{so}^{\downarrow\downarrow}(\hat{\mathbf{S}}) + E_{so}^{\uparrow\downarrow}(\hat{\mathbf{S}}) \,, \tag{6.17}$$

where

$$E_{so}^{\downarrow\downarrow}(\hat{\mathbf{S}}) = \frac{\xi^2}{4} \sum_{o^\downarrow, u^\downarrow} \frac{|\langle o^\downarrow|\mathbf{S} \cdot \mathbf{L}|u^\downarrow\rangle|^2}{\epsilon_{o^\downarrow} - \epsilon_{u^\downarrow}} \,, \tag{6.18}$$

$$E_{so}^{\uparrow\downarrow}(\hat{\mathbf{S}}) = \frac{\xi^2}{4} \sum_{o^\uparrow, u^\downarrow} \frac{|\langle o^\uparrow|\mathbf{S} \cdot \mathbf{L}|u^\downarrow\rangle|^2}{\epsilon_{o^\uparrow} - \epsilon_{u^\downarrow}} \,, \tag{6.19}$$

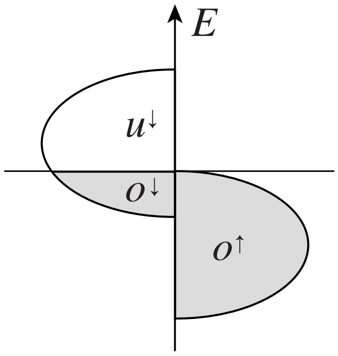

Figure 6.8: Schematic representation of a strong ferromagnet.

---

[4] The spin-orbit is a localized interaction: ξ depends on the variation of the potential near the nucleus and does not vary much considering a free atom or a solid.

and $o^{\downarrow}$ ($u^{\downarrow}$), $o^{\uparrow}$ ($u^{\uparrow}$) represent occupied (empty) majority and minority spin states. It can be shown [274] that the terms $\Delta E_{so}^{\downarrow\downarrow}$ and $\Delta E_{so}^{\uparrow\downarrow}$ derived by Eqs. 6.15 and 6.17 have opposite sign. However, the spin-flip contribution $\Delta E_{so}^{\uparrow\downarrow}$ is one order of magnitude smaller than $\Delta E_{so}^{\downarrow\downarrow}$ in $3d$ metals due to the large exchange splitting ($\Delta_{ex} \approx \epsilon_{u^{\downarrow}} - \epsilon_{o^{\uparrow}} \approx$ 3 eV) [274, 279], and it will be neglected in the following. Within this approximation the anisotropy energy 6.15 reads

$$E_a = E_{so}^{\downarrow\downarrow}(\hat{\mathbf{S}}_z) - E_{so}^{\downarrow\downarrow}(\hat{\mathbf{S}}_x) = \frac{\xi^2}{4} \sum_{o^{\downarrow},u^{\downarrow}} \frac{|\langle o^{\downarrow}|L_z|u^{\downarrow}\rangle|^2 - |\langle o^{\downarrow}|L_x|u^{\downarrow}\rangle|^2}{\epsilon_{o^{\downarrow}} - \epsilon_{u^{\downarrow}}} . \tag{6.20}$$

The MCA depends on the number of spin-down electrons (band filling) because of the sum over the $o^{\downarrow}$ and $u^{\downarrow}$ states, on the orbital character of the occupied states, on their coupling with the empty states through the orbital momentum operator, and on the minority spin bandwidth ($\epsilon_{o^{\downarrow}} - \epsilon_{u^{\downarrow}}$). It is easy to recognize in the above expression the expectation values of the orbital momentum $\langle L \rangle$ in the directions x and z given by first-order perturbation theory [277]:

$$\langle L_{x,z} \rangle = \sum_{o,u} \langle o|L_{x,z}|u\rangle \frac{\langle u|H_{so}|o\rangle}{\epsilon_o - \epsilon_u} \quad + \ c.c. \ . \tag{6.21}$$

Note that the $\langle L \rangle = 0$ for the filled spin-up band, therefore the sum in Eq. 6.21 is restricted to spin-down states. By substituting the expression for $\langle L \rangle$ into Eq. 6.20 we obtain the fundamental result

$$E_a = \frac{\xi}{4}(\langle L_z \rangle - \langle L_x \rangle) = \frac{\xi}{4\mu_B}(\mu_L^x - \mu_L^z) , \tag{6.22}$$

where μ_L^x and μ_L^z represent the projection of the orbital magnetic moment in the x and z directions, respectively. The spin-orbit energy anisotropy is therefore proportional to the orbital momentum anisotropy of the minority band.[5] The easy magnetization direction is given as the direction with the largest component of **L**. In transition metals, the orbital momentum is determined by the interplay of the spin-orbit coupling with the much stronger crystalline field interaction. As a consequence, we obtain different values of **L** if the spins are oriented along different crystal directions by a strong external magnetic field. The relationship between the orbital momentum and the MCA has been verified experimentally by Weller *et al* [232] and by Dürr *et al* [273]. A few remarks might help to understand the physical basis of Eq. 6.22. In the presence of an external magnetic field applied in a direction other than the easy axis, the spins will tend to

---

[5] The extension of the theory to the general case of a partially filled majority band is reported in Refs. [279] and [236]; van der Laan [279] has also shown that the spin-flip term $\Delta E_{so}^{\uparrow\downarrow}$ is related to the expectation value of the magnetic dipole operator **T** defined in Sec. 6.1.

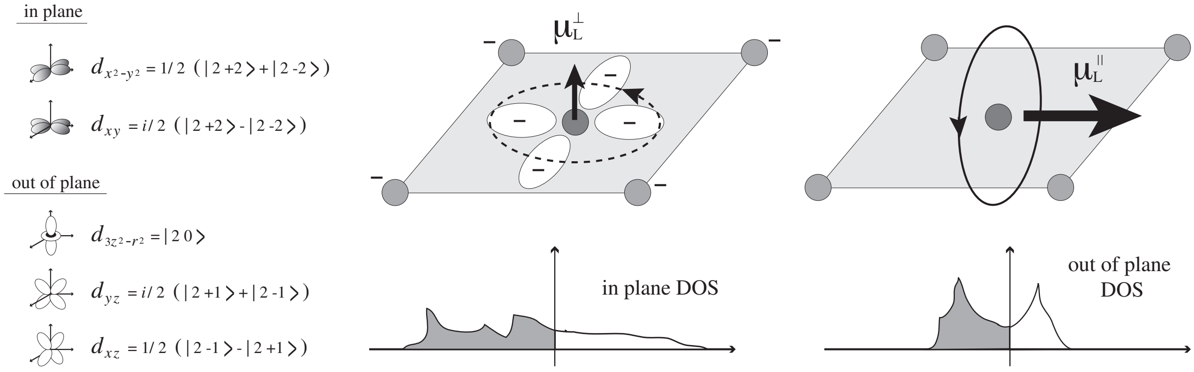

Figure 6.9: (a) Directional quenching of the orbital momentum of an atom in a monolayer film. (b) In-plane and out-of-plane d orbitals. (c) Projected densities of states. Adapted from Ref. [236]

follow the external field. The rotation of the orbital magnetic moment, on the other hand, is partially counteracted by the crystal field, which pulls μ_L towards the easy axis. Because of the spin-orbit interaction which couples μ_S to μ_L, the rotation of the spin will also be affected. Hence, the energy that is necessary to turn the overall magnetization (which is mainly due to μ_S) is proportional, through the spin-orbit constant, to the difference of the orbital magnetic moments that "pull" the spins along and away from the easy axis.

A further point remains to be elucidated: the MCA has been calculated as a second order perturbation due to the spin-orbit interaction. Why second order? In fact, in Eq. 6.22 ξ appears only in first order. The point is that the spin-orbit interaction is also responsible for the non zero expectation values of the orbital momentum operator $\mathbf{L}$ in Eq. 6.21; in other words, there would be no net orbital momentum without the spin-orbit interaction. This is easy to understand in 3D cubic crystals: the electronic states created by the crystal field alone (the $d_{x^2-y^2}$, $d_{3z^2-r^2}$, d_{xy}, d_{xz}, and d_{zy} states shown in Fig. 6.9) possess no orbital momentum, since all d orbitals have a perfect balance of $\pm m_l$ contributions. The m_l balance is broken by the spin-orbit interaction which mixes different d orbitals in a way to produce a non zero angular momentum. Since this momentum is small, the MCA is correspondingly small, the order of 10^{-6} eV/atom. It is also intuitive from Eq. 6.22 that a high symmetry environment does not favor the MCA. In low-dimensional systems such as thin films and small clusters, however, the orbital momentum is not quenched by the crystal field as in cubic systems. Its direction is determined by the particular symmetry of the system; however, in the absence of a long range interaction, the orientation of the single moments is free to fluctuate and the net orbital momentum of the system is zero. It is the spin-orbit interaction which defines, via the long-range exchange interaction carried by the spin, a common orientation for all the atomic orbital moments.

From the above it is also clear that low dimensional structures should have larger μ_L values with respect to bulk crystals. Enhanced orbital moments have in fact been observed with XMCD for Co films on Cu(100) [234], for Co clusters on Au(111) [235] and in a number of other systems [282]. Larger values of the MCA are also expected: asymmetric bonding configurations will result in an anisotropic d electron distribution and correspondingly in a marked anisotropy of the orbital momentum. As an example, consider the case of a free-standing Co monolayer shown in Fig. 6.9. Asymmetric bonds result in different in-plane and out-of-plane bandwidths, $W^{||}$ and $W^{\perp}$, respectively. Because the orbital momentum direction is perpendicular to the plane of the orbiting electrons, the in-plane momentum is determined by the out-of-plane orbitals and their bandwidth, and viceversa. According to the perturbative model described above we have therefore $\mu_L^{||} \propto \xi / W^{\perp}$, and $\mu_L^{\perp} \propto \xi / W^{||}$.

Magnetic anisotropy of the Co wires

Co monatomic chains, because of their peculiar symmetry, constitute a very promising model system for the study of the magnetocrystalline anisotropy. In order to make contact between theory and experiment, we start by applying the results derived in the previous paragraph to a diatomic molecule made of $3d$ atoms. This is the simplest model that we can use to approximate 1D atomic chains. The model presented here has been first proposed by Wang *et al.* [274]. Consider two identical d atoms: the d orbitals can be equivalently described by $|l = 2, m_l\rangle$ states or by appropriate linear combinations of the latter, such as those shown in Fig. 6.9. When the two atoms are brought together the hybridization of their d-electron orbitals leads to the formation of various bonding and antibonding states. Only the spin-down states are shown in Fig. 6.10, the spin-up states are assumed to be filled. If z is assumed as the molecular axis, the strongest interaction, denoted V_σ, would be given by the superposition of the two $3z^2 - r^2$ orbitals. This gives the lowest bonding and the highest antibonding states separated by $2|V_\sigma|$. The weakest interaction, V_δ, forms two doubly degenerate δ-bonding and antibonding states with the smallest separation, $2|V_\delta|$. Similarly, there are also two degenerate π orbitals. When the spin-orbit coupling is switched on, these states mix with each other assuming a net orbital momentum oriented parallel (for more than a half-filled d band) to the spin. The magnitude of this orbital momentum depends on the direction of the magnetization with respect to the symmetry axis of the molecule and on the filling of the perturbed orbitals. To calculate the MCA of this system we make use of Eq. 6.20. Due to the symmetry

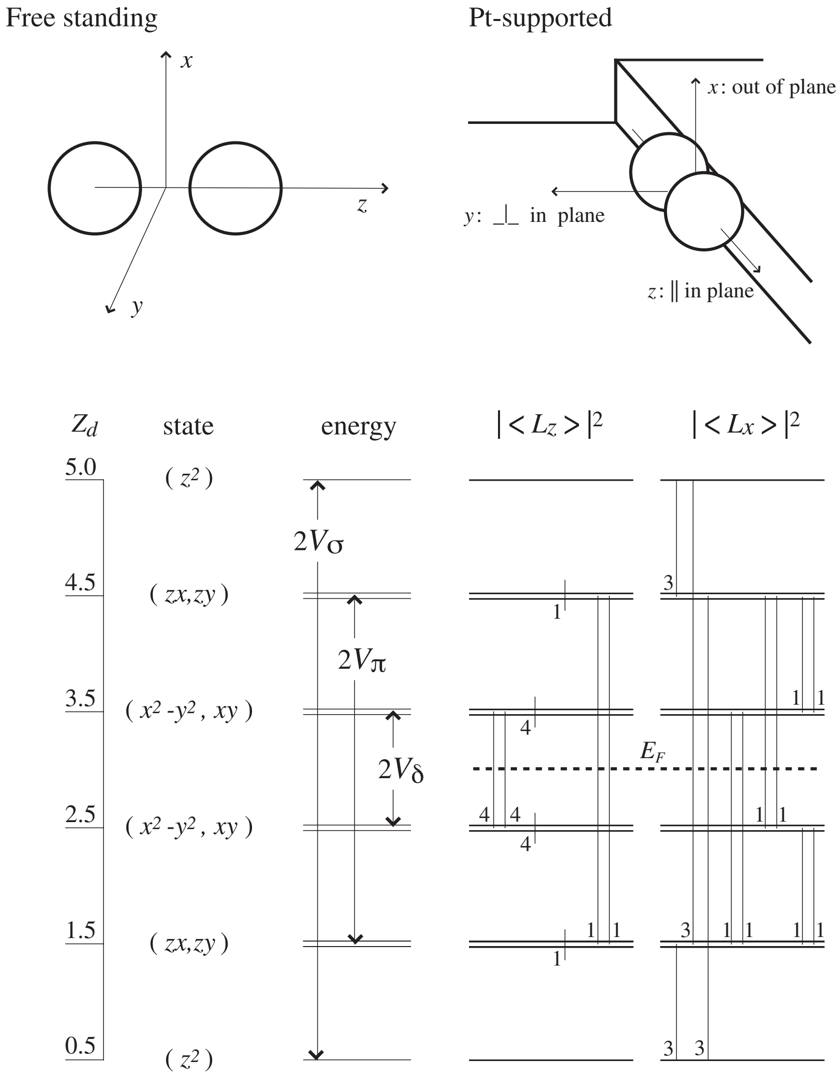

Figure 6.10: Diatomic pair model: d states formed by the hybridization of the atomic levels. The crystal field splitting corresponds to that of a free standing molecule. The non-vanishing angular momentum square matrix elements between the d levels are represented by the numbers beside the corresponding vertical lines. Z_d is the number of spin down electrons when the corresponding levels are occupied. Adapted from Ref. [274]

of the atomic orbitals, only a few angular momentum matrix elements between the d orbitals are non zero, as listed in Table 6.2. The vertical lines in Fig. 6.10 represent the correspondent coupled states. Double lines between degenerate states mean two non-vanishing matrix elements. In the energy (or orbital momentum) calculation we only need to count those lines (matrix elements) which are between occupied and empty states, i.e., those that are intersected by the Fermi level in Fig. 6.10. It is then evident that the charge filling of the minority band determines the relative amplitudes of $\langle L_z \rangle$ *vs* $\langle L_x \rangle$. Our diatomic molecule has 10 $d^{\downarrow}$ electrons. If we take a half filled minority

Matrix elements	$\langle L_z\rangle$		$\langle L_x\rangle$		$\langle L_y\rangle$
$\langle xz\vert L_z\vert yz\rangle$	1	$\langle z^2\vert L_x\vert yz\rangle$	$\sqrt{3}$	$\langle z^2\vert L_y\vert xz\rangle$	$\sqrt{3}$
$\langle x^2-y^2\vert L_z\vert xy\rangle$	2	$\langle xy\vert L_x\vert xz\rangle$	1	$\langle xy\vert L_y\vert yz\rangle$	1
		$\langle x^2-y^2\vert L_x\vert yz\rangle$	1	$\langle x^2-y^2\vert L_y\vert xz\rangle$	1

Table 6.2: Non vanishing angular momentum matrix elements between d states.

spin band as it seems appropriate for Co [244], this corresponds to a charge filling per atom $Z_d = 2.5$. We can now calculate the spin-orbit energy 6.20 for the magnetization perpendicular and parallel to the diatomic pair axis, $E_{so}(x)$ and $E_{so}(z)$, respectively. We obtain:

$$\begin{array}{cc} E_{so}(x) & E_{so}(z) \\ \text{Perpendicular to chain axis} & \text{parallel to chain axis} \\ -\dfrac{\xi^2}{4}\Big(\dfrac{4}{V_\pi+V_\delta}+\dfrac{6}{V_\sigma+V_\pi}\Big) & -\dfrac{\xi^2}{4}\Big(\dfrac{4}{V_\delta}+\dfrac{1}{V_\pi}\Big)\,. \end{array} \tag{6.23}$$

For a free standing diatomic pair (or monatomic chain) it is generally true that $|V_\sigma| > |V_\pi| > |V_\delta|$ because of the angular distribution of the atomic orbitals which determine the extent of the overlap. This means that $E_{so}(z) < E_{so}(x)$ and the magnetic moment will prefer to lie along the pair axis.

Look now at what happens if we deposit the diatomic Co molecule at the base of a Pt step. The Co $3d$ and Pt $5d$ bands are superposed in energy and hence they can hybridize. Hybridization is stronger for the Co orbitals pointing towards Pt atoms, i.e. for the orbitals that are extended in the x and y directions. If the Co-Co bonding strength is normalized to 1, then the corresponding Co-Pt bonding strength has been calculated to be 1.6 [283]. Opposite to the free standing case, the perpendicular bandwidth in the direction perpendicular to the diatomic pair axis becomes larger than the bandwidth in the parallel direction. Hence we have a situation where $|V_\pi| \approx |V_\delta| > |V_\sigma|$. This time Eq. 6.24 yields $E_{so}(x)$, $E_{so}(x), < E_{so}(z)$ and the easy axis is redirected in the direction perpendicular to the diatomic pair axis. This prediction, derived on the basis of a rather simplified model, is actually verified for the Co monatomic chains on Pt(997) by the measurements reported in Fig. 6.11. The peculiar symmetry of the Co chains turns out to be remarkably manifested by the anisotropy of the superparamagnetic response. Figure 6.11 shows a noticeable dependence of the induced magnetization of the 1D Co wires on the direction of the applied field. A field perpendicularly aligned to the monatomic wire induces a larger magnetization than a field parallelly oriented

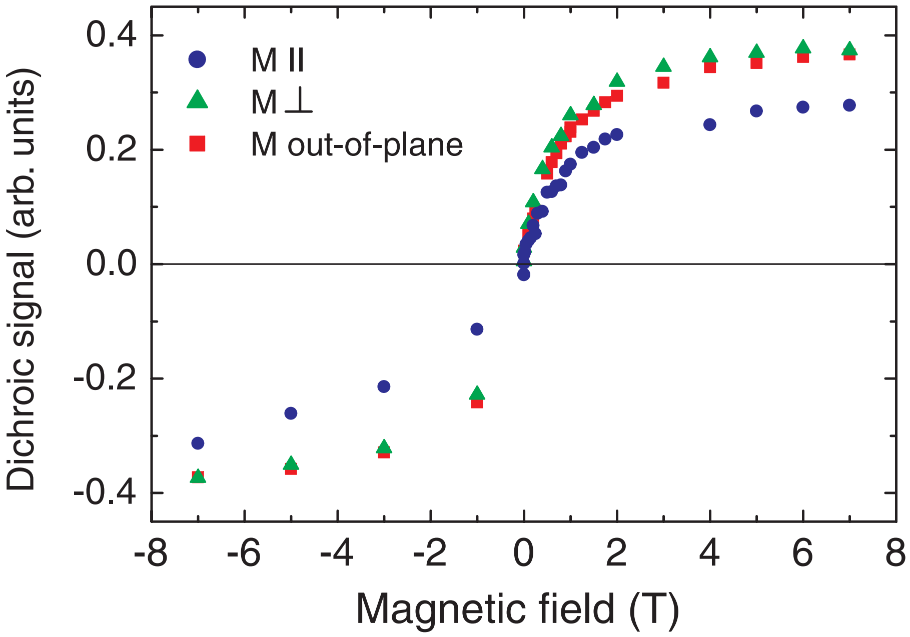

Figure 6.11: Dichroic signal measured at 10 K for a Co monatomic wire array as a function of the applied field in the directions parallel and perpendicular to the wire axis. The amplitude of the dichroic signal is given by Eq. 6.11.

to the wire axis, while only a weak difference distinguishes the two (i.e. in-plane and out-of-plane) directions perpendicular to the wire axis. Using a simple paramagnetic model for describing the magnetization dependence on the field and its direction one can obtain an estimate for the sign and magnitude of the magnetic anisotropy from the curves in Fig. 6.11. The resulting value of $\sim 10^{-3}$ eV/atom is in good agreement with tight-binding calculations for supported monatomic Co wires [258, 278].

Note that the curve measured parallel to the wire axis seems to saturate at a lower value compared to the other two. This suggests the magnetic moment per atom is different in the direction parallel and perpendicular to the wire axis. Since in $3d$ transition metals the anisotropy of the spin magnetic momentum is small compared to that of the orbital momentum [279], this difference can be largely attributed to the orbital part of the magnetization. As discussed in Sec. 6.1, by changing the direction of the incident photon beam with respect to the sample, we can measure the projection of $\boldsymbol{\mu}_L$ perpendicular and parallel to the wires (Eq. 6.4). To simplify the analysis of the data we actually measure the ratio μ_L/μ_S given by Eq. 6.9. Our measurements give $\mu_L/\mu_S = 0.14$ and 0.28 in the out of plane and in plane parallel direction, respectively. These values should be taken with caution because the integration of the L_3, L_2 intensities is heavily dependent on background fluctuations for the coverage corresponding to the monatomic wires. We can however get an order of magnitude for the MCA by means of Eq. 6.22.[6] Taking $\mu_S = 1.86\ \mu_B$ and $\xi = 50$ meV [251,281], the MCA results to be $\sim 7 \times 10^{-4}$ eV.

A contribution to the perpendicular MCA measured for the Co/Pt(997) system might also arise from the Pt atoms. X-ray diffraction measurements [91] have shown that for Co layers on Pt(111) the Pt atoms in contact with Co are weakly magnetized ($\sim 0.2\mu_B$). As pointed out by Solovyev *et al.* [275], the induced spin magnetization on Pt sites might result in non negligible induced orbital moments due to the large value of the Pt spin-orbit constant (0.32 eV). For a CoPt alloy Daalderop *et al.* [281] have calculated the induced orbital momentum of Pt to be 0.07 μ_B, while the spin and orbital momentum of Co are 1.86 μ_B and 0.25 μ_B, respectively.

6.4 Hybridization and orbital momentum *vs* Co coverage

The electronic structure and related magnetism in a metal system are strongly dependent on the atomic coordination. In this respect the Co/Pt(997) system is particularly interesting because an appropriate choice of the deposition parameters (Sec. 2.4) allows to create 1D to 3D structures in a continuous way. Here we report the XMCD results obtained for 0.05 - 14.5 ML Co films deposited at 300 K.

Figure 6.12(a) shows the corresponding XAS spectra normalized at a background value before the onset of the L_3 edge. The indicated Co coverage follows the same order of the spectra. A close analysis reveals the presence of a satellite (A) at the high energy tail of the L_3 edge. The energy difference between A and the L_3 main line is about 3 eV. Additional features are visible only in the XMCD spectra reported in Fig. 6.13. Denoted with B and C, these satellites are situated at 5.6 and 11 eV from the L_3 main line, respectively. Similar features should also be found above the L_2 edge, but the broader linewidth makes it harder to distinguish them. The presence of satellites in either the XAS or the XMCD spectra is due to electron correlation effects of the Co atoms such as those described in Sec. 5.1. A Co atom in the bulk can be described by a superposition of states with $3d^6$, $3d^7$, and $3d^8$ character. If the main line is attributed to a $2p^6 3d^7$ ground state configuration excited into a $2p^5 3d^8$ state, then the satellites might be due to $2p$ hole - $3d$ hole correlation effects in the $2p^5 3d^7$ final state corresponding to a

---

[6] Equation 6.22 was derived by Bruno assuming that the exchange splitting is much larger than the d bandwidth. Since this is not the case for transition metals, a proportionality factor equal to 0.2 should be introduced for Co [232].

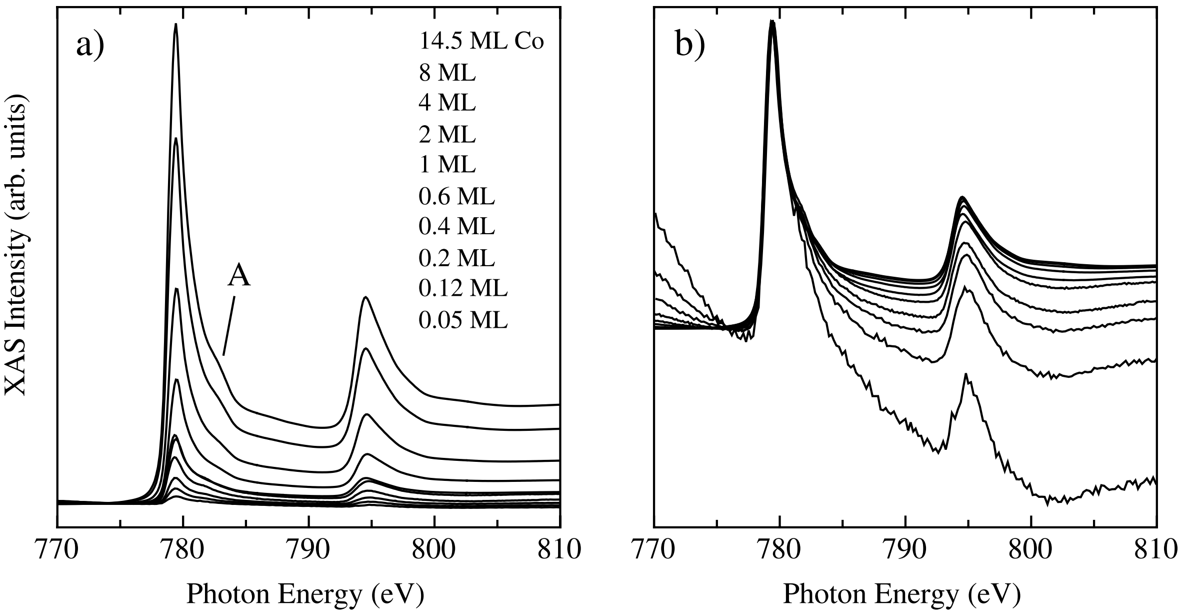

Figure 6.12: XAS spectra of Co/Pt(997) measured at room temperature for different Co coverages. (a) Spectra normalized to the background value at 774 eV. The letter A indicates a satellite peak. (b) Spectra normalized to the L_3 edge maximum. The distance between the L_3, L_2 peaks increases of about 0.4 eV going from 14.5 ML to 0.12 ML.

$2p^6 3d^6$ ground state configuration. A similar explanation has been indeed proposed for the 3.3 and 6 eV satellites observed in Ni spectra [206,248]. Changes in the hybridization of the Co electronic states as a function of the film thickness would lead to a variation of the relative weights of the $3d^n$ configurations. In particular, reducing the atomic coordination, we expect the ground state to become prevalently $3d^7$, as in Co atoms. Accordingly, satellites peaks should become less intense at low coverages. If this seems to be the case for peaks A and B, the C satellite does exactly the opposite (Fig. 6.13). We are then forced to conclude that detailed calculations of the Co excitations are needed to interpret the fine structure of the XAS and XMCD spectra. Bulk Co atoms have 12 nearest neighbors. In a Co monolayer film this number reduces to 6 Co plus 3 Pt neighbours. In a monatomic chain decorating the Pt step edge, Co has 2 Co and 5 Pt neighbours. The reduction of the atomic coordination number leads to the localization of the d states and to a decrease of the crystal field interaction. Low dimensional structures should then display enhanced atom-like properties such as the orbital polarization and the spin-orbit interaction. Figure 6.14 shows the branching ratio $L_3/(L_3+L_2)$ calculated by integrating the edge intensities after the subtraction of a linear background [as shown in Fig. 6.5(a)]. From 1 to 0.05 ML there is a net increase of the L_3 intensity with respect to L_2. This means (Sec. 6.1) that the empty states acquire a predominant $d_{5/2}$ over $d_{3/2}$

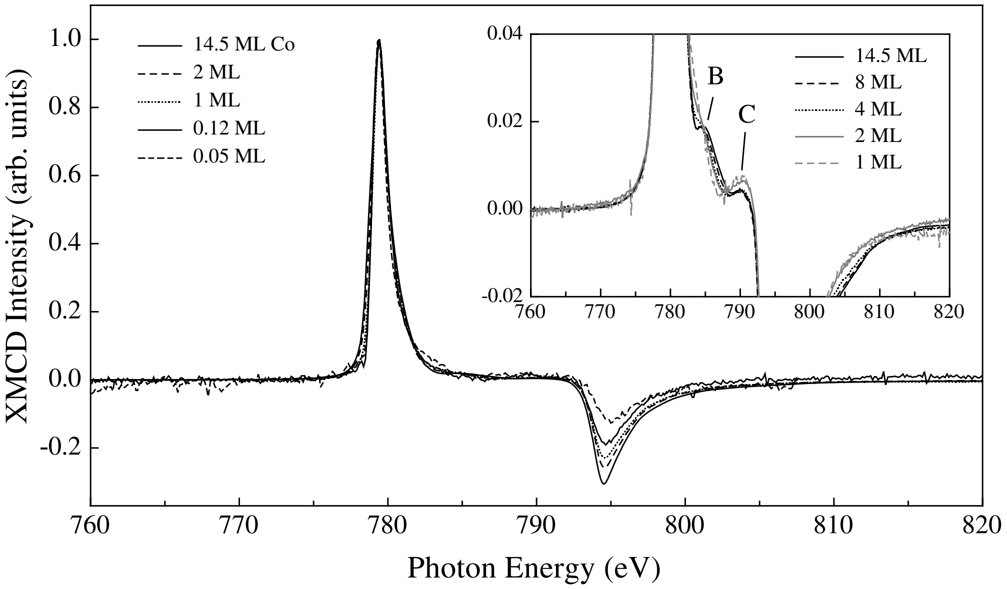

Figure 6.13: XMCD spectra of Co/Pt(997) normalized to the L_3 edge maximum. The inset shows the presence of satellites B and C superposed to the tail of the L_3 edge.

character, i.e. that the spin-orbit splitting of the final states is more effective at low coverage. Increasing the coverage, the *d* states mixing reduces the spin-orbit splitting, which is essentially a local interaction. Hence we assist to a marked change of the Co electronic structure in the very first stages of growth.

The orbital momentum should also be larger at low coverage due to the following

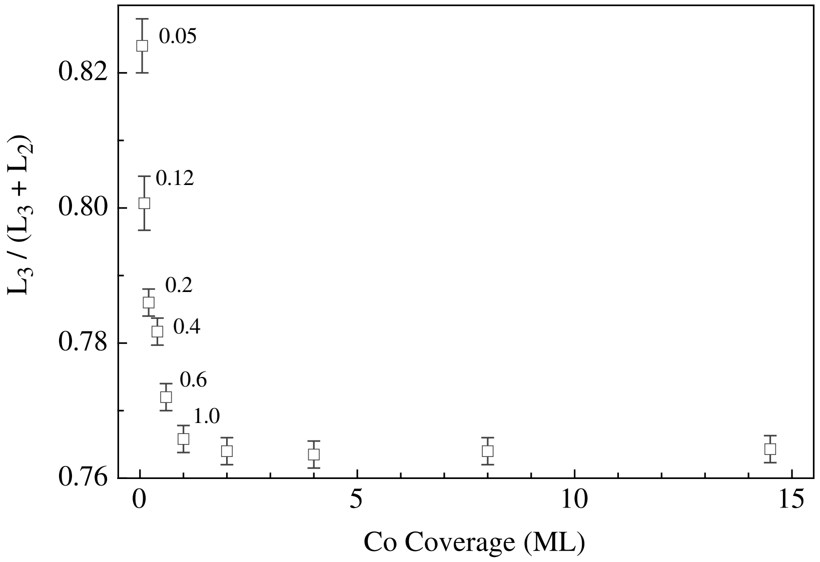

Figure 6.14: Branching ratio at the $L_{3,2}$ edge. The numbers next to the data points indicate submonolayer coverages.

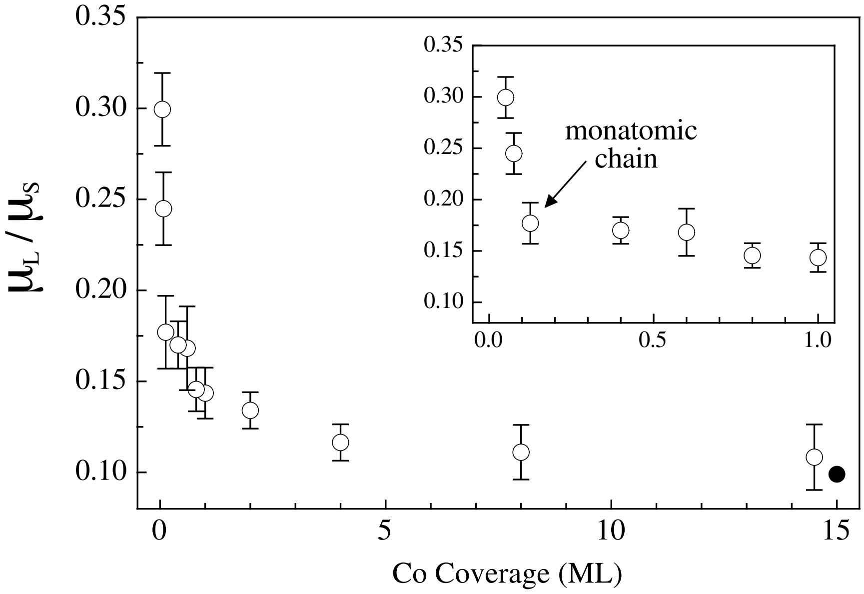

Figure 6.15: Orbital magnetic moment per spin *vs* Co coverage. The inset shows a close-up of the low coverage region.

reasons: (i) in low dimensional structures the d band is narrower, resulting in an increase of the spin magnetic moment. The spin-orbit interaction couples the orbit to the spin moment, so that the orbital magnetic moment will increase with the spin magnetic moment [284]. (ii) Symmetry reduction removes the quenching of the orbital moment, as discussed in Sec. 6.3. The marked decrease in intensity of the L_2 peak with respect to the L_3 peak in the dichroic spectra (Fig. 6.13) is a clear indication that the orbital momentum is increasing. Figure 6.15 shows the ratio μ_L/μ_S calculated by applying the dichroism sum rules (Eq. 6.9) to the spectra measured in the out of plane direction. We found an increase from $\mu_L/\mu_S = 0.11$ in the thick 14.5 ML film, to 0.14 in the monolayer film, to 0.18 in the monatomic chains. The black dot in Fig.6.15 shows the μ_L/μ_S value measured for bulk Co [233]. These changes are in line with the expected trend for the moments as a function of the atomic coordination. Both orbital and spin moment are expected to increase as the atomic coordination is reduced going from the bulk to the monatomic wire geometry. The size of the increase, however, is predicted to be very different for the two components of the moment [223]. The spin moment essentially reaches its asymptotic value when all 3d-holes have minority spin character. As this condition is approximately fulfilled already for a Co monolayer, only a small increase of the spin moment is expected from a monolayer (1.9 μ_B/atom) to a 1-D wire (2.1 μ_B/atom) [223]. The corresponding increase of the orbital moment is considerably larger. It becomes indeed a significant part of the total magnetic moment in the monatomic wire system. Assuming for the Co spin moment of the wires the calculated value of 2.1 μ_B/atom, the orbital moment of the monatomic wires is 0.4 μ_B/atom, i.e. $\sim$ 2.5 times larger than in bulk Co, which is quite remarkable for an itinerant 3d-electron system. At coverages below 0.12 ML the increase of μ_L/μ_S is even stronger. We cannot exclude, however, that part of this effect is due to Co-Pt intermixing which seems to occur in the order of 0.01 - 0.02 ML (Sec. 2.4). A comparison with μ_L/μ_S values measured for different systems is reported in Table 6.3.

System	direction	μ_L/μ_S	reference
Co bulk		0.10	[233]
1ML Co/Cu(100)	$\perp$	0.19	[234]
1 ML Co/Cu(1 1 13)	$\|\|$ to steps	0.39	[285]
Au/4 ML Co/Au(111)	$\perp$ $\|\|$	0.11 0.05	[232]
Co clusters on Au(111)	$\perp$	0.19 - 0.12[a]	[235]
(111) $CoPt_3$ homogenous alloy	$\perp$ $\|\|$	0.24 0.23	[263]
(111) $CoPt_3$ non-homog. alloy	$\perp$ $\|\|$	0.26 0.18	[263]
5 ML Co/Pt(111)	$\perp$	0.20	[262]
Pt/5 ML Co/Pt(111)	$\perp$	0.37	[262]

[a] The two values correspond to $\sim$ 300 and 8000 atoms per cluster, respectively.

Table 6.3: Comparison between μ_L/μ_S values measured with XMCD in different systems. The symbols $\perp$ and $||$ refer to the out of plane and in plane directions, respectively.

6.5 Update

During the last beamtime at ESRF, which was scheduled just before the completion of this thesis, we had the occasion to investigate the magnetic behavior of the Co wires in more detail. Although the latest data still have to be analyzed, we anticipate here a significant result. Due to improvements in the thermal shielding of the cryostat at the ID12B beamline, we were able to determine the blocking temperature of the Co monatomic wires. Figure 6.16 shows two hysteresis loops measured with the method described in Sec. 6.2 for an array of Co monatomic wires on Pt(997) at 10 and 5 K. The large value of the magnetic remanence at zero field measured at 5 K implies the existence of long range magnetic order. The difference between the remanent magnetization and

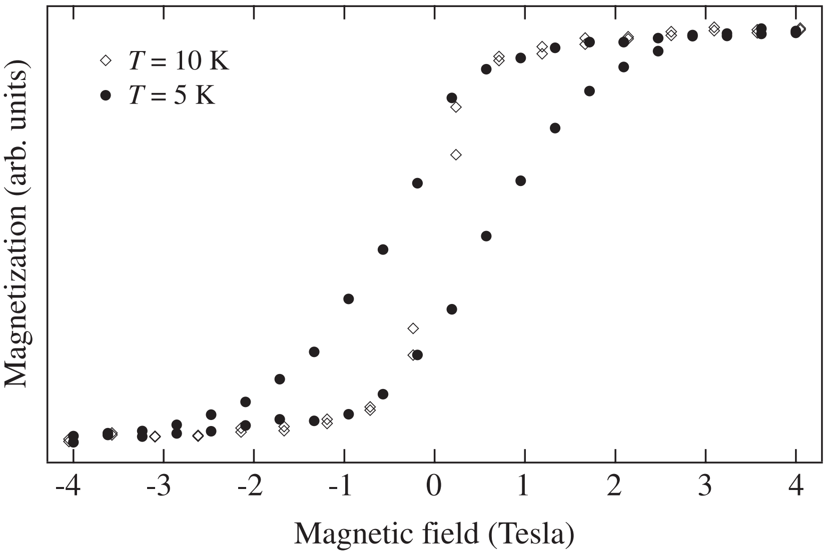

Figure 6.16: Hysteresis loops measured at 10 and 5 K for an array of Co monatomic wires on Pt(997).

the magnetization value at saturation can be probably attributed to inhomogeneities in the Co wires length (see, e.g., Figs. 2.7 and 2.21 about the wire growth process). In other words we suggest that the shortest Co wires have a lower blocking temperature than 5 K and that therefore they do not display any remanence at zero field. An alternative explanation could be the occurrence of thermal fluctuations in the vicinity of the blocking temperature.

In conclusion, our experimental results provide first insights into the magnetism of 1-D monatomic wires. The local magnetic properties and the collective magnetic behavior of the wires display distinct features that derive from the reduced atomic coordination and lowered symmetry. Circular dichroism effects at the $L_{3,2}$ absorption edges give evidence for an enhancement of the orbital Co moment by a factor ~ 2.5 with respect to the bulk metal. The 1-D wire array display a superparamagnetic behavior over a wide range of temperature and external field. The blocking temperature of the system is situated between 10 and 5 K. The 1-D character of the Co wires is manifested by the uniaxial anisotropic magnetic response to an external field.

Acknowledgements

I thank my thesis advisor, Professor Klaus Kern, for having given me the opportunity to work in his research group. His ongoing support has made it possible to pursue the different arguments treated in the present work. A two-years grant from the University of Genova, Italy, is also acknowledged. I am grateful to Dr. Klaus Kuhnke for his keen disposition at discussing any argument related to this thesis and for the careful reading of the manuscript. I would also like to thank Dr. Carlo Carbone and Professors Benoit Deveaud-Plédran, Giorgio Margaritondo, and Ugo Valbusa for serving on the jury committee of this thesis.

Martial Blanc and Vittorio Marsico, *très cheres collègues et néanmoins amis*, have welcomed me at the EPFL, taught me French and the functioning of the He-scattering apparatus. *Merci.* Samuel Sarbach has helped me during the last months in the laboratory and has very effectively fought my prejudices against the quality of the wine *du Valais.* I am grateful to Lukas Bürgi and Olivier Jeandupeux for getting me started with the STM, for their disinterested advices, and for some genuine swiss meals. In the course of this work I have also profited from many stimulating conversation about heteroepitaxial growth, surface chemistry, and STM with Professor Harald Brune and Dr. Johannes Barth. I have much appreciated the time spent during relax and working hours with my *Bürogenossen* Alex “Omone” Bittner, Alex Schneider, and Paolo Messina.

I thank Fabien Picaud, Dr. Cristophe Ramseyer, and Professor Claude Girardet of the Laboratoire de Physique Moléculaire de l’Université de Franche-Comté, Besançon, France, for their theoretical modelling of epitaxial growth on Pt stepped surfaces. The results presented in Secs. 3.2 and 3.3 are due to their work and have greatly helped our understanding of the Ag/Co/Pt system.

I am indebted to Dr. Carlo Carbone of the Institut für Festkörperforschung of the Forschungszentrum Jülich, Germany, for having introduced me to the study of low-dimensional magnetic structures, for having proposed and guided the experiments reported in Chapters 5 and 6. He has also greatly contributed to my understanding of

ARPES and XMCD. A heartly thank goes to the people of his group: Kalo Maiti, Cristina Malagoli, and, in particular, to Arne Dallmeyer with whom I have shared most of the beamtimes at BESSY and ESRF. The ID12B beamline staff at ESRF, Philippe Ohresser, Sarnjeet Dhesi, Kenneth Larsson, and Nick Brookes, has provided qualified assistance to the XMCD experiments. Philippe and Sarnjeet have earnestly enjoyed their stand-by periods with us.

The scientific and technical staff of the Institut de Physique Expérimentale of the EPFL has to be credited for creating an optimal working atmosphere made of friendliness, experience, and efficiency. It has been a pleasure to work here.

Finally, I would like to thank my family and friends, for their support is the most important of all.

Bibliography

[1] E. Hulpke, Helium Atom Scattering from Surfaces, in *Springer Series in Surface Sciences, Vol. 27* (Springer, Berlin, 1989).

[2] D. Farias and K. Rieder, Rep. Prog. Phys. **61**, 1575 (1998).

[3] B. Poelsema and G. Comsa, Scattering of Thermal Energy Atoms, in *Springer Tracts in Modern Physics, Vol. 115* (Springer, Berlin, 1989).

[4] O. Stern, Naturwissenschaften **17**, 391 (1929).

[5] K. Rieder and T. Engel, Phys. Rev. Lett. **43**, 373 (1979).

[6] T. Engel and K. Rieder, Structural Studies of Surfaces with Atomic and Molecular Beam Diffraction, in *Springer Tracts in Modern Physics, Vol. 91* (Springer, Berlin, 1982).

[7] G. Comsa, G. Mechtersheimer, B. Poelsema, and S. Tomoda, Surf. Sci. **89**, 123 (1979).

[8] V. Marsico, Ph.D. thesis, Ecole Polytechnique Fédérale de Lausanne, 1995.

[9] H. Schief, Ph.D. thesis, Ecole Polytechnique Fédérale de Lausanne, 1995.

[10] M. Blanc, K. Kuhnke, V. Marsico, and K. Kern, Surf. Sci. **414**, L964 (1998).

[11] B. Poelsema, L. Verheji, and G. Comsa, Surf. Sci. **148**, 117 (1984).

[12] H. Hopster, H. Ibach, and G. Comsa, J. Cat. **46**, 37 (1977).

[13] J. Gland, Surf. Sci. **93**, 487 (1980).

[14] H. Steininger, S. Lehwald, and H. Ibach, Surf. Sci. **123**, 1 (1982).

[15] M. McClellan, F. McFeely, and J. Gland, Surf. Sci. **123**, 188 (1983).

[16] A. Winkler *et al.*, Surf. Sci. **201**, 419 (1988).

[17] A. Rar and T. Matsushima, Surf. Sci. **94**, 89 (1994).

[18] H. Wang *et al.*, Surf. Sci. **372**, 267 (1997).

[19] K. Peterlinz and K. Sibener, Surf. Sci. **344**, L1239 (1995).

[20] C. Campbell, G. Ertl, H. Kuipers, and J. Segner, Surf. Sci. **107**, 220 (1981).

[21] T. Zambelli, J. Barth, J. Wintterlin, and G. Ertl, Nature **390**, 495 (1997).

[22] B. Poelsema *et al.*, Surf. Sci. **272**, 269 (1992).

[23] P. Gambardella *et al.*, Phys. Rev. B **61**, 2254 (2000).

[24] P. Gambardella *et al.*, Surf. Sci. **449**, 93 (2000).

[25] M. Blanc, Ph.D. thesis, Ecole Polytechnique Fédérale de Lausanne, 1998.

[26] D. Kandel and J. Weeks, Phys. Rev. Lett. **74**, 3632 (1995).

[27] K. Kuhnke *et al.*, Surf. Sci. **27**, 118 (1992).

[28] K. Kern, R. David, and G. Comsa, Rev. Sci. Instrum. **56**, 369 (1986).

[29] R. David, K. Kern, P. Zeppenfeld, and G. Comsa, Rev. Sci. Instrum. **57**, 2771 (1986).

[30] K. Kuhnke, K. Kern, R. David, and G. Comsa, Rev. Sci. Instrum. **65**, 3458 (1994).

[31] C. J. Chen, *Introduction to Scanning Tunneling Microscopy* (Oxford University Press, New York, 1993).

[32] F. Besenbacher, Rep. Prog. Phys. **59**, 1737 (1996).

[33] G. Binnig, H. Rohrer, C. Gerber, and E. Weibel, Phys. Rev. Lett. **49**, 57 (1982).

[34] G. Binnig and H. Rohrer, Helvetica Physica Acta **55**, 726 (1982).

[35] R. Hamers, Methods of Tunneling Spectroscopy with the STM, in *Scanning Tunneling Microscopy and Spectroscopy* (D.H. Bonell ed., VCH Publications, New York, 1993).

[36] J. Bardeen, Phys. Rev. Lett. **6**, 57 (1961).

[37] E. L. Wolf, *Principles of Electron Tunneling Spectroscopy* (Oxford University Press, New York, 1985).

[38] J. Tersoff and D. R. Hamann, Phys. Rev. Lett. **50**, 1998 (1983).

[39] A. Selloni, P. Carnevali, E. Tosatti, and C. D. Chen, Phys. Rev. B **31**, 2602 (1985).

[40] N. Lang, Phys. Rev. B **34**, 5947 (1986).

[41] M. F. Crommie, C. P. Lutz, and D. M. Eigler, Science **262**, 218 (1993).

[42] L. Bürgi *et al.*, Phys. Rev. Lett. **81**, 5370 (1998).

[43] L. Bürgi, Ph.D. thesis, Ecole Polytechnique Fédérale de Lausanne, 1999.

[44] J. Wintterlin *et al.*, Phys. Rev. Lett. **62**, 59 (1989).

[45] C. Chen, Phys. Rev. Lett. **65**, 448 (1990).

[46] T. Jung, Y. Mo, and F. Himpsel, Phys. Rev. Lett. **74**, 1641 (1995).

[47] J. Stroscio, D. Pierce, A. Davies, and R. Celotta, Phys. Rev. Lett. **75**, 2960 (1995).

[48] B. C. Stipe, M. A. Rezaei, and W. Ho, Science **280**, 1732 (1998).

[49] H. Röder, R. Schuster, H. Brune, and K. Kern, Phys. Rev. Lett. **71**, 2086 (1993).

[50] H. Röder, Ph.D. thesis, Ecole Polytechnique Fédérale de Lausanne, 1994.

[51] M. Paffet, C. Campbell, and T. Taylor, Langmuir **1**, 741 (1985).

[52] N. Lang, Scanning Tunneling Microscopy III, in *Springer Series in Surface Sciences, Vol. 29* (R. Wiedensanger and H.J. Güntherhodt eds., Springer, Berlin, 1993).

[53] A. Hirstein, Ph.D. thesis, Ecole Polytechnique Fédérale de Lausanne, 1998.

[54] H. Röder *et al.*, Nature **366**, 141 (1993).

[55] K. Besocke, Surf. Sci. **181**, 145 (1987).

[56] P. Gambardella *et al.* (unpublished).

[57] H. Brune, Surf. Sci. Rep. **31**, 121 (1998), and references therein.

[58] G. Bassett, Phil. Mag. **3**, 1042 (1958).

[59] H. Bethge, Surf. Sci. **3**, 33 (1964).

[60] P. Petroff, A. Gossard, and W. Wiegmann, Appl. Phys. Lett. **45**, 620 (1984).

[61] M. Tsuchiya, P. Petroff, and L. Coldren, Appl. Phys. Lett. **54**, 169 (1989).

[62] R. Nötzel *et al.*, Phys. Rev. B **54**, 3507 (1991).

[63] M. Sundaram, S. Chalmers, P. Hopkins, and A. Gossard, Science **254**, 1326 (1991).

[64] M. Miller *et al.*, Phys. Rev. Lett. **68**, 3464 (1992).

[65] F. J. Himpsel and J. E. Ortega, Phys. Rev. B **50**, 4992 (1994).

[66] M. Mundschau, E. Bauer, and W. Swiech, J. Appl. Phys. **65**, 581 (1989).

[67] T. Jung, Y. Mo, and F. Himpsel, Phys. Rev. Lett. **74**, 1641 (1994).

[68] T. Jung, R. Schlitter, J. Gimzewski, and F. Himpsel, Appl. Phys. A **61**, 467 (1995).

[69] D. Petrovykh, F. Himpsel, and T. Jung, Surf. Sci. **407**, 189 (1998).

[70] J. de la Figuera *et al.*, Appl. Phys. Lett. **66**, 1006 (1995).

[71] J. Camarero *et al.*, Mater. Res. Soc. Symp. Proc. **384**, 49 (1995).

[72] S. Papadia, M. Desjonquères, and D. Spanjaard, Phys. Rev. B **51**, 4083 (1996).

[73] E. Hahn *et al.*, Phys. Rev. Lett. **72**, 3378 (1994).

[74] H. Röder, K. Bromann, H. Brune, and K. Kern, Surf Sci. **376**, 13 (1997).

[75] H. Brune, H. Röder, C. Boragno, and K. Kern, Phys. Rev. Lett. **73**, 1955 (1994).

[76] A. Bogicevic, J.Strömquist, and B. Lundqvist, Phys. Rev. Lett. **81**, 637 (1998).

[77] H. Röder, H. Brune, J. Bucher, and K. Kern, Surf Sci. **298**, 121 (1993).

[78] F. Picaud, C. Ramseyer, C. Girardet, and P. Jensen (unpublished).

[79] Y. Mo and F. Himpsel, Phys. Rev. B **50**, 7868 (1994).

[80] H. Brune *et al.*, Surf. Sci. **349**, L115 (1996).

[81] R. Stumpf and M. Scheffler, Phys. Rev. Lett. **72**, 254 (1994).

[82] B. Holst, M. Nohlen, K. Wandelt, and W. Allison, Surf. Sci. **377-379**, 891 (1997).

[83] H. Brune, M. Giovannini, K. Bromann, and K. Kern, Nature **394**, 451 (1998).

[84] K. Wandelt (unpublished).

[85] P. Carcia, J. Appl. Phys. **63**, 5066 (1988).

[86] W. Zeper, F. Greidanus, P. Carcia, and C. Fincher, J. Appl. Phys. **65**, 4971 (1989).

[87] C. Lee *et al.*, Phys. Rev. B. **42**, 11384 (1990).

[88] N. McGee, M. Johnson, J. de Vries, and J. aan de Stegge, J. Appl. Phys. **73**, 3418 (1993).

[89] T. Kingetsu, J. Appl. Phys. **76**, 4267 (1994).

[90] P. Grütter and U. Dürig, Phys. Rev. B **49**, 2021 (1994).

[91] S. Ferrer *et al.*, Phys. Rev. B **56**, 9848 (1997).

[92] E. Lundgren *et al.*, Surf. Sci. **423**, 357 (1999).

[93] F. Himpsel, J. E. Ortega, G. Mankey, and R. Willis, Adv. in Phys. **47**, 511 (1998), and references therein.

[94] C. Chappert and P. Bruno, J. Appl. Phys. **64**, 5736 (1988).

[95] C. Lee *et al.*, Phys. Rev. B **42**, 1066 (1990).

[96] B. Engel, M. Wiedmann, R. V. Leeuwen, and C. Falco, Phys. Rev. B **48**, 9894 (1993).

[97] D. Weller *et al.*, Phys. Rev. Lett. **72**, 2097 (1994).

[98] H. Elmers *et al.*, Phys. Rev. Lett. **73**, 898 (1994).

[99] P. Gambardella, M. Blanc, K. Kuhnke, and K. Kern (unpublished).

[100] J. Shen *et al.*, Phys. Rev. B **56**, 11134 (1997).

[101] M. Saint-Leger *et al.*, Surf. Sci. **418**, 485 (1998).

[102] A. Atrei *et al.*, Surf. Sci. **339**, 323 (1995).

[103] S. Rusponi *et al.* (unpublished).

[104] C. Goyhenex and G. Tréglia, Surf. Sci. , in press.

[105] G. Kellogg, Phys. Rev. Lett. **67**, 216 (1991).

[106] G. L. Kellogg, Phys. Rev. Lett. **76**, 98 (1996).

[107] G. Kellogg, Surf. Sci **266**, 18 (1992).

[108] M. Sambi, E. Pin, and G. Granozzi, Surf. Sci **340**, 215 (1995).

[109] M. Wuttig, Y. Gauthier, and S. Blügel, Phys. Rev. Lett. **70**, 3619 (1993).

[110] M. Wuttig, S. Junghans, T. Flores, and S. Blügel, Phys. Rev. B **53**, 7551 (1996).

[111] J. Schneider, A. Rosenhahn, and K. Wandelt, Appl. Surf. Sci **142**, 68 (1999).

[112] S. Blügel, Appl. Phys. A **63**, 595 (1996).

[113] J. Rodriguez, Surf. Sci. Rep. **24**, 223 (1996).

[114] P. Poulopoulous, J. Lindner, and K. B. M. Farle, Surf. Sci. **437**, 277 (1999).

[115] F. den Broeder, D. Kuiper, A. van de Mosselaer, and W. Hoving, Phys. Rev. Lett. **60**, 2769 (1988).

[116] J. D. Miguel *et al.*, Surf. Sci. **211-212**, 732 (1989).

[117] E. Fullerton, D. Kelly, I. S. J. Guimpel, and Y. Bruynseraede, Phys. Rev. Lett. **68**, 859 (1992).

[118] P. Beliën *et al.*, Phys. Rev. B **50**, 9957 (1994).

[119] W. Chiang, W. Pratt, M. Herrold, and D. Baxter, Phys. Rev. B **58**, 5602 (1998), and references therein.

[120] R. Schad *et al.*, Phys. Rev. B **59**, 1242 (1999).

[121] W. Pratt *et al.*, Phys. Rev. Lett. **66**, 3060 (1991).

[122] E. van Alphen and W. de Jonge, Phys. Rev. B **51**, 8182 (1995).

[123] R. Hwang, Phys. Rev. Lett. **76**, 4757 (1996).

[124] E. Tober *et al.*, Phys. Rev. Lett. **81**, 1897 (1998).

[125] J. Tersoff, Phys. Rev. Lett. **74**, 434 (1995).

[126] E. Bauer and J. van der Merwe, Phys. Rev. B **33**, 3657 (1986).

[127] H. Skriver and N. Rosengaard, Phys. Rev. B **46**, 7157 (1992).

[128] A. Christensen *et al.*, Phys. Rev. B **56**, 5822 (1997).

[129] M. Desjonquères and D. Spanjaard, *Concepts in surface physics* (Springer, Berlin, 1996).

[130] A. L. J. Guevara and M. Weissmann, Phys. Rev. B **52**, 11509 (1995).

[131] M. Finnis and J. Sinclair, Phil. Mag. A **50**, 45 (1984).

[132] V. Rosato, M. Guiloppe, and B. Legrand, Phil. Mag. A **59**, 321 (1989).

[133] F. Ducastelle, Ph.D. thesis, Univ. Paris-Sud, 1972.

[134] R. Gupta and H. Kharoo, J. Chem. Phys. **74**, 3577 (1981).

[135] M. Desjonquères and D. Spanjaard, J. Phys. C **15**, 4007 (1982).

[136] G. Allan and M. Lannoo, Surf. Sci **40**, 375 (1973).

[137] A. Sutton and J. Chen, Phil. Mag. Lett. **61**, 139 (1990).

[138] C. Mottet, R. Ferrando, F. Hontinfinde, and A. Levi, Surf. Sci. **417**, 220 (1998).

[139] E. Fisher and J. Renken, Phys. Rev. **135**, A482 (1964).

[140] L. Vitos, A. Ruban, H. Skriver, and J. Kollar, Surf. Sci. **411**, 186 (1998).

[141] G. Somorjai, *Introduction to surface chemistry and catalysis* (John Wiley & Sons, New York, 1994).

[142] A. Eichler and J. Hafner, Phys. Rev. Lett. **79**, 4481 (1997).

[143] B. Stipe *et al.*, Phys. Rev. Lett. **78**, 4410 (1997).

[144] B. Stipe, M. Rezaei, and W. Ho, J. Chem. Phys. **107**, 6443 (1997).

[145] J. Nørskov, Rep. Prog. Phys. **53**, 1253 (1990).

[146] B. Hammer and J. Nørskov, in *Chemisorption and reactivity on supported metal clusters and thin films* (R.M. Lambert and G. Pacchion eds., Kluwer, Amsterdam, 1997).

[147] A. Zangwill, *Physics at surfaces* (Cambridge University press, Cambridge, 1988).

[148] R. Masel, *Principles of adsorption and reaction on solid surfaces* (John Wiley, New York, 1996).

[149] J. Slater, *Quantum theory of molecules and solids* (McGraw-Hill, New York, 1963).

[150] D. Newns, Phys. Rev. **178**, 1123 (1969).

[151] N. Lang and A. Williams, Phys. Rev. B **18**, 616 (1978).

[152] B. Hammer, O. Nielsen, and J. Nørskov, Cat. Lett. **46**, 31 (1997).

[153] I. Toyoshima and G. Somorjai, Cat. Rev. Sci. Eng. **19**, 105 (1979).

[154] B. Hammer and J. Nørskov, Nature **376**, 238 (1995).

[155] B. Hammer and J. Nørskov, Surf. Sci. **343**, 211 (1995).

[156] B. Hammer, Y. Morikawa, and J. Nørskov, Phys. Rev. Lett. **76**, 2141 (1996).

[157] B. Hellsing and S. Gao, Solid State Comm. **90**, 223 (1994).

[158] C. Puglia *et al.*, Surf. Sci. **342**, 119 (1995).

[159] W. Eberhardt, T. Upton, S. Cramm, and L. Incoccia, Chem. Phys. Lett. **146**, 561 (1988).

[160] S. Holloway and J. Gadzuk, J. Chem. Phys. **82**, 5203 (1985).

[161] A. Luntz, M. Williams, and D. Bethune, J. Chem. Phys. **89**, 4381 (1988).

[162] P. Feibelman, S. Esch, and T. Michely, Phys. Rev. Lett. **77**, 2257 (1996).

[163] A. Szabó, M. Anderson, and J. Yates, J. Chem. Phys. **96**, 6191 (1992).

[164] J. Wintterlin, R. Schuster, and G. Ertl, Phys. Rev. Lett. **77**, 123 (1996).

[165] P. Feibelman, private communication .

[166] B. Hammer and J. Nørskov, Phys. Rev. Lett. **79**, 4441 (1997).

[167] J. Luo *et al.*, Surf. Sci. **274**, 53 (1992).

[168] D. Jennison, P. Schultz, and M. Sears, Phys. Rev. Lett. **77**, 4828 (1996).

[169] A. Luntz, J. Grimblot, and D. Fowler, Phys. Rev. B **39**, 12903 (1989).

[170] S. Dahl *et al.*, Phys. Rev. Lett. **83**, 1814 (1999).

[171] B. Hammer, Phys. Rev. Lett. **83**, 3681 (1999).

[172] F. B. de Mongeot, U. Valbusa, and M. Rocca, Surf. Sci. **339**, 291 (1995).

[173] T. Zambelli, J. Wintterlin, J. Trost, and G. Ertl, Science **273**, 1688 (1996).

[174] Y. Lozovik and A. Popov, Surf. Sci. **414**, 57 (1998).

[175] Y. Yeo, L. Vattuone, and D. King, J. Chem. Phys. **106**, 392 (1997).

[176] P. Davies, M. Quinlan, and G. Somorjai, Surf. Sci. **121**, 290 (1982).

[177] V. Marsico, M. Blanc, K. Kuhnke, and K. Kern, Phys. Rev. Lett. **78**, 94 (1997).

[178] J. Sinfelt, *Bimetallic catalysts: discoveries, concepts, and applications* (John Wiley & Sons, New York, 1983).

[179] J. Bertolini, Surf. Rev. Lett. **3**, 1857 (1996).

[180] J. Sachtler and G. Somorjai, J. Cat. **81**, 77 (1983).

[181] M. Paffett, C. Campbell, and T. Taylor, Langmuir **1**, 741 (1985).

[182] C. Campbell, M. Paffett, and A. Voter, J. Vac. Sci. Tech. A **4**, 1342 (1986).

[183] F. Besenbacher *et al.*, Science **279**, 1913 (1998).

[184] J. Xu and J. Yates, J. Chem. Phys. **99**, 725 (1993).

[185] A. Anton and D. Cadogan, J. Vac. Sci. Tec. A **9**, 1890 (1991).

[186] L. Verheij *et al.*, Chem. Phys. Lett. **166**, 523 (1990).

[187] L. Verheij and M. Hugenschmidt, Surf. Sci. **324**, 185 (1995).

[188] L. Verheij and M. Hugenschmidt, Surf. Sci. **416**, 37 (1998).

[189] D. Collins, J. Lee, and W. Spicer, Surf. Sci. **35**, 592 (1975).

[190] M. Crommie, C. Lutz, and D. Eigler, Nature **363**, 524 (1993).

[191] Y. Hasegewa and P. Avouris, Phys. Rev. Lett. **71**, 1071 (1993).

[192] A. Biedermann *et al.*, Phys. Rev. Lett. **76**, 4179 (1996).

[193] J. Li, W.-D. Schneider, and R. Berndt, Phys. Rev. B **56**, 7656 (1997).

[194] P. Segovia, D. Purdie, M. Heisenberger, and Y. Baer, Nature **402**, 504 (1999).

[195] A. Dallmeyer *et al.*, Phys. Rev. B **61**, R5133 (2000).

[196] G. Margaritondo, Nuovo Cim. **18**, 1 (1995).

[197] G. Margaritondo, J. Synchrotron Rad. **2**, 148 (1995).

[198] R. Bachrach, *Synchrotron Radiation Research* (Plenum, New York, 1995).

[199] B. Feuerbacher, B. Fitton, and R. Willis, *Photoemission and the electronic properties of surfaces* (Wiley, New York, 1978).

[200] C. Brundle and A. Baker, *Electron spectroscopy: theory, techniques and applications* (Academic Press, New York, 1977).

[201] E. Plummer and W. Eberhardt, Adv. Phys. Chem. **49**, 533 (1982).

[202] F. Himpsel, Adv. in Physics **32**, 1 (1983).

[203] S. Kevan, *Angle-resolved photoemission: theory and current applications* (Elsevier, Amsterdam, 1992).

[204] S. Gasiorowicz, *Quantum physics* (Wiley, New York, 1974).

[205] S. Schiff, *Quantum mechanics* (Wiley, New York, 1980).

[206] T. Jo and G. Sawatzky, Phys. Rev. B **43**, 8771 (1991).

[207] G. van der Laan and B. Thole, J. Phys. Condens. Matter **4**, 4181 (1992).

[208] S. Hüfner, *Photoelectron spectroscopy: principles and applications* (Springer, Berlin, 1995).

[209] W. Peatman *et al.*, Rev. Sci. Instrum. **60**, 1445 (1989).

[210] R. Kläsges, Ph.D. thesis, Forschungszentrum Jüelich, 1995.

[211] J. Kessler, *Polarized electrons* (Springer, Berlin, 1976).

[212] J. Cooper, Phys. Rev. **128**, 681 (1962).

[213] M. Shek, P. Stefan, I. Lindau, and W. Spicer, Phys. Rev. B **27**, 7288 (1983).

[214] J. Yeh and I. Lindau, Atomic data and nuclear tables **32**, 1 (1985).

[215] H. Knoppe and E. Bauer, Phys. Rev. B **48**, 1794 (1993).

[216] E. Vescovo, C. Carbone, and O. Rader, Sol. State Comm **94**, 751 (1995).

[217] M. Shek, P. Stefan, I. Lindau, and W. Spicer, Phys. Rev. B **27**, 7277 (1983).

[218] U. Schneider, G. Castro, and K. Wandelt, Surf. Sci. **287-288**, 146 (1993).

[219] W. Clemens *et al.*, Solid State Commun. **81**, 739 (1992).

[220] C. Schneider *et al.*, J. El. Spectr. Rel. Phen. **51**, 263 (1990).

[221] U. Alkemper *et al.*, Phys. Rev. B **50**, 17496 (1994).

[222] M. Weinert and A. Freeman, J. Magn. magn. Mater. **38**, 23 (1983).

[223] G. Bihlmayer, X. Nie, and S. Blügel (unpublished).

[224] E. Ising, Z. Phys. **31**, 253 (1925).

[225] N. Mermin and H. Wagner, Phys. Rev. Lett. **17**, 1133 (1966).

[226] U. Gradmann, J. Magn. magn. Mater. **100**, 481 (1991).

[227] U. Gradmann, in *Handbook of Magnetic Materials* (Vol. 7/1 pp. 1-96, K.H.J. Buschow ed., Elsevier, Amsterdam, 1993).

[228] G. van der Laan *et al.*, Phys. Rev. B **34**, 6529 (1986).

[229] G. Schütz *et al.*, Phys. Rev. Lett. **58**, 737 (1987).

[230] C. Chen, N. Smith, and F. Sette, Phys. Rev. B **43**, 6785 (1991).

[231] Y. Wu *et al.*, Phys. Rev. Lett. **69**, 2307 (1992).

[232] D. Weller *et al.*, Phys. Rev. Lett. **75**, 3752 (1995).

[233] C. Chen *et al.*, Phys. Rev. Lett. **75**, 152 (1995).

[234] M. Tischer *et al.*, Phys. Rev. Lett. **75**, 1602 (1995).

[235] H. Dürr *et al.*, Phys. Rev. B **59**, R701 (1999).

[236] J. Stöhr, J. Mag. mag. Mat. **200**, 470 (1999).

[237] J. Erskine and E. Stern, Phys. Rev. B **12**, 5016 (1975).

[238] B. Thole, P. Carra, F. Sette, and G. van der Laan, Phys. Rev. Lett. **68**, 1943 (1992).

[239] N. Smith, C. Chen, F. Sette, and L. Mattheiss, Phys. Rev. B **46**, 1023 (1992).

[240] M. Altarelli, Phys. Rev. B **47**, 597 (1993).

[241] P. Carra, B. Thole, M. Altarelli, and X. Wang, Phys. Rev. Lett. **70**, 694 (1993).

[242] J. Stöhr and H. König, Phys. Rev. Lett. **75**, 3748 (1995).

[243] H. Dürr and G. van der Laan, Phys. Rev. B **54**, R760 (1996).

[244] R. Wu and A. Freeman, J. Mag. mag. Mat. **200**, 498 (1999).

[245] *American Institut of Physics Handbook* (Mc Graw Hill, New York, 1972).

[246] R. Wu and A. Freeman, J. Mag. mag. Mat. **132**, 103 (1994).

[247] G. Guo and H. Ebert, Phys. Rev. B **50**, 3861 (1994).

[248] G. van der Laan and B. Thole, J. Phys. Condens. Matter **4**, 4181 (1992).

[249] R. Wu, D. Wang, and A. Freeman, Phys. Rev. Lett. **71**, 3581 (1993).

[250] R. Wu and A. Freeman, Phys. Rev. Lett. **73**, 1994 (1994).

[251] G. Daalderop, P. Kelly, and M. Schuurmans, Phys. Rev. B **50**, 9989 (1994).

[252] N. B. J. Goulon *et al.*, Physica B **208-209**, 199 (1995).

[253] J. Ziman, *Principles of the theory of solids* (Cambridge university press, Cambridge, 1972).

[254] A. Aharoni, *Introduction to the theory of ferromagnetism* (Clarendon press, Oxford, 1996).

[255] M. Bander and D. Mills, Phys. Rev. B **38**, 12015 (1988).

[256] E. Lieb and D. Mattis, Phys. Rev. **125**, 164 (1962).

[257] M. Walker and T. Raijgrok, Phys. Rev. **171**, 513 (1968).

[258] J. Dorantes-Dávila and G. Pastor, Phys. Rev. Lett. **81**, 208 (1998).

[259] J. Shen *et al.*, Phys. Rev. B **56**, 2340 (1997).

[260] J. Hauschild, H. Elmers, and U. Gradmann, Phys. Rev. B **57**, R677 (1998).

[261] J. Mydosh and G. Nieuwenhuys, in *Ferromagnetic materials* (D.H. Wohlfart ed., North-Holland Publishing Company, New York, 1980), Chap. 2.

[262] J. Thiele, C. Boeglin, K. Hricovini, and F. Chevrier, Phys. Rev. B **53**, R11934 (1996).

[263] W. Grange *et al.*, Phys. Rev. B **58**, 6298 (1998).

[264] A. Berger, U. Linke, and H. Oepen, Phys. Rev. Lett. **68**, 839 (1992).

[265] H. Choi *et al.*, Phys. Rev. Lett. **82**, 1947 (1999).

[266] R. Kawakami, E. Escorcia-Aparicio, and Z. Qiu, Phys. Rev. Lett. **77**, 2570 (1996).

[267] R. Kawakami *et al.*, Phys. Rev. B **58**, R5924 (1998).

[268] D. Craik, *Structure and properties of magnetic materials* (Pion Ltd, London, 1971).

[269] S. Chikazumi, *Physics of ferromagnetiism* (Clarendon Press, Oxford, 1996).

[270] H. Draaisma and W. de Jonge, J. Appl. Phys. **64**, 3610 (1988).

[271] C. Stamm *et al.*, Science **282**, 449 (1998).

[272] M. Scheinfein, K. Schmidt, K. Heim, and G. Hembree, Phys. Rev. Lett. **76**, 1541 (1996).

[273] H.A.Dürr *et al.*, Science **277**, 213 (1997).

[274] D. Wang, R. Wu, and A. Freeman, Phys. Rev. B **47**, 14932 (1993).

[275] I. Solovyev, P. Dederichs, and I. Mertig, Phys. Rev. B **52**, 13419 (1995).

[276] G. Pastor, J. Dorantes-Dávila, S. Pick, and H. Dreyssé, Phys. Rev. Lett. **75**, 326 (1995).

[277] P. Bruno, Phys. Rev. B **39**, 865 (1989).

[278] L. Zhou, D. Wang, and Y. Kawazoe, Phys. Rev. B **60**, 9545 (1999).

[279] G. van der Laan, J. Phys.: Condens. Matter **10**, 3239 (1998).

[280] H. van Vleck, Phys. Rev. **52**, 1178 (1937).

[281] G. Daalderop, P. Kelly, and M. Schuurmans, Phys. Rev. B **44**, 12054 (1991).

[282] S. Dhesi *et al.*, Phys. Rev. B **60**, 12852 (1999).

[283] D. Wang, R. Wu, and A. Freeman, J. Mag. mag. Mat. **129**, 237 (1994).

[284] O. Hjortstam *et al.*, Phys. Rev. B **53**, 9204 (1996).

[285] H. Dürr *et al.*, Phys. Rev. B **58**, R11853 (1998).

Curriculum vitae

Name:	Pietro Gambardella
Nationality:	Italian
Date of Birth:	14 July, 1972.

Education:

June 2000	PhD thesis, EPF Lausanne.
Dec. 1996 – July 2000	Research and teaching assistant at the Institute for Experimental Physics of the Swiss Federal Institute of Technology in Lausanne.
1996	Fellowship "Borsa di studio di perfezionamento estero", Università degli studi di Genova, Italy.
1996	TOEFL and Graduate Record Examination (GRE) in Physics.
1991 – 1996	Diploma di Laurea in Fisica, Università degli studi di Genova, Italy.
Apr. 1995 – June 1995	Erasmus exchange program: Oxford Brookes University, Oxford, UK.
July 1995 – Sept. 1995	Summer placement: Oxford Applied Research Ltd, Witney, Oxon, UK.
1986 – 1991	High school at the Liceo Scientifico G.D. Cassini, Genova, Italy.